COLLECTED PAPERS

ON

NANO/ATOM PHOTONICS

Volume 14

August 1998－July 1999

Professor

Motoichi OHTSU

TOKYO INSTITUTE OF TECHNOLOGY

Interdisciplinary Graduate School of Science and Engineering

4259 Nagatsuta, Midori-ku, Yokohama, Kanagawa 226-8502, JAPAN

TEL : +81－45－924－5455

FAX : +81－45－924－5599

E-mail : ohtsu @ ae. titech. ac. jp

PREFACE

In order to realize the ultimate status of light and matter, M. Ohtsu tries to control the spatial properties of light. The approach he has used is through the research of near-field optics and its application to nano-structure fabrication and atom manipulation. This will open up a new era of nano/atom photonics. It should be pointed out that the nano/atom photonics is closely related to quantum optics, atom optics, high density optical storage, nano-structure fabrication technology, and so on (see the figure on the next page). And for this relationship of near-field optics with a variety of fields, nano/atom photonics exhibits rapid progress. Further research will be done to realize novel nanometric materials and devices.

A "NEAR FIELD PHOTONICS" research group, which is executed in Kanagawa Academy of Science and Technology(KAST) and directed by Ohtsu, has started from April,1998 in order to transfer the results of the research of the previous "PHOTON CONTROL" project to industry so as to produce commercial near field optical spectrometers, optical memories, fiber probes, and so on(*). From October, 1999, a "LOCALIZED PHOTON" project, which is supported as ERATO (Exploratory Research for Advanced Technology) by Japan Science and Technology Corporation and directed by Ohtsu, has started for exploring a novel theory of optical near-field, for studying nano-photonics and atom-photonics.(+) Results of the recent research carried out by Ohtsu are reviewed in this issue of the COLLECTED PAPERS.

August 1999

Motoichi OHTSU
大津　元一

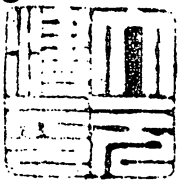

(*) Address: Near field photonics group,
Kanagawa Academy of Science and Technology
KSP East, Rm. 408, 3-2-1 Sakado, Takatsu-ku,
Kawasaki-shi, Kanagawa 213-0012, JAPAN
Phone: +81-44-819-2075
Fax: +81-44-819-2072

〒213-0012　神奈川県川崎市高津区坂戸３－２－１
ＫＳＰ東棟４０８号室
（財）神奈川科学技術アカデミー，光科学重点研究室
第２研究グループ

(+) Address: Localized photon project,
Japan Science and Technology
4th-floor, Tenko Building #17
687-1 Tsuruma, Machida-shi, Tokyo 194-0004
Phone:　+81-427-88-6030
Fax:　+81-427-88-6031
〒194-0004　東京都町田市鶴間 687-1
第１７天幸ビル４階
科学技術振興事業団　「局在フォトン」プロジェクト

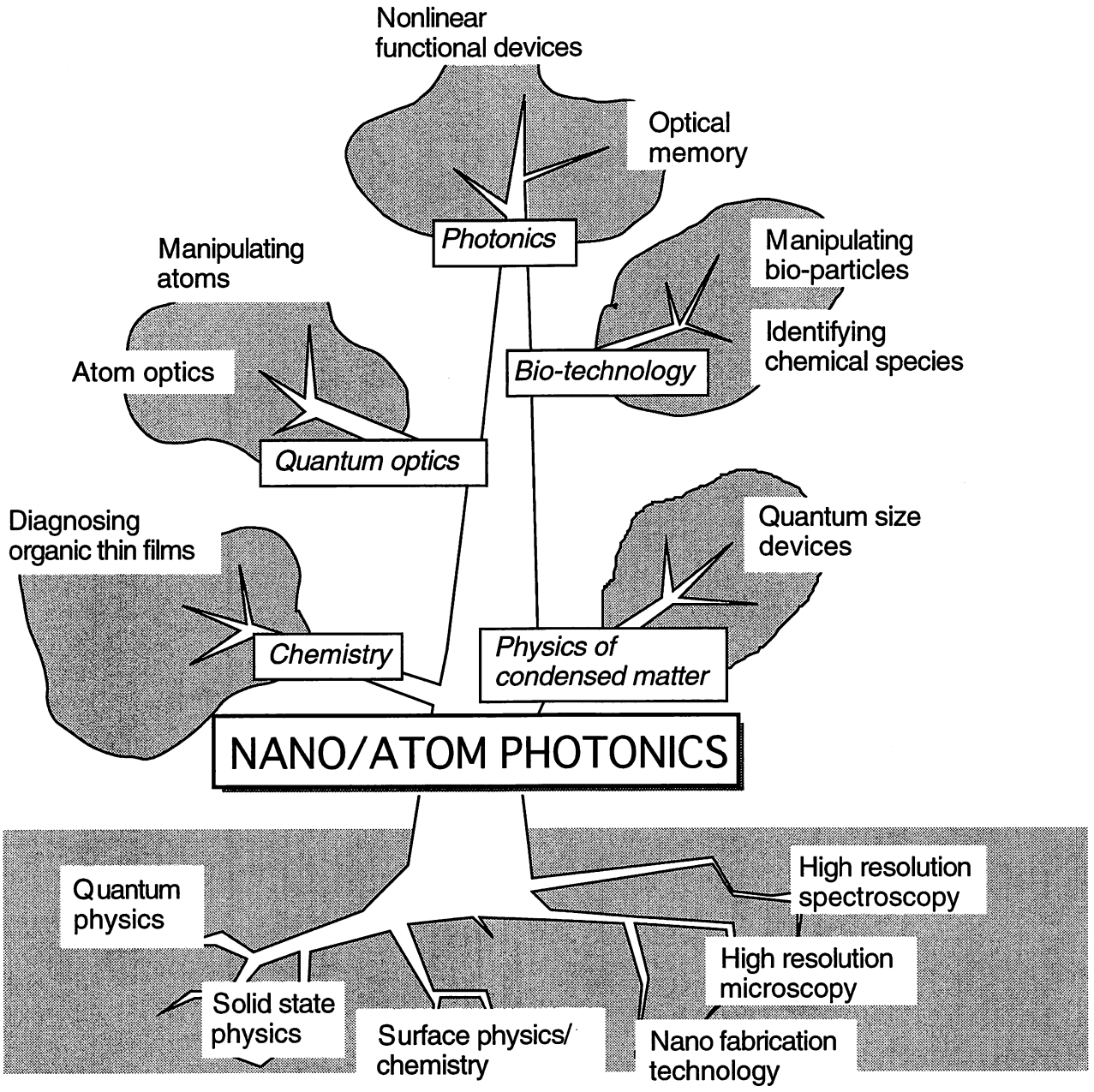

Nano/atom photonic tree with its roots and leaves covering a wide range of fields

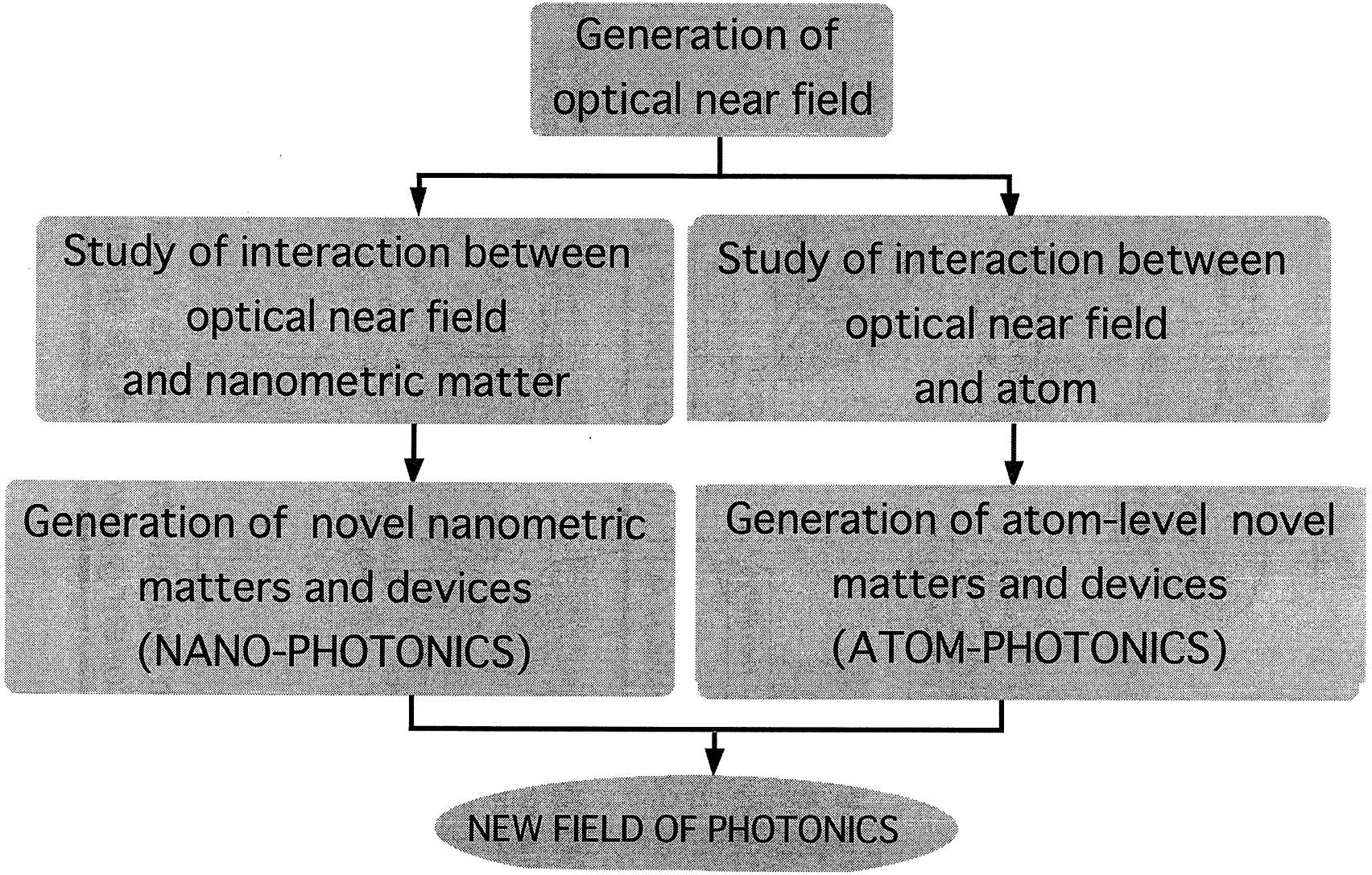
Generation of optical near field
Study of interaction between optical near field and nanometric matter
Study of interaction between optical near field and atom
Generation of novel nanometric matters and devices (NANO-PHOTONICS)
Generation of atom-level novel matters and devices (ATOM-PHOTONICS)
NEW FIELD OF PHOTONICS

MEMBERS

(From April 1, 1999)

[I] TOKYO INSTITUTE OF TECHNOLOGY

Professor

Motoichi OHTSU[a,b] (Dr. Eng.)

Associate Professor

Haruhiko ITO[c,d] (Dr. Sci.)

Research Associate

Motonobu KOUROGI[c] (Dr. Eng.)

Graduate Students (Doctor Candidates)

Vitali Vasilyevich POLONSKI
Takashi YATSUI
Bambang WIDIYATMOKO
Yoh YAMAMOTO
Hiroaki FUKUDA[e]

Graduate Students (Master Course)

Tsutomu ICHIMURA
Akifumi TAKAMIZAWA
Tomoto KAWAMURA
Shuko KOGISO
Takashi SHIMIZU
Yusuke SUMITA
Hideaki TANIOKA

Undergraduate Students

Taishi SUZUKI
Norio SASAKI

Visiting Scientists

Shaiki Mohammad Iftiquar[f] (PhD.)

Secretaries

Chikako ISHIDA
Kaoru OGURA

a) Also with Kanagawa Academy of Science and Technology
(Director, "Near field photonics"group)
b) Also with ERATO, Japan Science and Technology Corporation
(Director, "Localized photon" project)
c) Also with Kanagawa Academy of Science and Technology
(Part-time researcher, "Near field photonics"group)
d) Also with PRESTO(Precursory Research for Embryonic Science and Technology), Japan Science and Technology Corporation
e) Permanent affiliation: RICOH Co.Ltd.
f) Also with Japan Science and Technology Corporation

[II] "LOCALIZED PHOTON" PROJECT, ERATO, JAPAN SCIENCE AND TECHNOLOGY CORPORATION

Researchers

Theory Group

Kiyoshi KOBAYASHI[g]	(Dr. Sci.) (Group Leader)
Suguru SANGU	(Dr. Eng.)

Nano-photonics Group

Guen-Hyoung Lee	(Dr. Eng.)

Atom-photonics Group

Kouki TOTSUKA	(Dr. Sci.)

Managers

Akiyoshi ORIDE[h]
Takaaki MORIYAMA

Secretaries

Fumiko Ohta
Tomoko Ohta

g) Permanent affiliation: Japan IBM Co. Ltd.
h) Permanent affiliation: RICOH Co.Ltd.

[III] KANAGAWA ACADEMY OF SCIENCE AND TECHNOLOGY

Full-Time Researchers

Shuji MONONOBE

Part-Time Researchers

Haruhiko ITO[i] (Dr. Sci.)
Motonobu KOUROGI[i] (Dr. Eng.)

Visiting Scientist

Hiroaki FUKUDA[i]

Secretary

Yumiko MIYAHARA

i) Permanent affiliation: Tokyo Institute of Technology
i) Permanent affiliation: RICOH Co.Ltd.

LIST OF PAPERS

[(pp.XX-XX; pages in this issue of the COLLECTED PAPERS]

[I] PAPERS IN NANO/ATOM PHOTONICS

[I-1] ATOM PHOTONICS

(b) International Conferences

[I-2] NANO PHOTONICS

(a) Journal Papers

(pp.21-26)

[4] V.V. Polonski, Y. Yamamoto, M. Kourogi, H. Fukuda and M. Ohtsu, "Nanometric patterning of zinc by optical near-field photochemical vapour deposition", J. Microscopy, vol.194, pt.2/3, May/June 1999, pp.545-551

(pp.27-33)

[5] H. Fukuda, Y. Kadota and M. Ohtsu, "Estimation of the Minority Carrier Diffusion Length by Near-Field Photocurrent Measurement of p-n Junction in Silicon using Multiwavelength Excitation", Jpn. J. Appl. Phys., vol.38, part 2, no.5B, May 1999, pp.L571-L573

(pp.34-36)

[6] K. Nikawa, T. Saiki, S. Inoue and M. Ohtsu, "Imaging of current paths and defects in Al and TiSi interconnects on very-large-scale integrated-circuit chips using near-field optical-probe stimulation and resulting resistance change", Appl. Phys. Lett., vol.74, no.7, February 1999, pp.1048-1050

(pp.37-39)

[7] T. Matsumoto, T. Ichimura, T. Yatsui, M. Kourogi, T. Saiki and M. Ohtsu, "Fabrication of a Near-Field Optical Fiber Probe with a Nanometric Metallized Protrusion", Optical Review, vol.5, no.6, December 1998, pp.369-373

(pp.40-44)

[8] T. Yatsui, M. Kourogi and M. Ohtsu, "Increasing throughput of a near-field optical fiber probe over 1000 times by the use of a triple-tapered structure", Appl. Phys. Lett., vol.73, no.15, October 1998, pp.2090-2092

(pp.45-47)

[9] Y. Narita, T. Tadokoro, T. Ikeda, T. Saiki, S. Mononobe and M. Ohtsu, "Near-Field Raman Spectral Measurement of Polydiacetylene", Appl. Spectroscopy, vol.52, no.9, September 1998, pp.1141-1144

(pp.48-51)

(b) International Conferences

[1] K. Kobayashi and M. Ohtsu, "Quantum theoretical approach to near-field optical system", Technical Digest of the 5th International Conference on Near Field Optics and Related Techniques, 6-10 December, 1998, Shirahama,

Japan, pp.3-4 (paper number A3)

(pp.52-53)

[2] T. Matsumoto, K. Matsuda, K. Nishi, T. Saiki and M. Ohtsu, "Near-field nonlinear absorption spectroscopy of single quantum dots", Technical Digest of the 5th International Conference on Near Field Optics and Related Techniques, 6-10 December, 1998, Shirahama, Japan, pp.38-39 (paper number D2)

(pp.54-55)

[3] S. Mononobe and M. Ohtsu, "Fabrication of application-oriented near-field fiber probes based on hybrid selective etching of multistep index fibers", Technical Digest of the 5th International Conference on Near Field Optics and Related Techniques, 6-10 December, 1998, Shirahama, Japan, pp.157-158 (paper number PC5)

(pp.56-57)

[4] S. Mononobe, R. Uma Maheswari and M. Ohtsu, "Fabrication of a nanometer-level resolving probe with metal-dielectric-metal coat for near-field imaging of single strand DNA molecules", Technical Digest of the 5th International Conference on Near Field Optics and Related Techniques, 6-10 December, 1998, Shirahama, Japan, pp.159-160 (paper number PC6)

(pp.58-59)

[5] T. Matsumoto, T. Ichimura, T. Yatsui, M. Kourogi, T. Saiki and M. Ohtsu, "Fabrication of a near-field optical fiber probe with a nanometric metallized protrusion", Technical Digest of the 5th International Conference on Near Field Optics and Related Techniques, 6-10 December, 1998, Shirahama, Japan, pp.161-162 (paper number PC7)

(pp.60-61)

[6] M.B. Lee, A. Sato, K. Tsutsui, M. Ohtsu and N. Atoda,"Fabrication and SNOM characterization of planar probe array for near-field optical memory application", Technical Digest of the 5th International Conference on Near Field Optics and Related Techniques, 6-10 December, 1998, Shirahama, Japan, pp.169-170 (paper number PC11)

(pp.62-63)

[7] T. Saiki and M. Ohtsu, "Optimization of structure and aperture diameter of near-field probe for illumination-collection hybrid-mode operation", Technical Digest of the 5th International Conference on Near Field Optics and Related Techniques, 6-10 December, 1998, Shirahama, Japan, pp.214-

215 (paper number C1)

(pp.64-65)

[8] T. Suzuki, S. Koshihara, M. Yoshimoto, T. Saiki, S. Mononobe, M. Ohtsu, T. Miyazawa and M. Kira, "Observation of polysilane aggregates with scanning optical near-field microscope", Technical Digest of the 5th International Conference on Near Field Optics and Related Techniques, 6-10 December, 1998, Shirahama, Japan, pp.320-321 (paper number PE10)

(pp.66-67)

[9] V.V. Polonski, Y. Yamamoto and M. Ohtsu, "Photochemical vapor deposition of Zn by optical near-field", Technical Digest of the 5th International Conference on Near Field Optics and Related Techniques, 6-10 December, 1998, Shirahama, Japan, pp.438-439 (paper number I1)

(pp.68-69)

[10] K. Nikawa, T. Saiki, S. Inoue and M. Ohtsu, "Thermal and optical effects in the analysis of submicron aluminum and titanium-silicide lines by near-field-optical-probe-induced resistance-change", Technical Digest of the 5th International Conference on Near Field Optics and Related Techniques, 6-10 December, 1998, Shirahama, Japan, pp.445-446 (paper number I6)

(pp.70-71)

[11] H. Fukuda, Y. Kadota and M. Ohtsu, "Characterization of p-n junction on Si substrate by multiwavelength near-field photocurrent measurement", Technical Digest of the 5th International Conference on Near Field Optics and Related Techniques, 6-10 December, 1998, Shirahama, Japan, pp.449-450 (paper number I8)

(pp.72-73)

[12] T. Yatsui, M. Kourogi, K. Tsutsui and M. Ohtsu, "Read out capability of a planar apertured probe for optical near-field memory", Technical Digest of the 5th International Conference on Near Field Optics and Related Techniques, 6-10 December, 1998, Shirahama, Japan, pp.478-479 (paper number I15)

(pp.74-75)

[13] M. Ohtsu, "nano/atom fabrication and manipulation by near-field optics", Technical Digest of the 1998 Asian-Pacific Forum on Science and Technology: Optical Probing and Creation of Advanced Photoactive Materials, 10-13 November, 1998, Ishikawa, p.28 **[Invited presentation]**

(p.76)

[14] M. Kourogi, T. Yatsui, S. Ishimura, M.B. Lee, N. Atoda and M. Ohtsu, "A near field planar apertured probe array for optical near field memory", Technical Digest of the International Symposium on Optical Memory 1998, 20-22 October, 1998, Tsukuba, pp.150-151 **[Invited presentation]**

(pp.77-78)

[15] T. Yatsui, M. Kourogi K. Tsutsui and M. Ohtsu, "Enhancing throughput over 100 times by a triple-tapered structure for near-field optical fiber probe", Technical Digest of the SPIE Conference on Far-and Near-Field Optics: Physics and Information Processing, 23-24 July, 1998, San Diego, CA, vol.3467, pp.89-98

(pp.79-88)

[16] M. Kourogi, T. Yatsui, S. Ishimura, M.B. Lee, N. Atoda, K. and M. Ohtsu, "A near-field planar apertured probe array for optical near-field memory", Technical Digest of the SPIE Conference on Far-and Near-Field Optics: Physics and Information Processing, 23-24 July, 1998, San Diego, CA, vol.3467, pp.258-267

(pp.89-98)

[I-3] REVIEW PAPERS

[1] M. Ohtsu, "Nanometric fabrication by light and its applications", Monthly Journal of Appl. Phys. Japan, vol.68, no.4, April 1999, pp.431-434
【大津元一、「ナノ領域の光加工とその応用」、応用物理、第６８巻、第４号、１９９９年４月、pp.431-434】

(pp.99-102)

[2] M. Ohtsu, "What is Near Field Optics? -- Q&A for pedestrians", O plus E, vol.21, no.3, March, 1999, pp.248-254"
【大津元一、「近接場光学とは –パラダイム・シフトのための初歩的Ｑ＆Ａ」、O plus E、第２１巻、第３号、１９９８年３月、 pp.248-254】

(pp.103-109)

[3] M. Ohtsu, "Near-Field Optical Technology for Nano/Atom Photonics", Condensed Matter News, vol.7, issues 2-3, 1999, pp.49-51

(pp.110-112)

[4] M. Ohtsu(ed.), "Optical/Electrical Diagnostics and Control of Nanometric Materials", Technical Report of the Institute of Electrical Engineering of Japan, vol.715, February 1999, (total pages:51)

【大津元一編、「光と電子によるナノメータ領域材料評価と制御」、電気学会技術報告、第７１５号、１９９９年２月　（総ページ、５１）】

(pp.113-115)

[5] Y. Narita, T. Tadokoro, T. Ikeda, T. Saiki, S. Mononobe and M. Ohtsu, "Subwavelength spatial resolution mapping measurement using near-field spectrometers", American Laboratory news edition, vol.31, no.5, February 1999, pp.22-24

(p.116-117)

[6] M. Ohtsu, "Probes for near field optics", Solid State Physics, vol.33, no.10, October 1998, pp.835-839
【大津元一、「近接場光学用プローブ」、固体物理、第３３巻、第１０号、１９９８年１０月、pp.835-839】

(pp.118-122)

[7] M. Ashino and M. Ohtsu, "Development of a localized-plasmon-resonance probe and a novel near field microscope", Monthly Journal of Appl. Phys. Japan, vol.67, no.12, December 1998, pp.1404-1405
【芦野慎、大津元一、「局在プラズモン共鳴プローブの開発と新しいニアフィールド顕微鏡」、応用物理、第６７巻、第１２号、１９９８年１２月、pp.1404-1405】

(pp.123-124)

[8] M. Ohtsu, K. Tsutsui and M. Kourogi, "Near Field Optics and Its Application to Optical Memory", Electronics and Communications in Japan, part 2, vol.81, no.8, August 1998, pp.41-48

(pp.125-132)

[II] PAPERS IN OTHER FIELDS

(a) Journal Papers

[1] K. Imai, B. Widyatmoko, M. Kourogi and M. Ohtsu, "12-THz Frequency Difference Measurements and Noise Analysis of an Optical Frequency Comb in Optical Fibers", IEEE J. Quantum Electron., vol.35, no.4, April 1999, pp.559-564

(pp.133-138)

[2] B. Widyatmoko, M. Kourogi and M. Ohtsu, "Linking Two Optical

Frequency Combs by Heterodyne Optical Phase Locking Between Diode Lasers at 2.6-THz Frequency-Difference", IEEE Photonics Technol. Lett., vol.11, no.4, April 1999, pp.460-462

(pp.139-141)

[3] B. Widyatmoko, K. Imai, M. Kourogi, and M. Ohtsu, "Second-harmonic generation of an optical frequency comb at 1.55 um with periodically poled lithium niobate", Opt. Lett., vol.24, no.5, March 1999, pp.315-317

(pp.142-144)

[4] K. Imai, Y. Zhao, M. Kourogi, B. Didyatmoko and M. Ohtsu, "Accuracy of optical frequency comb generation in optical fiber", Opt. Lett., vol.24, no.4, February 1999, pp.214-216

(pp.145-147)

[5] T. Nayuki, T. Fujii, K. Nemoto, M. Kozuma, M. Kourogi and M. Ohtsu, "Continuous Wavelength Sweep of External Cavity 630nm Laser Diode without Antireflection Coating on Output Facet", Optical Review, vol.5, no.5, October1998, pp.267-270

(p.148-151)

[III] PUBLISHED BOOKS

[1] M. Ohtsu and H. Hori, Near-Field Nano-Optics, Kluwer Academic/Plenum Publishers, New York, (386pages)

[2] M. Ohtsu, Fundamentals of Quantum Electronics, Shokabo Publishers, Tokyo, 1999 (339pages)

【大津元一、「量子エレクトロニクスの基礎」、裳華房、１９９９年４月（３３９頁）】

[3] M. Ohtsu, Invitation to Optical Science, Asakura-shoten Publishers, Tokyo, 1999 (170pages)

【大津元一、「光科学への招待」、朝倉書店、１９９９年３月（１７０頁）】

[4] M. Ohtsu, Light (1, 2), in Material Science and Technology (ed. By A. Hirakawa and T. Doke), Hoso-daigaku Shuppankai, Tokyo, 1999, pp.87-119

【大津元一、「光(1),(2)」、平川暁子、道家達将編、物質の科学と技術開発（放送大学教材）、放送大学出版会、東京、１９９９年３月、pp.87-119】

[IV] PRESENTED PH.D THESIS

[1] V. V. Polonski, "A feasibility study of optical near-field photochemical vapour deposition", July 1999

[2] K. Imai, "Study on efficient generation of optical frequency comb by self-phase modulation", January 1999

【今井一宏、「自己位相変調による高効率光周波数コム発生に関する研究」、１９９９年１月】

[3] T. Matsumoto, "Evaluation of nonlinear optical response of a single semiconductor quantum dot by optical near field technique", January 1999

【松本拓也、「近接場光学手法による半導体単一量子ドットの非線形光学応答の評価」、１９９９年１月】

[4] T. Saito, "Waveguide-type optical frequency comb generator and its application", October 1998

【斉藤崇記、「導波路型光周波数コム発生器とその応用に関する研究」、１９９８年１０月】

[5] N. Ohkawa, "High-capacity and long-span optical fiber communication systems", August 1998

【大川典男、「無中継光ファイバ伝送システムの大容量化、長スパン化に関する研究」、１９９８年８月】

[I] PAPERS IN NANO/ATOM PHOTONICS

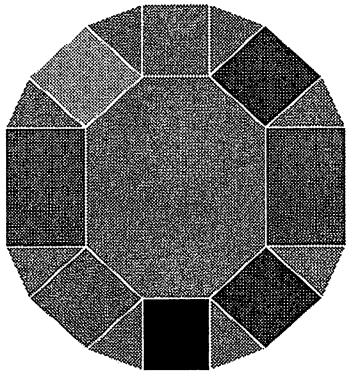

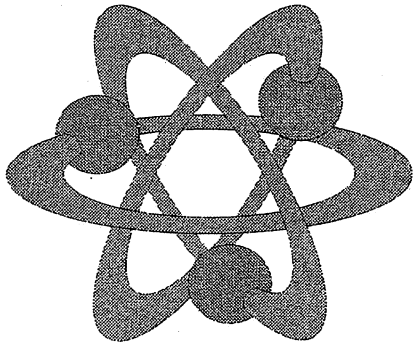

[I-1] ATOM PHOTONICS

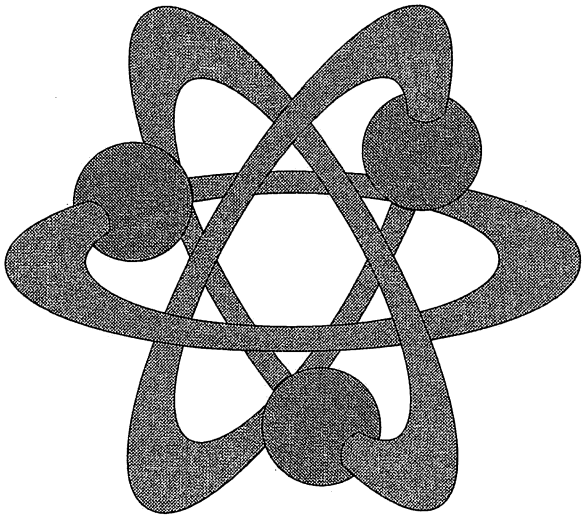

H2

DEFLECTION AND TRAP OF ATOMS WITH SHARPENED FIBERS

Haruhiko Ito[a,b,c] and Motoichi Ohtsu[b,c]

[a]PRESTO, Japan Science and Technology Corporation
[b]Interdisciplinary Graduate School of Science and Engineering, Tokyo Institute of Technology
4259 Nagatsuta, Midori-ku, Yokohama 226-8502, Japan
phone: +81-45-924-5455, fax: +81-45-924-5487
[c]Kanagawa Academy of Science and Technology
KSP East 408, 3-2-1 Sakado, Takatsu-ku, Kawasaki 213-0012, Japan
phone: +81-44-819-2075, fax: +81-44-819-2072, e-mail: haruhiko@net.ksp.or.jp

KEY WORDS: atom deflection, atom trap, sharpened fiber, Yukawa-type potential

Control of vapor atoms is now an important subject for an exact science, including microfabrication. The vapor atoms move at random with a high mean velocity of more than several hundred meters per second. Only way of controlling the thermal atoms is to use resonant forces of laser light. However, using the traditional methods with propagating light, we cannot control atoms with a high spatial accuracy beyond a limit determined by the wavelength used, due to diffraction. To overcome the diffraction limit, therefore, we consider the use of optical near fields. One of the strong advantages of the optical near fields consists in the localizability. It depends greatly on the size of matter: the production region is comparable to the radius of curvature. Such a localized optical field can be produced near the nanometric tip of a sharpened fiber. In this paper, we present an effective method of controlling atoms with sharpened fibers. In particular, we deal with deflection and trap of atoms.

The original idea of manipulating atoms with a nanometric sharpened fiber was proposed by Ohtsu, Hori and their collaborators [1-4]. Here, we introduce a new scheme involving the dipole force of an optical near field and the van der Waals force [5,6]: the total potential on atoms is composed of the optical potential from the dipole force and the attractive cavity potential from the van der Waals force. Note that the dipole force becomes repulsive when the light frequency is higher than an atomic resonant frequency, while it becomes attractive in the opposite case.

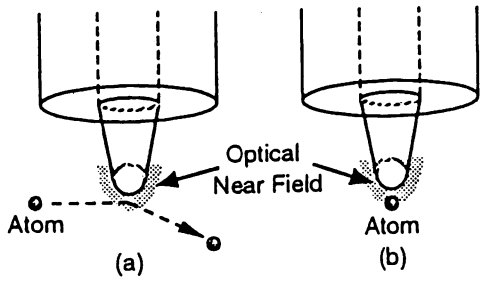

Fig. 1 Atom manipulation with a sharpened fiber: (a) deflection, and (b) trap.

Figure 1(a) shows the deflection of an atom flying ballistically: an atom passing through the neighborhood of the tip of a sharpened fiber can be deflected by a repulsive optical near field. Figure 1(b), on the other hand, shows the trap of an atom near the tip. An atom can be trapped at a minimum of the potential composed of a repulsive optical potential and an attractive van der Waals cavity potential.

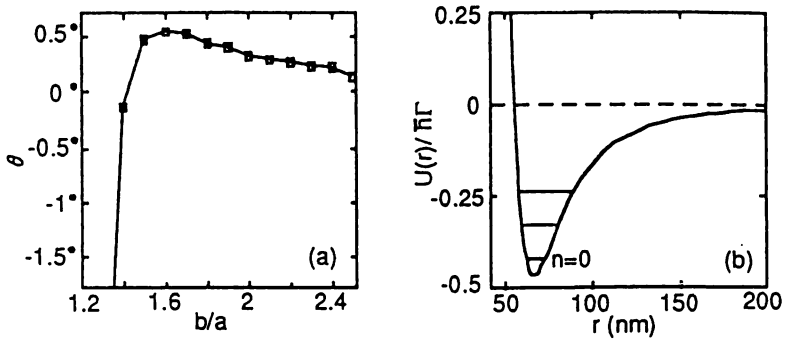

Fig. 2 Estimation of (a) deflection angle, and (b) trap potential with quantized vibrational levels.

To estimate the deflection angle and the trap potential, we need to know the intensity distribution of the optical near field produced near the tip of a sharpened fiber. To this end, the Yukawa-type potential can be used as a phenomenological expression [4,7]. Figure 2 shows the results obtained from the numerical calculations in typical cases. In Fig. 2(a), the deflection angle θ is plotted as a function of the impact parameter b normalized to the radius of curvature a, where we assume a slow Rb atom with a velocity of 10 m/s. From a deflection angle of 0.5 degree, the displacement from the incident axis is estimated to be about 100 μm at a distance of 10 cm downstream of the tip. Figure 2(b) shows the trap potential on a Rb atom near the tip with a=20 nm. The potential for the 5S, F=2 lower ground state is plotted as a function of the distance r from the tip surface. In this case, a slow atom can be trapped in one of the quantized vibrational levels. The lowest level corresponds to a temperature of about 10 μK.

[1] M. Ohtsu, "Photon STM(V), Single atom-level crystal growing", the 51st autumn meeting of the Japan Society of Applied Physics, extended abstracts 27a-L-9 (1990).

[2] M. Ohtsu, US patent 5,337,324 (Aug. 1994); M. Ohtsu and H. Hori, Japan patent 1,946,474 (July 1995).

[3] M. Ohtsu, S. Jiang, T. Pangaribuan, and K. Kozuma, "Nanometer resolution photon STM and single atom manipulation", Near-Field Optics, 131-139, Kluwer, Dordrecht (1993).

[4] H. Hori, "Quantum optical picture of photon STM and proposal of single atom manipulation", Near-Field Optics, 105-114, Kluwer, Dordrecht (1993).

[5] M. Ohtsu (ed.), Near-Field Nano/Atom Optics and Technology, Chap. 11, Springer-Verlag, Berlin (1998).

[6] H. Ito, K. Otake, and M. Ohtsu, "Near-field optical guidance and manipulation of atoms", Far- and Near-Field Optics: Physics and Information Processing, Proceedings of SPIE, Vol. 3467 (1998).

[7] M. Ohtsu and H. Hori, Near-Field Nano-Optics, Plenum, New York (1998).

Invited Paper

Near-field optical guidance and manipulation of atoms

H. Ito[a,b,c], K. Otake[b], and M. Ohtsu[b,c]

[a]PRESTO, Japan Science and Technology Corporation,
KSP East 408, 3-2-1 Sakado, Takatsu-ku, Kawasaki 213-0012, Japan

[b]Interdisciplinary Graduate School of Science and Engineering
Tokyo Institute of Technology
4259 Nagatsuta, Midori-ku, Yokohama 226-8502, Japan

[c]Kanagawa Academy of Science and Technology
KSP East 408, 3-2-1 Sakado, Takatsu-ku, Kawasaki 213-0012, Japan

ABSTRACT

We describe guiding of neutral atoms through a hollow optical fiber with a micron-sized hollow core. Two-step photoionization experiment shows the frequency dispersion properties of the dipole interaction between an atom and an optical near field. This characteristics are advantageous to species- and state-selective manipulation of atoms. Then, we discuss a new scheme of atom deposition by means of the guiding technique, including a numerical simulation. We also present two methods of controlling atomic motion using a sharpened optical fiber with a nanometric optical near field, i. e., atom deflection and atom trap. Deflection angle and trap potential are estimated based on a near-field intensity distribution derived from a Yukawa-type screened potential. The manipulation techniques are useful for precise control of atoms with a spatial accuracy beyond diffraction limit, which will lead to atomic-scale crystal growth.

Keywords: optical near field, atom guidance, atom manipulation, hollow fiber, sharpened fiber

1. INTRODUCTION

Fabrication of a three-dimensional atomic-scale structure is now an experimental subject with challenge. Owing to recent progress of atom optics,[1] creation of a nano-structure with laser light has attracted more interest. The essential problem with optical methods consists in overcoming the diffraction limit of light waves: when we use propagating light, the spatial accuracy of atom control is determined by the wavelength used due to diffraction. The best way of settling the problem is to use an optical near field because it is not affected by diffraction.[2–4] In this paper, we discuss a couple of near-field optical methods of controlling atomic motion toward realization of atomic scale crystal growth.

First, we describe guiding of atoms with a micron-sized hollow optical fiber. This scheme is based on the dipole interaction between an atom and an optical near field. The successful guidance of Rb atoms is confirmed by the spectroscopic experiment with two-step photoionization. Second, we discuss the feasibility of atom deposition using the guiding technique. The deposition rate depends on the guide-laser frequency and power, etc. To estimate the deposition rate, a numerical simulation is performed. Finally, we consider atom manipulation, including atomic deflection and atom trap, by means of a sharpened optical fiber with a nanometric tip. The possibility is discussed through estimation of the deflection angle and the trap potential based on a phenomenological Yukawa-type field intensity distribution.

2. ATOM GUIDANCE WITH HOLLOW FIBERS

A hollow fiber with an optical near field can transmit atoms to an arbitrary point.[3–12] Figure 1 schematically explains the method of guiding atoms. When a light beam is coupled to a hollow fiber, an optical near field is produced near the inner wall surface according to a propagating mode. If the light frequency is higher than an

Other author information: (Send correspondence to H.I.)
H.I.: E-mail: haruhiko@net.ksp.or.jp
M.O.: E-mail: ohtsu@ae.titech.ac.jp

Part of the SPIE Conference on Far- and Near-Field Optics: Physics and Information Processing
San Diego, California • July 1998
SPIE Vol. 3467 • 0277-786X/98/$10.00

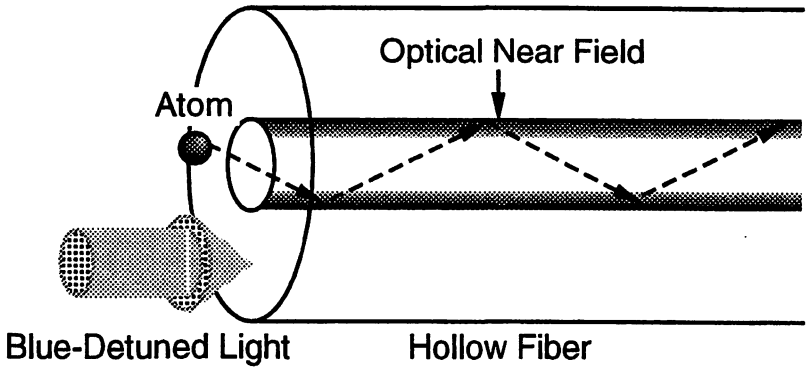

Figure 1. Sketch of atom guidance in a hollow optical fiber with a blue-detuned optical near field.

atomic resonant frequency, which is called blue detuning, the cylindrical optical near field works as a mirror to reflect atoms approaching the inner wall. The optical tunnel to carry atoms arises from the repulsive dipole force on atoms. Since the optical near field exponentially decays in a region below a wavelength and the dipole-force potential is in proportion to intensity gradient,[12,13] the potential barrier can be higher than an atomic transverse kinetic energy under feasible experimental conditions.

In the experiment mentioned below, we used a hollow optical fiber with a core-cladding structure. Figure 2 shows a CCD camera image of the cross section of a 2-μm-hollow fiber with a core thickness of 4 μm.[14] Since the relative refractive index difference between core and cladding is small, for example, 0.26 % in the hollow fiber shown in Fig. 2, the propagating modes, and then the optical near fields in the hollow region, are approximately described by the linearly polarized (LP) modes.[6,7] The fundamental mode is the LP_{01} mode (see Fig. 2). The LP_{01} mode is suitable for atom guidance because the near-field intensity distribution around the inner wall is homogeneous.

We made the experiment with rubidium (Rb) atoms to demonstrate the near-field optical guidance.[9] Figure 3 shows the experimental setup. In a vacuum chamber with a background pressure of 10^{-8} torr, a collimated Rb atomic beam from an oven with a typical temperature of 200°C is introduced into a hollow fiber that is placed coaxially. A guide light beam from a Ti:Sapphire laser tuned to the D_2 line with a wavelength of 780 nm is coupled to the core via a pinhole mirror with a coupling efficiency of about 40 %. In this case, we selectively excite the LP_{01} mode by monitoring the output facet of the fiber with a CCD camera and adjusting the incident angle.

To detect guided Rb atoms, we used a two-step photoionization method, which enables one to perform spectroscopy of the guided atoms with a high signal-to-noise ratio. In the current case, the two-step photoionization is

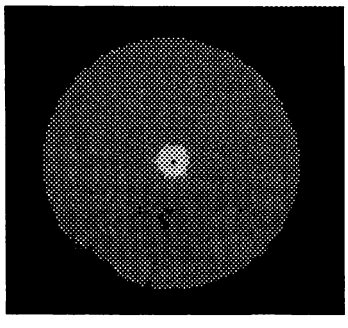

Figure 2. CCD camera image of the cross section of a 2-μm-hollow fiber under the excitation of the LP_{01} mode. The white region shows a core with a thickness of 4 μm. Note that a part of the light field leaks into the cladding layer, so that the white region is larger than the core thickness.

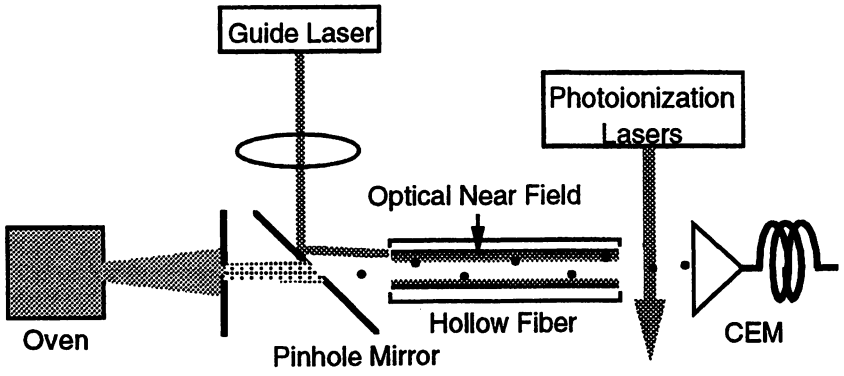

Figure 3. Experimental setup using Rb atoms. A guide light beam from a Ti:Sapphire laser with a wavelength of 780 nm is coupled to the core of a hollow fiber placed coaxially to a collimated atomic beam. Guided Rb atoms are detected by a channel electron multiplier (CEM) by way of two-step photoionization with a diode laser tuned to one of hyperfine transitions between the $5S_{1/2}$ ground state and the $5P_{3/2}$ excited state, and an Ar-ion laser with a wavelength of 476.5 nm.

carried out with two lasers, a diode laser and a high power Ar-ion laser. As shown in Fig. 3, the two laser beams from the direction perpendicular to the axis of the atomic beam are overlapped in just front of the rear facet. Note that this scheme gives rise to Doppler free spectra on guided atoms. The diode laser tuned to the D_2 line excites only Rb atoms from the $5S_{1/2}$ ground state to the $5P_{3/2}$ excited state, and then the Ar-ion laser with a wavelength of 476.5 nm excites the Rb atoms from the $5P_{3/2}$ excited state to the ionization level at 4.18 eV above the ground state. The positive Rb ions are collected and counted with a channel electron multiplier (CEM) biased by negative voltage of -3 kV, in which the quantum efficiency is 0.9.

Figure 4 shows a two-step photoionization spectrum on ^{87}Rb atoms guided through a 3.5-cm-long hollow fiber with a hollow diameter of 2 μm. In Fig. 4, the guided atom flux is plotted as a function of the frequency detuning of the guide laser, which is measured with respect to the transition from the $5S_{1/2}$, F=2 upper ground state. Here, the diode laser is tuned to the transition from the $5S_{1/2}$, F=2 upper ground state to the $5P_{3/2}$, F=3 excited state. Therefore, only ^{87}Rb atoms in the $5S_{1/2}$, F=2 upper ground state contribute to the spectrum. Note that the atomic beam employed in the experiment contains two stable isotopes ^{85}Rb and ^{87}Rb with a natural abundance ratio of about 7 : 3.

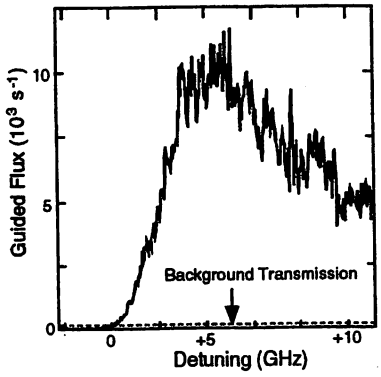

Figure 4. Two-step photoionization spectrum on ^{87} Rb atoms in the $5S_{1/2}$, F=2 upper ground state guided through a 3.5-cm-long hollow fiber with a hollow diameter of 2 μm. The guided atom flux is plotted as a function of the frequency detuning with respect to the transition from the $5S_{1/2}$, F=2 upper ground state. The broken line shows the background transmission level obtained in the case without the guide light.

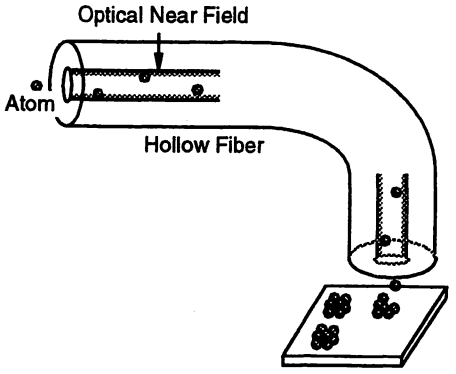

Figure 5. Fabrication of a dot-shaped pattern using atom guidance technique.

As shown in Fig. 4, the guided atom flux greatly increases in the blue-detuning region. Comparing the maximum flux at an optimal blue detuning of about +3 GHz with the background transmission level obtained in the case without the guide light, which is shown by a broken line, we get an enhancement factor of about 80. On the other hand, increase of the atom flux coming out of the hollow fiber is not observed in the red-detuning region. This is because the dipole force is attractive under a red-detuning condition. The result shows the frequency dispersion properties of the atom guidance.

3. TOWARD OPTICALLY CONTROLLED ATOMIC DEPOSITION

Several experimental demonstrations of creating small structures have been made with atom optical methods: for example, atom lithography and atom holography.[15–18] However, traditional methods using propagating light require additional elaborate tricks for attaining a submicron spatial accuracy, although it is not necessarily impossible. In addition, they have a disadvantage to making an arbitrary pattern. Moreover, few deposition techniques have been developed compared to lithography techniques. For the purpose of fabricating a nano-structure with an arbitrary shape, we can expect to use an optical near field. To this goal, we consider the simple scheme of atomic deposition by means of the atom guidance technique.

Figure 5 schematically shows making of a dot-shaped pattern with a hollow fiber. Note that an optical fiber is flexible. Using a bent hollow fiber, we can carry atoms to an arbitrary point on a substrate. In addition, we can control the deposition rate precisely and species- and state-selectively with guide-laser frequency. This advantage leads to high purity of the produced matter.

In our previous work,[19] we measured a spatial distribution of Rb atoms guided through a 7-μm-hollow fiber using surface ionization with a fine Pt hot wire. From the result, we roughly estimated the deposition rate. At the same time, we showed the feasibility of precise control of the deposition rate with frequency detuning. Now, to estimate the expectation value of the deposition rate in an ideal case, we performed a numerical simulation on the deposition rate.

As a function of the distance r from the center of the hollow region, the near-field intensity $P(r)$ under excitation of the LP_{01} mode is given by the square of the zeroth order modified Bessel function $\mathrm{I}_0(vr)$ of the first kind with $v = \sqrt{\beta^2 - k^2}$, where β and k are a propagation constant and a wave number, respectively.[7,9] From this near-field intensity, we can estimate the optical potential $U_{\mathrm{opt}}(r)$ given by[11,12]

$$U_{\mathrm{opt}}(r) = \frac{\hbar\Delta}{2} \ln\left\{1 + \frac{\Gamma^2}{4\Delta^2 + \Gamma^2} \frac{P(r)}{P_{\mathrm{sat}}}\right\}, \tag{1}$$

where Δ, Γ, and P_{sat} are a frequency detuning, a natural linewidth, and a saturation intensity, respectively.

Using Eq. (1), we simulated the supplying rate to a substrate in the case where ^{85}Rb atoms are guided through a 7-μm-hollow fiber. Figure 6 shows the atom flux density plotted as a function of the detuning Δ measured with respect to the $5\mathrm{S}_{1/2}$, F=3 upper ground state, in which we assume that the coupling power of the guide light is

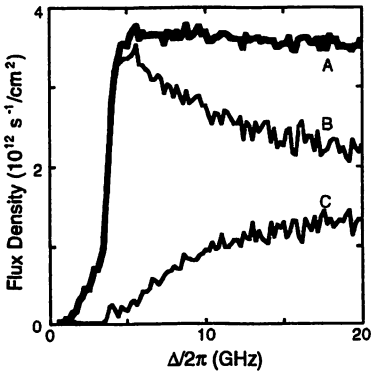

Figure 6. Numerical simulation of the supplying ^{85}Rb density from a 7-μm-hollow fiber plotted as a function of the detuning measured with respect to the $5S_{1/2}$, F=3 upper ground state. The curve A is the total ^{85}Rb density, while the curves B and C are the ^{85}Rb densities in the F=3 and F=2 ground states, respectively, where the atomic mean temperature of 200°C and the coupling light power of 100 mW are used.

100 mW and the mean temperature of the Rb atomic beam is 200°C. In this simulation, we also consider the loss of the spontaneous transition between two hyperfine ground states and the tunneling effect. In Fig. 6, the curve A is the total ^{85}Rb flux density, while the curves B and C are the flux densities of ^{85}Rb atoms in the F=3 upper and F=2 lower ground states, respectively. From the maximum value of 3.7×10^{12} s^{-1}/cm^2, we get the inverse of the maximum deposition rate of about 5 min/nm.

On the other hand, the evaporating atom density from a substrate with a temperature T can be estimated from the expression $p_{\rm sat}/\sqrt{2\pi m k_{\rm B} T}$, where $p_{\rm sat}$, m, and $k_{\rm B}$ are a saturation vapor pressure, an atomic mass, and the Boltzmann constant, respectively. From the equation, we find that the evaporating Rb density becomes comparable to the supplying Rb density obtained in Fig. 6 at a room temperature. Therefore, we will need cooling of a substrate for deposition of Rb atoms.

4. ATOM MANIPULATION WITH SHARPENED FIBERS

To control atoms with a high spatial accuracy far beyond the diffraction limit, we can use an optical near field localized in a nanometer region. In fact, such a localized field is induced on a nanometric tip of a sharpened (or tapered) optical fiber.[2–4,20,21] So far a sharpened fiber with a radius of curvature of about 1 nm has been produced.[2–4,20,21] The original idea of atom manipulation with a sharpened fiber has been proposed by M. Ohtsu, H. Hori and their collaborators.[22,23] Another scheme has been proposed by a Russian group.[24] Here, we introduce new schemes of controlling atomic motion with a sharpened fiber.

Let us consider two cases shown in Fig. 7: (a) deflection of a ballistically flying atom, and (b) trap of an atom near the tip. These techniques are very useful for carrying an atom to a point aimed at on a substrate. To show the possibility of the atom manipulation, we numerically estimated the deflection angle and the trap potential under suitable conditions, assuming a Yukawa-type screened potential given by[3,4,23]

$$\phi(r) = \int\int \frac{\exp(-r/a)}{r} \mathrm{dS} \,, \tag{2}$$

where a is a radius of curvature of the hemispherical tip and r is a distance from the surface. From this Yukawa-type potential, we obtain a near-field intensity distribution $P(r)$ given by

$$P(r) \sim |\nabla\phi(r)|^2 + \frac{1}{a^2}|\phi(r)|^2 \,. \tag{3}$$

Substituting Eq. (3) into Eq. (1), we can estimate the optical potential produced by an optical near field near a nanometric tip.

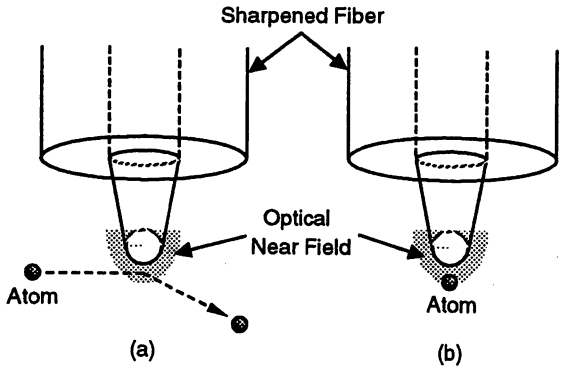

Figure 7. Control of atoms using a sharpened fiber with a nanometric optical near field: (a) deflection of atomic motion, and (b) atom trap.

Figure 8 shows the differential scattering cross section σ plotted as a function of the deflection angle θ, in which we use Born approximation. Here, we also assume that a ^{85}Rb atomic beam with a Maxwell-Boltzmann distribution whose mean temperature is 200 mK passes by a tip with $a = 50$ nm, on which an optical near field with a power of 50 nW and a blue detuning of +1.5 GHz is produced. As shown in Fig. 8, the cross section extends to about $\theta = 0.2°$. From this result, we find that the displacement from the incident axis is more than 100 μm at the position of 10 cm from downstream of the tip. This value is large enough for experimental observation of the atom deflection.

We can also make an atom trap near the tip of a sharpened fiber by combining a repulsive dipole force with an attractive van der Waals force under suitable conditions. In this scheme, the produced potential has the minimum value, so that an atom can be trapped near the bottom of the potential.

Figure 9 shows a trap potential on ^{85}Rb atoms in the $5S_{1/2}$, $F = 2$ lower ground state, where an optical near field with a power of 40 mW and a blue detuning of +1 GHz is produced near a tip with a radius of curvature of 20 nm. Note that the trap potential is made up of a repulsive optical potential and an attractive van der Waals potential. In this trap, the ^{85}Rb atom can be captured at one of the quantized vibration levels with a label n. The lowest level ($n = 0$) corresponds to a temperature of about 10 μK. Such cold atoms can be easily generated with the standard laser cooling technique. For the purpose of making a cold atomic beam, an atomic funnel with a hollow conical optical near field has been also proposed.[25] In this scheme, Sisyphus cooling induced by an optical near field is employed.[26–28]

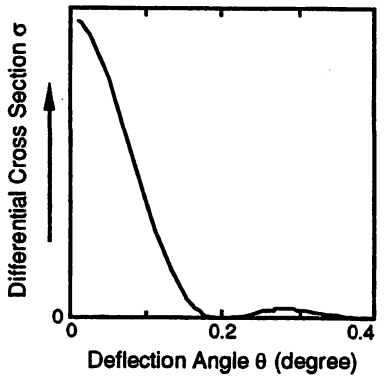

Figure 8. Differential scattering cross section σ derived with Born approximation plotted as a function of the deflection angle θ of ^{85}Rb atoms with a mean temperature of 200 mK, where an optical near field with a power of 50 nW and a blue detuning of +1.5 GHz is produced near a tip with a radius of curvature of 50 nm.

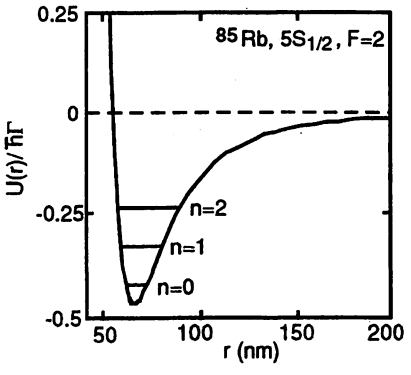

Figure 9. Potential to trap ^{85}Rb atoms, where an optical near field with a power of 40 mW and a blue detuning of +1 GHz is produced near a tip with a radius of curvature of 20 nm. The trap potential is a sum of a repulsive optical potential and an attractive van der Waals potential. A ^{85}Rb atom can be trapped in one of the quantized vibration levels labeled by a number n.

5. SUMMARY

Use of an optical near field greatly increases the spatial accuracy of atom control. The technique of atom guidance with a micron-sized hollow fiber is useful as a new scheme of atom deposition. In this method, we can not only make an arbitrary-shaped small structure, but also precisely control the deposition rate with frequency detuning. In addition, owing to the species- and state- selectivity based on the near-resonant dipole interaction, this method is advantageous to purity of the produced matter.

To overcome the diffraction limit, we can use a localized optical near field produced near the nanometric tip of a sharpened fiber. Under suitable conditions, near-field optical potentials to deflect and trap an atom can be produced. These manipulation techniques will be developed for atomic-scale crystal growth.

ACKNOWLEDGMENTS

We acknowledge Dr. S. Sudo and Dr. Y. Sakai of NTT Opto-Electronics Laboratories for their useful information on micron-sized hollow optical fibers. We also thank Prof. W. Jhe of Seoul National University for his collaboration on atom guidance experiment.

REFERENCES

1. V. I. Balykin and V. S. Letokhov, *Atom optics with laser light*, Harwood, Chur, 1995.
2. M. Ohtsu, "Progress of high-resolution photon scanning tunneling microscope due to a nanometric fiber probe", J. Lightwave Technol. **13**, pp. 1200-1221, 1995.
3. M. Ohtsu and H. Hori, *Near-field nano-optics*, Plenum, New York, 1998.
4. M. Ohtsu (ed.), *Near-field nano/atom optics and technology*, Springer-Verlag, Berlin, 1998.
5. S. Marksteiner, C. M. Savage, and P. Zoller, "Coherent atomic waveguides from hollow optical fibers: quantized atomic motion", Phys. Rev. A **50**, pp. 2680-2690, 1994.
6. H. Ito, K. Sakaki, T. Nakata, W. Jhe, and M. Ohtsu, "Optical potential for atom guidance in a cylindrical-core hollow fiber", Opt. Commun. **115**, pp. 57-64, 1995.
7. H. Ito, K. Sakaki, T. Nakata, W. Jhe, and M. Ohtsu, "Optical guidance of neutral atoms using evanescent waves in a cylindrical-core hollow fiber: theoretical approach", Ultramicroscopy **61**, pp. 91-97, 1995.
8. M. J. Renn, E. A. Donley, E. A. Cornell, C. E. Wieman, and D. Z. Anderson, "Evanescent-wave guiding of atoms in hollow optical fibers", Phys. Rev. A **53**, pp. R648-R651, 1996.

9. H. Ito, T. Nakata, K. Sakaki, M. Ohtsu, K. I. Lee, and W. Jhe, "Laser spectroscopy of atoms by evanescent waves in micron-sized hollow optical fibers", Phys. Rev. Lett. **76**, pp. 4500-4503, 1996.

10. H. Ito, K. Sakaki, M. Ohtsu, and W. Jhe, "Evanescent-light induced atom-guidance using a hollow optical fiber with light coupled sideways", Opt. Commun. **141**, pp. 43-47, 1997.

11. H. Ito and M. Ohtsu, "Atom guidance and manipulation using optical near field", Scanning Microscopy International, in press.

12. J. P. Dowling and J. Gea-Banacloche, "Evanescent light-wave atom mirrors, resonators, waveguides, and traps", in *Advances in atomic, molecular, and optical physics*, edited by B. Bederson and H. Walther, Vol. 37, pp. 1-94, Academic Press, San Diego, 1996.

13. V. I. Balykin, V. S. Letokov, Yu. B. Ovchinnikov, and A. I. Sidorov, "Quantum-state-selective mirror reflection of atoms by laser light", Phys. Rev. Lett. **60**, pp. 2137-2140, 1988.

14. S. Sudo, I. Yokoyama, H. Yasaka, Y. Sakai, and T. Ikegami, "Optical fiber with sharp optical absorption by vibrational-rotational absorption of C2H2 molecules", IEEE Photon. Technol. Lett. **2**, pp. 128-131, 1990.

15. G. Timp, R. E. Behringer, D. M. Tennant, J. E. Cunningham, M. Prentiss, and K. K. Berggren, "Using light as a lens for submicron, neutral-atom lithography", Phys. Rev. Lett. **69**, pp. 1636-1639, 1992.

16. J. J. McClelland, R. E. Scholten, E. C. Palm, and R. J. Celotta, "Laser-focused atomic deposition", Science **262**, pp. 877-880, 1993.

17. R. W. McGowan, D. M. Giltner, and S. A. Lee, "Light force cooling, focusing, and nanometer-scale deposition of aluminium atoms", Opt. Lett. **20**, pp. 2535-2537, 1995.

18. J. Fujita, M. Morinaga, T. Kishimoto, M. Yasuda, S. Matsui, and F. Shimizu, "Manipulation of an atomic-beam by a computer-generated hologram", Nature **380**, pp. 691-694, 1996.

19. H. Ito, K. Sakaki, M. Ohtsu, and W. Jhe, "Evanescent-light guiding of atoms through hollow optical fiber for optically controlled atomic deposition", Appl. Phys. Lett. **70**, pp. 2496-2498, 1997.

20. S. Mononobe and M. Ohtsu, "Fabrication of a pencil-shaped fiber probe for near-field optics by selective chemical etching", J. Lightwave Technol. **14**, pp. 2231-2235, 1996.

21. S. Mononobe and M. Ohtsu, "Development of a fiber used for fabrication application oriented near-field optical probes", IEEE Photonics Technol. Lett. **10**, pp. 99-101, 1998.

22. M. Ohtsu, S. Jiang, T. Pangaribuan, and M. Kozuma, "Nanometer resolution photon STM and single atom manipulation", in *Near-Field Optics*, edited by D. W. Pohl and D. Courjon, pp. 131-139, Kluwer, Dordrecht, 1993.

23. H. Hori, "Quantum optical picture of photon STM and proposal of single atom manipulation", in *Near-Field Optics*, edited by D. W. Pohl and D. Courjon, pp. 105-114, Kluwer, Dordrecht, 1993.

24. V. V. Klimov and V. S. Letokhov, "New atom trap configurations in the near field of laser radiation", Opt. Commun. **121**, pp. 130-136, 1995.

25. H. Ito, K. Sakaki, W. Jhe, and M. Ohtsu, "Atomic funnel with evanescent light", Phys. Rev. A **56**, pp. 712-718, 1997.

26. J. Söding, R. Grimm, and Yu. B. Ovchinnikov, "Gravitational laser trap for atoms with evanescent-wave cooling", Opt. Commun. **119**, pp. 652-662, 1995.

27. P. Desbiolles, M. Arndt, P. Szriftgiser, and J. Dalibard, "Elementary Sisyphus process close to a dielectric surface", Phys. Rev. A **54**, pp. 4292-4298, 1996.

28. N. Nha and W. Jhe, "Sisyphus cooling on the surface of a hollow-mirror atom trap", Phys. Rev. A **56**, pp. 729-736, 1997.

[I-2] NANO PHOTONICS

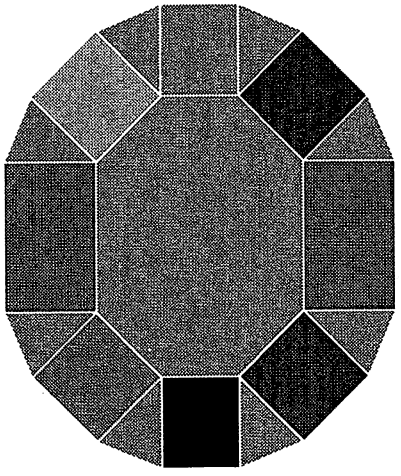

Jpn. J. Appl. Phys. Vol. 38 (1999) pp. L 826–L 829
Part 2, No. 7B, 15 July 1999

Vacuum Shear Force Microscopy Application to High Resolution Work

Vitali V. POLONSKI[1], Yoh YAMAMOTO[1], Jonathon D. WHITE[2,*], Motonobu KOUROGI[1,3] and Motoichi OHTSU[1,3]

[1]*Department of Applied Electronics, Tokyo Institute of Technology, 4259 Nagatsuta-cho, Midori-ku, Yokohama 226-8502, Japan*
[2]*Faculty of Engineering, University Telekom Multimedia, Melaka, 75450, Malaysia*
[3]*ERATO Ohtsu Localized Photon Project (Japan Science and Technology Corporation), 17-4 Tenko Building, 687-1 Tsuruma, Machida, Tokyo 194-0004, Japan*

(Received May 21, 1999; accepted for publication June 11, 1999)

A new technique—Vacuum Shear Force Microscopy (VSFM)—is introduced as a reliable method for maintaining a constant separation between a probe and sample. Elimination of many of the instabilities observed when applying the shear force mechanism to imaging under ambient conditions, allows for routine nanometer lateral and sub-nanometer normal resolution. In this paper this technique is applied, firstly, to the imaging of microtubules (biology) and, secondly, to the patterning and subsequent imaging of nanoscale metal lines (nanofabrication).

KEYWORDS: shear-force microscopy, nanofabrication, near-field optics, vacuum, scanning microscopy

1. Introduction

Significant economic benefits are to be obtained from the miniaturization. As a result there is a need for reliable nano-scale fabrication and imaging techniques. As past techniques, designed for the micro-scale, are often not applicable on the nano-scale, considerable research has gone into the development of new methodologies. In the area of surface imaging, the last two decades have seen first the discovery and then commercialization of a whole family of scanning probe microscopes. These include the atomic force microscope (AFM), scanning tunnelling microscope (STM), scanning near field optical microscope (SNOM or NOM) and shear force microscope (SFM). All members of this family provide sub-micron and, in certain cases, sub-nanometer imaging resolution.

Among the above techniques, that of SFM has proven to be the most controversial. Its well established use in NOM techniques has come under attack as a source of false optical contrast,[1,2] calling into question the results of many early experiments. In addition, the ability of the shear force (SF) images themselves to accurately represent surface topography has been questioned. It seems that the few nanometer thick surface layer may produce strange and non-reproducible results, including inverted topography,[3] resulting in the overall conclusion being that *constant SF signal does not necessarily mean constant height.* Considerable work has been done to illuminate the various interactions that collectively comprise "shear force". Key among these are Gregor *et al.*[4] investigation of the probe-surface interaction at a single point under vacuum conditions, and Davy *et al.*[5]'s investigation of the rise, under ambient conditions, of a thin water and pollutant surface film. In concluding their paper, Davy *et al.*,[5] make the radical comment that SF images must be taken within 10′ of exposure to air in order to be correlated with the surface topography. In this letter, we will show that the placing of a high quality SFM in a vacuum not only overcomes many of the problems associated with its application under ambient conditions but also provides higher resolution, image clarity and stability in the control of probe-sample separation. [It should be noted in passing that Behme *et al.*[6] have made considerable efforts improving SF instrumentation for variable cryogenic temperatures with a view towards spectroscopic studies. In their work resolution in vacuum is a secondary concern.[7]]

In addition to imaging, VSFM has found application in the area of nanofabrication. One example of the need for reliable distance control is the new and promising technique of near field optical photochemical vapour deposition (NFO-PCVD).[8] In this technique, an optical near field brush is used to write a pattern on a flat surface. Just as in Shodo (the art of Japanese brush calligraphy), reliable distance control is crucial to maintaining a constant line width, as, for a given brush, the separation between the brush and the writing surface determines each stroke's width. In this letter we will also show that by using VSFM one can accurately control the separation between the brush and writing tablet, allowing for uniform lines of uniform thickness to be written.

Currently, lines as narrow as 15 nm and as thin as 1–4 nm can be reliably written and then imaged. This is limited by the properties of the optical field rather than that of the shear force feedback system. We believe that the VSFM will become the method of choice for work in this exciting new field of nano-calligraphy.

2. Experimental Conditions

A schematic of a typical combination vacuum shear force, near field optical microscope is shown in Fig. 1. For explanation purposes, we can consider the VSFM as being composed of four separate systems: vacuum chamber, microscope head, shear-force distance control, and scanning electronics. In our case, the vacuum system is an encapsulated type reaction chamber designed with photochemical vapour deposition in mind. As well as operating in the presence of a few hundred Pa of Argon buffered metal alkyl gases (used for NFO-PCVD), a turbo molecular pump allows evacuation below 1 mPa vacuum. In addition to standard valves and ports, two aspects of the design deserve special mention. A special port passes an optical fibre, the tip of which is used both as a SF probe and near field optical source, through a sealed gasket, while a special window allows the approach of the sample to the SF tip to be observed using an external CCD camera.

The second key component is the microscope head. It must provide relative movement between the sample and probe tip in three dimensions while at the same time minimizing the effect of external vibrations and temperature fluctuations on probe-sample separation. In our initial prototype, the head was designed in a concentric configuration (Fig. 1), utilizing two coaxial 4 quadrant piezoceramic tubes (PZT). The inner

*E-mail address: whitejd@bigfoot.com

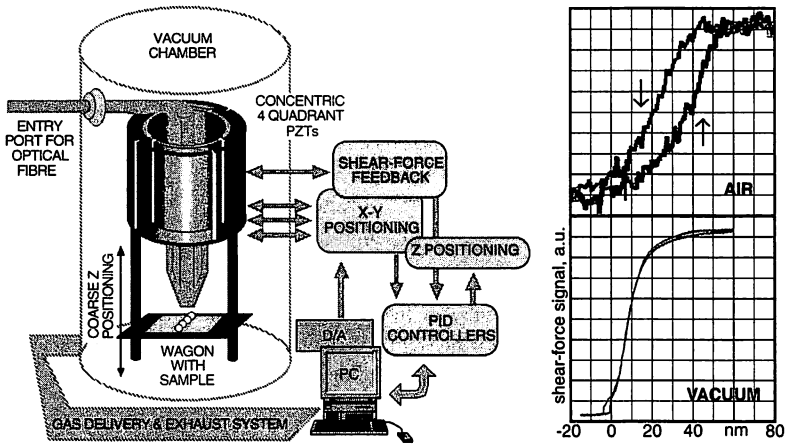

Fig. 1. Left: chematic of the vacuum shear force microscope. Right: typical shear force approach (arrow down) and retreat (arrow up) curves. These curves are taken under ambient and vacuum conditions (after 50′ at 2.7 Pa).

tube holds the sharpened optical fibre, while the outer supports the sample. Coarse lateral positioning is sacrificed in order to allow for higher mechanical stability. Coarse vertical positioning is provided by a piezoelectric-induced slip-stick motion scheme[9] utilizing the outer PZT. The typical amplitude of the tip lateral dithering did not exceed 1 nm, while the gap distance was 2–3 nm for imaging experiments and ~5 nm for deposits patterning.

The third aspect of a VSFM concerns the excitation and detection of the SF signal. In our setup we have used both optical and non-optical methods to monitor the separation dependent SF signal. In the first case, the inner tube served to vibrate the fibre—its four quadrants to allowing bistability to be suppressed[10]—and the SF amplitude was monitored using reflected laser diode light. A photo diode was used for detection. In the second, non-optical case, a tuning fork, mounted on the end of the inner tube, provided the detection signal. In both cases, the changes in the amplitude of the SF signal, after passing through a lock-in amplifier, were used in either an analogue or digital feedback loop to maintain a constant probe-sample separation.

A separate system provided the voltage to the outer PZT for raster scanning (imaging mode) or movement along a defined trajectory (NFO-PCVD write mode).

In actual operation, the sample is placed on the wagon far from the probe tip, the vacuum chamber closed, and air evacuated. After withdrawing the inner PZT, a coarse approach is made by alternately applying cycloid pulses to the outer PZT (slip-stick motion) to move the sample slightly less than 10 μm (the scan length of our PZT) up towards the fiber tip, and scanning the outer PZT its entire length. This procedure is repeated until a drop in the SF signal is detected (usually after a cup of coffee). At this point the voltage on the inner PZT is adjusted to position the outer PZT close to the center of its operating range thus minimizing PZT drift. An image is obtained, or a line written by moving the sample laterally, while using the feedback loop to keep the probe-sample separation constant.

3. Results and Discussion

The work described here involved three different components: observation of changes in the SF detection system in moving to low pressures, a comparison of ambient SFM and VSFM imaging of a well-known biological sample and, finally, a demonstration of the use of VSFM in conjunction with NFO-PCVD for nanofabrication. In the latter case, VSFM is used both to maintain a constant separation during patterned prenucleation as well as to provide a high-resolution topographical image of the sample after the completion of deposition.

The shear force signal as a function of probe-sample separation as the probe is first approached to the sample surface and then retreated away at both ambient and vacuum conditions is shown in Fig. 1 (right). In both cases, the shear force mechanism is only active at separations of a few tens nanometers or less. Of crucial importance to the matter at hand are the significant differences between operation under ambient and vacuum conditions. 1. As a result of the decrease of the damping coefficient at lower pressures, is a significant increase in the Q factor of the probe resonance. In the case of an optical fibre glued on one prong of a 33 kHz piezoelectric tuning fork, the Q factor at 2 mPa was 30% higher than that under ambient conditions (Q = 1900). 2. There is a slight blue shift of the resonance frequency.[6] This shift ranges from a few Hz for high-Q probes to a few tens of Hz for low-Q probe assemblies. 3. There is significantly less noise seen in the approach and retreat curves taken under vacuum conditions which allows for much more stable operation under feedback. One possible explanation for this is the absence of the surface layer of water and contaminates under vacuum. Further elucidation of the shear force mechanism will be published elsewhere.[11]

Our initial VSFM studies involved the observation of microtubules—a well studied biological polymer that forms the basis of the mammalian cytoskeleton and information expressway. These 25 nm diameter (TEM measurement) hollow polymer tubes are many micrometers in length. In non-contact AFM measurements[12] by Vaters *et al.* (1995), microtubules appeared to have a diameter of 60 nm. Authors pointed out a structural broadening due to the well known effect of AFM tip-sample convolution (tip profile acts as a higher spatial cut filter), reducing resolution. In our previous work under dry ambient conditions microtubules were measured to be about 40 nm in diameter and 15 nm in height[10] which we contributed to the slightly oval shape taken by these tubes when affixed to a glass cover slip. NOM measurements

confirmed that the MTs have a diameter of less than 40 nm.[13] Figure 2 is a typical VSFM image of microtubules, demonstrating the enhanced image quality of VSFM over both published AFM[12] and SFM measurements[10] done under ambient conditions. In the upper left a large microtubule bundle shines brightly while in the lower right a single 25 nm diameter microtubule crosses the picture from left to right. In comparing images (cf ref. 10) taken under ambient and vacuum conditions, it is readily apparent that individual microtubules are much more clearly visible along their entire length and at a higher signal-to-noise ratio. This is despite the fact that vacuum conditions have caused the tubes to collapse from 15 nm to about 3–4 nm in height. Without going into any further discussion of the distortion of microtubules under vacuum conditions, we can very conservatively estimate our horizontal resolution to be well in excess of 5 nm, making VSFM a highly competitive alternative to non-contact AFM and even TEM in certain cases. But more important than just this resolution is the improvement in image quality at low pressure. This indicates that the vacuum shear force mechanism allows the sample-probe separation to be kept in a stable manner at a given distance. We attribute this not only due to the removal of the surface water layer and other impurities and the higher Q-value of the system but also the elimination of most air induced noise.

Encouraged by the quality of these images we decided to apply vacuum shear force as the distance control mechanism in NFO-PCVD. NFO-PCVD is a new technique that enables maskless production of nanometric structures with controllable size, chemical composition and morphology.[8] In this two step technique an illumination mode NOM is placed inside the reaction chamber for PCVD. In the first step, prenucleation, a pattern is written on the substrate using the NOM in vacuum. In the second step, pattern formation, the optical tip is moved away from sample surface and the pattern grown using standard PCVD techniques. As the optical field density falls away exponentially as one moves away from the fibre tip, precise sub-nanometer control of the fibre tip—sample separation is required to ensure a constant line width. As images taken with NOM/SFM usually involve only a low number of pixels, image clarity, as shown by power spectral analysis,[14] provides good evidence of high resolution. To be more precise, pixelation is a technical problem of the digital image acquisition on this specific system, rather than a fundamental problem of the analogue technique. In contrast to a conventional NOM, in the case of NFO-PCVD, the role of the optical detector is performed by highly sensitive metal alkyl molecules, selectively rupturing their chemical bonds under the induced optical field. An example of NFO-PCVD shown in Fig. 3. Although the probe used to draw this line had a 100 nm aperture, it is really the sharp exponential decay of the optical near field which most greatly impacts the width variations during patterning. Writing a line of constant width thus requires that the probe-sample separation to be held constant at a sub-nanometer scale. As can be seen by the even width of the Zinc line drawn in Fig. 3, VSFM is clearly up to the task of providing the high level of distance control necessary for NFO-PCVD patterning. In addition, the 15–20 nm wide, 2–4 nm high lines clearly attest to the superior imaging abilities and high resolution of the VSFM technique.

It is interesting to note that of the currently used techniques to maintain a constant gap separation, only SFM and possibly NOM can meet the requirements of NFO-PCVD. STM methods are inappropriate since the substrate is an insulator. While AFM can provide surface topography images of high resolution, its reliance on cantilever-based vertical dithering make it unsuitable for NFO-PCVD. Moreover, with digital signal processor controlled fast phase-tracking data acquisition,[15] when thousands of pixels can be gathered within seconds, VSFM can be a very attractive method for a wide range of applications.

4. Summary

In conclusion, we have presented a new technique of probe-surface distance control and imaging Vacuum Shear Force Microscopy (VSFM) that overcomes many of the limitations and instabilities associated with the shear force mechanism operating under ambient conditions. It thus obtains unprece-

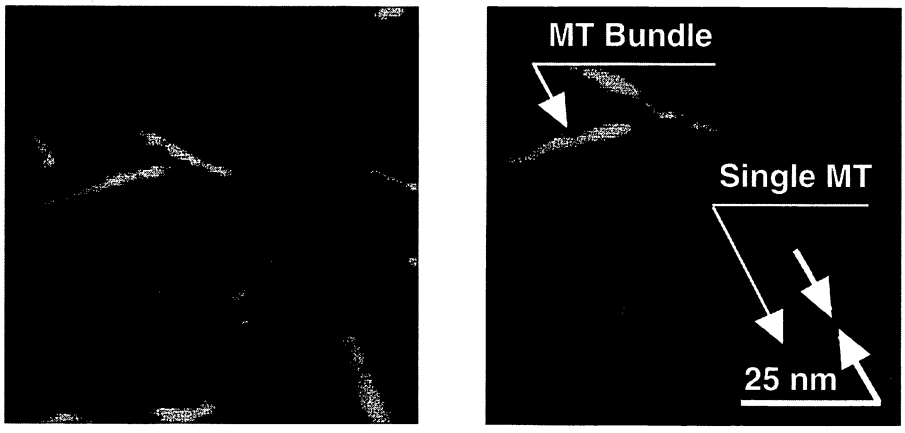

Fig. 2. Two consequent VSFM images of a microtubule taken at 2 mPa. Areas of the images on the left and on the right are $1028 \times 1028\,nm^2$ and $720 \times 720\,nm^2$ respectively. The microtubule was assembled from fluorescent rhodamine labelled tubulin using conventional techniques. A carefully cleaned hydrophilic quartz cover slip served as the substrate. A drop of poly-L-rezine (1 mg/ml) was placed on the substrate for 15 minutes and then washed off. The solution containing microtubules was then placed on the quartz cover slip and washed off after 30 seconds. A bunble of microtubules is indicated in the upper left portion of the image while a single microtubule crosses the lower part of the image. Single microtubules affixed using this method have an apparent full width half maximum FWHM of 25 nm in agreement with TEM measurements.

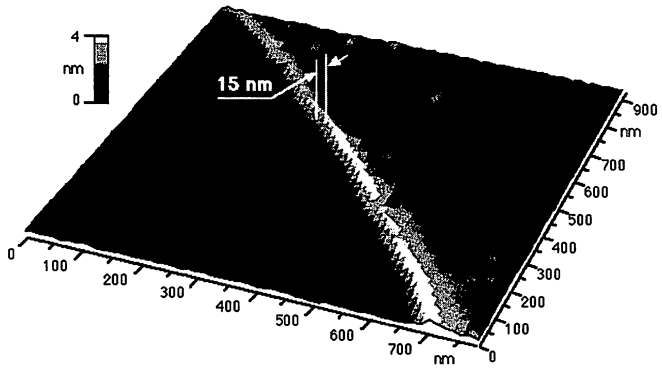

Fig. 3. VSFM image of Zinc lines written on Corning glass substrate by means of NFO-PCVD. The vacuum shear force mechanism is used not only to image the Zinc deposit but also to maintain a constant separation between the substrate and the NFO probe during patterning. The probe used in this case had a 100 nm light emitting aperture.

dented resolution and image clarity. The high vertical and horizontal resolution inherent in this technique enables its use in a wide array of applications, ranging from topographic imaging, nanofabrication, and surface energy transfer studies. This should make it a ready competitor to standard AFM and even to TEM in some cases. In addition, we have shown its unique applicability as a distance control mechanism in NFO-PCVD and its subsequent application in imaging lines deposited using this technique.

Acknowledgement

Authors would like to express their thanks to H. Fukuda (Kanagawa Academy of Science and Technology) and Dr. G. H. Lee (ERATO) for support and discussions. One of the authors (JDW) would also like to acknowledge the assistance of Dr. S. Hisanaga (Tokyo Metropolitan University) and Dr. W. Fann (Institute of Atomic and Molecular Sciences, Academia Sinica, Taipei).

1) B. Hecht, H. Bielefeldt, Y. Inoue, D. W. Pohl and L. Novotny: J. Appl. Phys. **81** (1997) 2492.
2) *Near-Field Nano/Atom Optics and Technology*, ed. M. Ohtsu (Springer-Verlag, Tokyo/Berlin/Heidelberg/New York, 1998) Chap. 1, p. 10.
3) A. Jalocha, M. H. P. Moyers, A. G. T. Ruiter and N. F. van Hulst: *Ultramicroscopy* **61** (1995) 221–226.
4) M. J. Gregor, P. G. Blome, J. Schöfer and R. G. Ulbrich: Appl. Phys. Lett. **68** (1996) 307.
5) S. Davy, M. Spajer and D. Courjon: Appl. Phys. Lett. **73** (1998) 2594.
6) G. Behme, A. Richter, A. M. Süptitz and Ch. Lienau: Rev. Sci. Instrum. **68** (1997) 3458.
7) Ch. Lienau: private communications.
8) V. V. Polonski, Y. Yamamoto, M. Kourogi, H. Fukuda and M. Ohtsu: J. Microscopy **194** (1999) 545.
9) Ch. Renner, Ph. Niedermann, A. D. Kent and Ø. Fisher: Rev. Sci. Instrum. **61** (1990) 965.
10) A. V. Zvyagin, J. D. White, M. Kourogi, M. Kozuma and M. Ohtsu: Appl. Phys. Lett. **71** (1997) 2541.
11) A separate manuscript, devoted to the overlooked interaction mechanism in shear-force microscopy, is in preparation.
12) W. Vater, W. Fritzche, A. Schaper, K. J. Böhm, E. Unger and T. M. Jovin: J. Cell Sci. **108** (1995) 1063.
13) A. V. Zvyagin, J. D. White and M. Ohtsu: Opt. Lett. **22** (1997) 955.
14) R. Uma Maheswari, H. Kadono and M. Ohtsu: Opt. Commun. **131** (1996) 133.
15) A. Scherz, W. Atia and C. C. Davis: Tech. Dig. 5th Int. Conf. on Near-Field Optics and Related Techniques (NFO-5), Shirahama, Japan, 1998, p. 117.

Silicon planar-apertured probe array for high-density near-field optical storage

Myung Bok Lee, Motonobu Kourogi, Takashi Yatsui, Kazuo Tsutsui, Nobufumi Atoda, and Motoichi Ohtsu

We propose a novel, to our knowledge, silicon planar-apertured probe array as an optical head for high-density near-field optical storage. In comparison with a conventional fiber probe employed for near-field optical storage the apertured probe array has a higher readout data-transmission rate and better mechanical durability. A probe array with an aperture size of 100 nm was fabricated by use of photolithography and wet etching of a silicon wafer. Subwavelength-readout capability was demonstrated by use of one aperture of the probe array. Furthermore, we achieved a 16 times increase in the light-transmission efficiency of the probe array by installing glass-sphere microlenses on each aperture. The increase was confirmed by measurement of the near-field optical intensity.

OCIS codes: 210.4680, 220.4000, 040.1240, 110.1220, 180.5810.

1. Introduction

In current optical storage systems the areal storage density is determined by the spot size of the focused laser beam, which is limited by the diffraction of light to $0.61\lambda/NA$, where λ is the wavelength of the laser and NA is the numerical aperture of the focusing lens. For higher density the use of a shorter-wavelength light source and a solid immersion lens[1] has been proposed. On the other hand, near-field optical recording has the potential to increase the storage density drastically without limitation by diffraction because the spot is formed not by means of focusing a propagating light but by a localized light on the apex of the probe. Several groups have successfully demonstrated near-field optical recording on the surfaces of various media such as magneto-optic,[2] photochromic,[3] and phase-change materials.[4] A sharpened and metal-coated optical fiber probe with a subwavelength aperture on its tip was employed in their experiments.

The fiber probe, however, has several deficiencies for applications in actual near-field optical storage systems. First, fiber probes lack durability because deformation and wear of the probe tip caused by its crashing into the sample rather frequently occur in near-field scanning schemes. Second, the light-transmission efficiency (throughput) of fiber probes is usually low, typically 10^{-5} when the aperture diameter is 100 nm.[5] This low efficiency of the near-field excitation of fiber probes limits the scanning speed and the data-transmission rate of the probe to low levels. To obtain a high enough near-field optical intensity, it is necessary to use high laser power, which often leads to thermal damage of a probe tip.[6] The scanning speed v of the readout head is given by $v = sr$, where s is the separation between the adjacent stored bits and r is the data-transmission rate. By substituting expected values for future 1-Tbit/in.^{2} density storage ($s = 30$ nm and $r = 1$ Gbit/s) into this relation, we obtain $v = 30$ m/s for the scan speed. However, it is impractical to scan the fiber probe by a piezoelectric actuator at such a high speed while maintaining a tip–medium separation as close as of the order of 10 nm.

We propose a two-dimensional probe array in place of a conventional fiber probe to achieve a high data-transmission rate in near-field optical storage. If a

M. B. Lee (mblee@nair.go.jp) and N. Atoda are with the Advanced Optical Memory Research Group, National Institute for Advanced Interdisciplinary Research, 1-1-4 Higashi, Tsukuba, Ibaraki 305-8562, Japan. M. Kourogi, T. Yatsui, K. Tsutsui, and M. Ohtsu are with the Interdisciplinary Graduate School of Science and Engineering, Tokyo Institute of Technology, 4259 Nagatsuta, Midorti-ku, Yokohama 226-8502, Japan. M. Kourogi and M. Ohtsu are also with the Kanagawa Academy of Science and Technology, KSP East Room 408, 3-2-1 Sakado, Takatsu-ku, Kawasaki 213-0012, Japan.

Received 21 December 1998; revised manuscript received 4 March 1999.

0003-6935/99/163566-06$15.00/0

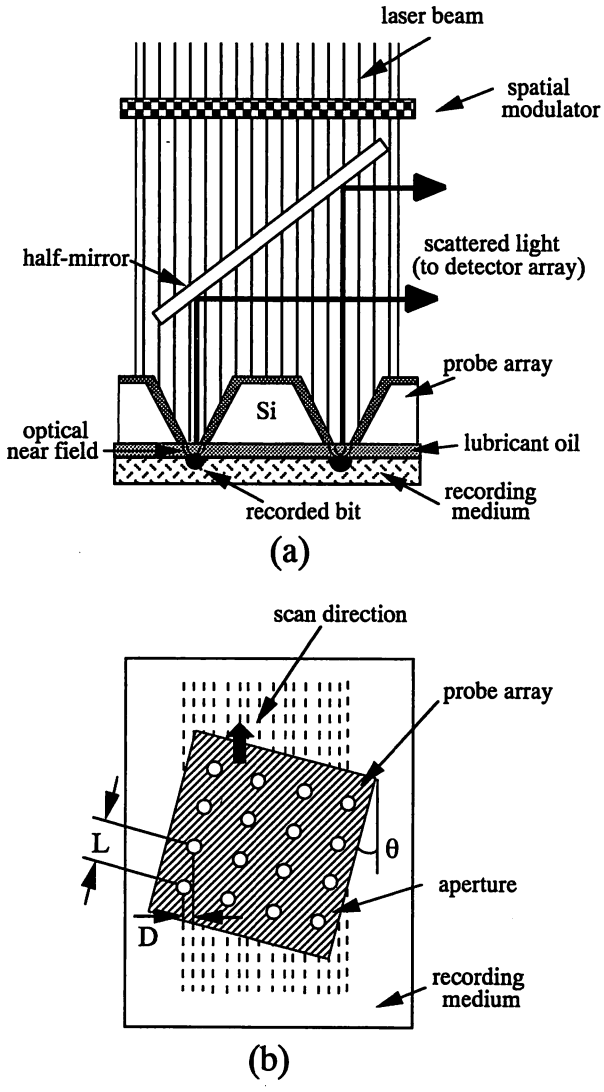

Fig. 1. Schematic diagrams of the recording and the readout principles for the proposed probe array: (a) Setup for recording by use of a spatially modulated propagating light incident upon the probe array and for readout by detection of the scattered light. (b) Readout by means of scanning the array with a tilt angle θ. The dashed lines represent the scanning trajectories of each aperture. L, separation between adjacent apertures in the array; D, separation between adjacent dashed lines.

probe array with n ($n \geqq 10^3$) elements is used the scanning speed can be reduced to $v' = v/n$, which can be realized easily even with a conventional driving technology, for obtaining a data-transmission rate equivalent to that given above. The principles, fabrication method, and readout capability of the planar-apertured probe array are described in this paper.

2. Concept of a Planar-Apertured Probe Array

Schematic diagrams of the recording and the readout principles of the proposed probe array are illustrated in Fig. 1. Figure 1(a) shows the setup for recording and readout. The probe array, which is fabricated with a silicon plate, has inverted pyramid-shaped grooves with nanometric apertures on their bottom ends. Through a spatial modulator the light intensity incident upon each aperture of the array is modulated, depending on the information to be recorded. Thus the optical near-field intensity generated on each aperture is modulated to be used for recording. Free-space propagation of a laser beam from a light source to the upper surface of the array enables the support of the array to be independent of the other far-field optical components. This lack of dependence can maintain the total weight of the array at a low level. This low weight is advantageous for fast scanning of the array. In readout the near-field light from the aperture array is scattered by bits recorded on the medium surface, converted into propagating light, and detected by a photodetector array placed at a far-field location. Although Fig. 1(a) illustrates reflection readout, transmission readout is possible as well by the placement of the detector array beneath the medium if the medium is properly chosen. Other configurations of the source light and the probe and the detector arrays are also possible.

Figure 1(b) shows an in-plane configuration of the probe array with respect to the medium's surface during readout. The array is tilted slightly with respect to the direction of rotation of the medium, and each aperture passes through the neighboring line on which recorded bits are aligned.[7] We can thus make the spacing D of the trajectories of each aperture coincide with that of the bit lines, even though the spacing of the apertures L is large compared with the light wavelength. The tilted angle can be represented by $\theta = \sin^{-1}(D/L)$. Because the aperture diameter d is smaller than the stored-bit diameter d_M, all the spatial Fourier frequency components of the scattered light lower than $1/d_M$ can be picked up by the array, which enables the retrieval of the spatial distribution of the scattered-light intensity along the scanning direction. For the direction transverse to the scanning direction the sampling theorem ensures complete regeneration if $D \leqq d_M/2$ (Ref. 8).

The planar-apertured probe array has advantages not only for reducing the scanning speed but also for the following: (1) The mechanical and the thermal durability of the proposed probe array is explicitly higher than that of a fiber probe. (2) The array is able to scan the storage medium smoothly while maintaining a constant narrow gap between the apertures and the medium surface by use of a coating of lubricating oil of nanometric thickness,[9] as in the case of the contact-type slider head of a hard disk. (3) The proposed probe is compatible with the integration of interfacing devices, such as a slab waveguide and a photodetector array.

3. Fabrication of the Planar-Apertured Probe Array

Figure 2 shows the fabrication process for our probe array. A silicon-on-insulator (SOI) wafer with a 10-μm-thick top layer [Si(100)] and a 2-μm-thick buried oxide layer was used as the starting material [Fig. 2(a)]. First, the SOI wafer was thermally oxidized to form a 1.2-μm-thick SiO_2 film. Window regions with areas of 0.5–1 mm^2 are formed by photolithog-

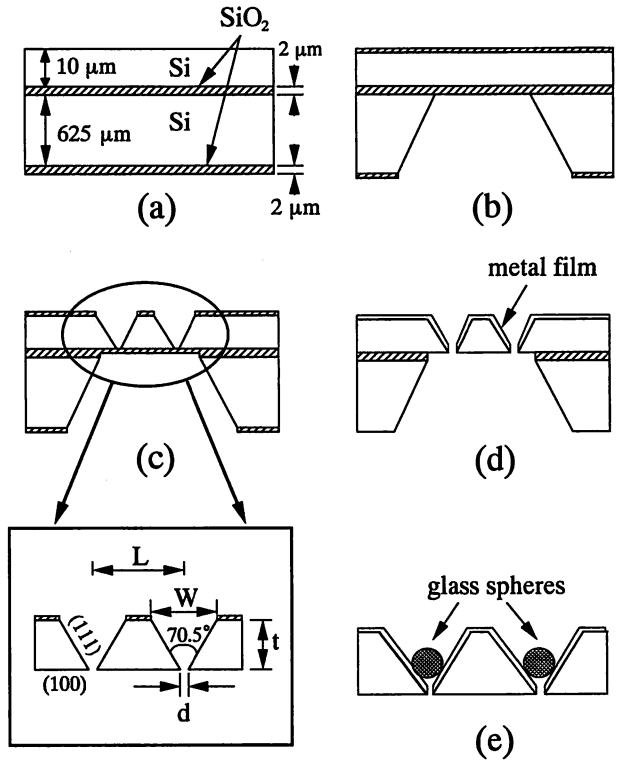

Fig. 2. Fabrication process for the silicon planar-apertured probe array: (a) the initial wafer, (b) formation of the window regions, (c) formation of the inverted pyramid-shaped grooves, (d) oxide removal and gold deposition, (e) installation of the glass spheres and cutting of the edge. The inset shows that the aperture size d is determined by the pattern size W and the SOI wafer thickness t.

raphy and a subsequent anisotropic etching process with a KOH aqueous solution (10 wt. %, 80 °C) on the back side of the wafer [Fig. 2(b)]. The thin silicon membrane in the window region in Fig. 2(b) usually bulges out because of a stress unbalance between the silicon and the SiO_2. Therefore we strip away the oxides with a buffered hydrofluoric acid ($HF:NH_4F$ = 1:9) and reoxidize the wafer to form a 0.1-μm-thick SiO_2 film. The formation of the new thin oxide film makes the surface flat and clean and thus increases adhesion of the photoresist. Then inverted pyramid-shaped grooves are formed on the front side of the wafer by photolithography and a subsequent etching process with the KOH solution [Fig. 2(c)]. Etching continues until the apexes of the grooves reach the oxide layer. Oxides are again stripped away with buffered hydrofluoric acid to form small apertures in the bottoms of the inverted pyramids, and if necessary a metallic film is deposited on the front side to block far-field light transmission [Fig. 2(d)]. In practical usage as an optical head the edge of the silicon bulk can be cut off.

To increase further the light throughput of the probe array by automatically focusing the propagating light on each aperture, we installed glass-sphere microlenses on each inverted pyramid [Fig. 2(e)]. The glass spheres (refractive index of ~1.5 with a 10-μm diameter) were suspended in isopropyl alcohol to form a colloidal solution. Although the focal point of a glass-sphere lens is determined by the diameter and the refractive index of the lens, these parameters were not optimized in this preliminary experiment. The silicon wafer with the fabricated probe array, as shown in Fig. 2(d), was spin coated with the solution. The glass spheres settled onto each aperture by aspiration force through the apertures generated by evacuation that was applied to fix the wafer during the spinning process.

Figure 3 shows typical scanning electron micrographs of the fabricated probe arrays. A homogeneous aperture array was formed, as shown in Fig. 3(a). The size of the aperture of the array was approximately 100 nm after a 50-nm-thick deposition of gold film, as Fig. 3(b) demonstrates. This dimension is much smaller than the wavelength of light, a relation that was seldom achieved in conventional micromachined structures based on the anisotropic wet etching of silicon. Figure 3(c) shows that the glass-sphere lens array was installed successfully on the aperture array in one step by the simple method described above. The advantage of the current process is that the near-field optical probe array is fabricated

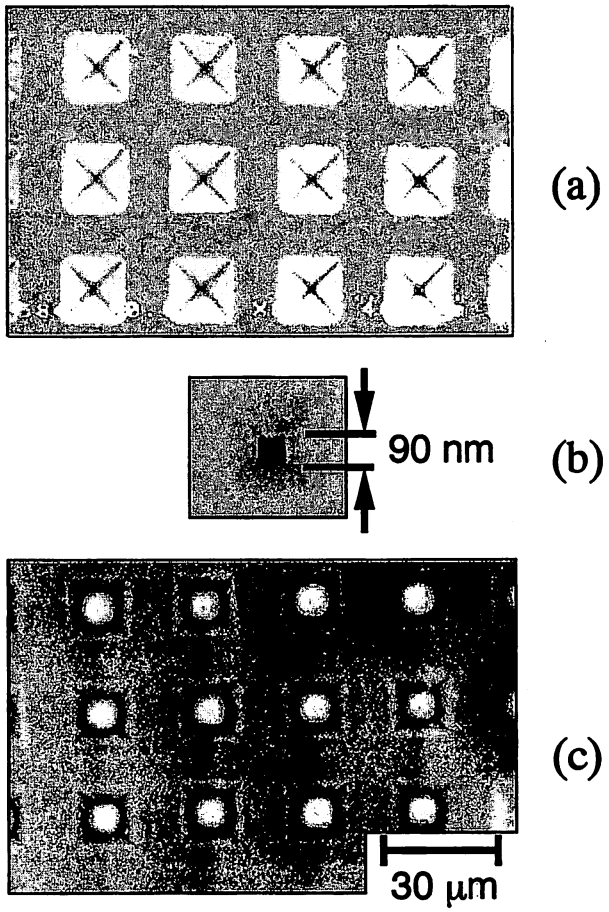

Fig. 3. Scanning electron micrographs of the fabricated probe arrays: (a) before installation of the glass-sphere lenses, (b) enlargement of one aperture viewed from the bottom side, (c) after installation of the glass-sphere lenses.

effectively and reproducibly by use of only the established techniques of lithography and etching for a silicon planar process even though the aperture size is smaller than the resolution limit achievable with photolithography.

As is shown in the inset of Fig. 2(c), the apex angle (i.e., 70.5°) of the pyramid is governed by the crystallographic orientation of the Si(111) planes. The aperture size d is determined by the thickness t of the substrate and the edge length of the basal plane of the pyramid W, which is given by $d = W - \sqrt{2}t$. The accuracy of W depends on that of the lithography. The use of a SOI wafer provides sufficient homogeneity and a high enough accuracy of t. Another factor affecting the aperture size d is the thickness of the coated metal film. Fluctuations of the aperture size d may induce fluctuations of the scattered-light intensity from each aperture, which could decrease the signal-to-noise ratio for signal detection. However, this decrease can be avoided by appropriate adjustment of a threshold level for discriminating the temporal-signal sequence. The separation L between adjacent apertures rather than fluctuations of the aperture size should be regulated to realize a readout process free of bit errors. The accuracy of L can be maintained at a sufficiently high level by conventional photomask techniques because the value of L is set to be larger than the light wavelength to prevent signal interference between adjacent apertures.

4. Readout Capability of the Probe

To demonstrate the readout capability of the probe array as a near-field optical head, we observed the near-field image of a sample with one of the apertures of the probe array. The experimental setup is shown in Fig. 4. A probe array without lenses, as shown in Fig. 3(a), was cut from the wafer by use of focused-ion-beam etching and attached to a suspension made with a beryllium copper thin plate. The probe array was then put on a sample that was fixed on a scanning stage. We fabricated the sample by drawing several lines, the width and the separation of which were 100 nm and 1 μm, respectively, with focused-ion-beam etching on a glass plate covered with a 100-nm-thick aluminum film. A thin lubricating film was coated onto the sample. A laser beam was focused on one of the grooves of the probe array whose aperture size was 100 nm. The sample was X–Y scanned, and the light transmitted through both the aperture and the sample was detected with a photomultiplier.

Figure 5 shows the cross-sectional distribution of the transmitted light. Curves A and B represent the results obtained without and with the probe, respectively. Curve A was obtained by means of focusing the laser beam directly on the sample. The vertical axis represents the detected optical power normalized to the peak power of the light detected without the probe. A comparison of curves A and B shows that the light throughput of the probe is 10^{-3}, which is 2 orders of magnitude higher than that of a typical fiber probe with the same aperture size. Because the focused spot size is estimated to be approximately 1 μm, no line pattern can be resolved in curve A, whereas several clear peaks are observed in curve B. From the magnified intensity curve shown in the inset of Fig. 5, the full width at half-maximum (FWHM) of the peak can be seen to be 250 nm, which is more than twice that of the drawn linewidth. The major reason for this greater value is considered to be the light transmission through the silicon at the periphery of the aperture because the probe was not coated

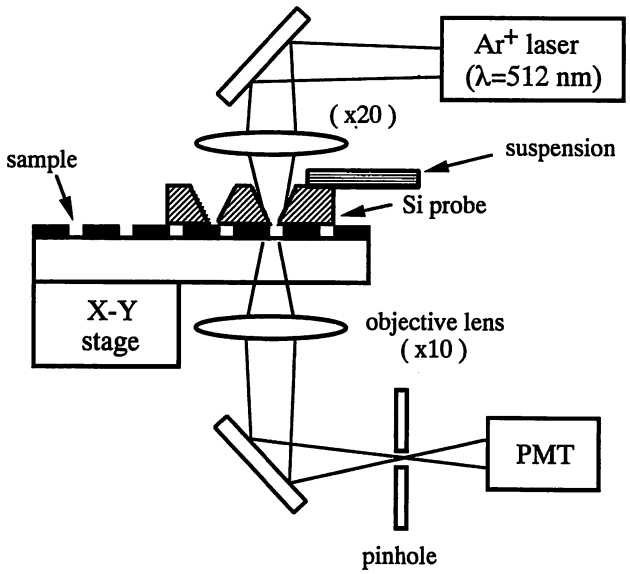

Fig. 4. Experimental setup for readout by use of the planar-apertured probe. PMT, photomultiplier.

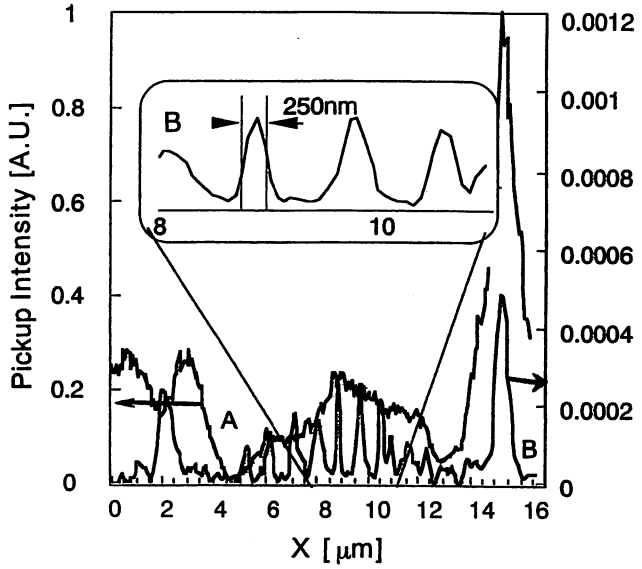

Fig. 5. Cross-sectional distribution of the transmitted light. Curves A and B represent results obtained without and with the probe, respectively. The vertical axis gives the detected optical power normalized to the peak power of the light detected without the probe.

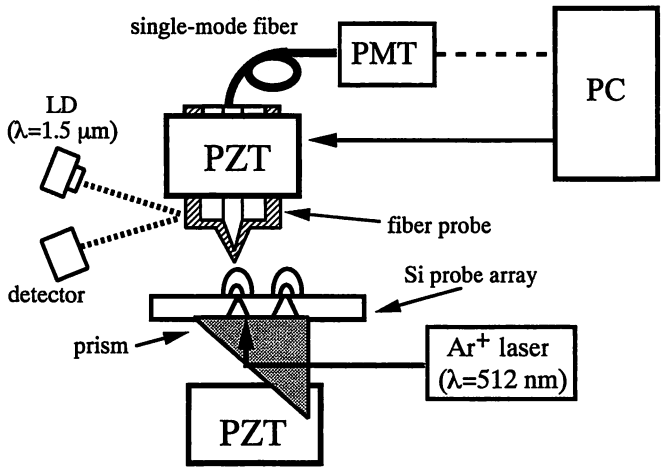

Fig. 6. Experimental setup of the SNOM for evaluation of the probe. LD, laser diode; PZT, piezoelectric transducer; PMT, photomultiplier.

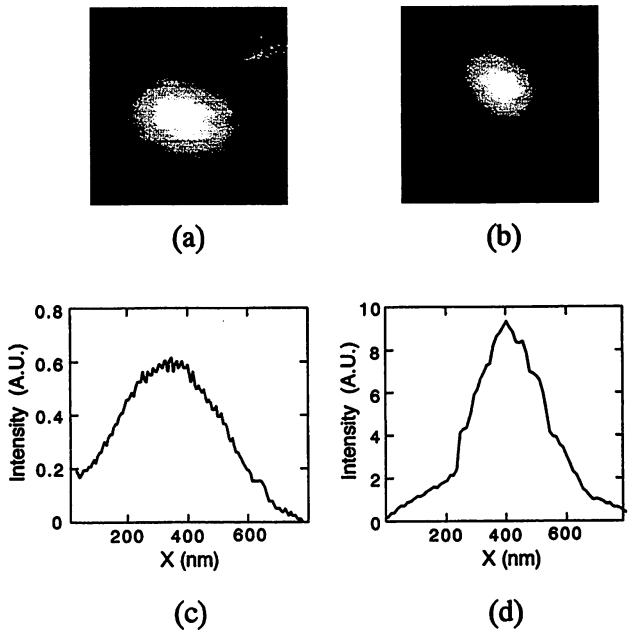

Fig. 7. SNOM images of the apertures with a scan area of 700 nm × 700 nm in the probe array (a) without and (b) with a glass-sphere lens. SNOM cross-sectional spatial distributions of the output light (c) shown in (a) and (d) shown in (b).

with metal in this experiment. That is, the effective aperture size for the light became wider than the geometrical aperture size.

5. Near-Field Optical Evaluation

We evaluated the optical efficiency of our probe array by measuring the optical near-field intensity generated on the aperture. In this experiment, we used the two types of probe, with and without microlenses, with an aperture size of 500 nm to investigate the effect of the lens on the near-field optical intensity. The experimental setup is shown in Fig. 6. A laser beam irradiated the front side of the sample perpendicularly. The sample was attached to a prism that was fixed to a piezoelectric stage. We scattered the optical near fields emerging from the apertures by scanning them with a sharpened fiber probe tip, which was fabricated by use of selective chemical etching[10] and subsequent deposition of a 30-nm-thick gold film, and detected the fields with a photomultiplier. The tip–sample separation was maintained to within several nanometers with the shear-force feedback technique.[11,12]

Figures 7(a)–7(d) show scanning near-field optical microscope (SNOM) images and their corresponding intensity profiles of the output light from one element of the aperture array without and with a glass-sphere lens. Clear single-peaked profiles of the optical intensity distribution are observed. The intensity distribution of the aperture with a glass lens is narrower than that of the aperture without a lens. Comparison of the curves shown in Figs. 7(c) and 7(d) shows that use of the glass-sphere lens increases the light intensity as much as 16 times by concentration of the light energy. Highly efficient ultrahigh-density near-field optical recording and readout are expected to be achieved by use of the microlens-installed aperture array combined with a much smaller aperture than was used in our case.

6. Summary

To realize a high data-transmission rate in ultrahigh-density near-field optical storage, we have proposed a silicon planar-apertured probe array. A probe array with an aperture size of 100 nm was fabricated by means of photolithography and wet etching. We have demonstrated the subwavelength-readout capability of our probe by using it to scan lines formed on a metal film. The observed linewidth was 250 nm. Installing glass-sphere lenses on each aperture enhanced the near-field optical intensity by as much as 16 times.

We thank H. Ishiwara and E. Tokumitsu (Tokyo Institute of Technology) for their support in the fabrication process.

References

1. B. D. Terris, H. J. Mamin, D. Rugar, W. R. Studenmund, and G. S. Kino, "Near-field optical data storage using a solid immersion lens," Appl. Phys. Lett. **65,** 388–390 (1994).
2. E. Betzig, J. K. Trautman, R. Wolfe, E. M. Gyorgy, P. L. Finn, M. H. Kryder, and C.-H. Chang, "Near-field magneto-optics and high density data storage," Appl. Phys. Lett. **61,** 142–144 (1992).
3. S. Jiang, J. Ichihashi, H. Monobe, M. Fujihira, and M. Ohtsu, "High localized photochemical processes in LB films of photochromic material by using a photon scanning tunneling microscope," Opt. Commun. **106,** 173–177 (1994).
4. S. Hosaka, T. Shintani, M. Miyamoto, A. Hirotsune, M. Terao, M. Yoshida, K. Fujita, and S. Kammer, "Nanometer-sized phase-change recording using a scanning near-field optical microscope with a laser diode," Jpn. J. Appl. Phys. **35,** 443–447 (1996).
5. G. A. Valaskovic, M. Holton, and G. H. Morrison, "Parameter control, characterization, and optimization in the fabrication of

optical fiber near-field probes," Appl. Opt. **34,** 1215–1228 (1995).
6. M. Stahelin, M. A. Bopp, G. Tarrach, A. J. Meixner, and I. Zschokke-Granacher, "Temperature profile of fiber tips used in scanning near-field optical microscopy," Appl. Phys. Lett. **68,** 2603–2605 (1996).
7. K. Goto, "Proposal of ultrahigh density optical disk system using a vertical cavity surface emitting laser array," Jpn. J. Appl. Phys. **37,** 2274–2278 (1998).
8. M. Ohtsu, K. Tsutsui, M. Kourogi, and M. B. Lee, "Near field optics and its application to optical memory," Electron. Commun. Jpn. Part 2, **81**(8), 41–48 (1998).
9. M. Kourogi, T. Yatsui, S. Ishimura, M. B. Lee, N. Atoda, K. Tsutsui, and M. Ohtsu, "A near-field planar apertured probe array for optical near-field memory," in *Far- and Near-Field Optics: Physics and Information Processing*, S. Jutamulia and T. Asakura, eds., Proc. SPIE **3467,** 258–267 (1998).
10. T. Pangaribuan, S. Jiang, and M. Ohtsu, "High controllable fabrication of fiber probe for photon scanning tunneling microscope," Scanning **16,** 362–367 (1994).
11. E. Betzig, P. L. Finn, and J. S. Weiner, "Combined shear force and near-field scanning optical microscopy," Appl. Phys. Lett. **60,** 2484–2486 (1992).
12. R. Toledo-Crow, P. C. Yang, Y. Chen, and M. Vaez-Iravani, "Near-field differential scanning optical microscope with atomic force regulation," Appl. Phys. Lett. **60,** 2957–2959 (1992).

Journal of Microscopy, Vol. 194, Pt 2/3, May/June 1999, pp. 249–254.
Received 6 December 1998; accepted 9 February 1999

Quantum theoretical approach to a near-field optical system

K. KOBAYASHI* & M. OHTSU*†
**ERATO Ohtsu Localized Photon Project, Japan Science and Technology Corporation, 687-1 Tsuruma, Machida, Tokyo 194-0004, Japan*
†Interdisciplinary Graduate School of Science and Engineering, Tokyo Institute of Technology, 4259 Nagatsuta-cho, Midori, Yokohama, Kanagawa 226-8502, Japan

Key words. Probe tip–sample interaction, projection operators, quantum theory, virtual photon model, Yukawa-type interaction.

Summary

The paper proposes a quantum theoretical formulation of an optical near-field system based on the projection-operator method. Special attention is paid to a nanometric probe tip–quantum mechanical sample system, whose interactions are essential for describing such phenomena as atom guidance and manipulation, or local excitation of a single quantum dot. The relationship to the virtual photon model – an intuitive model – is discussed, and the latter's empirical assumption of the Yukawa-type interaction between probe and sample is justified theoretically. Several applications of the theory are briefly outlined.

1. Introduction

Recent experimental study has revealed the possibility of local excitation of a sample by means of an optical near field beyond the diffraction limit, as well as high-resolution imaging. The fluorescence lifetime of a single molecule, for example, has been measured and its quenching behaviour has been discussed in terms of the sample–probe distance and the aperture size of the probe (Trautmann & Ambrose, 1997).

Photoluminescence spectroscopy of a single quantum dot at low temperature has been also investigated to obtain information about electronic-level structures, the spin-relaxation mechanism, and the switching effect (Flack *et al.*, 1996; Matsumoto *et al.*, 1998; Saiki & Ohtsu, 1998; Saiki *et al.*, 1998; Toda *et al.*, 1998). Such experimental results exemplify the need for quantum theoretical treatment of optical near-field problems. Several authors, in fact, have semi-classically analysed near-field spectroscopic problems (Girard *et al.*, 1995; Cho *et al.*, 1996; Kobayashi, 1998), formulating electronic structures in terms of quantum mechanics and optical near fields in terms of classical electromagnetics.

Correspondence to: K. Kobayashi. Tel: + 81 42 788 6036; fax: + 81 42 788 6031; e-mail: kkoba@ohtsu.jst.go.jp

An atom, as a small sample, may be considered as an ultimate candidate for nano/atom photonics. To this end, atom reflection by a near field induced over a prism surface has been experimentally verified (Balykin *et al.*, 1988; Aminoff *et al.*, 1993; Landragin *et al.*, 1996), and atoms have been guided through a micrometre-sized hollow fibre by means of blue-detuned optical near field (Ito *et al.*, 1996).

Atomic deposition with nanometric precision using very-low-energy atom deflection or manipulation has also been proposed (Ito *et al.*, 1997; Ito *et al.*, 1998), and experimental verification is expected after technical challenges such as fibre probe improvement (Mononobe *et al.*, 1998; Yatsui *et al.*, 1998) and manipulation and detection schemes (Hori, 1993; Ohtsu *et al.*, 1993; Klimov & Letokov, 1995; Ito & Ohtsu, 1998).

Atom–substrate interactions via a propagating light field, being a more basic physics issue, have been investigated both theoretically and experimentally. Classical antenna theory can predict some kinds of atomic behaviour, but the existence of pure cavity quantum electrodynamic (QED) effects is well known (Hinds, 1994). The energy shift in the ground state of an atom is one example in which quantum theory is essential for explaining the phenomenon.

From the above observation it is natural to quantum-theoretically formulate a near-field optical system consisting of an atom or molecule and an optical near-field probe. Such a formulation would be preferable if it could be related to an intuitive model giving clear insights into the near-field optical system as well as scanning image characteristics. It may be possible to use a semi-classical approach in order to predict the quantum-mechanical states of matter, but we will employ a full quantum-mechanical approach, for the following reasons. Experimental progress shows that an optical near-field probe tip reaches 1–50 nm in diameter (Ohtsu, 1995), and it is not clear to deal with such a microscopic tip and an atom or a molecule as two isolated systems when they are coupled via a macroscopic bath system (incident light, substrate, and/or fibre probe). Under

this condition, the states of the total system should be different from those of the two isolated systems, and it is very important to consistently handle the interaction between the two from the quantum-mechanical viewpoint, although the existing theoretical approaches have neglected to do so from the outset. Moreover there have been no attempts to give any intuitive model from microscopic approaches.

We pay special attention to a nanometric probe tip–quantum mechanical sample system whose interactions are essential for describing such phenomena as those in atom deflection or manipulation experiments using optical near fields. The purpose of this paper is to propose a unified and systematic formulation of optical near-field problems in order to discuss the quantum-mechanical observables of such a system. We will then discuss the relationship to the virtual photon model (Hori, 1993; Kobayashi & Ohtsu, 1998; Ohtsu & Hori, 1998) – an intuitive model based on experimental results – which assumes the Yukawa-type interaction between a probe tip and sample as an elementary process. Taking advantage of the characteristics of the virtual photon model, we will then describe a potential application of the theory.

The paper is organized as follows. The next section outlines the method on which our approach is based. In Section 3, Yukawa-type interaction between sample and probe tip, which was empirically assumed in the virtual photon model, is derived as an effective sample–probe interaction. One example of a case in which the virtual photon model can offer physical insight is discussed in Section 4, and we also give an example of the application of our formulation on the basis of the virtual photon model. Finally, Section 5 offers some concluding remarks.

2. Method of projection operators

We will employ the method of projection operators and discuss the near-field optical system, since we have to describe the difference between coupled and isolated quantum-mechanical states in a unified and systematic way. It is very appropriate to extract an arbitrary number of degrees of freedom from the many degrees of freedom of the system, and to renormalize the effects of the other degrees of freedom. Even if we are, for example, not able to obtain all of the exact states for the total system, we can derive the exact effective interaction in terms of a few states for the isolated system, as will be shown below (see Eqs.(10–11)).

First, let us briefly outline the method of static projection operators (Hyuga & Ohtsubo, 1978; Kobayashi & Kohmura, 1984; Fulde, 1995). Let the total Hamiltonian $\hat{H}$ for a near-field optical system such as a near-field optical microscope and spectroscope be

$$\hat{H} = \hat{H}_0 + \hat{V}, \tag{1}$$

$$\hat{H}_0 = \hat{H}_A + \hat{H}_B + \hat{H}_{bath}, \tag{2}$$

where the Hamiltonians $\hat{H}_A$ and $\hat{H}_B$ describe the states of the probe tip and sample, respectively, as isolated quantum-mechanical systems. The Hamiltonian $\hat{H}_{bath}$ represents the states of light and infinite matter (substrate or fibre probe), while $\hat{V}$ denotes the interaction between the system A (or B) and the bath system (Fig. 1). Steady states of $\hat{H}$ and $\hat{H}_0$ are assumed in the following discussion, and the eigenvalues and eigenstates of $\hat{H}$ are written as E_λ and $|\Psi_\lambda\rangle$, respectively, i.e.

$$\hat{H}|\Psi_\lambda\rangle = (\hat{H}_0 + \hat{V})|\Psi_\lambda\rangle = E_\lambda|\Psi_\lambda\rangle. \tag{3}$$

Defining the static projection operators P and $Q = 1 - P$ in the usual manner as

$$|\Psi_\lambda^{(1)}\rangle = P|\Psi_\lambda\rangle, \quad |\Psi_\lambda^{(2)}\rangle = Q|\Psi_\lambda\rangle, \tag{4}$$

$$P^2 = P, \quad PQ = QP = 0, \tag{5}$$

we divide the eigenstates $|\Psi_\lambda\rangle$ into two groups, $|\Psi_\lambda^{(1)}\rangle$ in P-space and $|\Psi_\lambda^{(2)}\rangle$ in Q-space. It is possible to formally express $Q|\Psi_\lambda^{(2)}\rangle$ by $P|\Psi_\lambda^{(1)}\rangle$ as

$$Q|\Psi_\lambda^{(2)}\rangle = J(E_\lambda - \hat{H}_0)^{-1}Q\hat{V}P|\Psi_\lambda^{(1)}\rangle, \tag{6}$$

$$J = \left[1 - (E_\lambda - \hat{H}_0)^{-1}Q\hat{V}\right]^{-1}, \tag{7}$$

and the eigenstates $|\Psi_\lambda\rangle$ for the total Hamiltonian can then be expressed in terms of the eigenstates in P-space as

$$|\Psi_\lambda\rangle = (P + Q)|\Psi_\lambda\rangle = JP|\Psi_\lambda^{(1)}\rangle. \tag{8}$$

Since both of the states satisfy the normalization condition, we can rewrite this as

$$|\Psi_\lambda\rangle = JP(PJ^\dagger JP)^{-1/2}|\Psi_\lambda^{(1)}\rangle. \tag{9}$$

We thus obtain an effective operator $\hat{O}_{eff}$ in the P-space, which is equivalent to an arbitrary operator $\hat{O}$ in the full space, corresponding to physical observables (Kobayashi & Kohmura, 1984):

$$\langle\Psi_\mu|\hat{O}|\Psi_\lambda\rangle = \langle\Psi_\mu^{(1)}|\hat{O}_{eff}|\Psi_\lambda^{(1)}\rangle, \tag{10}$$

$$\hat{O}_{eff} = (PJ^\dagger JP)^{-1/2}(PJ^\dagger\hat{O}JP)\,(PJ^\dagger JP)^{-1/2}. \tag{11}$$

From the above Eqs (10–11), it follows that relevant quantities such as the probe tip–sample interaction and transition dipole moments can be exactly expressed by using a small number of bases in P-space after renormalizing the effects from Q-space. This is one of the advantages of the method, and is desirable from the computational viewpoint.

3. Effective sample–probe interaction and virtual photon model

On the basis of the above formalism, we now discuss the virtual photon model (Hori, 1993; Kobayashi & Ohtsu, 1998; Ohtsu & Hori, 1998) – a unique and intuitive model – in particular, its empirical assumption regarding

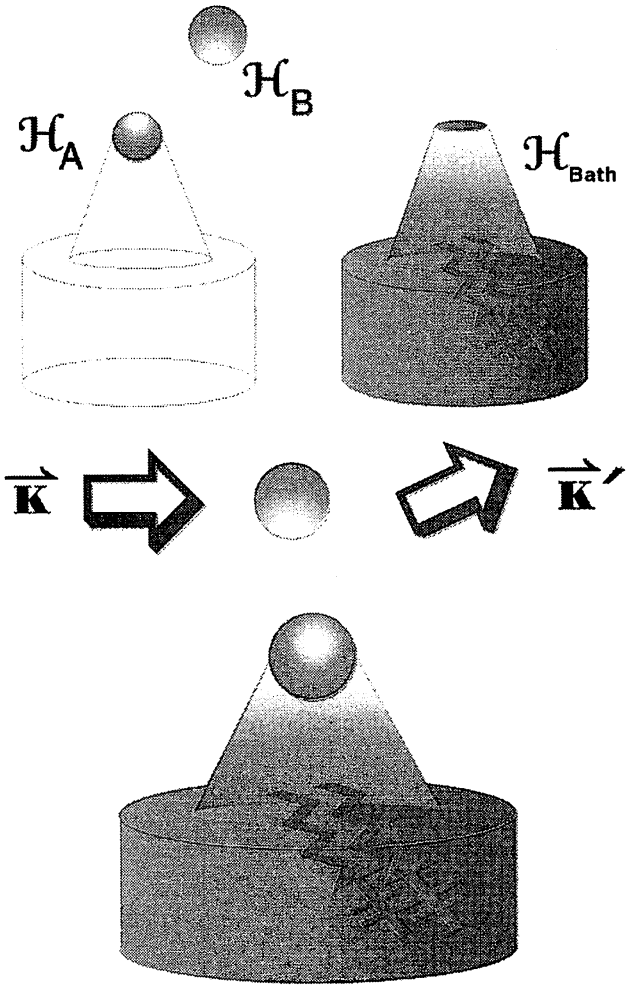

Fig. 1. Schematic illustration of how to compose a total Hamiltonian $\hat{H}$ for a near-field optical system from three components, $\hat{H}_A$, $\hat{H}_B$, and $\hat{H}_{bath}$. (a) The states of the probe tip, the sample, and the bath system, as each isolated system, are described by the Hamiltonian $\hat{H}_A$, $\hat{H}_B$, and $\hat{H}_{bath}$, respectively. Depending on the sample, $\hat{H}_B$ may contain the centre of mass motion as well as internal degrees of freedom. Atom deflection system by the optical near field described by the total Hamiltonian $\hat{H}$ as an example. Incident and deflected atoms have the momenta $\hbar\vec{k}$ and $\hbar\vec{k}'$, respectively.

the probe–sample interaction in a fundamental process. The model assumes virtual photons with nonzero mass (m_{eff}) tunnelling between nanometric objects, similar to electron tunnelling in scanning tunnelling microscopy (STM). This means that the Yukawa-type interaction is responsible for the interaction between a nanometric probe tip and sample. In other words, the Yukawa potential ($e^{-m_{eff}r}/r$) is assumed to be generated near the nanometric object (source) as a result of the interaction between incident light and the object, for both of the illumination and collection modes in near-field optical microscopy and spectroscopy. Owing to the assumption, it can describe optical near fields localized on the material surface without solving the Maxwell equation, and a novel scheme for manipulating atoms by using the optical near field was successfully proposed and analysed (Hori, 1993; Ohtsu *et al.*, 1993).

Let us now adopt more specific Hamiltonians as components of $\hat{H}_0$ in order to derive an explicit form of the effective sample–probe interaction. First we choose a Hamiltonian for $\hat{H}_\alpha$ ($\alpha = A, B$),

$$\hat{H}_\alpha = \sum_n E_n(\alpha)\hat{e}^\dagger_{n\alpha}\hat{c}_{n\alpha}, \tag{12}$$

$$E_n(\alpha) = \frac{\hbar^2 k_\alpha^2}{2m_c} = \frac{\hbar^2}{2m_e}\left(\frac{n\pi}{a}\right)^2 \quad \text{or} \quad \frac{\hbar^2}{2m_e}\left(\frac{n\pi}{b}\right)^2, \tag{13}$$

where the creation and annihilation operators are denoted as $\hat{c}^\dagger_{n\alpha}$ and $\hat{c}_{n\alpha}$, and the relevant energy levels are designated as $E_n(\alpha)$, and electric dipole transitions between those levels are allowed. Note that this Hamiltonian corresponds to one in which electrons with effective mass m_e and wave number k_α are confined in an infinite well potential of size $a(b)$. The ground and excited states will be designated as $|A\rangle$, $|A^*\rangle$, $|B\rangle$, $|B^*\rangle$, for later use.

Next, let us describe $\hat{H}_{bath}$ in terms of excitons ($\hat{B}^\dagger$, $\hat{B}$), photons ($\hat{a}^\dagger$, $\hat{a}$), and their interactions. Excitons with energy $\hbar\Omega$ represent an infinite crystal lattice with site number j. Photons with a wave vector $\vec{k}+\vec{G}$ and energy $\hbar\omega$ interact with the excitons as $-\hat{\vec{\mu}}_j\cdot\hat{\vec{D}}(\vec{r}_j)$ in a multipolar QED Hamiltonian (Craig & Thirunamachandran, 1984), where $\hat{\vec{\mu}}$ and $\hat{\vec{D}}(\vec{r}_j)$ are the dipole operator of matter and the displacement field operator at site j, respectively. As is well known (Hopfield, 1958; Knoester & Mukamel, 1989; Juzeliunas & Andrews, 1994), this Hamiltonian can be diagonalized in terms of exciton-polariton modes (energy $\hbar\omega_{\vec{k}\nu}$, creation/annihilation operator $\xi^\dagger_{\vec{k}\nu}$, $\hat{\xi}_{\vec{k}\nu}$ as

$$\hat{H}_{bath} = \sum_j\sum_{i=1}^{3}\hbar\Omega\hat{B}^\dagger_{ji}\hat{B}_{ji} + \sum_{\vec{k},\vec{G}}\sum_{\lambda=1}^{2}\hbar\omega_{\vec{k}+\vec{G}}\hat{a}^\dagger_{\vec{k}+\vec{G},\lambda}\hat{a}_{\vec{k}+\vec{G},\lambda} - \sum_i\hat{\vec{\mu}}_j\cdot\hat{\vec{D}}(\vec{r}_j) \tag{14}$$

$$= \sum_{\vec{k},\nu}\hbar\omega_{\vec{k}\nu}\hat{\xi}^\dagger_{\vec{k}\nu}\hat{\xi}_{\vec{k}\nu}. \tag{15}$$

Here the indices i and λ label the three Cartesian axes and the transverse polarization of light, respectively. The $\vec{k}$ summation extends over the first Brillouin zone, and $\vec{G}$ runs over the reciprocal lattice. The summation of υ runs over all branches of exciton-polaritons. We will use the ground state of $\hat{H}_{bath}$, $|0\rangle$ as one component of the P-space. It follows from Eq. (15) that photons and infinite matter may be a collection of harmonic oscillators. In this representation, a near-field optical probe tip interacts with a nanometric sample via exciton-polariton mediation as

follows:

$$\hat{V} = -\sum_{\alpha=A}^{B} \hat{\vec{\mu}}_\alpha \cdot \hat{\vec{D}}(\vec{r}_\alpha)$$
$$= -\sum_{\alpha=A}^{B}\sum_{\vec{k}\nu} \frac{i\hbar}{\sqrt{V_0}}\sqrt{\frac{2\pi}{\hbar}}(K'_{\vec{k}\nu}(\alpha)\hat{\xi}_{\vec{k}\nu} - K'^{*}_{\vec{k}\nu}(\alpha)\hat{\xi}^{\dagger}_{\vec{k}\nu})(\hat{b}^{\dagger}_{\alpha} + \hat{b}_{\alpha}), \quad (16)$$

where $K'_{\vec{k}\nu}(\alpha)$ and $K'^{*}_{\vec{k}\nu}(\alpha)$ are the coupling coefficients between the probe (sample) and exciton-polaritons, and $\hat{b}^{\dagger}_{\alpha}$ and $\hat{b}_{\alpha}$ are the creation and annihilation operators leading to electric dipole transitions of the sample–probe system, relating to Eq. (12). It is worth reminding ourselves that there is no direct interaction between sample and probe tip in this Hamiltonian.

As explained in the previous section, one can exactly express the relevant interaction by using a small number of bases in the *P*-space, after renormalizing the effects from the *Q*-space. We then choose a combination of the five states, $|A\rangle$, $|A^*\rangle$, $|B\rangle$, $|B^*\rangle$ and $|0\rangle$, as the *P*-space bases illustrated in Fig. 2, and set $|\vec{\Psi}^{(1)}_{\lambda}\rangle = |A\rangle\ |B^*\rangle\ |0\rangle$, $|\Psi^{(1)}_{\mu}\rangle = |A^*\rangle\ |B\rangle\ |0\rangle$, in order to evaluate the effective sample–probe interaction V_{eff} (AB) from Eqs (10) and (11):

$$V_{\text{eff}}(AB) = \langle \Psi^{(1)}_{\mu} | \hat{V}_{\text{eff}} | \Psi^{(1)}_{\lambda} \rangle$$
$$= \left\langle \Psi^{(1)}_{\mu} \middle| (PJ^{\dagger}JP)^{-1/2}(PJ^{\dagger}\hat{V}JP)\ (PJ^{\dagger}JP)^{-1/2} \middle| \Psi^{(1)}_{\lambda} \right\rangle \quad (17)$$

Noting that the operator J satisfies the equation

$$[J, \hat{H}_0]P = (E - \hat{H}_0)JP - J(E - \hat{H}_0)P$$
$$= \hat{V}JP - JP\hat{V}JP, \quad (18)$$

let us expand J as $J = P + \Sigma_{n=1}^{\infty} g^{(n)} J^{(n)}$, and obtain perturbative solutions of J. We can then determine V_{eff} (AB) perturbatively in the order of $\hat{V}$. Since there are no contributions in the lowest order of $\hat{V}$ because $P\hat{V}P = 0$, the nonzero contributions to V_{eff} (AB) come from the second order of $\hat{V}$ as

$$V_{\text{eff}}(AB) = \langle A^* | \langle B | \langle 0 | \left[P\hat{V}Q(E^0_P - E^0_Q)^{-1}\hat{V}P + P\hat{V}(E^0_P - E^0_Q)^{-1}Q\hat{V}P \right] | A \rangle | B^* \rangle | 0 \rangle \quad (19)$$

$$= \frac{4\pi}{(2\pi)^3}\sum_{\nu}\int d^3k \left[\frac{K'_{\vec{k}\nu}(A)K'^{*}_{\vec{k}\nu}(B)}{\omega_{\vec{k}\nu} - \Omega_0(B)} + \frac{K'_{\vec{k}\nu}(B)K'^{*}_{\vec{k}\nu}(A)}{\omega_{\vec{k}\nu} + \Omega_0(A)} \right]. \quad (20)$$

Here the summation of $\vec{k}$ is replaced by integrating $\vec{k}$, and $\hat{H}_0$ in the denominators with respect to the corresponding eigenvalues. The excitation energies, $\hbar\Omega_0(A)$ and $\hbar\Omega_0(B)$, are

$$\hbar\Omega_0(A) = \frac{3\hbar^2}{2m_e}\left(\frac{\pi}{a}\right)^2, \quad \hbar\Omega_0(B) = \frac{3\hbar^2}{2m_e}\left(\frac{\pi}{b}\right)^2, \quad (21)$$

from Eq. (13). We can similarly show how $\langle \Psi^{(1)}_{\lambda} | \hat{V}_{\text{eff}} | \Psi^{(1)}_{\mu} \rangle$ contribute to the effective sample–probe interaction V_{eff}(BA).

On the basis of the dispersion relation of an exciton-polariton (effective mass: m_p, one of the solutions of the dispersion relation: $\omega_{\parallel}$) obtained from Eq. (15), we make the following assumptions, which would be appropriate for actual near-field experiments:

(i) $\omega_{\vec{k}\nu} = \omega_{\parallel} + \frac{\hbar}{2m_p}k^2 \sim \frac{\hbar}{2m_p}k^2$, $(\omega_{\parallel} < \Omega_0)$,

(ii) $K'_{\vec{k}\nu} \sim \text{const} \cdot \exp(i\vec{k}\cdot\vec{r})$.

Defining the ratio $\gamma = (3m_p/m_e)^{1/2}$ for exciton-polaritons and electrons in the probe tip (sample), we apply these assumptions to Eq. (20), and obtain the explicit function form of

$$V_{\text{eff}}(AB) + V_{\text{eff}}(BA) \propto \frac{\exp[(i\gamma\pi\tau)/b]}{\tau} + \frac{\exp[-(\gamma\pi\tau)/a]}{\tau} + \frac{\exp[(i\gamma\pi\tau)/a]}{\tau} + \frac{\exp[-(\gamma\pi\tau)/b]}{\tau},$$
$$\tau = |\vec{r}_A - \vec{r}_B|. \quad (22)$$

This gives the effective sample–probe interaction derived from microscopic consideration, and the second and fourth terms are the Yukawa function, which was empirically assumed in the virtual photon model. The formula also shows that optical near field is effectively localized near the sample–probe system, and that the decay length is proportional to the inverse of the probe (sample) size and consistent with the experimental results (Saiki *et al.*, 1996). In addition, we can infer the so-called resonance condition that a similar size gives maximum coupling between sample and probe tip, as can be determined by a simple estimation based on the static dipole model.

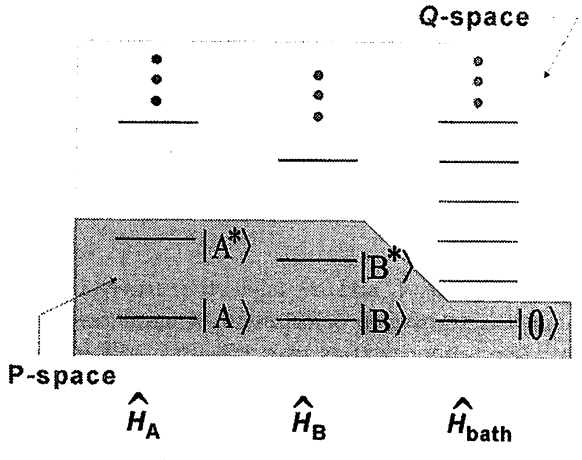

Fig. 2. *P*- and *Q*-space spanned by bases each of which corresponds to an eigenstate of $\hat{H}_A$, $\hat{H}_B$, and $\hat{H}_{\text{bath}}$. The *P*-space is depicted by hatching.

4. Practical implications of the virtual photon model and application of our formulation

Since the empirical assumption of the virtual photon model was justified on the basis of microscopic theory in the previous section, we can take advantage of the characteristics of the model to develop an application of our formulation. We have, so far, emphasized the quantum-mechanical aspects of the optical near-field systems. The model also predicts the fundamental performance of near-field optical microscopy much faster than the conventional approach in computation time, that is, the intensity distribution in the near-field region of a subwavelength metallic circular aperture irradiated by the propagating light. The resolution of the microscope was also clearly explained by the model. In addition, we can easily handle more realistic probe–sample systems, and discuss the dependence of detected signals on the probe shape, or on the taper angle θ (see Fig. 3). Let the probe be a set of dielectric spheres of different diameters that approximates a conical shape. From Eq. (22), the Yukawa potential is generated between two arbitrary points on the surfaces of the probe sphere p_i and sample sphere s_j. Thus pickup signal I can be written as

$$I \propto \sum_{i}^{\text{probe}} \sum_{j}^{\text{sample}} \left| \int_{\delta j} \mathrm{d}r_1 \int_{pi} \mathrm{d}\tau_2 V_{\text{eff}}(\tau_{12}) \right|^2, \quad \tau_{12} = |\vec{\tau}_1 - \vec{\tau}_2|. \tag{23}$$

If the so-called resonance condition is satisfied, the pickup signal becomes proportional to $\exp[-\text{const}/\sin(\theta/2)]$.

Turning to the quantum-mechanical system again, we discuss the possibility of applying the formulation to atom deflection and manipulation with a sharpened fibre probe. These techniques are unique and will be essential for carrying an atom to a desired point on a substrate with high spatial accuracy far beyond the diffraction limit. As shown in Fig. 1, suppose that an incident atom with momentum $\hbar\vec{k}$ is deflected into momentum $\hbar\vec{k}'$ by an optical near field V_{eff}. Then the differential cross-section or angular distribution of the deflected atom is given by

$$\frac{\mathrm{d}\sigma}{\mathrm{d}\Omega} \propto \left| \frac{M}{2\pi\hbar^2} \left\langle \vec{k}' \middle| V_{\text{eff}} \middle| \vec{k} \right\rangle \right|^2 \tag{24}$$

where M is the mass of the atom. This kind of evaluation will be required in the design of atom guidance and manipulation systems using the optical near field, as well as in the discussion of basic experimental results.

One implication related to cavity QED problems is that the transition dipole moment of an atom or a molecule $\vec{\mu}_0$ is changed by the influence of the probe tip and optical near field, that is, the difference between the isolated and coupled states. Perturbative evaluation of Eqs (10) and (11) with $\hat{O} = \hat{\vec{\mu}}$ shows that the renormalized transition dipole moment $\vec{\mu}_{\text{eff}}$ can be categorized into two classes: one directly renormalized into $\vec{\mu}_0$, and the other not renormalized into $\vec{\mu}_0$, owing to transitions between higher energy levels. It is interesting to estimate these effects numerically.

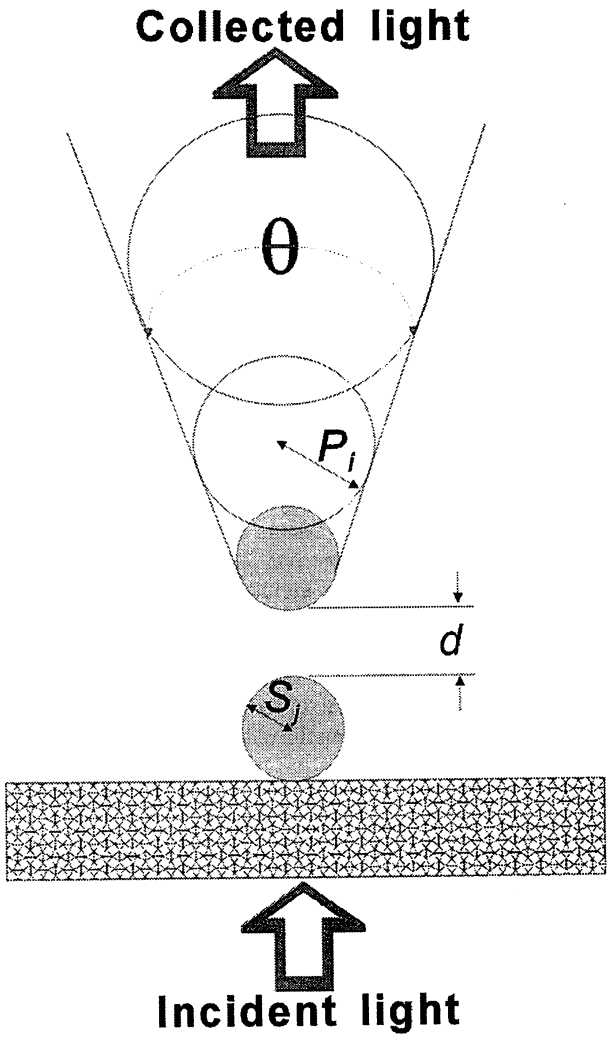

Fig. 3. Fibre probe tip with taper angle θ as a collection of dielectric spheres with different radii. The i-th and j-th spheres of the probe and sample are denoted as p_i and s_j, respectively. The probe–sample separation is shown as d.

5. Conclusion

We have developed a microscopic theory for an optical near-field system, using a quantum-mechanical technique known as the projection-operator method. It was shown that the Yukawa-type interaction is involved in effective probe tip–sample interaction, indicating that the empirical assumption of the virtual photon model is justified. The key points are that a probe tip exists near the sample, and that the electron energies in the probe tip or sample are inversely proportional to the square of its size, owing to the

confinement effect. We discussed a few applications of the theory, taking advantage of the characteristics of the virtual photon model. In future, we need to examine in detail the assumptions and approximations used, as well as what kind of normal modes should be included for optical near-field problems, in order to make the formulation more rigid.

Acknowledgements

The authors gratefully acknowledge fruitful conversations with H. Hori of Yamanashi University and H. Ito of Tokyo Institute of Technology. K.K. also appreciates valuable suggestions from T. Kohmura of University of Tsukuba.

References

Aminoff, C.G., Steane, A.M., Bouyer, P., Desbiolles, P., Dalibard, J. & Cohen-Tannoudji, C. (1993) Cesium atoms bouncing in a stable gravitational cavity. *Phys. Rev. Lett.* **71**, 3083–3086.

Balykin, V.I., Letokov, V.S., Ovchinnikov, Yu, B. & Sidorov, A.I. (1988) Quantum-state-selective mirror reflection of atoms by laser light. *Phys. Rev. Lett.* **60**, 2137–2140.

Cho, K., Ohfuti, Y. & Arima, K. (1996) Theory of resonant SNOM (scanning near field optical microscopy): breakdown of the electric dipole selection rule in the reflection mode. *Surf. Sci.* **363**, 378–384.

Craig, D.P. & Thirunamachandran, T. (1984) *Molecular Quantum Electrodynamics*. Academic Press, New York.

Flack, F., Samarth, N., Nikitin, V., Crowell, P.A., Shi, J., Levy, J. & Awschalom, D.D. (1996) Near-field optical spectroscopy of localized excitons in strained CdSe quantum dots. *Phys. Rev. B.* **54**, R17312–R17315.

Fulde, P. (1995) *Electron Correlations in Molecules and Solids*. Series in Solid-State Sciences 100, 3rd edn. Springer-Verlag, Berlin.

Girard, C., Martin, O.J.F. & Dereux, A. (1995) Molecular lifetime changes induced by nanometer scale optical fields. *Phys. Rev. Lett.* **75**, 3098–3101.

Hinds, E.A. (1994) Peturbative cavity quantum electrodynamics. *Cavity Quantum Electrodynamics* (ed. by P. R. Berman), pp. 1–56. Academic Press, San Diego.

Hopfield, J.J. (1958) Theory of the contribution of excitons to the complex dielectric constant of crystals. *Phys. Rev.* **112**, 1555–1567.

Hori, H. (1993) Quantum optical picture of photon STM and proposal of single atom manipulation. *Near Field Optics* (eds D. W. Pohl and D. Courjon), pp. 105–114, Kluwer, Dordrecht.

Hyuga, H. & Ohtsubo, H. (1978) Breakdown of the Siegert theorem and the many-body charge density operators. *Nucl. Phys.* **A294**, 348–356.

Ito, H., Nakata, T., Sakaki, K., Ohtsu, M., Lee, K.I. & Jhe, W. (1996) Laser spectroscopy of atoms guided by evanescent waves in micron-sized hollow optical fibers. *Phys. Rev. Lett.* **76**, 4500–4503.

Ito, H. & Ohtsu, M. (1998) Near-field optical atom manipulation: toward atom photonics. *Near-Field Nano/Atom Optics and Technology* (ed. M. Ohtsu), pp. 217–266. Springer-Verlag, Tokyo.

Ito, H., Otake, K. & Ohtsu, M. (1998) Near-field optical guidance and manipulation of atoms. *Proceedings SPIE*, **3467**, 250–257.

Ito, H., Sakaki, K., Ohtsu, M. & Jhe, W. (1997) Evanescent-light guiding of atoms through hollow optical fiber for optically controlled atomic deposition. *Appl. Phys. Lett.* **70**, 2496–2498.

Juzeliunas, G. & Andrews, D.L. (1994) Quantum electrodynamics of resonant energy transfer in condensed matter. *Phys. Rev. B*, **49**, 8751–8763.

Klimov, V.V. & Letokov, V.S. (1995) New atom trap configurations in the near field of laser radiation. *Opt. Commun.* **121**, 130–136.

Knoester, J. & Mukamel, S. (1989) Intermolecular forces, spontaneous emission, and superradiance in a dielectric medium: Polariton–mediated interactions. *Phys. Rev. A*, **40**, 7065–7080.

Kobayashi, K. (1998) Spin polarization in near-field optical microscopy. *Appl. Phys. A*, **66**, S391–S395.

Kobayashi, K. & Kohmura, T. (1984) Momentum-transfer dependence of nuclear spin-isospin transitions. *Prog. Theor. Phys.* **71**, 327–338.

Kobayashi, K. & Ohtsu, M. (1998) Related theories. *Near-Field Nano/Atom Optics and Technology* (ed. M. Ohtsu), pp. 267–293. Springer-Verlag, Tokyo.

Landragin, A., Courtois, J.-Y., Labeyrie, G., Vansteenkiste, N., Westbrook, C.I. & Aspect, A. (1996) Measurement of the van der Waals Force in an Atomic Mirror. *Phys. Rev. Lett.* **77**, 1464–1467.

Matsumoto, T., Matsuda, K., Nishi, K., Saiki, T. & Ohtsu, M. (1998) Near-field nonlinear absorption spectroscopy of single quantum dots. *Technical Digest of the 5th International Conference on Near Field Optics and Related Techniques*. pp. 38–39. Shirahama.

Mononobe, S., Saiki, T., Kourogi, M., Kurihara, K. & Ohtsu, M. (1998) Probe fabrication, high-throughput probes and functional probes. *Near-Field Nano/Atom Optics and Technology* (ed. M. Ohtsu), pp. 31–100. Springer-Verlag, Tokyo.

Ohtsu, M. (1995) Progress of high-resolution photon scanning tunneling microscope due to a nanometric fiber probe. *J. Lightwave Technol.* **13**, 1200–1221.

Ohtsu, M. & Hori, H. (1998) *Near-field nano-optics – from Basic Principles to Nano-Fabrication and Nano-Photonics*. Plenum, New York.

Ohtsu, M., Jiang, S., Pangaribuan, T. & Kozuma, M. (1993) Nanometer resolution photon STM and single atom manipulation. *Near Field Optics* (eds D. W. Pohl and D. Courjon), pp. 131–139, Kluwer, Dordrecht.

Saiki, T., Nishi, K. & Ohtsu, M. (1998) Low temperature near-field photoluminescence spectroscopy of InGaAs single quantum dots. *Jpn. J. Appl. Phys.* **37**, 1638–1642.

Saiki, T. & Ohtsu, M. (1998) Diagnosing semiconductor nanomaterials and devices. *Near-Field Nano/Atom Optics and Technology*. (ed. M. Ohtsu), pp. 153–192. Springer-Verlag, Tokyo.

Saiki, T., Ohtsu, M., Jang, K. & Jhe, W. (1996) Direct observation of size-dependent features of the optical near field on a subwavelength spherical surface. *Opt. Lett.* **21**, 674–676.

Toda, Y., Shinomori, S., Suzuki, K. & Arakawa, Y. (1998) Polarized photoluminescence spectroscopy of single self-assembled InAs quantum dots. *Phys. Rev. B*, **58**, R10147–R10150.

Trautmann, J. & Ambrose, W.P. (1997) Near-field optical imaging and spectroscopy of single molecules. *Single Molecule Optical Detection, Imaging and Spectroscopy* (eds T. Basche, W. E. Moerner, M. Orrit and U. P. Wild), pp. 191–222. VCH, Weinheim.

Yatsui, T., Kourogi, M. & Ohtsu, M. (1998) Increasing throughput of a near-field optical fiber probe over 1000 times by the use of a triple-tapered structure. *Appl. Phys. Lett.* **73**, 2090–2092.

Journal of Microscopy, Vol. 194, Pt 2/3, May/June 1999, pp. 545–551.
Received 6 December 1998; accepted 30 January 1999

Nanometric patterning of zinc by optical near-field photochemical vapour deposition

V. V. POLONSKI,* Y. YAMAMOTO,* M. KOUROGI,*†‡ H. FUKUDA*†§ & M. OHTSU*†‡
**Department of Applied Electronics, Tokyo Institute of Technology, 4259 Nagatsuta-cho, Midori-ku, Yokohama 226-8502, Japan*
†Kanagawa Academy of Science and Technology, KSP East 408, 3-2-1 Sakado, Takatsu, Kawasaki, 213-0012, Japan
‡ERATO Ohtsu Localized Photon Project (Japan Science and Technology Corporation), 17-4 Tenko Building, 687-1 Tsuruma, Machida, Tokyo 194-0004 Japan
§RICOH Co, Ltd, R & D Center, 16-1 Shineityo, Tsuzuki-ku, Yokohama 224-0035 Japan

Key words. Nanoelectronic devices, nanofabrication, near-field optics, patterned prenucleation, photochemical vapour deposition.

Summary

A new technique, optical near-field photochemical vapour deposition (NFO-PCVD) enables maskless production of nanometric structures with controllable size, chemical composition and morphology. By placing a near-field optical microscope inside the reaction chamber for photochemical vapour deposition we have deposited nanoscale metal patterns. We demonstrate for the first time, successfully deposited in the near-field region, lines of metallic zinc with the observed stripe width of 20 nm.

Introduction

Reliable mask-free sub-wavelength deposition of metals, oxides and semiconductors is required for a wide range of applications including, but not limited to, photomask repair of DRAM, nanophotonic devices and the fabrication of hybrid systems of molecular electronics. Although there has been a number of attempts to substitute desirable pattern deposition by removal of unwanted parts from the nanoscale structures, it seems that no further progress in nanofabrication can be made without introducing new flexible techniques analogous to those widely used for microscale photochemical vapour deposition (PCVD).

Laser direct writing of thin films as a maskless method for producing metallization patterns on microchips has attracted particular attention with the rapid development of integrated circuit technology. However, diffraction, the very nature of focused optical far-field laser light, imposes the limit of resolution of this kind of work. Instead, conventional photolithography has become well established and has matured as information technology has moved towards miniaturization with the exponential increase in the density of transistors on computer chips. The first reported fully working 1-Gbit DRAM was produced using 0·18-μm lithography (Kim *et al.*, 1997). In a laboratory, lithographic patterns with line resolution of 120 nm have been obtained in a 1-Gbit DRAM chip using 193 nm UV radiation (Nugent, 1998), which seems to be a minimum size limit for conventional transistor technology until the turn of the century. Other approaches with relatively easy scalability to manufacturing include electron beam and X-ray lithography, which are currently used for nanocale (sub-100 nm) patterning of thin film. Apart from being complicated multi-step techniques, dependence on inaccuracy of the mask, photoresist characteristics and exposure latitude leaves much room for improvement. Although several studies of near-field optical lithography on photoresist films have recently been reported (Rogers *et al.*, 1997), it is unlikely to find industrial application and can be considered only as a complementary method to other photolithographic techniques. Other approaches, still at the research stage, include ultrafast laser ablation and scanning probe microscope lithography. Scanning tunnelling microscopy and atomic force microscopy (AFM) techniques yielded record pattern widths down to few nanometres, but as a rule require either preferential etching or conductivity of the materials involved.

During the last few years, the noninvasive nature of near-field optical microscopy (NOM) has attracted the increasing interest of researchers world-wide, with sub-wavelength resolution imaging of samples for different applications being performed (Ohtsu, 1998). In the work described here, our primary targets were to achieve direct-write deposition

Correspondence to: V. V. Polonski.

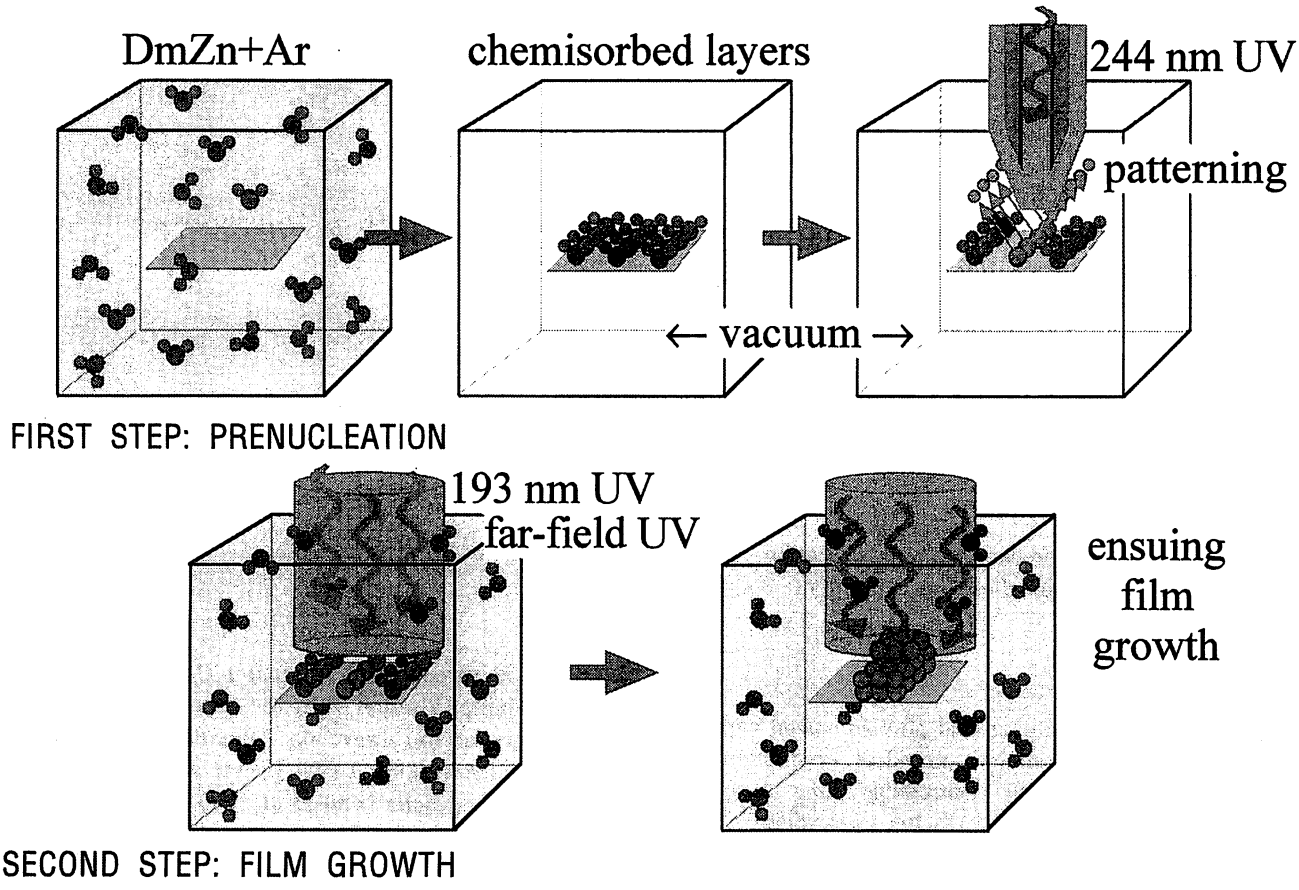

Fig. 1. Overview of the NFO-PCVD patterned film growth through prenucleation. In the first step, a pattern is drawn using near-field light, while in the second step, conventional far-field light is used to 'develop' the pattern.

of metal with a fibre tip and to obtain results on the applicability of this new technique.

Principle

To revitalize attempts to obtain highly reproducible direct writing of fine metallization patterns we decided to combine near-field microscopy with PCVD. We employed a two-step process for depositing metal layers on the surface, thereby bypassing the etching steps of traditional microfabrication. In the first step, prenucleation, patterning was performed under vacuum conditions, utilizing the optical near-field of illuminated UV light. This light, when directed onto the chemisorbed layers of metal alkyls, forms metal nuclei on the substrate surface (Fig. 1). Apart from the advantages described below, patterning in vacuum avoids possible deposition of a metal onto the fibre tip. In the second step, film growth, far-field UV light (i.e. a conventional propagating light beam) is directed onto the prenucleated area in the presence of a parent gas and the decomposed metal atoms are deposited on the pre-existing nuclei. This results in a highly controllable sub-wavelength deposit, which, in turn, serves as a sample for topography imaging. The deposition is evaluated by the shear-force microscopy, utilizing the same fibre tip as a probe.

Dimethylzinc (DmZn; $Zn(CH_3)_2$) was chosen as a parent gas for the experiment. Earlier reports of the far-field deposition of Zn from the same precursor using prenucleation (Ehrlich *et al.*, 1981) and its well-established characteristics (Eden, 1992) for UV-light-assisted deposition led us to expect similar behaviour of the film growth in the near-field using a UV fibre tip for light delivery. As a result, surface molecules of DmZn decompose selectively, forming Zn nucleation centres. The second stage of the final deposition is performed using unfocused UV pulses with parent gas inside the deposition chamber. The prenucleated area was irradiated from the optical far-field. Maintaining constant DmZn molecule flux in the vicinity of the surface, the Zn is deposited around previously prenucleated centres and the pattern is grown.

Experimental set-up

We have chosen the encapsulated type of reaction chamber since, in our case, very low atom flux is enough to achieve

film growth. Prior to the patterning stage the deposition chamber was evacuated to below 10^{-3} Pa and then filled with 130 Pa (partial pressure) of DmZn in an Ar buffer. After 20 min the chamber was thoroughly re-evacuated using a turbomolecular pump, leaving a chemisorbed molecular layer a few monolayers thick on the substrate. Patterning was performed at 10^{-3} Pa by illuminating the area beneath the aperture while keeping the tip in the near-field region and moving it across the substrate. For the second stage, film growth, the reaction chamber was refilled with a few tenths Pa of DmZn.

The UV light source used for prenucleation was SHG cavity, similar to that described in Zimmermann *et al.* (1995). Reliably adjustable up to 10 mW power, 244 nm UV light from a frequency doubled Ar-ion laser was coupled into the optical fibre so that it could be used for patterning in vacuum. Unfocused 193 nm pulses from an excimer laser with a maximum energy of 10 mJ were used for the far-field irradiation on the prenucleated substrate in the presence of DmZn during the film growth stage.

The core of our experimental set-up is an illumination mode near-field optical microscope, placed inside the deposition chamber (Fig. 2). The compact and rigid mechanical head used for steerable positioning and dithering of the fibre tip had an excellent mechanical stability, having two coaxial piezo tubes (PZT) responding synchronously to mechanical perturbations. We employed a piezoelectric-induced slip–stick motion scheme (Renner *et al.*, 1990) for coarse vertical positioning of the sample, thus sacrificing the coarse horizontal positioning ability of our set-up since the shear-force imaging was planned to be constructed within the area reachable by horizontal translation of the corresponding piezo tube sections only.

Crucial in the first step is the use of a NOM fibre tip with a sufficiently small aperture. We used an aluminium-coated tip with a sub-100 nm aperture for the desired resolution of the pattern. However, we also succeeded in deposition with an apertureless tip coated with a 20-nm aluminium layer. The sharpened tip was fabricated on a 10-μm pure silica core multimode UV fibre (Mononobe *et al.*, 1998). Transmission loss at 244 nm for such fibres is $1{\cdot}1\,\mathrm{dB\,m^{-1}}$, which means that the throughput of the tip was as high as 1×10^{-4}, and the power density for 1 mW of light coupled into the fibre was $1\,\mathrm{kW\,cm^{-2}}$. Since the power distribution of the evanescent light varies across the cross-section moving away from the aperture plane, one can obtain prenucleation spots even smaller than the aperture size, as shown later.

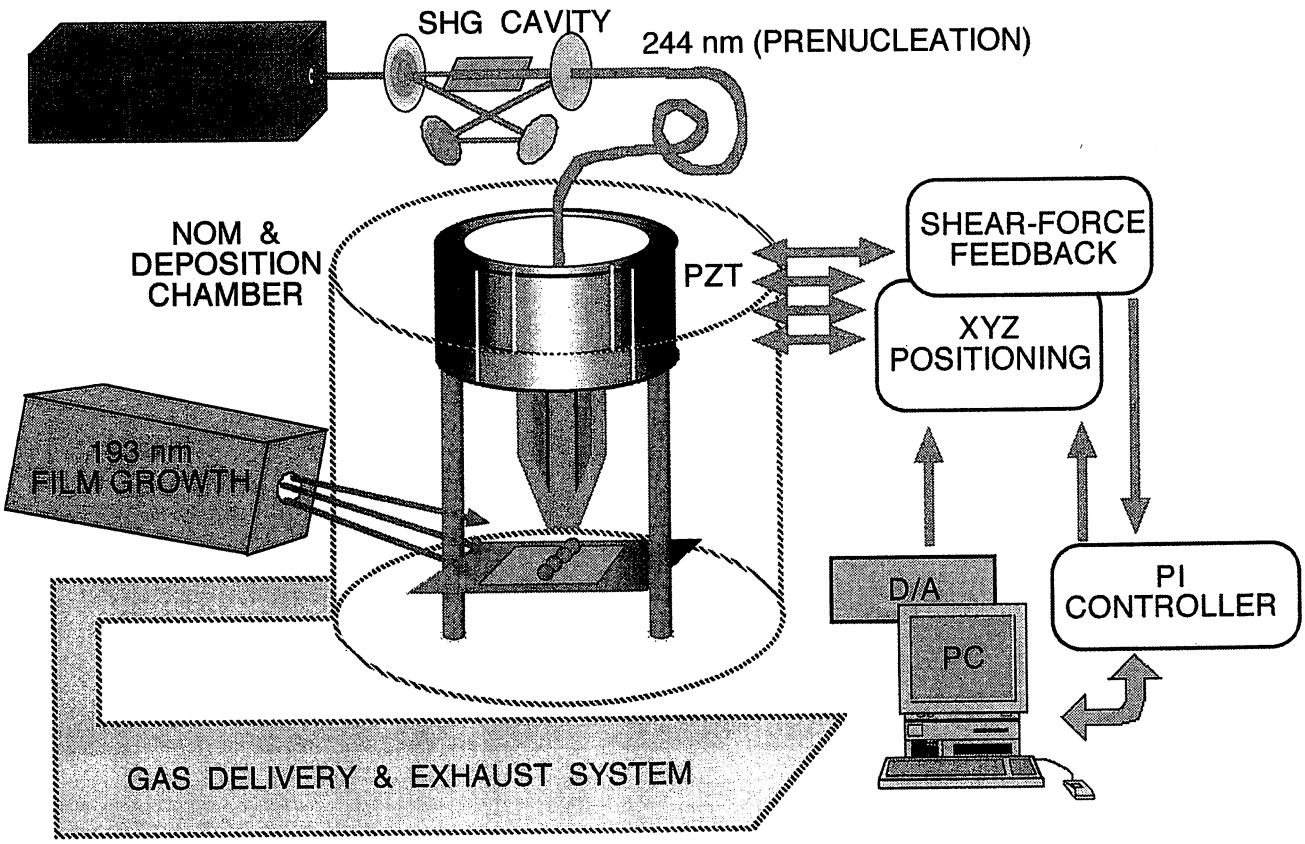

Fig. 2. Schematic diagram of the experimental set-up used in NFO-PCVD.

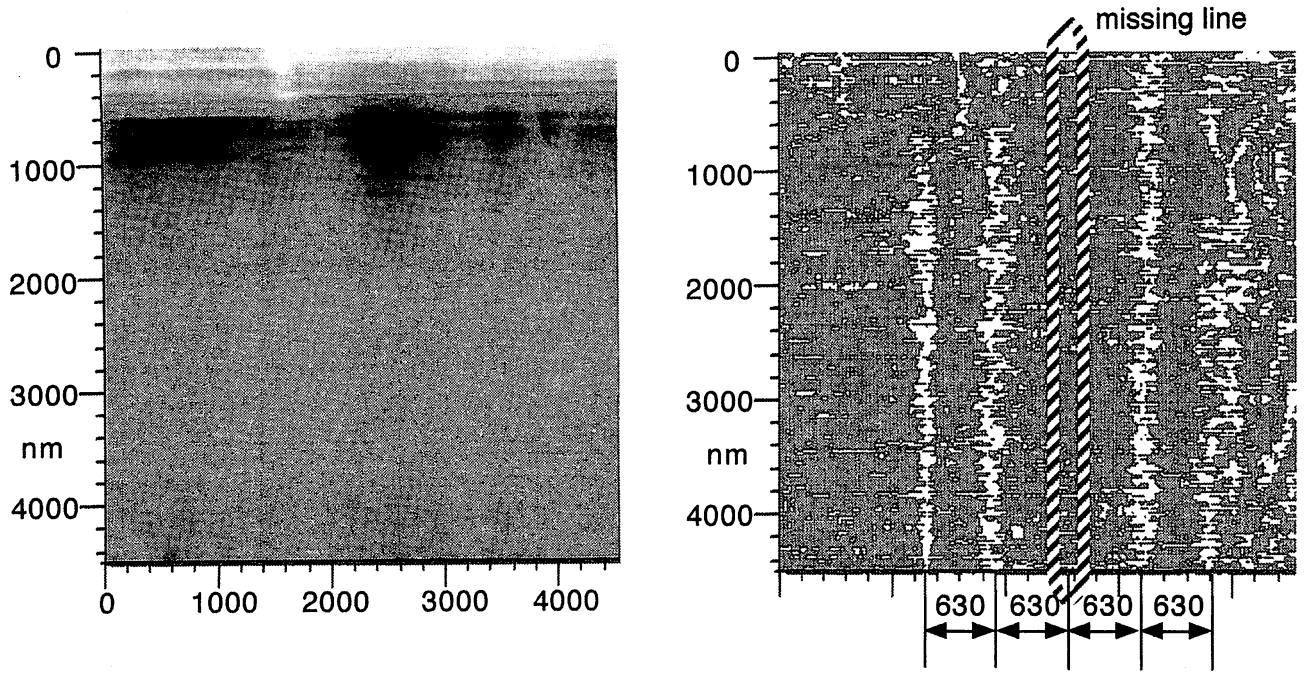

Fig. 3. Demonstration of controllable patterning through prenucleation. Left: unprocessed topography image of developed parallel lines of Zn. Right: after background subtraction and contrast enhancement. The 'missing line' corresponds to the period when near-field UV light was switched off during the prenucleation stage.

A tuning-fork-based probe is attached to a dithering PZT, which drives the probe at its resonant frequency parallel to the sample surface. As the probe approaches the substrate, the oscillation amplitude decreases due to damping from the probe–surface shear-force interaction. Changes in the tip-to-sample separation are thus detected and fed to a PI controller for fine vertical positioning. The vacuum environment brought a certain degree of instrumental complexity, but also an incommensurate gain in microscope performance, as contaminants and water present under ambient conditions

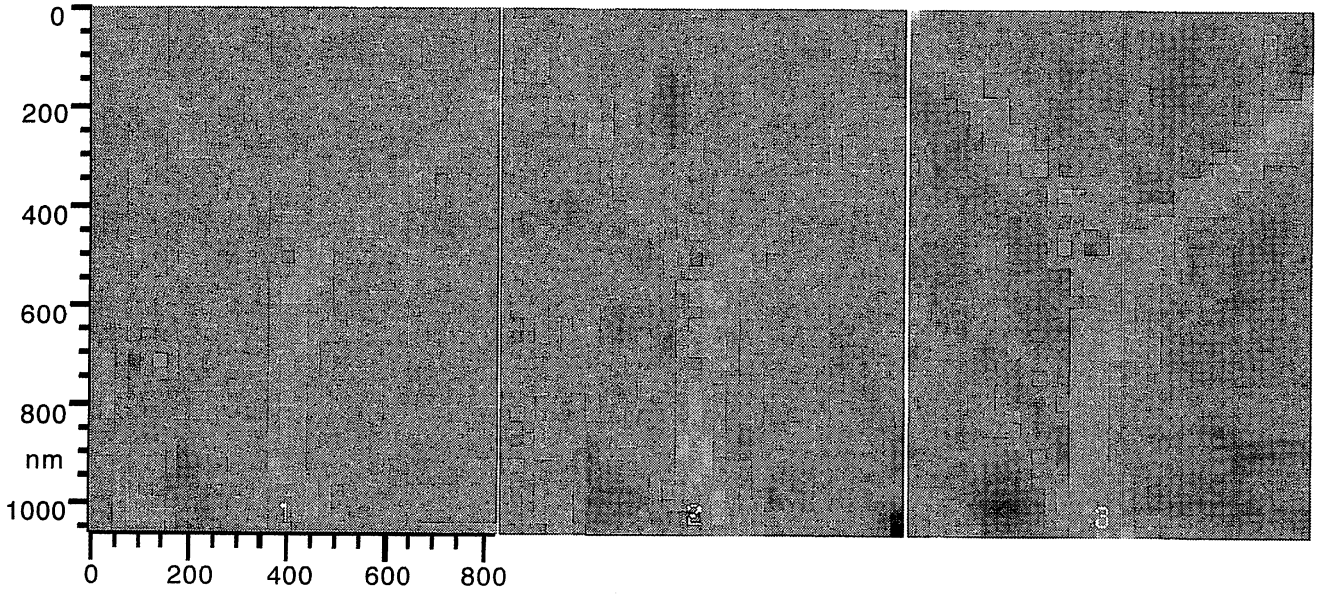

Fig. 4. Build-up of deposit upon irradiation with 193-nm pulses. Increasing contrast of subsequent shear-force images over time validates the growth of the zinc deposit.

represent a serious obstacle for near-field imaging. Moreover, drastic decreasing of the dumping coefficient in a vacuum chamber means a higher Q factor of the scanning system. With an optical fibre glued along one prong of a 33 kHz piezoelectric tuning fork with resulting $Q = 1900$ in air, we observed a 30% increase in the Q factor in 2 mPa vacuum. As a result, we can routinely obtain enhanced (sub-5 nm) resolution with shear-force imaging, and the performance of our microscope is highly competitive with that of noncontact AFM. To our knowledge, to date there has been only one recent publication, describing operation in vacuum NOM. Behme *et al.* (1997) reported blue shift of the shear-force resonances in vacuum, which has been also observed in our experiments, but did not mention enhanced resolution of the instrument.

Results

Figure 3 demonstrates the appropriateness of near-field prenucleation. Parallel lines spaced by 630 nm, as well as a missing line (near-field UV light switched off during the prenucleation stage) can easily be distinguished. As the height of the deposited lines are fewer than 10 atomic layers; the signal-to-noise ratio of the raw data (first image) is low. However, background subtraction and contrast enhancement (second image) reveal excellent correspondence of the resulting lines to computer-generated patterns used for prenucleation. Deviations can be attributed to the inertial PZT drift, tuning fork response (Karrai & Grober, 1995) and characteristics of the PI controller used (SPI 3700 from Seiko Instruments). The width of lines is about 100 nm; the substrate is thoroughly polished sapphire. Prenucleation is accomplished using an apertureless fibre tip coated with a 20-nm aluminium layer. In the second step, lines were developed at a DmZn partial pressure of 0·67 Pa.

Figure 4 illustrates the development of a Y-shaped deposit upon irradiation with 193 nm pulses under 0·13 Pa of precursor pressure. The increasing contrast of shear-force images with time reflects the growth of the Zn film. The average width of patterns for three images are derived to be 50, 80 and 80 nm, with average heights of 0·8, 1 and 3 nm, respectively. The substrate used was Corning glass #7059.

Figure 5 shows the shear force image of the loop-shaped pattern produced. Film growth was performed under 0·13 Pa DmZn pressure by 12 000 pulses of 193 nm pulses with 10 mJ energy. Before the patterning the chemisorbed layers were formed by exposing the substrate to 130 Pa pressure of DmZn for 20 min. A width as small as 20 nm is attained. We verified that the substrate (Corning glass #7059) was flat prior to deposition. After deposition, the height of the pattern was found to vary between 0·5 and 3 nm. The shape of the resulting loop is in accordance with (within the instrumentation accuracy) the computer-generated pattern. Quantitative verification of the amount of the deposit was made by considering the adsorption cross-sections at given UV wavelength, gas pressure during the film growth and UV light energy delivered to the substrate. This estimate is in agreement with the volume of deposit estimated from the topographical images.

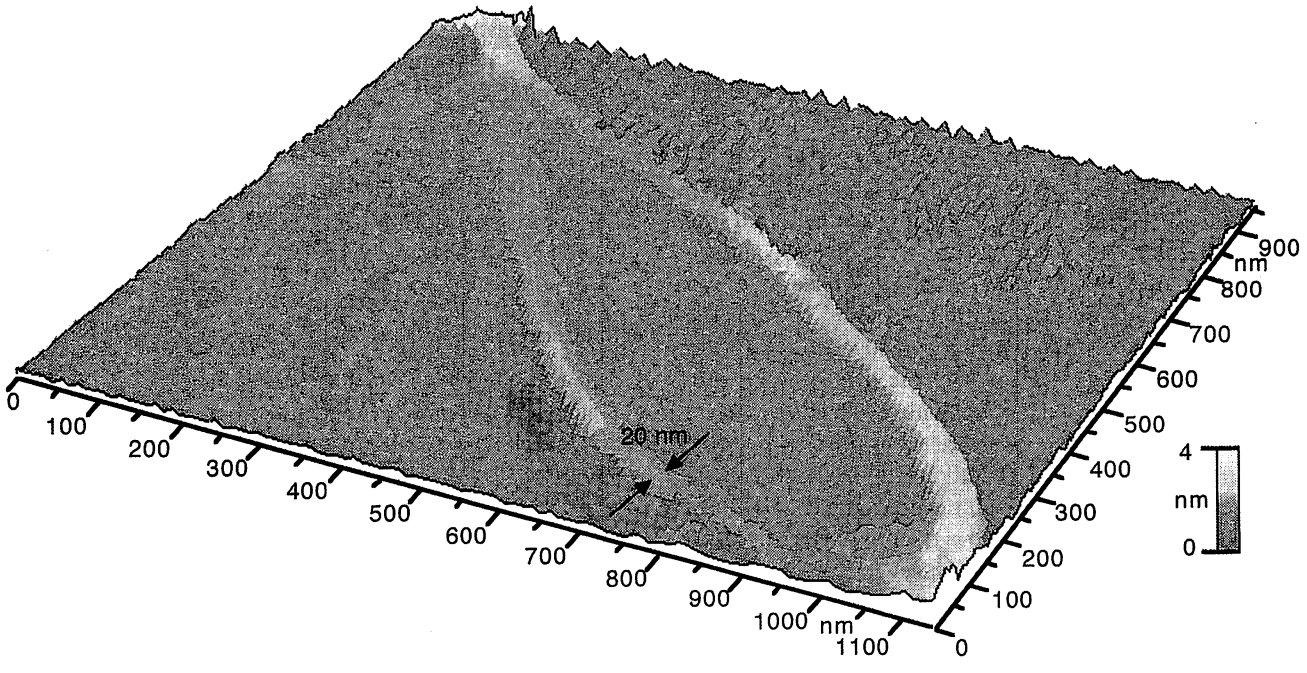

Fig. 5. Shear-force image of a loop-shaped Zn deposit produced on Corning glass. Stripe width as small as 20 nm is indicated.

Discussion

In this paper we present preliminary results on NFO-PCVD; we do not discuss the purity and intrinsic characteristics of the metal deposits obtained. However, they depend strongly on the UV wavelength used, as shown for the far-field case by Shaw *et al.* (1991). Such analysis for near-field deposits will be the subject of a separate study involving Auger electron spectroscopy and conductivity measurements. Moreover, far-field experiments (Ehrlich *et al.*, 1981) have shown that films of one metal can be grown on nucleation centres of a second dissimilar material, which is most probably also true for near-field film growth. It is to be noted that the far-field UV-absorption spectrum of chemisorbed DmZn molecules on a quartz substrate is consistent with the release of methyl groups from the adsorbed layer and the formation of a higher purity metal film on the surface upon extensive irradiation with 193 nm laser (Shaw *et al.*, 1991). (The absorption cross-section of DmZn at this wavelength is $\approx 10^{-17}\,cm^2$, which is one order higher of magnitude than at 244 nm light used for prenucleation.)

Based on the images shown, we can conclude that PCVD processes can be extended to nanoscale fabrication. Indeed, the only parameter which could possibly lead to the big differences is the size of the reacting molecules. Therefore the wealth of experimental data accumulated for decades of CVD/PCVD development gives many options to choose from for NFO-PCVD investigations. Size, which has a direct effect on the deposit width smaller than the aperture of a fibre tip, is also important. In comparison with near-field optical imaging, the function of the light collection detector is performed by sensitive adsorbed molecules decomposing under the induced radiation. Prenucleation spot size, or the number of surface molecules involved in pattern formation, depends strongly on the tip-to-sample separation and hence on the power of the UV light, which selectively ruptures the chemical bonds of the molecules. With the central peak of a power distribution far from the aperture, the resulting prenucleation spot size can be much smaller than the aperture of a fibre tip. This explains the different pattern width on Fig. 5, which in this case was governed by the PI controller which caused variations in the size of the prenucleation spots (assuming a homogeneously clean substrate). Thus, having a fast and accurate response of the near-field probe, a light source with reliable PID process control is the key to realizing an excellent tool for etch-free *in situ* nanofabrication. In addition, the growth of the pattern ensues primarily by adding new vertical layers of material (as shown on Fig. 4) above the prenucleation spots. Although the growth rate may vary depending on the sticking coefficient of PCVD materials, we can conclude that the patterns of a desired morphology can easily be produced with the present method. Moreover, depositions of Al, W, etc. are possible by changing the parent gas or gas mixture. Similar studies in the far-field region (e.g. Tsao & Ehrlich, 1984) provide sufficient data for new near-field experiments.

Conclusion

Analysis of Zn patterns deposited by means of NFO-PCVD allow us to confirm the feasibility of highly reproducible direct writing of nanoscale structures employing this technique. This new method overcomes the diffraction limitation inherent in optical techniques, and etch-deterioration common in other methods of surface modification. In addition, the expected reproducibility of NFO-PCVD in fabricating nanometric stripes and dots at desired positions is much higher than, for example, the conventional self-organized growth technique of semiconductor quantum dots. Moreover, by varying the wavelength of light and parent gases, selective growth of not only metals, but also semiconductors and insulators, can be accomplished. Fabrication of novel electron-wave devices of high scientific importance, such as cavity or interferometer for electron waves, plasmons and polaritons utilizing this approach can be envisioned. While it has some drawbacks in comparison with conventional photo-, e-beam and X-ray lithography, NFO-PCVD's integrity and a reproducibility not attainable by other developing methods will undoubtedly lead to its application in the diverse areas of nanoscale electrochemical studies and *in situ* fabrication of nanoelectronic devices.

Acknowledgements

The authors would like to thank to Dr S. Mononobe from the Kanagawa Academy of Science and Technology for his invaluable help and advice on the art of making fibre probes, and Dr G.H. Lee (ERATO) for his critical comments and useful discussions. We are also grateful to Professors M. Konagai and A. Yamada of the Tokyo Institute of Technology for introducing the general concept of PCVD and for instructions for designing the reaction chamber and gas flow controller.

References

Behme, G., Richter, A., Süptitz, M. & Lienau, Ch. (1997) Vacuum near-field scanning optical microscope for variable cryogenic temperatures. *Rev. Sci. Instrum.* **68**, 3458–3463.

Eden, J.G., ed. (1992) Metal films. *Photochemical Vapor Deposition*, Chapter 4. John Wiley, New York.

Ehrlich, D.J., Osgood, R.M. Jr & Deutsch, T.F. (1981) Spatially delineated growth of metal films via photochemical prenucleation. *Appl. Phys. Lett.* **38**, 946–948.

Karrai, Kh. & Grober, R.D. (1995) Piezoelectric tip–sample distance control for near field optical microscopes. *Appl. Phys. Lett.* **66**, 1842–1844.

Kim, K.N., Lee, J.Y., Lee, K.H., Noh, B.H., Nam, S.W., Park, Y.S.,

Kim, Y.H. *et al.* (1997) Highly manufacturable 1Gb SDRAM. Digest of Technical Papers of 1997 Symposium on VLSI Technology, June 10–13 Kyoto, Japan.

Mononobe, S., Saiki, T., Suzuki, T., Koshihara, S. & Ohtsu, M. (1998) Fabrication of triple tapered probe for near-field optical spectroscopy in UV region based on selective etching of a multistep index fiber. *Opt. Commun.* **146**, 45–48.

Nugent, J. (1998) Thin Films/Nanolithography. Home Page. Department of Materials Science and Engineering, Rensselaer Polytechnic Institute, Troy, NY. Available on the World-Wide Web at the URL: http://www.rpi.edu/~nugenj/nano/index.html; lith.html

Ohtsu, M., ed. (1998) *Near-Field Nano/Atom Optics and Technology.* Springer, Tokyo.

Renner, Ch., Niedermann, Ph., Kent, A.D. & Fisher, Ø. (1990) A vertical piezoelectric inertial slider. *Rev. Sci. Instrum.* **61**, 965–967.

Rogers, J.A., Paul, K.E., Jackman, R.J. & Whitesides, G.M. (1997) Using an elastometric phase mask for sub-100 nm photolithography in the optical near field. *Appl. Phys. Lett.* **70**, 2658–2660.

Shaw, P.S., Sanchez, E., O'Neil, J.A., Wu, Z. & Osgood, R.M. (1991) Surface photochemistry of divalent metal alkyls on SiO_2. *J. Chem. Phys.* **94**, 1643–1652.

Tsao, J.Y. & Ehrlich, D.J. (1984) Patterned photonucleation of chemical vapor deposition of Al by UV-laser photodeposition. *Appl. Phys. Lett.* **45**, 617–619.

Zimmermann, C., Vuletic, V., Hemmerich, A. & Hänsch, T.W. (1995) All solid state laser source for tunable blue and ultraviolet radiation. *Appl. Phys. Lett.* **66**, 2318–2320.

Jpn. J. Appl. Phys. Vol. 38 (1999) pp. L 571–L 573
Part 2, No. 5B, 15 May 1999

Estimation of the Minority Carrier Diffusion Length by Near-Field Photocurrent Measurement of p-n Junction in Silicon using Multiwavelength Excitation

Hiroaki FUKUDA[1,2], Yasushi KADOTA[2] and Motoichi OHTSU[1]

[1]*Interdisciplinary Graduate School of Science and Engineering, Tokyo Institute of Technology, 4259 Nagatsuta, Midori-ku, Yokohama 226-8502, Japan*
[2]*Research and Development Center, RICOH Co. Ltd., 16-1 Sineityou, Tsuzuki-ku, Yokohama 224-0035, Japan*

(Received January 25, 1999; accepted for publication March 26, 1999)

Near-field photocurrent measurement is applied for the characterization of p-n junction of silicon devices. By using a multiwavelength excitation source, the penetration depth into the silicon substrate can be tuned from 10 nm to 685 nm. We have measured the minority carrier diffusion length from near-field photocurrent signals. The minority carrier diffusion lengths of an electron L_n and a hole L_p are estimated as 0.47 and 0.37 μm.

KEYWORDS: near-field optical microscope, near-field photocurrent, p-n junction, minority carrier, diffusion length, silicon device, fiber probe

Miniaturization of semiconductor devices and circuits have made their diagnostics and analyses more difficult. In order to overcome this difficulty, the device structure is tentatively estimated by computer simulation from the macroscopic electric characterization of devices. The diffusion length of minority carriers is an important parameter for successful optimization of the design of bipolar and field-effect transistors and photodetectors. The electron beam induced current method (EBIC)[1,2] and the optical beam induced method (OBIC)[3] have been employed as useful tools for analysis of semiconductor devices and circuits, and have been used to measure the diffusion length of the minority carriers. However, in the EBIC method, the spatial resolution is limited to $\sim$1 μm and sample contamination and damage are serious problems. In the OBIC method, the diffraction limits its resolution.

A near-field optical microscope (NOM)[4,5] has been employed for the spatially resolved observation of subwavelength structure on the surface by breaking the diffraction limit of conventional optical microscope. Furthermore, NOM has been applied for photocurrent measurement of semiconductor and photonic devices such as transistors, laser diodes, photodetectors, and light-emitting devices.[6–9]

In this letter, using multiwavelength excitation sources, near-field photocurrent measurement is applied to evaluate the p-n junction of a commercial silicon (Si) bipolar transistor. Using the UV region excitation wavelength, the small penetration depth decreases the generated region of photoexcited carriers. The minority carrier diffusion length is determined from near-field photocurrent signals.

The experimental setup and sample structure are shown in Fig. 1. After removing the mold package of the commercial bipolar transistor, the passivation layer and local oxidatized Si layer are etched by reactive ion etching. Furthermore, the surface of the p-n junction on the Si substrate is exposed by hydrofluoric acid wet etching. The configuration of the electrode for photocurrent measurement is depicted in Fig. 1.

A novel fiber probe with a pure silica core is prepared for an ultraviolet (UV) near-field light source because the conventional GeO_2-doped fiber has strong optical absorption in the UV region. A 1.3 μm single mode fiber with a pure silica core and fluorine cladding is used to fabricate the fiber probe. The core diameter of this fiber is 10 μm and the clad diameter is 125 μm. After the sharpening using a micropipette puller with CO_2 laser as the heat source, the fiber probe is fabricated by selective chemical etching in buffered hydrofluoric acid solution.[5,10] Because of the pulling process, the core diameter at the tip of the tapered core is reduced to approximately 1 μm. The fiber is etched for 9 min in a buffered hydrogen fluoride (BHF) solution containing NH_4F (40% weight), HF (50% weight) and H_2O with the respective volume ratio of 1.7 : 1 : 1. The temperature of the BHF solution is 25$\pm$0.1°C. This etching process is performed until the core is exposed from the cladding of fluoride doped glass. To fabricate the aperture with subwavelength diameter ($\sim$100 nm), the sharpened fiber probe is coated with Al (300 nm thick). The transmission coefficient is 1×10^{-5}, which is estimated by collecting the far-field throughput with a 0.4 numerical aperture objective lens. Figure 2 shows scanning electron micrographs of the fabricated fiber probe.

As the multiwavelength excitation light source, the output light beam from an Ar^+ laser (wavelength λ = 351, 458, and 515 nm) is coupled to the fiber probe. By using these lights, the penetration depth in the Si substrate can be tuned from 10 nm to 250 nm.[11] The photocurrent induced by the excitation light through the fiber probe is collected at the electrode

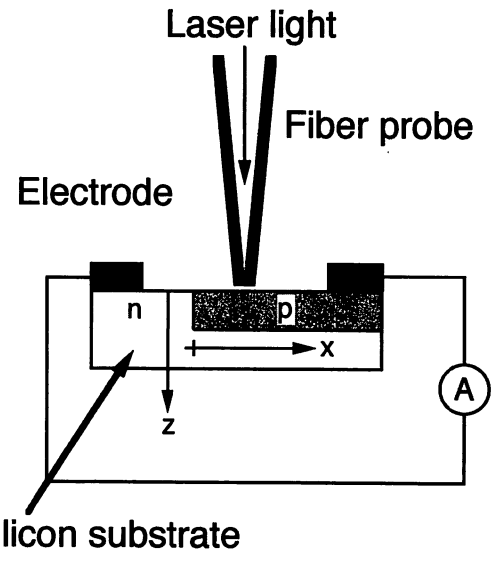

Fig. 1. Cross-sectional structure of p-n junction and the experimental setup.

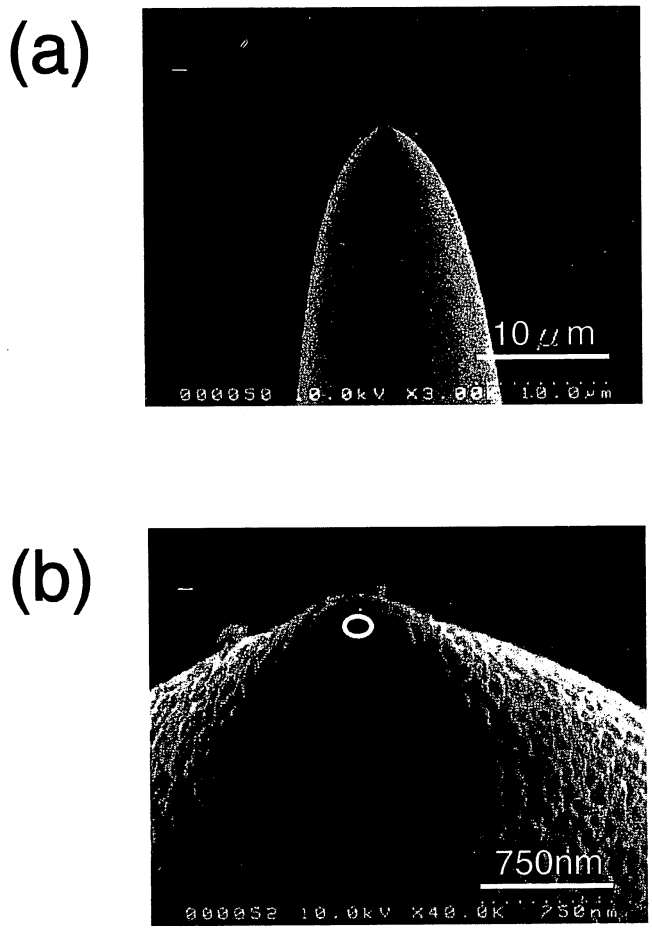

Fig. 2. Scanning electron micrographic images of a fiber probe (a) and the tip of that probe (b). The white circle in (b) represents the aperture.

and amplified with a current injection preamplifier. The signal is synchronously detected with a lock-in amplifier. In order to maintain at near-field excitation, the distance between the fiber probe and the sample is maintained at about 20 nm by applying the shear-force technique. The near-field induced photocurrent across the p-n junction is measured as a function of the position of the fiber probe as the probe is scanned across the surface of the p-n junction.

Figures 3(a)–3(c) show near-field photocurrent images for $\lambda = 351$, 458, and 515 nm, respectively. The cross-sectional profiles of the near-field photocurrent signals obtained along the two arrows in these figures are shown in Fig. 3. The full-width at half maximum (FWHM) of the cross-sectional profile is 0.6, 0.9, and 1.1 μm, respectively. This wavelength dependence of the FWHM is due to that of the penetration depth. At the excitation wavelength of 351 nm, the resolution is determined by the aperture size of the fiber probe and the diffusion length of photogenerated carriers because the penetration depth is shallow. Therefore, longer excitation wavelengths deteriorate the resolution.

The near-field light through the fiber probe has both evanescent modes and propagating ones. The distribution of evanescent modes is determined by the aperture radius of the fiber probe. However, since silicon is a much denser semiconductor material (refractive index of silicon is ~5.44) than the silica fiber probe (refractive index ~1.5) and surrounding air, almost all evanescent modes from the fiber probe are coupled with propagating ones for the entire excitation wavelength

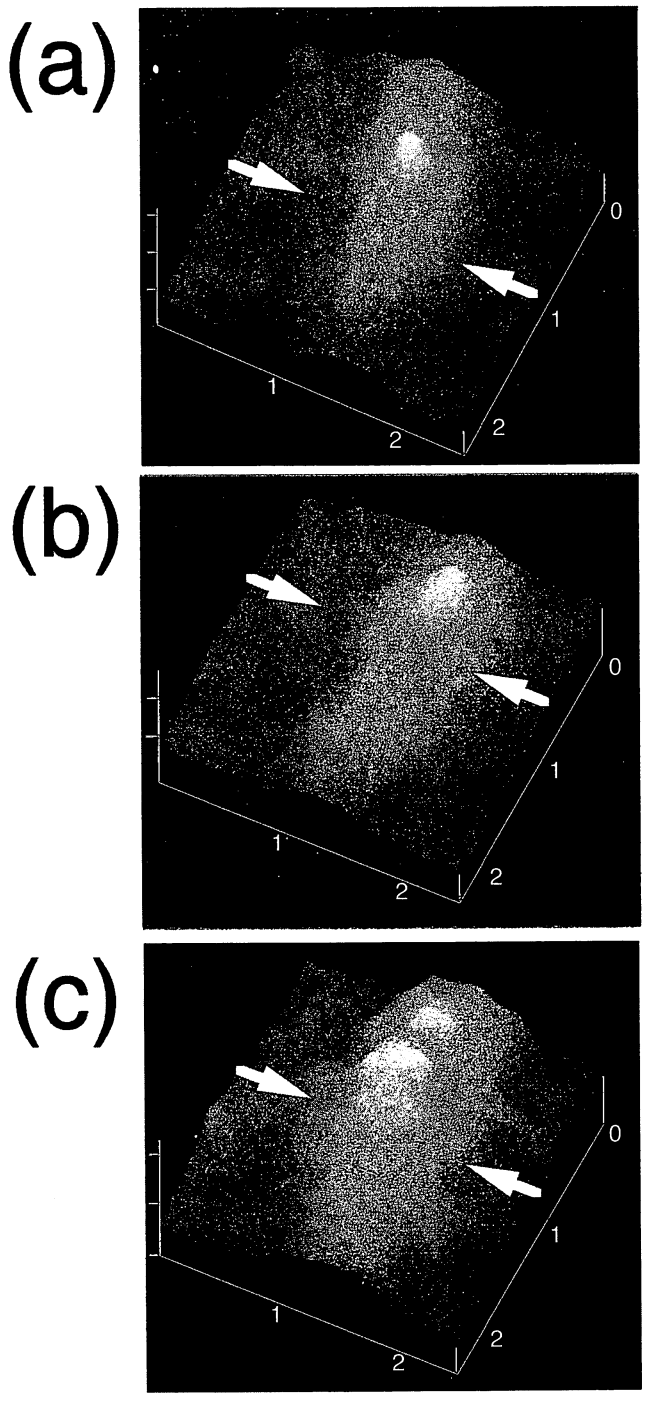

Fig. 3. Perspective views of the near-field photocurrent images at the excitation wavelength (a) $\lambda = 351$ nm, (b) $\lambda = 458$ nm, and (c) $\lambda = 515$ nm. The image size is $2.5 \times 2.5\ \mu m^2$.

($\lambda = 351$–515 nm). The propagation modes are governed by the bulk absorption characteristics of a substrate material. Therefore, the resolution is limited not only by the size of the aperture radius but also the penetration depth of the semiconductor material.

After the near-field light trough from the fiber probe generates the electron-hole pair in the Si substrate, the corresponding minority carrier diffuses away over an average diffusion length before the recombination. The near-field photocurrent signal is proportional to the number of carriers to reach the p-n junction. The spatial response profile of p-n junction is described by the asymmetric form

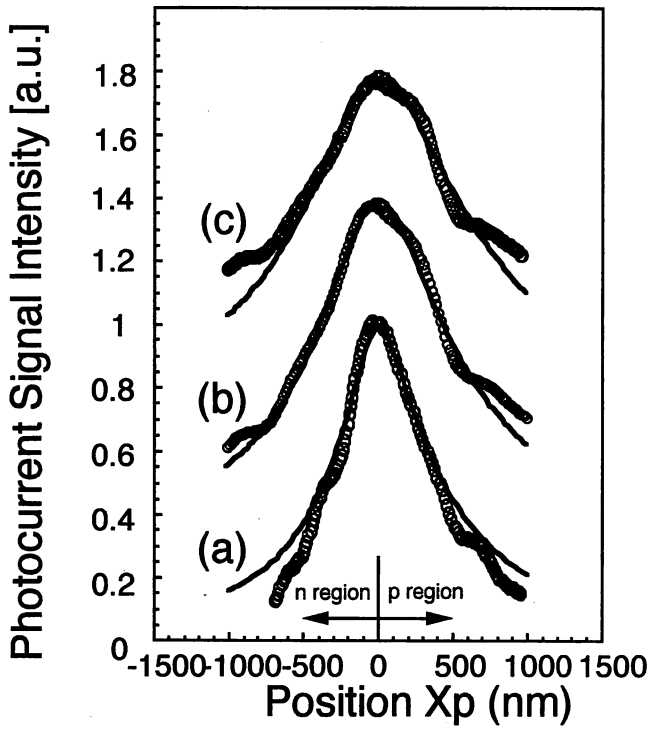

Fig. 4. Cross-sectional profiles of the near-field photocurrent signals at the excitation wavelength (a) $\lambda = 351$ nm, (b) 458 nm, and 515 nm obtained along the two arrows in Figs. 3(a)–3(c), respectively (circles). The solid curve denotes the calculated results from eq. (4).

$$p(x, z) = \left.\begin{array}{ll} C\exp(x/L_p) & \text{(n region)} \\ C\exp(-x/L_n) & \text{(p region)} \end{array}\right\}, \quad (1)$$

where x represents the horizontal position (see Fig. 1). C is a normalized constant, L_p and L_n are the minority carrier diffusion lengths of the hole and the electron, respectively.

The spatial distribution of propagating light into the Si substrate is expressed as

$$D(x, z) = [\exp(-l/L_{pd})]/l^2, \quad (2)$$

where $l^2 = (x - \mathrm{Xp})^2 + z^2$, and Xp is the position of the fiber probe. The penetration depth L_{pd} for the excitation wavelengths of 351, 458, and 515 nm is 10, 277, and 685 nm, respectively. The intensity of the photocurrent signal is proportional to

$$I(X_p) = \int_0^d \int_{-\infty}^{\infty} D(x, z)p(x, z)\,dx\,dz. \quad (3)$$

where $d = 0.6\,\mu$m is the depth of the p-n junction in the substrate.

By fitting this integral calculation to the experimental values of Fig. 4, the diffusion lengths of minority carriers, L_n and L_p are estimated as 0.47 ± 0.03 and $0.37 \pm 0.02\,\mu$m, respectively. This difference in the diffusion length between electron and hole can be observed through the slower rise of photocurrent signal in the n region than in the p region.

In this letter, we have reported the near-field photocurrent measurements with multiwavelength excitation sources applied to the investigation of a p-n junction on a silicon substrate. By using 351, 458, and 515 nm, from blue to ultraviolet wavelength light sources, the penetration depth into the silicon substrate is varied from 10 nm to 685 nm. The increase of penetration depth results in the decrease of the resolving power. The minority carrier diffusion lengths for electron L_n and hole L_p are estimated to be 0.47 ± 0.03 and $0.37 \pm 0.02\,\mu$m, respectively, from the near-field photocurrent signals.

The authors wish to express their thanks to Dr. Toshiharu Saiki and Dr. Shuji Mononobe of the Kanagawa Academy of Science and Technology for their valuable discussions and comments.

1) H. J. Leamy: J. Appl. Phys. **53** (1982) R51.
2) W. H. Hackett, Jr.: J. Appl. Phys. **43** (1972) 1649.
3) H. Komoda and K. Shimizu: Jpn. J. Appl. Phys. **33** (1994) 3393.
4) M. Ohtsu: J. Lightwave Technol. **13** (1995) 1200.
5) M. Ohtsu: *Near-field Nano/Atom Optics and Technology* (Springer, Tokyo, 1998).
6) S. K. Buratto, J. W. P. Hsu, E. Betzig, J. K. Trautman, R. B. Bylsma, C. C. Bahr and M. J. Cardillo: Appl. Phys. Lett. **65** (1994) 2654.
7) M. S. Ünlü, B. B. Goldberg, W. D. Hrzog, D. Sun and E. Towe: Appl. Phys. Lett. **67** (1995) 1862.
8) K. Karrai, G. Kolb, G. Abstreiter and A. Schmeller: Ultramicroscopy **61** (1995) 299.
9) T. Saiki, N. Saito, J. Kusano and M. Ohtsu: Appl. Phys. Lett. **69** (1996) 644.
10) T. Pangaribuan, K. Yamada, S. Jiang, H. Ohsawa and M. Ohtsu: Jpn. J. Appl. Phys. **31** (1992) L1302.
11) E. D. Palik: *Handbook of Optical Constants of Solids* (Academic Press, Orlando, 1985).

Imaging of current paths and defects in Al and TiSi interconnects on very-large-scale integrated-circuit chips using near-field optical-probe stimulation and resulting resistance change

K. Nikawa
NEC Device Analysis Technology Laboratories, Nakahara-ku, Kawasaki-shi, Kanagawa-ken 211-8666, Japan

T. Saiki
Kanagawa Academy of Science and Technology, Takatsu-ku, Kawasaki-shi, Kanagawa-ken 213-0012, Japan

S. Inoue
T.D.I. (Technological Development of Information Processing), Co., Ltd., Nakahara-ku, Kawasaki-shi, Kanwagawa-ken 211-8666, Japan

M. Ohtsu[a)]
Interdisciplinary Graduate School of Science and Engineering, Tokyo Institute of Technology, Midori-ku, Yokohama-shi, Kanagawa-ken 226-0026, Japan

(Received 2 November 1998; accepted for publication 8 December 1998)

The optical-beam-induced resistance-change-detection (OBIRCH) method has been improved by using a near-field optical probe as the heat source instead of a laser beam. The near-field OBIRCH method has two advantages over the conventional one: (1) its spatial resolution is higher (50 vs 400 nm) and (2) the optical-probe-induced resistance change caused by heating can be observed using a metallized probe without interference from a photocurrent created by electron–hole-pair generation. In the conventional-OBIRCH method, the laser beam creates not only a resistance change, but also a photocurrent that can mask the resistance change signals. © *1999 American Institute of Physics.* [S0003-6951(99)04305-3]

Identifying voids and Si nodules in the Al stripes of very-large-scale integrated-circuit (VLSI) chips is a key part of failure analysis and process monitoring in the semiconductor industry. Several approaches to void identification have been proposed, including thermal-wave-modulated optical reflectance imaging,[1] backscattered electron imaging using field-emission scanning-electron microscopy,[2] and ultra-high-voltage transmission electron microscopy.[3] The optical-beam-induced resistance-change-detection (OBIRCH) method (proposed by Nikawa and Tozaki[4]) has been shown to be, in some respects, more useful in detecting voids than the other methods. It can identify Si precipitates in metal lines,[5] voids under vias,[6] high-resistance areas at the bottoms of vias, and high-resistance sections in TiSi lines.[7] Moreover, it can localize current paths on VLSI chips.[8]

The OBIRCH method simultaneously uses two main processes: laser-beam heating and resistance-change detection. The resistance change caused by laser-beam heating depends on the temperature increase. When a laser beam is irradiated, the generated heat is transmitted freely across areas that are free of defects: however, heat transmission is impeded at defects, such as voids and Si precipitates. This creates a nonuniform temperature increase, which results in imaging defects. Since it was first introduced, it has been modified and improved in various ways. The sensitivity of its resistance-change-detection capability has been improved by reducing the sample temperature during measurement,[9] by increasing the laser power,[6,7] and by improving the technique used for detecting the resistance change.[7,10,11] Changing the wavelength of the laser used for heating from 633 to 1300 nm (Refs. 8, 10, and 12) makes it possible to heat Al stripes on Si chips from the backside and eliminate the optical-beam-induced current (OBIC), which thereby allows only the OBIRCH signal to be observed without any interference.

We have modified the OBIRCH method so that it uses a near-field optical probe as a heat source instead of a laser beam. Tests of this near-field OBIRCH (NF-OBIRCH) method showed that it is superior to the conventional OBIRCH method.

A schematic diagram of the experimental setup we used for testing NF-OBIRCH is shown in Fig. 1(a). We introduced an Ar^+ laser (with a mixed wavelength of 488 and 514.5 nm) into a near-field optical probe. A schematic explanation of the cross-sectional profile of a typical aperture near-field optical probe[13,14] is shown in Fig. 1(b). A schematic explanation of the cross-sectional profile of a typical metallized probe we used is shown in Fig. 1(c). The probe was scanned in the area of interest, using a shear-force feedback technique, which is typically used for near-field optical microscopy. The voltage changes during scanning were introduced into the external input terminal of a typical scanning probe microscope system so as to produce an image of the resistance change.

The voltage change is simply expressed as

$$\Delta V = I \Delta R, \tag{1}$$

where ΔV is the voltage change when heated, I is the current applied by the constant-current source, and ΔR is the resistance change when heated. The current paths can be observed because ΔV is proportional to I, and various defects

[a)]Also with Kanagawa Academy of Science and Technology, Takatsu-ku, Kawasaki, Kanagawa 213-0012, Japan.

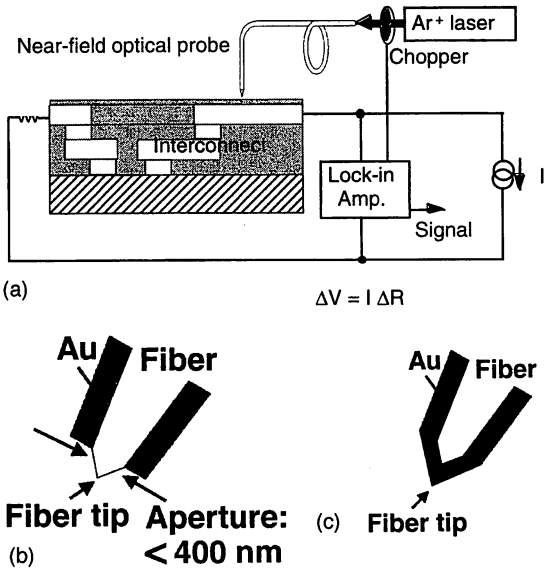

FIG. 1. (a) Experimental setup, fiber tip of an aperture probe (b) and (c) a metallized probe.sectional profile].

can be observed because ΔV is proportional to ΔR. The samples were 0.3-μm-wide Al lines and 0.2-μm-wide TiSi lines fabricated using VLSI development processes.

The results of Al-line-test-structure observation showed that the spatial resolution of the OBIRCH image using a 633 nm laser was about 400 nm. Figures 2(a), 2(b), and 2(c) show the observed results of another test structure of Al interconnects containing voids. Figure 2(a) shows the NF-OBIRCH image when the probe had an apex aperture of 400 nm: note that the bright and dark contrasts are reversed com-

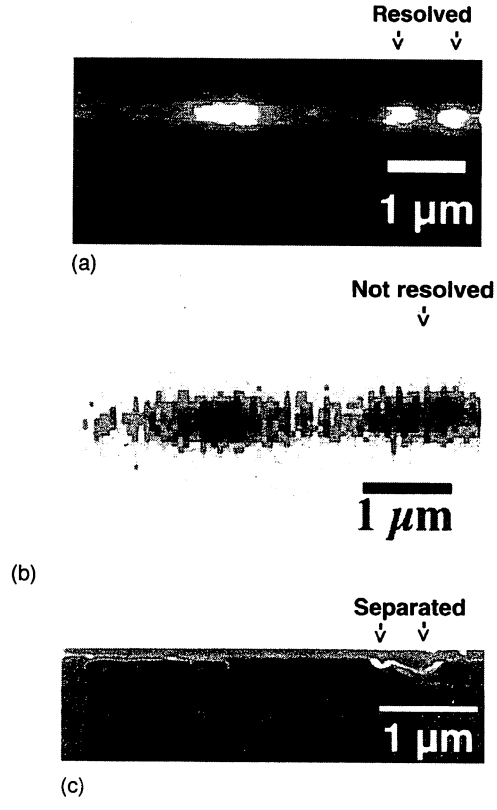

FIG. 2. (a) NF-OBIRCH image, (b) conventional-OBIRCH image (633 nm), and (c) cross-sectional SIM image of a 0.3-μm-wide Al line.

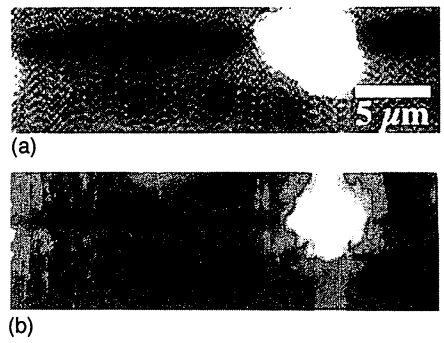

FIG. 3. Conventional-OBIRCH images of a 0.2-μm-wide TiSi interconnect including defective area: (a) IR-OBIRCH image (1300 nm laser) and (b) VL-OBIRCH image (633 nm laser).

parison with the conventional-OBIRCH images because the resistance increase corresponds to an increase in the signal (voltage) in the NF-OBIRCH method, instead of a decrease in the signal (current) in the conventional method. Figure 2(b) shows the conventional-OBIRCH image using a 633 nm laser. The existence of voids identified using the NF and conventional OBIRCH methods was confirmed by using cross-sectional scanning ion microscopy (X-SIM). As shown in the X-SIM image [Fig. 2(c)], there were two voids: a longer one on the left and a separated one on the right. The one on the left is clearly visible in both the NF- and conventional-OBIRCH images. The separation of the one on the right is resolved only in the NF-OBIRCH image. These results show that the spatial resolution for void identification is better with the NF-OBIRCH method than with the conventional one. Though the heating mechanism of the NF-OBIRCH is not clearly understood yet, three possible mechanisms can be considered: (1) heating by light irradiation, (2) direct heat transfer by contact, and (3) heat transfer by gas molecules. We infer that the heating by light irradiation through the aperture is the main mechanisms from the measurement of the dependence of NF-OBIRCH signal intensity on the probe–sample distance, where the decay length is almost equal to the aperture diameter.

The TiSi lines, which had a higher resistance than the normal one had, were first observed using conventional-OBIRCH methods: infrared OBIRCH (IR-OBIRCH: 1300 nm) and VL-OBIRCH. As shown in Fig. 3, the spatial resolution in the VL-OBIRCH image [Fig. 3(b)] is better than in the IR-OBIRCH image [Fig. 3(a)]. Both images show dark and bright contrasts. The dark ones correspond to an OBIRCH effect (resistance change caused by thermal effect) in a normal area of the TiSi line. The origin of the bright ones may also be the OBIRCH effect (negative temperature coefficient of resistance causes bright contrast) or an OBIC effect (photocurrent caused by electron–hole-pair generation), but this has yet to be confirmed.[7]

The NF-OBIRCH method can cause only the OBIRCH effect when a metallized probe is used. Figures 4(a) and 4(b) show images observed using a metallized probe. The bright contrast in Fig. 4(a) corresponds to the OBIRCH effect. No contrast (0.00 V) is shown in Fig. 4(a) in the area where bright contrasts are shown in Figs. 3(a) and 3(b), suggesting that those bright contrast were caused by an OBIC effect. Figure 4(b) shows the highest spatial resolution observed in

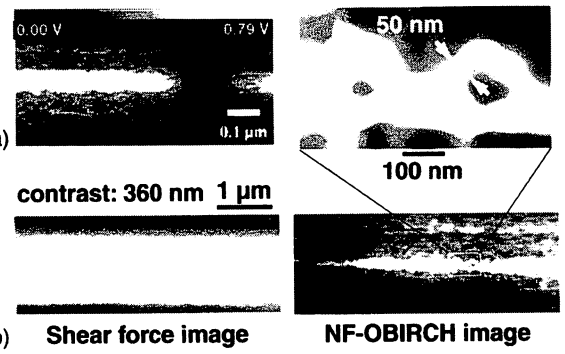

FIG. 4. (a) NF-OBIRCH image of 0.2-μm-wide TiSi interconnect including a defective area obtained using a metallized probe, and (b) NF-OBIRCH image showing 50 nm spatial resolution obtained using a metallized probe.

our NF-OBIRCH observations of TiSi interconnects. A spatial resolution of 50 nm was obtained in the NF-OBIRCH image in an area where no contrast was observed in a shear-force image. In this measurement, the NF-OBIRCH signal appears only when the probe approaches the sample within a range where the shear force can be sensed. This signal behavior demonstrates that the direct heat transfer by contact is the main mechanism of heating.

To confirm our hypothesis about the physical cause of the contrasts, we used cross-sectional transmission electron microscopy (X-TEM), and dark-field-scanning TEM (D-STEM) to observe a 0.2-μm-wide TiSi line that had the defective area. Figure 5(a) shows the X-TEM image. The right side of Fig. 5(a) clearly shows a normal structure whose upper half is TiSi and lower half is polycrystalline silicon. The left side is the defective area, and it is not clearly resolved in this X-TEM image. We thus used D-STEM to get a clear image [Fig. 5(b)]. The white areas correspond to the heavier atoms, and the gray areas correspond to the lighter ones. To identify the elements, we analyzed the points numbered from 1 to 7 in Figs. 5(a) and 5(b) by using energy-dispersive x-ray analysis (EDX). We found that both Ti and Si atoms are present in the white area, while only Si atoms are present in the gray areas. As shown in Fig. 5(b), the gray areas, shown as the Ti-depleted part, exist across the TiSi line. This must be the cause of higher resistance in the line.

The exact mechanism of the OBIC effect in the Ti-depleted parts still needs to be clarified. It is not clear why a bright contrast corresponding to the OBIC effect is observed when a 1300 nm laser is used [Fig. 3(a)]. A 1300 nm laser is usually used in the conventional-OBIRCH method so that an OBIC effect is not produced[8,10,12] because the energy of a 1300 nm laser (0.95 eV) is less than the Si band-gap energy (1.12 eV). The key to solving this puzzle is the Ti-detection limit of the EDX, which is about 1%. It is possible that at less than 1%, the Ti may generate impurity energy levels that produce enough carriers detectable by our system. The impurity energy level of Ti is 0.21 eV under the conduction band and 0.91 eV above the valence band. A 1300 nm laser can, therefore, generate electron–hole pairs via the Ti energy levels.

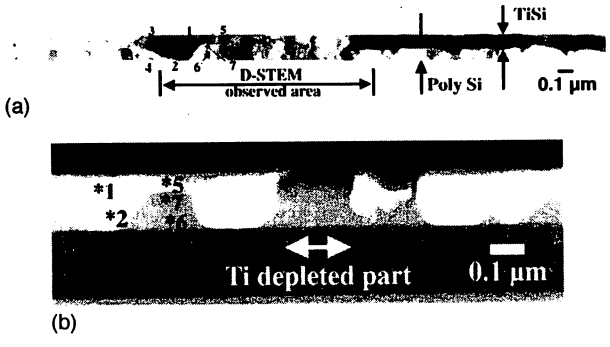

FIG. 5. Cross-sectional (a) TEM and (b) D-STEM images of a 0.2-μm-wide TiSi line including a defective area: the sample thickness is about 0.2 μm.

In summary, we have improved the optical-beam-induced resistance-change-detection method by using a near-field optical probe as the heat source instead of a laser beam. The resulting NF-OBIRCH method has two advantages over the conventional-OBIRCH method. (1) Its spatial resolution is higher: 50 vs 400 nm. (2) The OBIRCH caused by heating can be observed using a metallized probe without interference from an optical-beam-induced current. In the conventional-OBIRCH method, the laser beam creates not only an OBIRCH effect, but also an OBIC effect that can mask the OBIRCH effect.

The authors wish to thank H. Iida, E. Inuzuka, H. Terada, Y. Nakajima, and H. Suzuki of Hamamatsu Photonics for their very valuable technical support of the IR-OBIRCH method we used. The authors wish to thank N. Suyama and H. Shinjo of MST (Foundation for Promotion of Material Science and Technology of Japan) for their TEM analysis; they also wish to thank T. Fukase, H. Tsuda, Y. Yamada, and Y. Kakuhara of NEC for supplying the samples and for their technical suggestions.

[1] W. L. Smith, C. Welles, A. Bivas, F. G. Yost, and J. E. Campbell, *1990 International Reliability Physics Symposium* (Institute of Electrical and Electronic Engineers, New York, 1990), p. 200.
[2] P. R. Besser, M. C. Madden, and P. A. Flinn, J. Appl. Phys. **72**, 3792 (1992).
[3] A. Tanikawa, H. Okabayashi, H. Mori, and H. Fujita, *1990 International Reliability Physics Symposium* (Institute of Electrical and Electronic Engineers, New York, 1990), p. 209.
[4] K. Nikawa and S. Tozaki, *1993 International Symposium on Testing and Failure Analysis* (ASM International, Materials Park, OH, 1993), p. 303.
[5] K. Nikawa, C. Matsumoto, and S. Inoue, Jpn. J. Appl. Phys., Part 1 **34**, 2260 (1995).
[6] K. Nikawa and S. Inoue, *European Symposium on Reliability of Electron Devices, Failure Physics and Analysis* (ADERA, Bordeaux, France, 1995), p. 307.
[7] K. Nikawa and S. Inoue, IEICE Trans. Inf. Syst. **E81-D**, 743 (1998).
[8] K. Nikawa and S. Inoue, *1996 International Reliability Physics Symposium* (Institute of Electrical and Electronic Engineers, New York, 1996), p. 346.
[9] N. Kawamura, T. Sakai, and M. Shimaya, IEICE Trans. Electron. **E77-C**, 579 (1994).
[10] E. I. Cole, Jr., P. Tangyunyong, and D. L. Barton, *1998 International Reliability Physics Symposium* (Institute of Electrical and Electronic Engineers, New York, 1998), p. 129.
[11] Q. Wen and D. R. Clarke, Appl. Phys. Lett. **72**, 1920 (1998): This paper describes a modification of the OBIRCH method, but does not refer to papers related to the OBIRCH method.
[12] K. Nikawa and S. Inoue, *1996 International Symposium on Testing and Failure Analysis* (ASM International, Materials Park, OH, 1996), p. 387.
[13] T. Saiki, S. Mononobe, M. Ohtsu, N. Saito, and J. Kusano, Appl. Phys. Lett. **68**, 2612 (1996).
[14] M. Kourogi and T. Saiki, in *Near-Field Nano/Atom Optics and Technology*, edited by M. Ohtsu (Springer, Tokyo, 1998), Chap. 4, p. 71.

OPTICAL REVIEW Vol. 5, No. 6 (1998) 369-373

Fabrication of a Near-Field Optical Fiber Probe with a Nanometric Metallized Protrusion

Takuya MATSUMOTO,[1] Tsutomu ICHIMURA,[1] Takashi YATSUI,[1] Motonobu KOUROGI,[1] Toshiharu SAIKI[2] and Motoichi OHTSU[1,2]

[1]*Interdisciplinary Graduate School of Science and Engineering, Tokyo Institute of Technology, 4259, Nagatsuta, Midori-ku, Yokohama, 226-8502 Japan,* [2]*Kanagawa Academy of Science and Technology, KSP East 408, 3-2-1, Sakado, Takatsu-ku, Kawasaki, 213-0012 Japan*

(Received June 26, 1998; Accepted August 21, 1998)

We have developed a novel probe with a nanometric metallized protrusion extending through a subwavelength aperture to increase optical near-field excitation and collection efficiencies. The apex diameter of the fabricated metallized protrusion was 35 nm. The Intensity distribution of the optical near-field at the apex of the probe was measured by scanning another probe across the apex, and it was observed that strong optical near-field was generated at the apex of the metallized protrusion. The width of the intensity distribution was 150 nm including instrumental resolution. Probes with spherical and ellipsoidal metallized protrusion were also fabricated, by which enhancement of the optical near-field is expected due to localized plasmon excitation.

Key words: near field optical microscope, fiber probe, metallized protrusion, subwavelength aperture, localized plasmon

1. Introduction

A near-field optical microscope (NOM) is a scanning probe optical microscope realizing a spatial resolution beyond the diffraction limit of light.[1,2] One of its applications is a spectroscopy of quantum structures, such as semiconductor quantum dots and microdisks.[3-5] In this application, a serious problem is low light excitation and collection efficiencies due to low light transmission efficiency of the probe. In the widely used apertured probe (i.e., a metal-coated tapered fiber having a nanometric aperture at its apex), light transmitted through the aperture suffers huge loss. For example, the throughput of the probe (the ratio between the power of the light emitted from the aperture and the power of light coupled into the probe) is less than 10^{-5} when the aperture diameter is 100 nm. For a quantum structured sample with low quantum efficiency, the spatial resolution is sacrificed because the aperture diameter must be increased to ensure sufficiently high detection efficiency.

High efficiency probes, such as a double tapered probe,[6] an asymmetrically tapered probe,[7] a metallic needle[8,9] and a coaxial probe[10,11] have been proposed to solve the problem mentioned above. In the double tapered and the asymmetrically tapered probes, the throughputs have been increased by 10 times as compared with the conventional apertured probe. In the metallic needle, the high efficiency is due to illumination of the sample by an external light and collection of the signal light by a far-field external collection optics. However, it is not straightforward to detect selectively high spatial Fourier frequency components of light generated at the apex of the probe which is buried in the large background light. Further, in the photoluminescence spectroscopy of semiconductor quantum structures, the spatial resolution is limited by the carrier diffusion area when the photoluminescence is detected by the far-field external collection optics.[12] In the coaxial probe, the high throughput is expected by exciting the transverse electromagnetic (TEM) mode in a metallic core surrounded by an outer metallic film. However, to our knowledge, a probe with an apex diameter of less than 100 nm has not yet been developed.

To solve the problem of low efficiency, we propose here the probe shown in Fig. 1. It consists of a subwavelength aperture with a metallized protrusion extending through it. For illumination mode NOM* or illumination-collection mode NOM, the metallized protrusion works as a nanometric light source. When the metallized protrusion is illuminated by light, strong optical near-field is generated at its apex. The spatial profile of the field is governed by the apex diameter of the protrusion.[13] The aperture suppresses generation of the background light. For collection mode NOM or illumination-collection mode NOM, the metallic protrusion works as a high efficiency scatterer for the optical near-field on the sample surface. High spatial frequency components are selectively scattered by the metallic protrusion, and are coupled to the fiber waveguide mode, while low frequency components are cut off by the aperture. Sections 2 and 3 describe the fabrication process and the characteristics of this probe, respectively.

E-mail: takuya@ae.titech.ac.jp

*The following three operation modes have been widely used in the NOM: (1) *illumination mode*: a sample is illuminated by light from the probe, and the light from the sample is collected by an external collection optics; (2) *collection mode*: the sample is illuminated by external light (under total internal reflection condition), and the light is collected by the probe; (3) *illumination-collection mode*: the sample is illuminated by light from the probe, and the light is collected by the same probe.

2. Probe Fabrication

The fabrication process consists of the following five steps as is schematically explained in Fig. 2.

(a) Etching an Optical Fiber

An optical fiber (single mode fiber with a 27 mol% GeO_2 doped SiO_2 core of 2 μm diameter and a 125 μm diameter pure SiO_2 cladding) is sharpened by two step chemical etching method,[14] where cladding diameters can be controlled by controlling the etching time. This control capability is essential for controlling the aperture diameter of the probe as will be described later.

(b) Coating Resin

The fiber is dipped in resin solution (photoresist, Tokyo Okakogyo TSMR-V50 with 60 cp viscosity), and drawn up with a constant speed of 1 cm/s. This process coats the foot of the core with resin. The fiber is then baked at 120°C for 20 min to harden the resin.

(c) Etching the Apex of the Core

The fiber is dipped in a solution containing HF and H_2O (volume ratio=1:100) for around 3 min to etch the uncoated core apex and form a depression. The etching solution does not peel the resin off the fiber because the etching speed of the cladding is much slower than that of the core.

(d) Forming the Aperture

The fiber is coated with metal by a vacuum evaporation to form the aperture. During evaporation, the fiber is tilted at an angle of θ=20° which prevents the apex of the core from being coated. In our experiment, gold is coated because it is hardly oxidized and thus chemically stable. The aperture diameter corresponds to the diameter of the depression (D in Fig. 2). This diameter D can be controlled by changing the cladding diameter as long as the viscosity of the resin is constant. (The depression diameter becomes larger with decrease in the cladding diameter). In our experiment, values of D from 100 nm to 700 nm were obtained by changing the cladding diameter from 20 μm to 11 μm.

(e) Coating the Apex of the Core with Metal

The apex of the sharpened core is coated with metal. Figure 3 shows scanning electron microscope (SEM) images of the probe fabricated by this method. The aperture diameter D is 400 nm. The apex diameter of the protrusion prior to metal coating is less than 5 nm (refer to Fig. 3(c)). Since the thickness of the gold film surrounding the apex of the protrusion is around 15 nm, the apex diameter of the metallized protrusion is 35 nm or even smaller. Further reduction of the apex diameter of this protrusion is possible by optimizing the condition of metal coating.

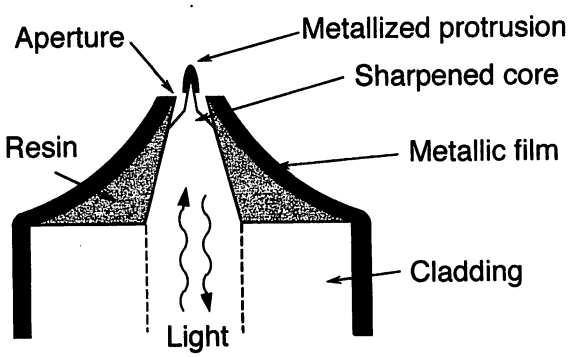

Fig. 1. Schematic of a probe with a metallized protrusion.

3. Characterization of Near-Field Optical Properties

The throughput of the fabricated probe was first checked as follows: A He-Ne laser light (λ=633 nm) was coupled into the fiber, and the light power emitted from the aperture was measured using a power meter with broad detection area (1 cm^2) placed as close as 5 mm from the aperture to integrate almost all the output light. For the aperture of D=400 nm, throughput, i.e., the ratio between output and input powers was as high as 5%, which is the expected value for this aperture diameter.[6]

Next, the spatial distribution of the optical near-field intensity at the apex of the fabricated probe (probe A) was measured using the apparatus shown in Fig. 4. Light from a laser diode (wavelength=690 nm) was coupled into the fiber (probe A), and the optical near-field generated at the

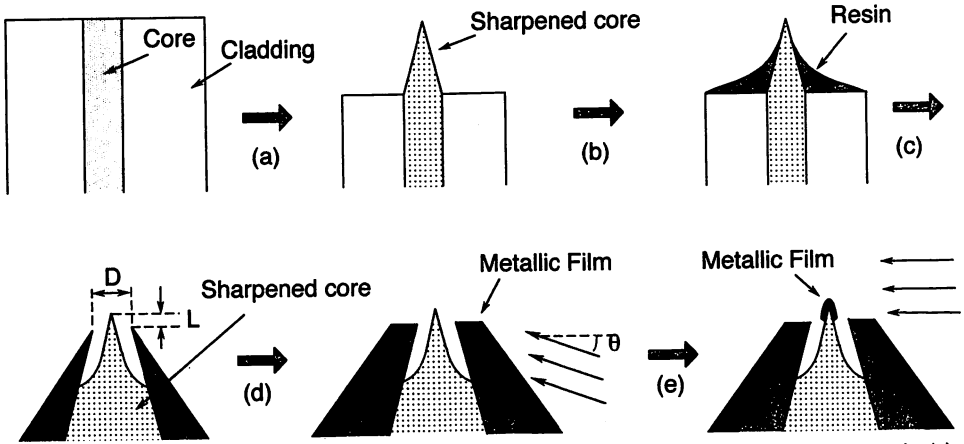

Fig. 2. Fabrication process of the probe with the metallized protrusion: (a) etching an optical fiber, (b) coating resin (c) etching the apex of the core, (d) forming an aperture, (e) coating apex of the protruded core with metal.

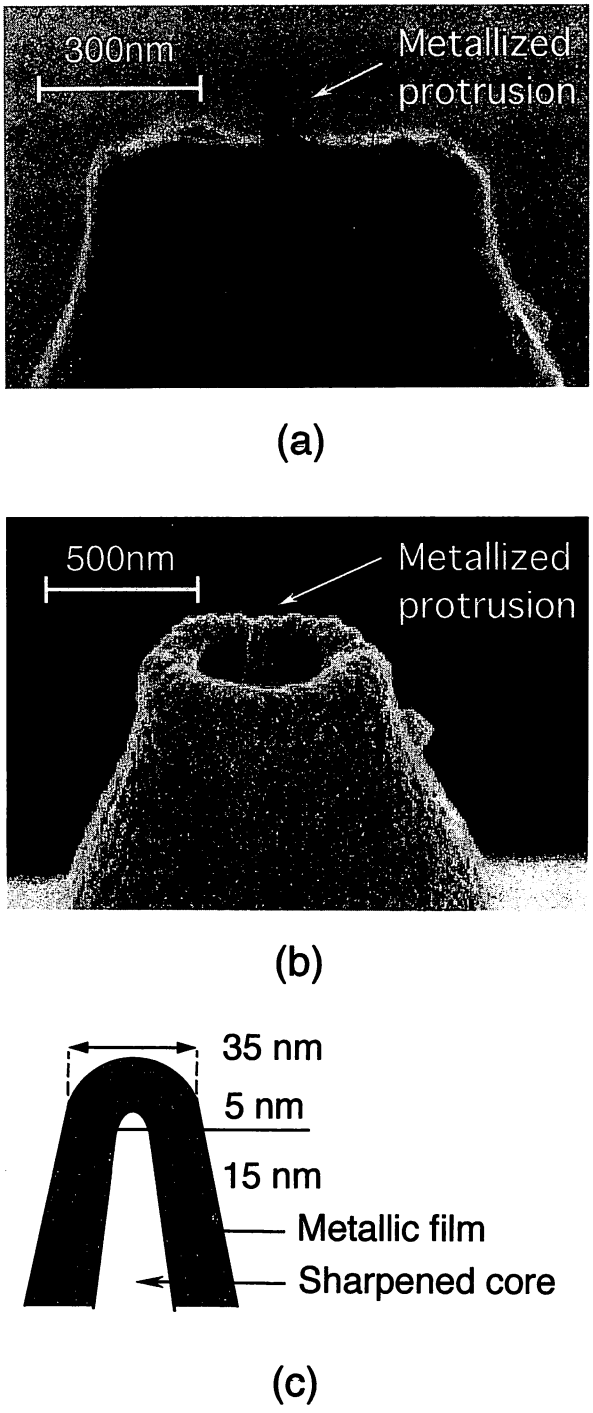

Fig. 3. SEM images of the fabricated probe: (a) side view and (b) bird's-eye view. (c) Schematic explanation of the apex of the metallized protrusion.

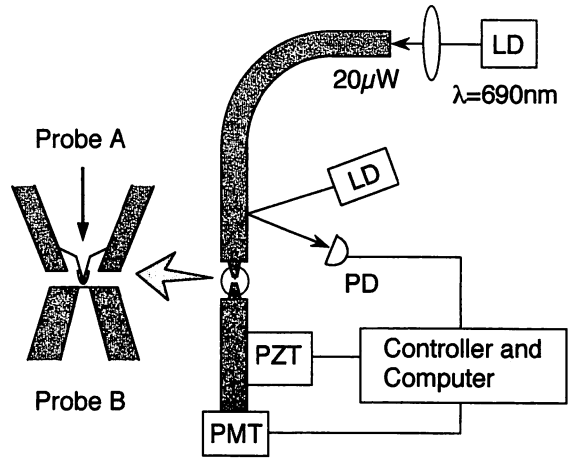

Fig. 4. Experimental setup for measuring the optical near-field at the apex of the probe. Probe A is the fabricated probe under measurement. Probe B is an apertured probe for detecting the optical near-field at the apex of probe A.

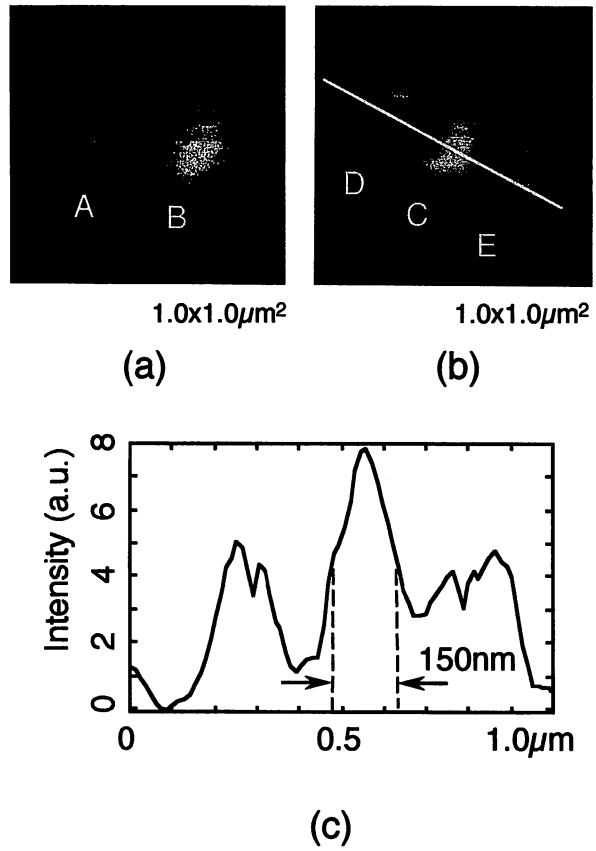

Fig. 5. Intensity distribution of the optical near-field generated at the apex of the probe: (a) with the bare protrusion and (b) the metallized protrusion. (c) Cross sectional intensity distribution along the line in (b).

apex of this probe was scattered and detected by a conventional apertured probe fabricated by ion beam etching[7] (aperture diameter=100 nm: probe B). Two-dimensional spatial distribution of the optical near-field at the apex of the probe was measured by scanning the probe B, where the shear force technique[15,16] was used to maintain a constant separation between the two probes. Distributions for the probe with the metallized protrusion and a probe with a bare protrusion were measured and compared. The probe with the bare protrusion was fabricated by excluding step (e) of the fabrication process.

Figure 5(a) shows the measured distribution for the bare protrusion probe. In this image, we can see two bright

spots A and B separated 400 nm, which corresponds to the aperture diameter D. These two spots are caused by the EH_{11} mode, which propagates to the end of the tapered waveguide most efficiently.[7] The difference between their intensity is due to the fact that the two probes were slightly tilted toward each other.

Figure 5(b) shows the measured distribution obtained for the metallized protrusion probe. This figure has a central bright spot C with two darker spots D and E on its sides. The spots D and E are due to the EH_{11} mode as in Fig. 5(a). The central bright spot C indicates that the optical near-field is enhanced by the metallized protrusion. Figure 5(c) shows the cross sectional intensity distribution along the line in Fig. 5(b). The full-width at half maximum of the central part of this curve is 150 nm. Note that this width includes the instrumental resolution, i.e., the contribution of the aperture diameter of probe B.

Finally, we measured the scattering characteristics of the fabricated probe for the collection mode NOM. Light from a laser diode (wavelength=633 nm) was introduced into a prism at an angle of 60° satisfying the total internal reflection condition to generate a planar optical near-field (i.e., evanescent wave), and the probe was approached the prism surface. The light scattered by the probe was coupled to the fiber waveguide mode, and detected by a photomultiplier. The probe-prism separation was measured by the shear force technique. Figures 6(a) and (b) show the dependencies of the scattered light intensity on the probe-prism separation for the probes with metallized and bare protrusions, respectively. Open circles show the values measured when the polarization of the incident light is parallel to the plane of incidence (p-polarization). Closed circles are for the s-polarization. Figure 6(a) shows that in the case of the metallized protrusion, the picked up light intensity for the p-polarization is 10 times larger than that for the s-polarization. The reason is that the charges in the metallic film move along the protrusion axis and concentrate at the protrusion apex when the protrusion is illuminated by the p-polarized light, whereas when the protrusion is illuminated by the s-polarized light they move perpendicularly to the axis and do not concentrate at the protrusion apex.[17]

Broken exponential curves in Fig. 6 were fitted to the measured values. The measured values vary super-

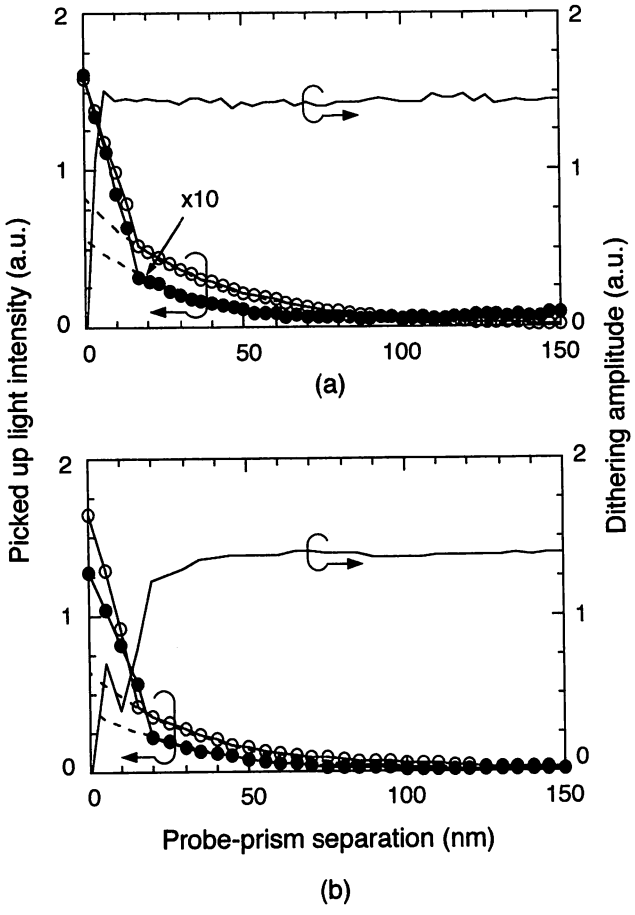

Fig. 6. Dependence of the intensity of scattered light from the apex of the probe on probe-prism separation: (a) with the metallized protrusion (b) with the bare protrusion. Open circles are with p-polarization, and closed circles are with s-polarization. Solid curves are the dithering amplitudes of the optical fiber for detecting the shear force. Broken curves are exponential curves fitted to the measured values. In (a), the measured values for s-polarization are magnified 10 times.

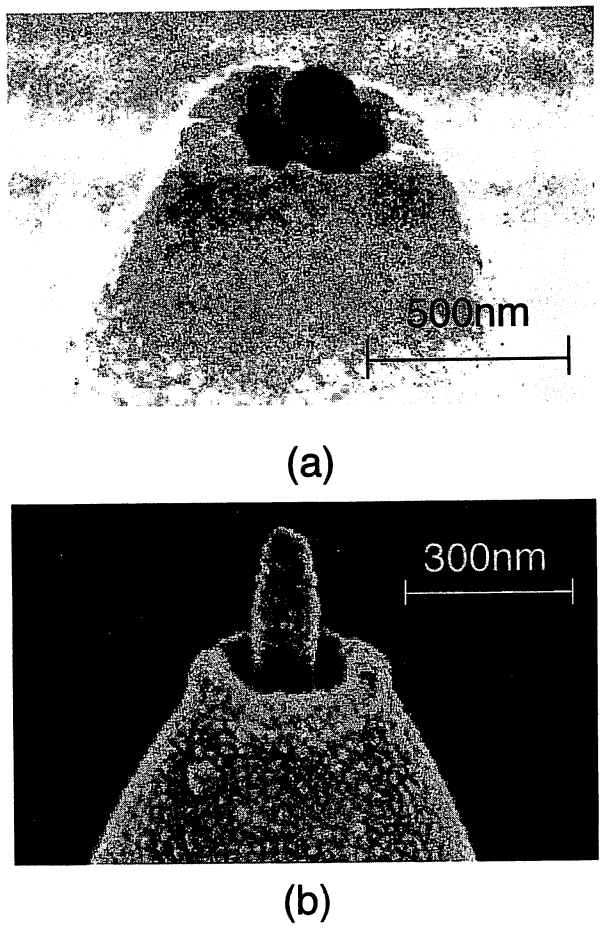

Fig. 7. SEM images of the probes with (a) spherical and (b) ellipsoidal metallized protrusion for exciting localized plasmon. Ratio of the major and minor axes of the ellipsoid in (b) is 2.5:1.

exponentially when the probe-prism separation is less than 20 nm. The reason for this is being studied.

4. Toward the Probe with Field Enhancing Capability

Figures 7(a) and (b) show SEM images of the probe with spherical and ellipsoidal metallized protrusions, respectively. These probes are fabricated by increasing the thickness of the metallic film at the apex of the probe in step (e) of the fabrication process. The size of the metallized protrusion can be controlled by changing the thickness of the film. Further, the shape of the metallized protrusion is controlled by changing the length of the protruded core (L in Fig. 2(c)). As L becomes larger, the spheroid becomes elongated. We were able to fabricate ellipsoidal protrusions with major and minor axis ratios ranging from 1:1 (sphere) to 2.5:1. Spherical protrusions with diameters from 50 to 200 nm were also fabricated.

It is theoretically possible to enhance the optical near-field intensity by 10^2 to 10^5 times if the localized plasmon is excited on these spheres and ellipsoids.[18] To excite the plasmon on the ellipsoid efficiently, the light should be polarized along the major axis of the ellipsoid (along the core axis). Although in the illumination mode NOM the component of the electric field along the axis of the conventional probe is small, the probe employing an asymmetrically tapered waveguide can realize a large electric field polarized along the probe axis because it can excite the HE_{11} mode.[7] Note that the intensity distribution pattern of this mode has a single spot at the center, which is advantageous to remove the side spots in Fig. 5(b).

Finally, it should be noted that fixing other materials such as semiconductors and polymers on the apex of the probe is also possible, by which fabrication of a new class of functional super tips[19] is possible.

5. Conclusions

We developed a probe with a nanometric metallized protrusion to increase optical near-field excitation and collection efficiency. The apex diameter of this protrusion was 35 nm, aperture diameter was 400 nm, and throughput of the probe was as high as 5%. The intensity distribution of the optical near-field at the apex of the probe was measured by scanning another probe across the apex, and strong optical near-field generated at the apex of the metallized protrusion was observed. The width of the intensity distribution was 150 nm including instrumental resolution. We also measured the dependence of the picked up light intensity on the probe-prism separation in the collection mode configuration, and found that the picked up light intensity given by the p-polarized incident light was greater than that by the s-polarized incident light. Probes with spherical and ellipsoidal metallized protrusion were also fabricated, by which enhancement of the optical near-field is expected due to localized plasmon.

Acknowledgments

We would like to thank Dr. Y. Zhao of the University of Sydney, and Dr. J.D. White and Dr. R. Uma Maheswari of the Kanagawa Academy of Science and Technology for critically reading and commenting on the manuscript.

References

1) W. Pohl and D. Courjon eds.: *Near-field optics* (Kluwer Acad. Publ., Dordrecht, 1993).
2) M. Ohtsu: IEEE J. Lightwave Technol. **13** (1995) 1200.
3) H.F. Hess, E. Betzig, T.D. Harris, L.N. Pfeiffer and K.W. West: Science **264** (1994) 1740.
4) T. Saiki, K. Nishi and M. Ohtsu: Jpn. J. Appl. Phys. **37** (1998) 401.
5) J.B. Stark, U. Mohideen and R.E. Slucher: in Quantum Electronics and Laser Science Conference OSA Technical Digest Series (Optical society of America, Washington DC, 1995) Vol. 16, paper QTuJ1
6) T. Saiki, S. Mononobe and M. Ohtsu: Appl. Phys. Lett. **68** (1996) 2612.
7) T. Yatsui, M. Kourogi and M. Ohtsu: Appl. Phys. Lett. **71** (1997) 1756.
8) F. Zenhausern, Y. Martin and H.K. Wickramasinghe: Science **269** (1995) 1083.
9) Y. Inoue and S. Kawata: Opt. Lett. **19** (1994) 159.
10) U.Ch. Fischer and M. Zapletal: Ultramicroscopy **42-44** (1992) 393.
11) M. Fee, Steven Chu and T.W. Hänsch: Opt. Commun. **69** (1989) 219.
12) F. Flack, N. Samarth, V. Nikitin, P.A. Crowell, J. Shi, J. Levy and D.D. Awschlom: Phys. Rev. B **54** (1996) R17 312.
13) T. Saiki, M. Ohtsu, K. Jang and W. Jhe: Opt. Lett. **21** (1996) 674.
14) T. Pangaribuan, S. Jiang and M. Ohtsu: Scanning **16** (1994) 362.
15) R. Toledo-Crow, P.C. Yang, Y. Chen and M. Vaez-Iravani: Appl. Phys. Lett. **60** (1992) 2957.
16) E. Betzig, P.L. Finn and J.S. Weiner: Appl. Phys. Lett. **60** (1992) 2484.
17) L. Novotny, R.X. Bian and X.S. Xie: Phys. Rev. Lett. **79** (1997) 645.
18) H. Raether: *Surface Plasmons* (Springer-Verlag, Berlin, 1988) Chap. 2, p. 37
19) W. Tan, Z. Shi and Raoul Kopelman: Anal. Chem. **64** (1992) 2985.

Increasing throughput of a near-field optical fiber probe over 1000 times by the use of a triple-tapered structure

T. Yatsui[a)]
Interdisciplinary Graduate School of Science and Engineering, Tokyo Institute of Technology, Midori-ku, Yokohama, Kanagawa 226-8502, Japan

M. Kourogi and M. Ohtsu
Interdisciplinary Graduate School of Science and Engineering, Tokyo Institute of Technology, Midori-ku, Yokohama, Kanagawa 226-8502, Japan and Kanagawa Academy of Science and Technology, Takatsu-ku, 213-0012, Japan

(Received 15 May 1998; accepted for publication 10 August 1998)

We fabricated a new probe with extremely high throughput introducing a triple-tapered structure to reduce the loss in a tapered core, to focus the light, and to excite effectively the HE_{11} mode. A focused ion beam and selective chemical etching were used for fabrication. Over a 1000-fold increase in the throughput of the triple-tapered probe with the aperture diameter $D<100$ nm was realized in comparison with the conventional single-tapered probe. Furthermore, due to the third taper with a small cone angle, the localized optical near field on the triple-tapered apertured probe with $D=60$ nm has been confirmed. © *1998 American Institute of Physics.*
[S0003-6951(98)03041-1]

For studying optical properties of various surfaces in a nanometer scale, a near-field optical microscope has made a remarkable contribution to subwavelength-resolution imaging and spectroscopy by scanning a metallic fiber probe with a subwavelength aperture.[1,2] A conventional single-tapered probe with a protruding apex [Fig. 1(a)] has been fabricated by selective chemical etching,[3] followed by selective resin coating (SRC).[4] However, the most serious problem of using the metallic fiber probe is its low throughput of a metallic tapered core, which rapidly decreases by decreasing the aperture diameter (D).[5,6] It is less than 1×10^{-5} with $D<100$ nm in the conventional single-tapered probe.[7] Furthermore, since the input power is limited by thermal damage of the probe tip,[8] signal-to-noise ratio is extremely low.

Recently, the highly efficient excitation of the HE_{11} mode[9] which is hardly excited in the conventional probe, is realized in an edged probe [Fig. 1(b)].[10] Since the edged probe has a sharp edge at the foot of the probe, a part of the radiated power can be scattered and converted to the HE_{11} mode.[11] Consequently, a tenfold increase in optical near-field intensity on the probe was achieved. However, since the attenuation of light through the metallic tapered core is extremely large,[9] the probe with an aperture at the flat end of the fiber [Fig. 1(c)] is expected to be optimum with regard to the lowest propagation loss.[12] However, since the D is much smaller than the beam spot size, the coupling efficiency from the guided mode in the optical fiber to the mode in the aperture might be extremely low. Recently, Saiki *et al.* have reported that the sharpened probe with large cone angle functions as focusing,[13] implies that the throughput might be increased if the aperture is fabricated at the focal point of the sharpened probe. Based on this consideration, we propose "a steeple-on-mesa" probe as shown in Fig. 1(d), where D_m is the mesa diameter. The mesa works as focusing, where the focal point is at the center of the plateau of the mesa. The propagation loss can be decreased by a short tip length. Furthermore, highly resolved images can be obtained by the steeple with a small cone angle on the mesa which protrudes from the metallic aperture. Figure 1(c) shows the shape of the fabricated apertured probe with a triple-tapered core, which will be described later.

In this letter, we determined the tip parameters which are required to focus light at the plateau of the mesa. By preparing single-tapered apertured probes with different D, the spatial distribution of the optical near-field intensity on the ap-

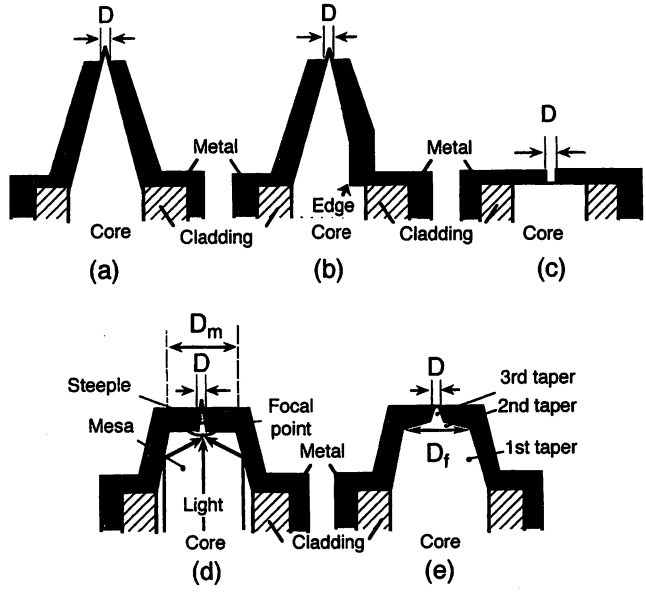

FIG. 1. A schematic of a metal-coated fiber probe (D: aperture diameter): (a) conventional single-tapered probe; (b) edged probe; (c) probe with a small aperture at the flat end of the fiber; (d) proposed steeple-on-mesa probe (D_m: mesa diameter); (e) fabricated triple-tapered apertured probe (D_f: foot diameter of the second taper).

[a)]Electronic mail: yatsui@ae.titech.ac.jp

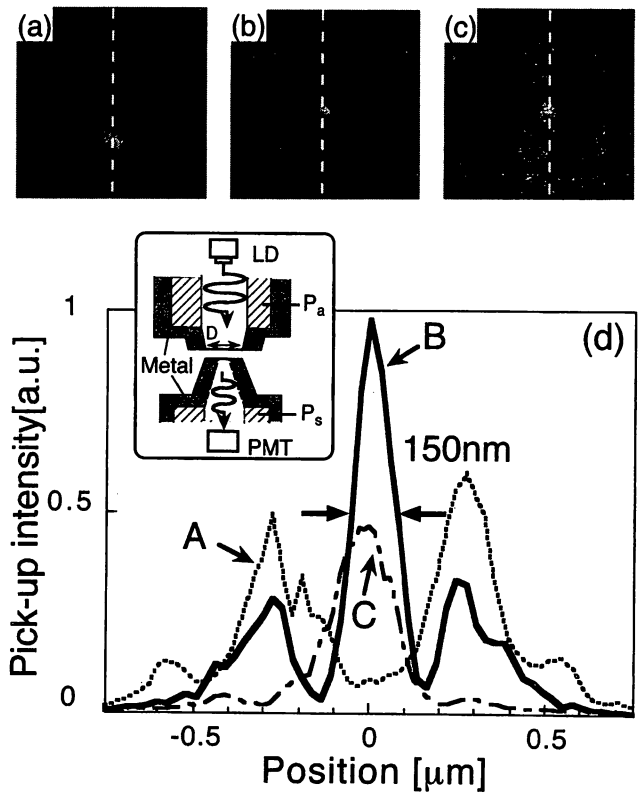

FIG. 2. Spatial distribution of the optical near-field intensity on the conventional single-taped apertured probe. (a), (b), (c) are for the single-tapered apertured probe with $D=1.4$ μm, 1 μm, and 550 nm, respectively. The image size is 1.5×1.5 μm^2. Curves A (dashed line), B (solid line), and C (dashed-and-dot line) in (d) are the cross-sectional profile along the white dashed line in (a), (b), and (c), respectively. Inset: probe-to-probe method. P_a: apertured probe, P_s: scanning probe.

erture was observed. On the basis of these results, we optimized the shape of the probe tip. To confirm the high resolution capability of the probe, the spatial distribution of the optical near-field intensity on the aperture was observed.

The optical near-field generated on the apertured probe was observed by scanning another apertured probe with $D=100$ nm over the aperture to scatter and detect the optical near field. The experimental setup, i.e., probe-to-probe method, is shown in the inset of Fig. 2(d),[10] where the separation between the probes was maintained within several nanometers with shear-force technique. Linearly polarized light from a laser diode (830 nm) was coupled into the single-tapered apertured probe, which was fabricated by following three steps:

(i) The GeO_2 doped core of the fiber was tapered by selective chemical etching, where the core diameter and cone angle were 3 μm and 20°, respectively.[3]
(ii) The core was coated with 500-nm-thick gold film.
(iii) The top of the core was removed to form an aperture with the focused ion beam (FIB).

Figures 2(a), 2(b), and 2(c) show the observed spatial distribution of the optical near-field intensity on the aperture. Figure 2(d) shows the cross-sectional distribution along the white dashed line in Figs. 2(a), 2(b), and 2(c). One can find in Fig. 2(d) that the decrease of full width at half maximum (FWHM) of the spatial distribution is not monotonous by decreasing D and that the optical near-field intensity at the

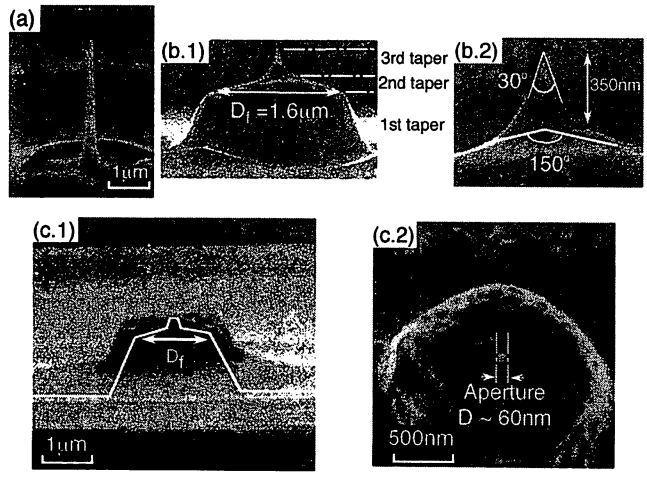

FIG. 3. SEM images of a triple-tapered probe: (a) results of step (ii); (b1), (b2) the triple-tapered probe formed by step (iii) and a magnified image of the third taper, respectively; (c1), (c2) side and top views of the probe by steps (iv) and (v), respectively.

center of the core takes the maximum at $D=1$ μm. It suggests that there is a focal point in the metallic tapered core. Note that FWHM of the central part of curve B was as small as 150 nm ($<\lambda/5$). These results indicate that the throughput is increased if the probe has an aperture at the focal point.

We fabricated the steeple-on-mesa probe by the following five steps. However, due to several technical restrictions the fabricated probe had a triple-tapered core with an aperture [Fig. 1(e)]:

(i) The GeO_2 doped core of the fiber was tapered by selective chemical etching, where the cone angle was 20°.[3]
(ii) The FIB was shined over the sharpened core to reduce the core diameter.
(iii) The first and second tapers of the core were formed by chemical etching. The foot diameter of second taper D_f is 1.6 μm. The length and apex diameter of the third tapers are 350 and 25 nm, respectively. The cone angles of the second and third tapers are 30° and 150°, respectively.
(iv) The core was coated with 300-nm-thick gold film.
(v) The top of the third taper was removed by FIB to form an aperture.

Figures 3(c1) and (c2) show scanning electron microscopic (SEM) images of a fabricated triple-tapered apertured probe with $D=60$ nm. The length of the third taper (350 nm) is much shorter than the length of the single-tapered probe (5 μm), and a decrease of the propagation loss is expected.

To estimate the optimum shape of the fabricated triple-tapered probe, we compared the throughput of two triple-tapered probes with $D_f=1.2$ and 1.6 μm, the single-tapered probe with a cone angle of 20°, and the edged probe.[10] Since the quantity D cannot be determined exactly by the angled evaporation,[7] the top of the core was removed by the FIB to form a clear aperture, where the quantity D is determined by SEM images. For estimating the throughput, light from the laser diode (830 nm) was coupled into the fiber, and the output light power ejected from the aperture was measured with a broad area optical power meter placed in the proxim-

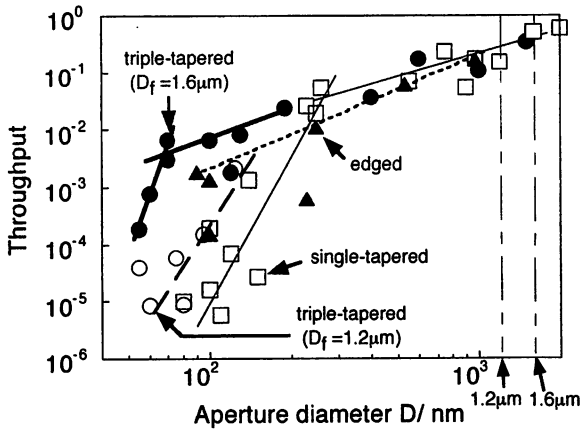

FIG. 4. Throughput as a function of aperture diameter: the triple-tapered probe with $D_f = 1.2\ \mu$m (open circles) and $D_f = 1.6\ \mu$m (closed circles), conventional single-tapered probe (open squares), and the edged probe (closed triangles).

ity of the aperture. The throughput is defined as the ratio of the output power to the input power coupled into the fiber.

In Fig. 4, the throughput is plotted as a function of the D for the triple-tapered apertured probes, the single-tapered apertured probe, and the edged apertured probe. This figure shows that the triple-tapered apertured probes with $D_f = 1.2\ \mu$m and that with $D_f = 1.6\ \mu$m have throughputs 10 and 1000 times higher than that of the single-tapered apertured probe for $D < 100$ nm, respectively. Since the throughput of the single-tapered apertured probe with $D = 1.2\ \mu$m is as high as that with $D = 1.6\ \mu$m (see Fig. 4), the large difference of the throughput between the two triple-tapered apertured probes implies that focused light at the foot of the third taper increases the throughput for the triple-tapered apertured probe with $D_f = 1.6\ \mu$m. The difference between the optimum mesa diameter D_m [Fig. 1(d)] and the optimum foot diameter D_f [Fig. 1(e)] is due to the presence of the second taper, which suggests that further increase in the throughput will be expected by improving the shape of the fabricated probe.

A drastic increase in the throughput of the triple-tapered probe can be attributed to effective excitation of an HE_{11} mode. Since the dependence of the throughput on D for the triple-tapered apertured probe ($D_f = 1.6\ \mu$m) is similar to that of the edged apertured probe in 70 nm<D<200 nm (see Fig. 4), the HE_{11} mode should be excited in the triple-tapered probe. The efficient excitation of the HE_{11} mode can be attributed to the scattering coupling at the foot of the third taper.[11]

A rapid decrease in the throughput of the triple-tapered apertured probe with $D < 60$ nm in Fig. 4, where D is nearly equal to the cutoff diameter of the HE_{11} mode (30 nm), can be attributed to the extremely high propagation loss of the HE_{11} mode.[9]

Finally, we checked whether the triple-tapered structure led to high spatial resolution. For this purpose we observed the spatial distribution on the triple-tapered apertured probe with $D_f = 1.6\ \mu$m and $D = 60$ nm by the probe-to-probe method. To enhance the efficiency of light scattering, we used a sharpened probe with 50-nm-thick gold as a scanning probe.[10,14] Figures 5(a) and 5(b) show the observed spatial distribution of the optical near-field intensity on the aperture.

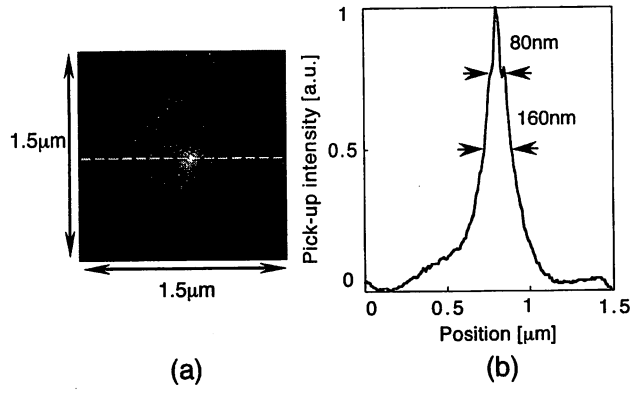

FIG. 5. Spatial distribution of optical near-field intensity on the triple-tapered apertured probe with $D_f = 1.6\ \mu$m and $D = 60$ nm. (a) Two-dimensional profile of the distribution. (b) Cross-sectional profile along the white dashed line in (a).

The FWHM of the spatial distribution is 160 nm, which is considered to be due to the leakage of propagating far field because of the thin coating of the metallic sharpened probe used for the measurement. However, one can also find a very sharp and narrow (80 nm) peak at the center of the curve, which is attributed to localization of the optical near field due to the third taper with a small cone angle.

In conclusion, we have fabricated a triple-tapered apertured probe to demonstrate our proposal and have realized an over 1000-fold increase in the throughput with $D < 100$ nm in comparison with the conventional single-tapered probe, which can be attributed to focusing light, the reduction of the propagation loss, and effective excitation of an HE_{11} mode. In addition, the localized optical near field on the apertured triple-tapered probe with $D = 60$ nm was observed. It can be expected that such a high throughput triple-tapered probe is advantageously used for highly sensitive photoemission spectroscopy, ultrahigh speed and high density optical recording/readout, and so on.

Valuable discussions with Professor K. Tsutsui of The Tokyo Institute of Technology are greatly appreciated.

[1] *Near Field Optics*, edited by D. W. Pohl and D. Courjon (Kluwer, Dordrecht, 1993).
[2] M. Ohtsu, J. Lightwave Technol. **13**, 1200 (1995).
[3] T. Pangaribun, K. Yamada, S. Jiang, H. Ohsawa, and M. Ohtsu, Jpn. J. Appl. Phys., Part 2 **31**, L1302 (1992).
[4] S. Mononobe, M. Naya, T. Saiki, and M. Ohtsu, Appl. Opt. **36**, 1496 (1997).
[5] U. Dürig, D. W. Pohl, and F. Rohner, J. Appl. Phys. **59**, 3318 (1986).
[6] L. Novotny, D. W. Pohl, and B. Hecht, Opt. Lett. **20**, 970 (1995).
[7] G. A. Valaskovic, M. Holton, and G. H. Morrison, Appl. Opt. **34**, 1215 (1995).
[8] M. Stahelin, M. A. Bopp, G. Tarrach, A. J. Meixner, and I. Z. Granacher, Appl. Phys. Lett. **68**, 2603 (1996).
[9] L. Novotny and C. Hafner, Phys. Rev. E **50**, 4094 (1994).
[10] T. Yatsui, M. Kourogi, and M. Ohtsu, Appl. Phys. Lett. **71**, 1756 (1997).
[11] D. Marcuse, *Light Transmission Optics* (Van Nostrand–Reinhold, New York, 1972), Chap. 10.
[12] T. Saiki, S. Mononobe, M. Ohtsu, N. Saito, and J. Kusano, Appl. Phys. Lett. **68**, 2612 (1996).
[13] T. Saiki, K. Nishi, and M. Ohtsu, Jpn. J. Appl. Phys., Part 1 **37**, 1638 (1998).
[14] Y. Inoue and S. Kawata, Opt. Lett. **19**, 159 (1994).

Near-Field Raman Spectral Measurement of Polydiacetylene

YOSHIHITO NARITA,* TOSHIYASU TADOKORO, TERUKI IKEDA, TOSHIHARU SAIKI, SYUJI MONONOBE, and MOTOICHI OHTSU†

JASCO Corporation, 2967-5, Ishikawa-cho, Hachioji-shi, Tokyo 192-8537, Japan (Y.N., T.T., T.I.); and Kanagawa Academy of Science and Technology, KSP east 408, 3-2-1 Sakado, Takatsu-ku, Kawasaki, Kanagawa 213-0012, Japan (T.S., S.M., M.O.)

Two-dimensional near-field Raman spectra and topographic images of the polydiacetylene surface are measured simultaneously by using a near-field Raman spectrometer. The spectra (located 100 nm apart) have different spectral features. The peak intensity ratio of two C=C peaks at 1520 and 1457 cm^{-1} does not correlate with the topographic image and shows differences in the subwavelength scale. These differences can be interpreted as spatial differences in the number of successive bonds on the polydiacetylene surface. In contrast, the near-field Raman intensity of the C=C bond at 1457 cm^{-1} correlates strongly with the topographic image. This phenomenon can be interpreted as a change in the efficiency of collecting Raman scattering light.

Index Headings: **Near field; Raman spectroscopy; Polydiacetylene; Subwavelength.**

INTRODUCTION

The near-field optical microscope (NOM) is a newly developed measurement system that exploits the unique properties of the optical near field.[1,2] The most important characteristic of the NOM is that it can exceed the diffraction limit of the spatial resolution in conventional optical microscopes because the spatial resolution depends not on the wavelength of light but on the apex size of the probe.[3] The NOM is a unique system among the scanning probe microscope family because it can be directly applicable in other fields such as spectroscopy, optical memory, and nanofabrication. The NOM has been used in spectroscopy to measure photoluminescence.[4–9]

Recently, NOMs have been used in Raman spectroscopy to measure silicon, polydiacetylene, diamond, Rd-doped KTP, rhodamine 6G, 3-hydroxykynurenine, cobalt phthalocyanine, benzoic acid, CCl_4, and poly(phenylene vinylene).[10–16] Although subwavelength resolution is demonstrated by one-dimensional traverse measurement of a microcrystal,[13] there are only a few examples of two-dimensional mapping measurement because of the extreme weakness of the Raman signal.[14]

This paper describes the first two-dimensional mapping measurement of polydiacetylene with the use of a near-field Raman spectrometer—in other words, the two-dimensional characterization of sample properties with subwavelength spatial resolution using a near-field Raman spectrometer.

EXPERIMENTAL

Sample. A single polydiacetylene (PDA)–polyETCD crystal on an Al plate was prepared for this experiment. This crystal is typically tabular in shape (Fig. 1). Its typical size is 100 μm × 100 μm with a thickness of 10 μm. The optical properties of PDA (i.e., organic nonlinear optical crystal) have been discussed by several authors,[17–21] and the resonance Raman effect is well known.

Figure 2 shows the typical Raman spectrum of PDA as measured by using a conventional laser micro-Raman spectrometer (JASCO NRS-2000). The peaks at 1457 cm^{-1} and at 2080 cm^{-1} are assigned to a C=C bond and a C≡C bond, respectively. The wavenumber of the C=C peak depends on the number of successive bonds.[17] More successive bonds result in the C=C peak shifting to a lower wavenumber. Thus, the number of successive bonds can be estimated by observing the shift of the C=C peak.

Setup. Figure 3 shows a block diagram of the near-field Raman spectrometer. The system consists of a probe, a shear force feedback loop,[22,23] and a monochromator. The probe is used to illuminate the sample. The Raman scattering light is collected by an objective lens. A pencil-shaped probe is fabricated via etching by using a hydrofluoric (HF)-buffered solution.[24] The subwavelength aperture is formed by oblique evaporation of aluminum with 200 nm thickness. A scanning electron microscopy (SEM) photograph of the probe after the measurement (Fig. 4) showed the aperture size to be approximately 150 nm. Background noise from the optical fiber used for the probe also has Raman peaks in the region lower than 1000 cm^{-1} which overlap the obtained Raman spectrum. Therefore, we selected optical fiber having low Raman intensity to avoid such background noise, and no Raman peaks are observed in the region discussed in the present study. Details of the fiber used will be published elsewhere. The conical probe allows us to illuminate the sample with high throughput and to collect Raman scattering light very efficiently.

Received 31 December 1997; accepted 2 June 1998.

* Author to whom correspondence should be sent.

† Also with the Interdisciplinary Graduate School of Science and Engineering, Tokyo Institute of Technology, 4259, Nagatsuta-cho, Midori-ku, Yokohama 226-8502 Japan.

0003-7028/98/5209-1141$2.00/0

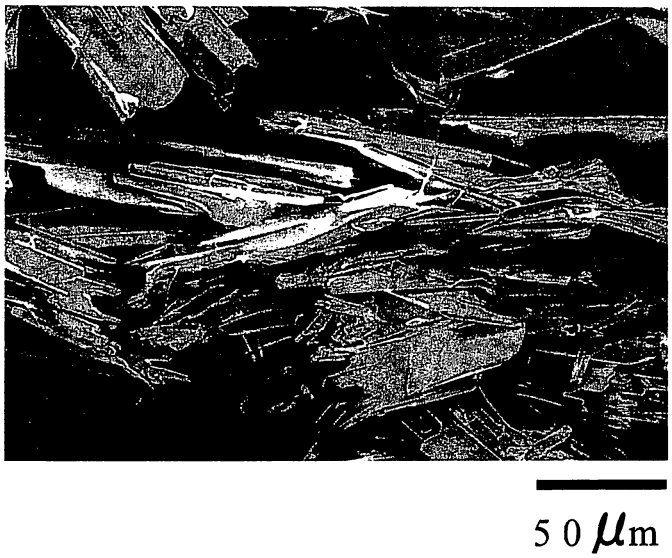

FIG. 1. A SEM photograph of polydiacetylene crystals used in this near-field Raman measurement. Each crystal is typically tabular in shape. The typical size of each crystal is 100 μm × 100 μm with a thickness of 10 μm.

The sample–probe separation is regulated by shear force feedback. For this regulation, the probe is oscillated laterally by using a piezo scan tube (PZT) crystal. The amplitude of PZT oscillation was less than 1 nm at the first-order resonance frequency (10.5 kHz) of the probe. The amplitude of the probe vibration is detected with the use of a 1.3 μm laser diode and a pin photodiode. The signal from the pin photodiode is locked at the frequency of probe oscillation and output is fed back to control the height of the sample PZT stage. As a result, the sample–probe separation was regulated to be 10 nm.

The second harmonics (532 nm wavelength) of a Nd: YAG laser are used as the excitation source. Ten mW power is coupled to the probe, and about 10 μW is used to illuminate the sample through the probe. This throughput is approximately equal to that of probes fabricated via etching in other studies.[25,26] Raman scattering light is collected by an objective lens with a numerical aperture

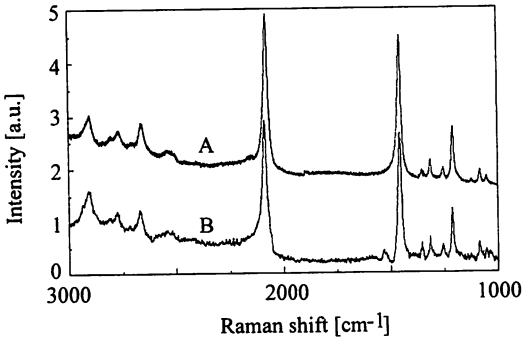

FIG. 2. Conventional micro-Raman spectrum of polydiacetylene. The PDA crystal of spectrum A is used for near-field Raman mapping measurement. Spectrum B is that of another PDA crystal and shows a peak at 1520 cm^{-1}. The peak at 2080 cm^{-1} is assigned to a C≡C bond and the peak at 1457 cm^{-1} to a C=C bond. The peak at 1520 cm^{-1} in spectrum B is assigned to a C=C bond having fewer successive bonds. The spectrum is measured by using a 400 mm triple polychromator and a CCD detector. The spectral resolution is 0.1 cm^{-1}, and the accumulation time is 200 s.

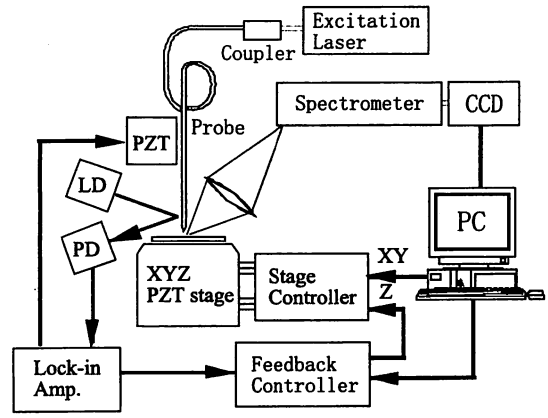

FIG. 3. Block diagram of the near-field Raman spectrometer. The system consists of a probe, an excitation source, a shear force feedback loop, and a Raman spectrometer.

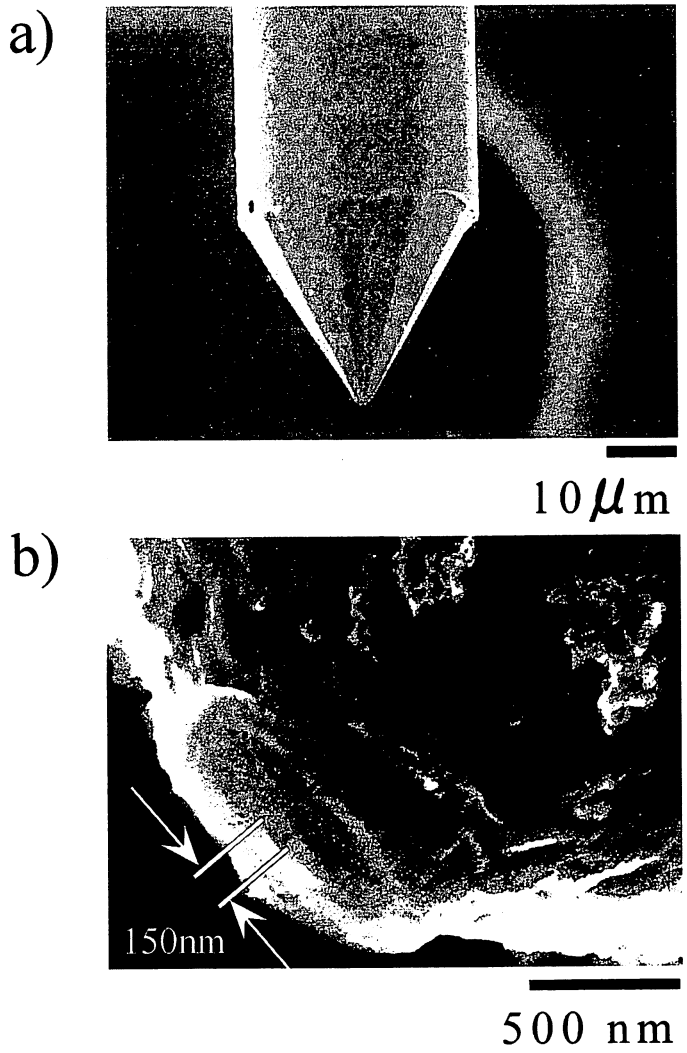

FIG. 4. A SEM photograph of the probe taken after this measurement. (**a**) The pencil-shaped probe is fabricated by etching using an HF-buffered solution. (**b**) Magnified image of the tip. The aperture size is about 150 nm.

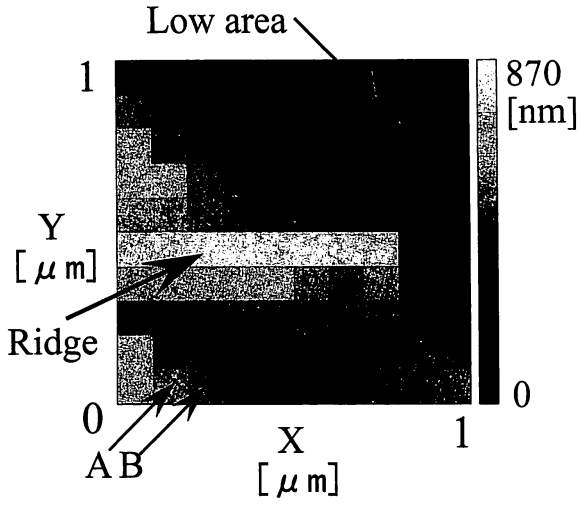

FIG. 5. Shear force topographic image of a single polydiacetylene crystal surface. A ridge is observed in the middle of the measured area.

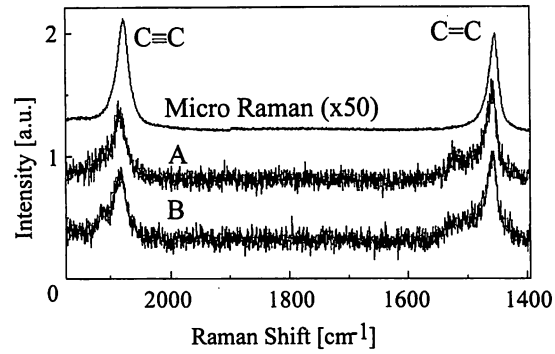

FIG. 6. Near-field Raman spectra of polydiacetylene. The spectra at points A and B in Fig. 5 are compared with spectra obtained by using a conventional micro-Raman spectrometer. A relatively strong 1520 cm^{-1} peak is observed in spectrum A, and in spectrum B a relatively strong 2110 cm^{-1} peak is observed.

(NA) of 0.73 and a magnification of 100. Collected Raman scattering light is introduced into the single monochromator through a multimode optical fiber. This multimode optical fiber mechanically separates the NOM head and the monochromator, which improves the mechanical stability of the NOM head. The Raman signal is detected by using a liquid nitrogen-cooled charge-coupled device (CCD) detector.

RESULTS AND DISCUSSION

The 10 points × 10 points topographic data and Raman spectra were measured simultaneously over a 1 μm × 1 μm area of the single tabular PDA crystal surface. Raman signals were integrated for 600 s at each point; it took approximately 17 h for all 100 points to be measured.

Figure 5 shows the topographic image of the PDA surface obtained by shear force feedback. A ridge approximately 400 nm in height was observed laterally across the center of the area measured. There was also a relatively low area at the top-right corner of the surface. Figure 6 shows the Raman spectra at points A and B in Fig. 5 obtained by using a near-field Raman spectrometer. Note that the distance between A and B is only 100 nm. Figures 7A and 7B show the intensity distribution at the 1457 cm^{-1} peak and the intensity ratio distribution of the 1520 cm^{-1} peak to the 1457 cm^{-1} peak, respectively.

As shown in Fig. 6, the 1520 cm^{-1} peak can be observed only by using a near-field Raman spectrometer. The peaks at 1457 and 1520 cm^{-1} are assigned to C=C bonds that contain a different number of successive bonds as described above. The 1457 cm^{-1} peak is assigned to the vibration of more successive bonds than the 1520 cm^{-1} peak. The 1520 cm^{-1} peak of polyacetyrene (PA) corresponds to about 10 successive bonds, whereas the 1457 cm^{-1} peak corresponds to about 100 successive bonds.[17] Because the Raman spectra of PA and PDA vary little regarding the C=C peak, the two C=C peaks observed in this study can be assigned to approximately 10 and 100 successive bonds, respectively.

Furthermore, the 1520 cm^{-1} peak intensity is different in terms of the spectra at points A and B, which are separated by 100 nm, as shown in Fig. 6. This result suggests that the spectral difference of PDA is observed with subwavelength spatial resolution. The two-dimensional distribution of 1520 cm^{-1} peak intensity (Fig. 7B) indicates that the number of successive bonds differs spatially even with a resolution of 100 nm. These differences have never be detected with the spatial resolution of the conventional micro-Raman spectrometer (shown as a circle in Fig. 7B).

Figures 5 and 7A show that the intensity of Raman scattering light is weaker in both topographically lower areas and the area shaded by the ridge that extends across the measured area. The PDA sample prepared has about an 800 nm height difference in the measured area, and the Raman scattering light is collected by an objective lens from the negative side of the Y axis, as shown in Fig. 7A. Thus, the change in light collection efficiency may explain the observed correlation between Raman peak intensity and the topographic image.

In contrast, no correlation is observed between the peak ratio of the 1520 cm^{-1} peak to the 1457 cm^{-1} peak and the topographic images shown in Figs. 5 and 7B. By subtracting the intensity of the 1457 cm^{-1} peak from that of the 1520 cm^{-1} peak, one nullifies the influence of topography, because the topographic image is included in both the 1520 and 1457 cm^{-1} peak intensities. Therefore, Fig. 7B can be interpreted as showing only the optical properties of PDA without topographic image correlation.

Mapping more than 100 points is possible; however, doing so takes much more time due to the low efficiency of Raman scattering. In our system, the collection and detection efficiency for the Raman system is about 0.1%. Assuming the Raman scattering efficiency is 1×10^{-6}, the rate of photon detection possible is on the order of 10 photons/second because the excitation power at the probe is approximately 10 μW. The photon detected in this experiment is 100 photons/second due to the resonance Raman effect of PDA crystal. To obtain more data points in less time, one must perform excitation and collection of Raman scattering more efficiently. Our probe fabrication technique is very flexible.[24] Thus, future progress in probe fabrication technology will improve the photon collection efficiency drastically.

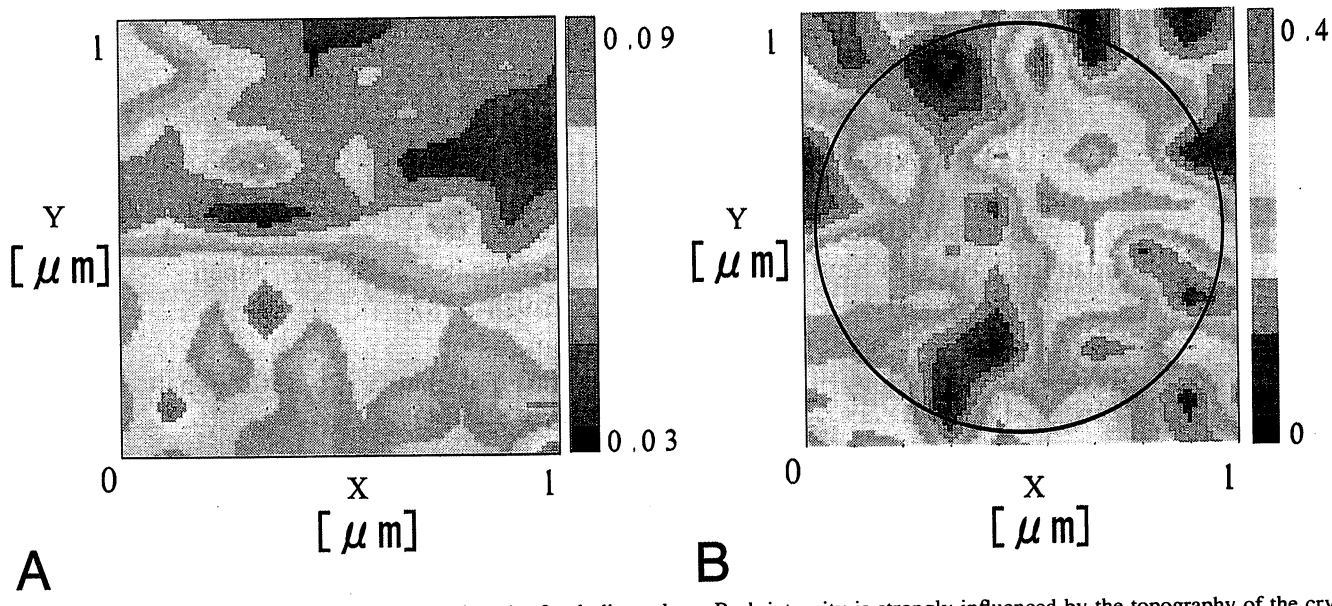

FIG. 7. (A) Intensity distribution of the 1457 cm^{-1} peak of polydiacetylene. Peak intensity is strongly influenced by the topography of the crystal location as shown in Fig. 5. The intensity distribution is interpolated linearly. (B) Peak ratio distribution of 1520 cm^{-1} peak to 1457 cm^{-1} peak of polydiacetylene. The circle in the figure represents the resolution of conventional Raman spectrometers. The peak ratio distribution is interpolated linearly.

CONCLUSION

A near-field Raman spectrometer was designed to measure two-dimensional near-field Raman spectra and topographic mapping images simultaneously on the surface of polydiacetylene. The spatial differences at a peak intensity ratio of 1520 to 1457 cm^{-1} were observed in the subwavelength spatial resolution. These differences are attributed to the spatial differences for the number of successive bonds. Strong correlation between near-field Raman intensity and a topographic image was also observed.

ACKNOWLEDGMENT

This work was funded by the Japan Science and Technology Corporation.

1. D. W. Pohl and D. Courjon, *Near Field Optics,* D. W. Pohl and D. Courjon, Eds. (Kluwer Academic, Dordrecht, 1993), Vol. 242 of NATO ASI Series E.
2. M. Ohtsu, J. Lightwave Technol. **13,** 1200 (1995).
3. E. H. Synge, Phil. Mag. **6,** 356 (1928).
4. M. A. Paesler, P. J. Moyer, and C. J. Jahncke, Phys. Rev. B, **42,** 6750 (1990).
5. R. D. Grober, T. D. Harris, J. K. Trautman, and E. Betzig, Rev. Sci. Instrum. **65,** 626 (1994).
6. S. F. Hess, E. Betzig, T. D. Harris, L. N. Pfeiffer, and K. W. West, Science **264,** 1740 (1994).
7. H. Muramatsu, N. Chiba, T. Ataka, S. Iwabuchi, N. Nagatani, E. Tamiya, and M. Fujihira, Opt. Rev. **3,** 470 (1996).
8. Y. Toda, M. Kourogi, and M. Ohtsu, Appl. Phys. Lett. **69,** 827 (1996).
9. T. Saiki, K. Nishi, and M. Ohtsu, JJAP Jpn. J. Appl. Phys. **37,** 1638 (1998).
10. S. L. Sharp, R. J. Warmack, J. P. Goudonnet, I. Lee, and T. L. Ferrell, Acc. Chem. Res. **26,** 377 (1993).
11. D. P. Tsai, A. Othonos, and M. Moskovits, Appl. Phys. Lett. **64,** 1768 (1994).
12. C. L. Jahncke, M. A. Paesler, and H. D. Hallen, Appl. Phys. Lett. **67,** 2483 (1995).
13. D. A. Smith, S. Webster, M. Ayad, S. D. Evans, D. Fogherty, and D. Batchelder, Ultramicroscopy **61,** 247 (1995).
14. C. L. Jahncke, H. D. Hallen, and M. A. Paesler, J. Raman Spectrosc. **27,** 579 (1996).
15. J. Grausem, B. Humbert, A. Burneau, and J. Oswalt, Appl. Phys. Lett. **70,** 1671 (1997).
16. S. R. Emory and S. Nie, Anal. Chem. **69,** 2631 (1997).
17. G. J. Exarbos, W. M. Risen, Jr., and R. H. Baughman, J. Am. Chem. Soc. **98,** 481 (1976).
18. R. R. Chance, R. H. Baughman, H. Muller, and C. J. Eckhardt, J. Chem. Phys. **67,** 3616 (1977).
19. R. R. Chance, G. N. Patel, and J. D. Witt, J. Chem. Phys. **71,** 206 (1979).
20. T. Kanetake, Y. Tokura, T. Koda, T. Kotaka, and H. Ohnuma, J. Phys. Soc. Jpn. **54,** 4014 (1985).
21. T. Kobayashi, M. Yoshizawa, U. Stamm, M. Taiji, and M. Hasegawa, J. Opt. Soc. Am. B **7,** 1558 (1990).
22. E. Bezig and J. K. Trautman, Science **257,** 189 (1992).
23. M. Vaez-Iravan, R. Toledo-Crow, and Y. Chen, J. Vac. Sci. Technol. A **11,** 742 (1993).
24. S. Mononobe and M. Ohtsu, J. Lightwave Technol. **14,** 2231 (1996).
25. T. Saiki, S. Mononobe, M. Ohtsu, N. Saito, and J. Kusano, Appl. Phys. Lett. **68,** 2612 (1996).
26. S. J. Bukofsky and R. D. Grober, Appl. Phys. Lett. **71,** 2749 (1997).

A3

QUANTUM THEORETICAL APPROACH TO NEAR-FIELD OPTICAL SYSTEM

Kiyoshi Kobayashi (*) and Motoichi Ohtsu (**)
(*) IBM Japan Ltd., 1623-14 Shimotsuruma, Yamato, Kanagawa 242-8502 , Japan
phone: +81-462-73-2777 fax: +81-45-924-5487
e-mail: KKOBA@jp.ibm.com
(**) Tokyo Institute of Technology, 4259 Nagatsuta, Midori, Yokohama 226-8502, Japan
phone: +81-45-924-5455 fax: +81-45-924-5487
e-mail: ohtsu@ae.titech.ac.jp

KEY WORDS: Projection operator, quantum theory of near field optics, tip--sample interaction, virtual photon model.

1. INTRODUCTION

Experimental advances in near-field optics studies have stimulated theoretical work based on macroscopic electromagnetics (classical) and the Maxwell-Schrödinger equations (semi-classical). These approaches, however, still involve unresolved issues. For example, they are not formulated consistently to deal with quantum-mechanical phenomena in a nanometric sample--probe system coupled to a totally macroscopic system. We propose a unified and systematic formulation as a trial approach to resolving the above problems [1], and discuss its relationship to the virtual photon model — a unique and intuitive quantum model based on experimental results [2].

2. PROJECTION OPERATOR METHOD AND EFFECTIVE INTERACTION IN SAMPLE -- PROBE SYSTEM

On the basis of the projection operator method, we address optical near-field problems, including quantum-mechanical observables of a mesoscopic sample--probe system that interacts with light and is coupled to a macroscopic system such as a substrate or fiber probe.

Let us suppose that the total Hamiltonian of a near-field optical system is H; this consists of the Hamiltonian H_0 and the interaction V. As an isolated system, H_0 describes a probe tip, sample, and bath system of incident light and infinite matter. Defining the static projection operators P and $Q = 1 - P$ as

$$|\Psi_\lambda^{(1)}\rangle = P|\Psi_\lambda\rangle, \qquad |\Psi_\lambda^{(2)}\rangle = Q|\Psi_\lambda\rangle, \tag{1}$$

we divide the eigenstates $|\Psi_\lambda\rangle$ of H into two groups, $|\Psi_\lambda^{(1)}\rangle$ in P-space (a small number of bases) and $|\Psi_\lambda^{(2)}\rangle$ in Q-space. It is possible to formally express $Q|\Psi_\lambda^{(2)}\rangle$ by $P|\Psi_\lambda^{(1)}\rangle$, and to obtain an effective operator O_{eff} in the P-space, equivalent to an arbitrary operator O in the full space, that corresponds to physical observables.

As an example, we focus on the sample--probe interaction as $O = V$. We employ the probe (sample) Hamiltonian, in which electrons with effective mass (m_e) and wave number

$k_a (a = \mathrm{A}, \mathrm{B})$ are confined in an infinite well potential of size $a(b)$. For the bath system, we use the Hamiltonian diagonalized in terms of exciton-polariton modes. We then choose a combination of the five states as the P-space bases; the ground and excited states of the probe and sample, $|\mathrm{A}\rangle$, $|\mathrm{A}^*\rangle$ and $|\mathrm{B}\rangle$, $|\mathrm{B}^*\rangle$, and the ground state of the bath system, $|0\rangle$. In order to evaluate the effective sample--probe interaction $V_{\mathrm{eff}}(\mathrm{AB}) \equiv \langle \Psi_\mu^{(1)} | V_{\mathrm{eff}} | \Psi_\lambda^{(1)} \rangle$, we set $|\Psi_\lambda^{(1)}\rangle = |\mathrm{A}\rangle|\mathrm{B}^*\rangle|0\rangle$ and $|\Psi_\mu^{(1)}\rangle = |\mathrm{A}^*\rangle|\mathrm{B}\rangle|0\rangle$. Using the exact expression

$$V_{\mathrm{eff}} = (PJ^\dagger JP)^{-1/2}(PJ^\dagger VJP)(PJ^\dagger JP)^{-1/2} \tag{2}$$

and the perturbative expression of J, we have, in the second order of V,

$$V_{\mathrm{eff}}(\mathrm{AB}) = \langle \mathrm{A}^*|\langle \mathrm{B}|\langle 0|\left[PVQ\left(E_{\mathrm{P}} - E_{\mathrm{Q}}\right)^{-1} VP \right]|\mathrm{A}\rangle|\mathrm{B}\rangle|0\rangle, \tag{3}$$

where E_{P} and E_{Q} are eigenvalues of H_0 in the P- and Q-space, respectively. If we assume that (1) the energy of an exciton-polariton can be expressed in terms of effective mass (m_{p}) and (2) the coupling coefficients of the probe (sample) and exciton-polaritons are constant, then we can obtain an explicit function form of $V_{\mathrm{eff}}(\mathrm{AB})$ that involves the Yukawa function empirically assumed in the virtual photon model. This explicit form also shows that the optical near field is effectively localized near the sample--probe system, and that the decay length is proportional to the inverse of the probe (sample) size, which is consistent with the experimental results [3].

3. SUMMARY

We have developed a microscopic theory for an optical near-field system, using quantum-mechanical techniques. It was shown that effective sample--probe interaction involves the Yukawa type of interaction, which indicates that the virtual photon model is not a physical assumption, but has an identity corresponding to microscopic theory. The key points are that a probe tip exists near the sample, and that the electron energies in the probe tip and sample are inversely proportional to the squares of their sizes, owing to the confinement effect.

The authors gratefully acknowledge fruitful conversation with H. Hori of Yamanashi University, and members of Ohtsu laboratory at Tokyo Institute of Technology and Kanagawa Academy of Science and Technology.

REFERENCES

[1] K. Kobayashi and M. Ohtsu, to be published.
[2] M. Ohtsu and H. Hori, NEAR-FIELD NANO-OPTICS, Academic, New York, (1998).
[3] M. Ohtsu eds., Near-field nano/atom optics and technology, Springer, Berlin, (1998).

D2

NEAR-FIELD NONLINEAR ABSORPTION SPECTROSCOPY OF SINGLE QUANTUM DOTS

Takuya Matsumoto[1)], Kazunari Matsuda[2)], Kenichi Nishi[3)], Toshiharu Saiki[2)], and Motoichi Ohtsu[1, 2)]

1) Ohtsu Laboratory,Interdisciplinary Graduate School of Science and Engineering
Tokyo Institute of Technology, 4259 Nagatsuta, Midori-ku, Yokohama 226-8502, Japan
phone: +81-45-924-5476, fax: +81-45-924-5487
e-mail: takuya@ae.titech.ac.jp

2) Kanagawa Academy of Science and Technology, Kawasaki, Japan

3) Optoelectronics and High Frequency Device Research Laboratories, NEC Corporation, Tsukuba, Japan

KEYWORDS: Quantum dot, nonlinear absorption spectroscopy, pump-probe measurement

1. INTRODUCTION

Quantum dots (QDs) are the most attractive nano-artificial due to their atom-like discrete level structures. The concentration of oscillator strength at narrow spectral region is expected to attribute to the gigantic optical nonlinearity advantageous towards the single QD devices, such as an optical memory, switching, modulator, and so on.

For the accurate evaluation of nonlinear parameters of single QDs, conventional microscopic spectroscopy with far-field configuration is insufficient due to the large discrepancy between the size of QD and that of focusing spot. Near-field probing is the most promising technique for the restriction of observation area as small as ~100 nm, which is equal to only several times of the dot diameter. The sensitivity of detection is also important factor since the signal to noise ratio of 10^{-4}-10^{-6} must be attained. Recently simultaneous achievement of high spatial resolution and high detection sensitivity is realized by optimizing the shape of the near-field probe and the aperture diameter. We have successfully measured the optical nonlinear absorption of single QDs by employing the near-field differential transmission spectroscopy for the first time.

2. EXPERIMENTAL

The experimental configuration is shown in Fig. 1. The sample investigated is self-assembled InGaAs quantum dots covered by a cap layer with a thickness of 180 nm. As a near-field probe, chemically etched probe with doubled tapered structure and 300-nm aperture was employed for high-sensitivity detection. The spatial resolution of the probe was evaluated as 100-200 nm through the photoluminescence imaging of single QD [1]. The sample and the probe were mounted in a continuous He-gas flow optical cryostat and all the measurement were performed at 8 K.

For the measurement of the nonlinear transmission of single QD, cw pump-probe technique is employed. Photoexcited carriers are generated in quantum dots by the pump beam (λ=633 nm) passing through the aperture. The nonlinear change of the absorption coefficient due to the occupation of carriers in quantized states of single QD is probed by the transmitted light (λ=920 nm), which is collected through the same aperture. The pump and probe beams are modulated at the frequencies of ω_1 and ω_2, respectively. Nonlinear transmission signal (ω_1- ω_2) was extracted by means of synchronous lock-in detection.

3. RESULTS AND DISCUSSION

Figure 2 shows the distribution of the nonlinear transmission signal. The bright spots correspond to single QDs. Figure 3 shows the dependence of the signal intensity on the pump power density when the fiber probe is placed above a single QD. In the weak excitation region, the signal intensity linearly increases with the pump power. (The linear dependence on the probe power is also confirmed). Above 300 W/cm^2 excitation, the signal intensity saturates due to the continuous occupation of carriers in a quantized state. In the same excitation intensity, we also observe the saturation of ground-state emission in photoluminescence spectrum. It is deduced that the observed signal originates from the nonlinear transmission due to the ground-state occupation of one electron-hole pair. From the maximum differential transmission ($\Delta T/T$) of as large as 10^{-4}, the absorption cross section of the single QD is estimated as 0.01% of observation area.

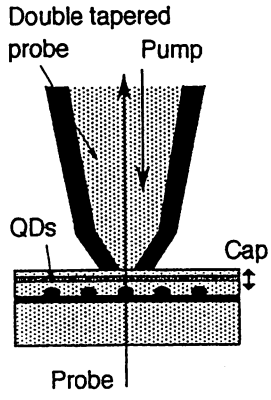

Fig 1 Experimental configuration

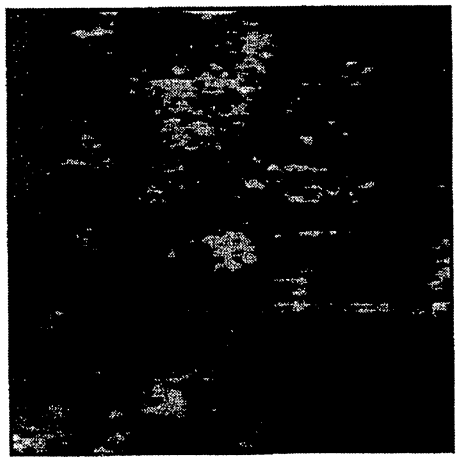

Fig.2 Near-field nonlinear transimission image (scan range 5.4x5.4μm^2)

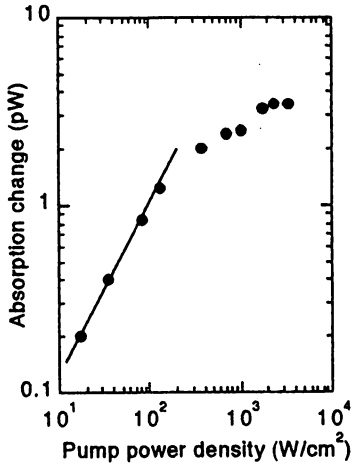

Fig.3 Dependence of the absorption change on the pump power

4. REFERENCES

[1] T. Saiki, K. Nishi, and M. Ohtsu, "Low temperature near-field photoluminescence spectroscopy of InGaAs single quantum dots", Jpn. J. Appl. Phys. **37**, 1638-1642 (1998).

PC5

FABRICATION OF APPLICATION-ORIENTED NEAR-FIELD FIBER PROBES BASED ON HYBRID SELECTIVE ETCHING OF MULTISTEP INDEX FIBERS

Shuji Mononobe and Motoichi Ohtsu*
Kanagawa Academy of Science and Technology
KSP 408–B, 3–2–1 Sakado, Takatsu, Kawasaki 213–0012, Japan
fax : +81–44–819–2072
e-mail : mononobe@net.ksp.or.jp

* M. Ohtsu is also with the Tokyo Institute of Technology, Yokohama 226-8502, Japan.

KEY WORDS : Near-field optics, fiber probe

In near-field imaging applications requiring high-spatial resolution, a tapered probe with small cone angle and a nanometric apex diameter has to be fabricated because the resolution capability of the probe is determined by its parameters such as the cone angle and apex diameter. However, the transmission efficiency of the probe is diminished on decreasing the cone angle. In spectroscopic applications, where one must bear with extremely low detected power, the probe should have high-transmission efficiency in illumination-mode and be highly sensitive in collection-mode. In illumination-mode, to avoid thermal damage of the sample, the probe should be used with an input power as low as possible. The resolution capability and the transmission efficiency of the probe have to be optimized depending on the application of near-field optics to imaging or spectroscopy. This should be done through tailoring the probe.

To fabricate application-oriented probes [1], we proposed several methods which were based on hybrid selective etching of specially designed multistep index fiber. [1, 2] We succeeded in fabricating application-oriented probes such as a pencil-shaped probe with high resolution capability, one with high transmission efficiency, a triple-tapered probe with high resolution capability and high transmission efficiency [1], and ultraviolet probe [2].

In this paper, we will present these application-oriented probes [3] and propose a new type of fiber probe with single-mode and multimode cores for illumination-collection (i-c) mode near-field optical microscopy. In i-c mode employing single-mode/multimode fiber probe, the input light propagates within the single-mode core, and the scattered light from the apex is effectively coupled with the multimode core. Figures 1(a)-(e) show schematic illustrations of a pencil-shaped probe, triple-tapered probe, a protrusion-type probe [4, 5], UV triple-tapered probe [2], and single-mode/multimode fiber probe. Here, θ is the cone angle of a probe. θ_1 and θ_2 are the first and second cone angles of the triple-tapered probe, respectively. d_B is the base diameter of the first taper. These parameters are controlled to optimize the resolution and the transmission capability. Figure 2 shows a scanning electron micrograph of a single-mode/multimode fiber probe with a cone angle of 30 degrees. Details of methods for tailoring these probes will be presented in the session.

REFERENCES

[1] S. Mononobe and M. Ohtsu, "Development of a fiber used for fabricating application oriented near-field optical probes," *IEEE Photonics Technol. Lett.*, 10, 99–101 (1998).
[2] S. Mononobe et al., "Fabrication of a triple tapered probe for near-field optical spectroscopy in UV region based on selective etching of a multistep index fiber," *Opt. Commun.*, 146, 45–48(1998).
[3] S. Mononobe and M. Ohtsu, "Probe fabrication," in Near-field nano/atom optics and technology, M. Ohtsu ed., Springer-Verlag, Tokyo, (1998).
[4] S. Mononobe et al., "Reproducible fabrication of a fiber probe with the nanometric protrusion for near-field optics," *Appl. Opt.*, 36, 1496–1500 (1997).
[5] S. Mononobe, R. Uma Maheswari, M. Ohtsu, "Fabrication of a pencil-shaped fiber probe with a nanometric protrusion from a metal film for near-field optical microscopy," *Opt. Express*, 1, 229–233, http://epubs.osa.org/opticsexpress/.

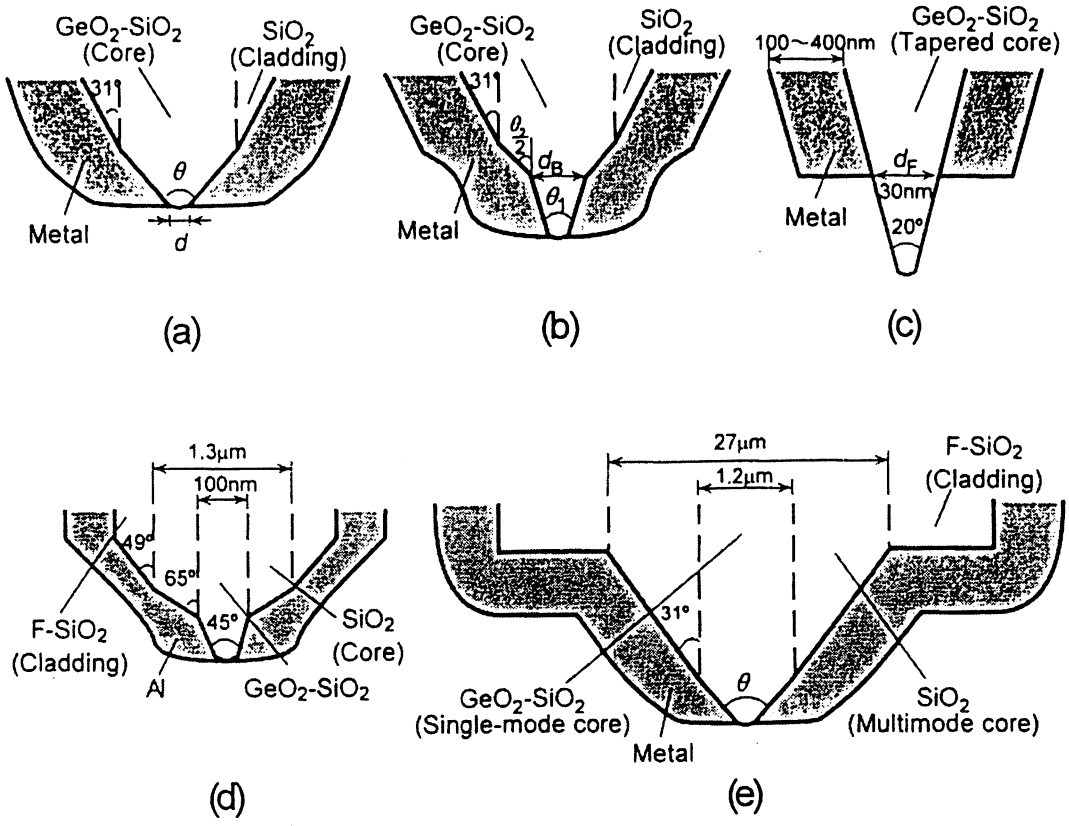

Fig. 1 Schematic illustration of (a) a pencil-shaped probe, (b) a triple-tapered probe, (c) a protrusion-type probe, (d) an UV-triple tapered probe, and (e) a single-mode/ multimode hybrid fiber probe.

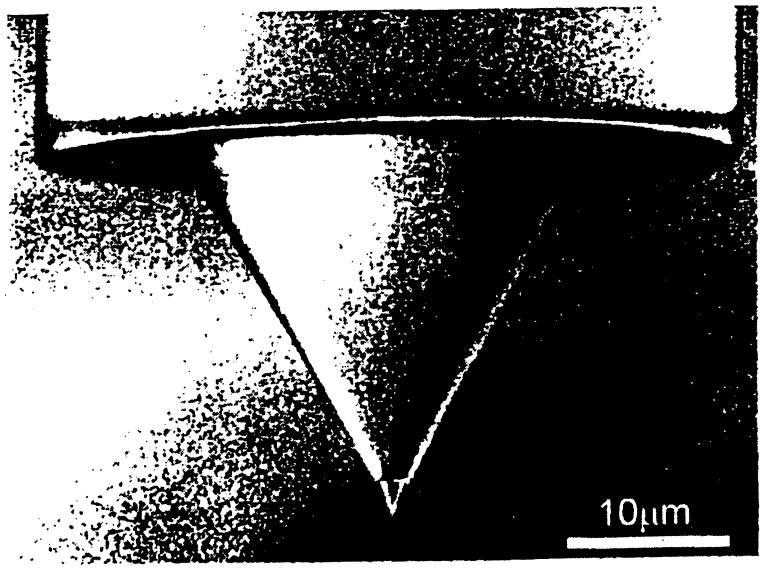

Fig. 2 Scanning electron micrograph of a single-mode/ multimode fiber probe. θ=30°, d<10nm

NEAR FIELD OPTICS - 5, Technical Digest of the 5th International Conference
on Near Field Optics and Related Techniques, December 6-10, 1998

PC6

FABRICATION OF A NANOMETER-LEVEL RESOLVING PROBE WITH METAL-DIELECTRIC-METAL COAT FOR NEAR-FIELD IMAGING OF SINGLE STRAND DNA MOLECULES

Shuji Mononobe, R. Uma Maheswari *, and Motoichi Ohtsu **
Kanagawa Academy of Science and Technology
KSP 408–B, 3–2–1 Sakado, Takatsu, Kawasaki 213–0012, Japan
fax : +81–44–819–2072
e-mail : mononobe@net.ksp.or.jp

* Present address: RIKEN, Hirosawa 2-1, Wako, Saitama 351–0106, Japan
** M. Ohtsu is also with the Tokyo Institute of Technology, Yokohama 226–8502, Japan.

KEY WORDS : Near-field optics, fiber probe, deoxyribonucleic acid

1. INTRODUCTION

Recently, we succeeded in obtaining a high-resolved optical image of deoxyribonucleic acid (DNA) molecules with collection mode near-field optical microscopy employing a fiber probe with metal-dielectric-metal coat. In this paper, we present a method to fabricate this nanometer-level resolving probe.

2. NANOMETER-LEVEL RESOLVING PROBE

Figure 1 shows a schematic illustration of the probe, which has the GeO_2-doped silica core, the silver (Ag) film, the magnesium fluoride (MgF_2) film, and the aluminum (Al) film. In this probe, the Ag tip works an effective scatterer of high spatial frequency components of optical near-field, and the Al film suppresses the propagating component and low spatial frequency components of optical near-field. Since MgF_2 is a transparent material with a low refractive index of 1.3, the scattered light from the Ag apex is effectively coupled with GeO_2-doped silica core through the MgF_2 film.

3. PROBE FABRICATION AND IMAGING OF DNA

To fabricate the probe, first a pencil-shaped probe with an apex diameter of less than 10nm and a cone angle of 30 degrees is fabricated based on hybrid selective etching of a multistep index fiber in buffered HF splutions. For details of this process, see Ref. 2. Next, the probe was consecutively coated with Ag, MgF_2, and Al films by a vacuum evaporation unit. The thickness of these films are 5–10nm, 100nm, and 200nm, respectively.

We performed observation of DNA by collection mode near-field optical microscopy employing the probe. Figure 2 shows the near-field image under constant-distance of mode obtained by optical near-field intensity feedback [1]. Arrows at the left-hand of the figure indicate propagation k and electric field E vectors. The bright portions corresponds to single strands of DNA As seen, the individual stands are clearly resolved to have a full width at half-maximum of 20nm. Further, much narrower image (<4nm) has been obtained recently. Its details will be presented at the session.

4. REFERENCES

[1] R. Uma Maheswari and M. Ohtsu, "Imaging biological specimens," in Near-field nano/atom optics and technology, M. Ohtsu ed., Springer-Verlag, Tokyo, (1998).
[2] S. Mononobe and M. Ohtsu, "Development of a fiber used for fabricating application oriented near-field optical probes," *IEEE Photonics Technol. Lett.*, 10, 99–101 (1998).
[3] K. Yoshida, M. Yoshimoto, K. Sasaki, T. Ohnishi, T. Ushiki, J. Hitomi, S. Yamamoto, M. Sigeno, "Fabrication of a new substrate for atomic force microscopic observation of DNA molecules," *Biophysical J.*, 74, 1654–1657(1998).

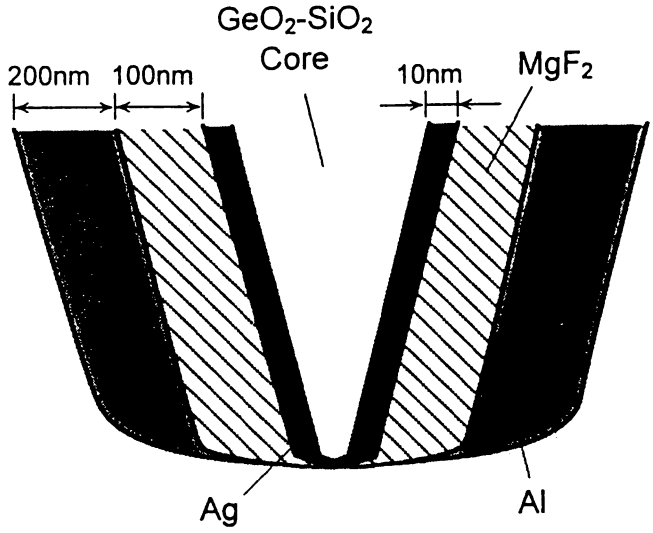

Fig. 1 Schematic illustration of a fiber probe with metal-dielectric-metal coat for near-field imaging of DNA.

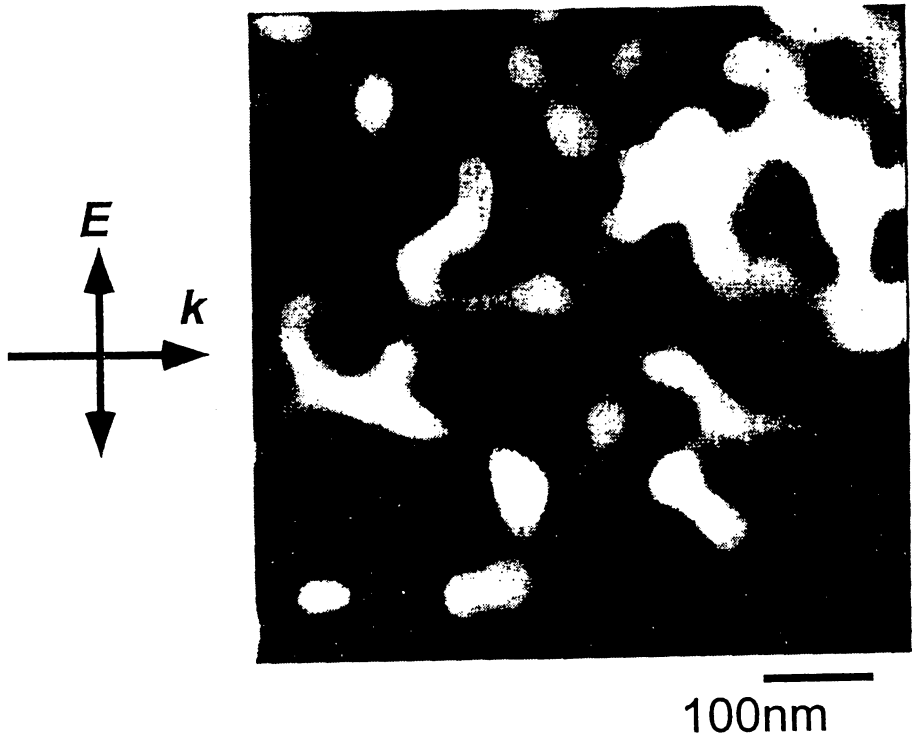

Fig. 2 Collection-mode near-field optical image of DNA obtained under constant-distant mode with optical near-field intensity as the control signal.

NEAR FIELD OPTICS - 5, Technical Digest of the 5th International Conference
on Near Field Optics and Related Techniques, December 6-10, 1998

PC7

FABRICATION OF A NEAR-FIELD OPTICAL FIBER PROBE WITH A NANOMETRIC METALLIZED PROTRUSION

Takuya Matsumoto[1)], Tsutomu Ichimura[1)], Takashi Yatsui[1)], Motonobu Kourogi[1)], Toshiharu Saiki[2)] and Motoichi Ohtsu[1),2)]

1) Ohtsu Laboratory, Interdisciplinary Graduate School of Science and Engineering, Tokyo Institute of Technology, 4259 Nagatsuta, Midori-ku, Yokohama 226-8502, Japan
Phone: +81-45-924-5476, Fax: +81-45-924-5487
e-mail: takuya@ae.titech.ac.jp
2) Kanagawa Academy of Science and Technology
KSP East 408, 3-2-1 Sakado, Takatsu-ku, Kawasaki, 213, Japan

KEYWORDS: fiber probe, metallized protrusion, aperture, localized plasmon

1. INTRODUCTION

Near-field optical microscopy has an ability to perform various forms of optical spectroscopy, such as photoluminescence spectroscopy and Raman spectroscopy, with subwavelength resolution. However, in such spectroscopy, a serious problem is low light excitation and collection efficiencies due to low throughput of the probe.

In order to solve the problem, we propose a probe with a nanometric metallized protrusion extending through a subwavelength aperture (Fig.1). In the illumination mode, the metallized protrusion works as a nanometric light source. When the metallized protrusion is illuminated by light, strong optical near-field is generated at its apex. The aperture suppresses generating the background light. In the collection mode, the metallic protrusion works as a high efficiency scatterer for the optical near-field on the sample surface. The aperture suppresses detecting the low spatial frequency components of the scattered light.

2. FABRICATION OF THE PROBE

First, an optical fiber is sharpened by two step chemical etching method [1] and the foot of the sharpened core is coated with resin (Fig.2). Secondly, the fiber is dipped in a HF solution to etch the core apex forming a depression. Thirdly, the resin film is coated with metal to form the aperture, and finally, the core apex is coated with metal. Figure 3 shows the SEM image of the fabricated probe. The aperture diameter is 400 nm, and the apex diameter of the metallic protrusion is 35 nm.

3. CHARACTERIZATION OF NEAR-FIELD OPTICAL PROPERTIES

The intensity distribution of the optical near-field at the apex of the probe was measured by scanning another probe across the apex. It was observed that strong optical near-field was generated at the apex of the metallized protrusion. The width of the intensity distribution was 150 nm including instrumental resolution.

4. PLASMON PROBE

Probes with spherical and ellipsoidal metallized protrusion were also fabricated (Fig.4). The diameters of the spherical protrusions were from 50 to 200 nm. Enhancement of the optical near-field by 10^2 to 10^5 times is expected due to localized plasmon excitation [2].

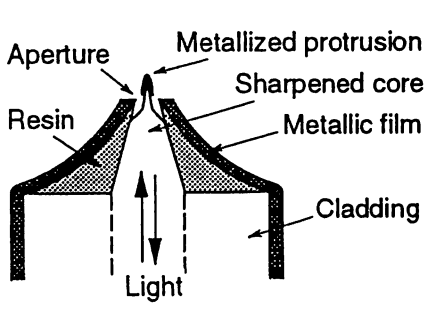

Fig.1 Schematic of the proposed probe

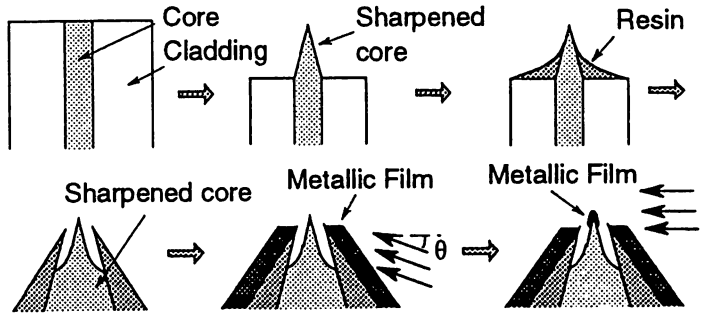

Fig.2 Fabrication process

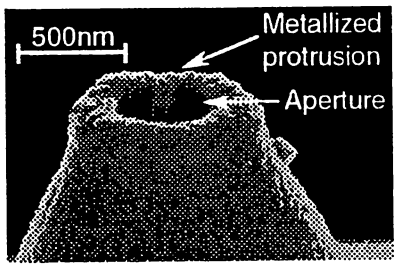

Fig.3 Fabricated probe with the metallized protrusion

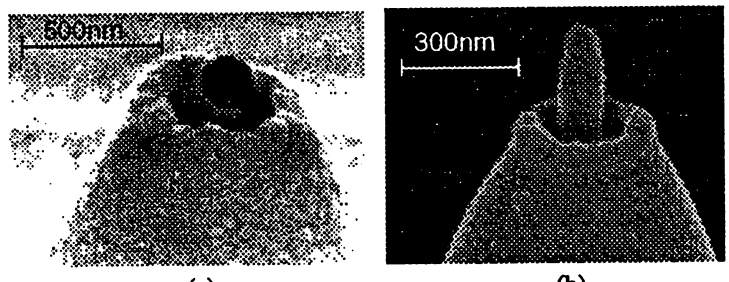

Fig.4 Fabricated probes with (a) spherical and (b) ellipsoidal metallized protrusion

5. REFERENCES

[1] T.Pangaribuan *et.al*, "Two-step etching method for fabrication of fiber probe for photon scanning tunneling microscope," Electronics Lett., **29**, 1978-1979 (1993)
[2] H.Raether, Surface plasmons, Springer-Verlag, Berlin (1988)

NEAR FIELD OPTICS - 5, Technical Digest of the 5th International Conference
on Near Field Optics and Related Techniques, December 6-10, 1998

PC11

Fabrication and SNOM Characterization of Planar Probe Array for Near-Field Optical Memory Application

M. B. Lee[1], A. Sato[2], K. Tsutsui[3], M. Ohtsu[3], and N. Atoda[1]

[1] Optical Memory Group, National Institute for Advanced Interdisciplinary Research
1-1-4 Higashi, Tsukuba, Ibaraki 305-8562, Japan
phone: +81-298-54-2914, fax: +81-298-54-2919
e-mail : mblee@nair.go.jp

[2] Takatsuki Laboratory, Minolta Co., Ltd.
1-2 Sakura-Machi, Takatsuki-Shi, Osaka 569-8503, Japan

[3] Interdisciplinary Graduate School of Sci. and Eng., Tokyo Institute of Technology,
4259 Nagatsuta, Midori-ku, Yokohama, Kanagawa 226-8502, Japan

Keywords: near-field optical memory, planar probe array, apertured probe, micromachining, FDTD simulation, light intensity profile

Near-field optical memory of recording density as high as ~100 Gb/in^2 has already been demonstrated using fiber type probe. However, extension of the technique to actual storage system is difficult due to limited scan area and low data transmission rate in conventional near-field optical memory employing fiber probe. In order to increase the data transmission rate, we have proposed a planar-type apertured probe array [1] and demonstrated fabrication of probe array with lateral aperture size of 80 nm by silicon micromachining based on wet anisotropic etching. Although parallel data recording/readout is possible with the probe array, the light transmission efficiency of individual probe in the array should be high enough for obtaining high data rate. Focusing of incident laser beam by spherical lens on the aperture region is one of the promising methods for that purpose [2].

In this paper, we demonstrate the increase of the light transmission efficiency of planar probe array by modifying the probe structure. By combining dry etching technique with the anisotropic etching, we successfully fabricated probe array with parabolic apex shape while maintaining aperture sizes less than 100 nm. Figures 1(a) and 1(b) show the schematic structure and scanning electron micrograph (SEM) of typical aperture of one element

of probe array with modified apex profile. We also fabricated SiN probe array with sharpened apex embedded in Si planar structure. Two-dimensional FDTD simulation showed optical near-field intensity increased much for the two kinds of probes compared to our previous probe with inverted pyramidal shape. Light intensity profiles emitting from the apertures were measured with scanning near-field optical microscopy (SNOM) technique. The simulation resuls and experimental SNOM characterization will be compared each other.

REFERENCES

[1] M. Ohtsu, Tech. Digest of the Joint MORIS/ISOM Symp., (1997) p. 180.

[2] M. Kourogi *et al*, Ext. Abst. of the 58th Symp. of Japan Applied Physics Society, (1997), p. 984.

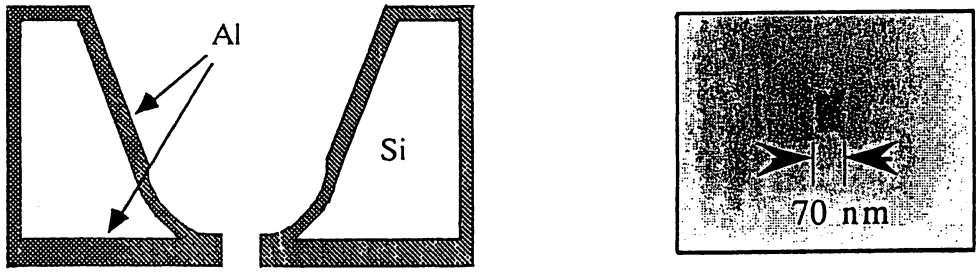

Fig. 1 Silicon planar apertured probe with modified apex shape.
(a) schematic cross-sectional structure (b) SEM of typical aperture

C1

OPTIMIZATION OF STRUCTURE AND APERTURE DIAMETER OF NEAR-FIELD PROBE FOR ILLUMINATION-COLLECTION HYBRID-MODE OPERATION

Toshiharu Saiki[1)] and Motoichi Ohtsu[1, 2)]
[1)] Kanagawa Academy of Science and Technology
KSP East 408, 3-2-1 Sakado, Takatsu, Kawasaki, Kanagawa 213-0012, Japan
phone: +81-44-819-2071 fax: +81-44-819-2072
e-mail: saiki@net.ksp.or.jp
[2)] Interdisciplinary Graduate School of Science and Engineering
Tokyo Institute of Technology
Yokohama, Japan

KEYWORDS: Illumination-collection hybrid mode, aperture diameter, double-tapered structure, photoluminescence spectroscopy

1. INTRODUCTION

In the near-field spectroscopy of semiconductor nano-structures, we often encounter several severe problems to be overcome. First, opaque materials or quantum structures grown on opaque substrates should be investigated. In this case, we cannot employ the conventional illumination-mode operation, where the signal light is collected in the opposite side with large NA lens. In the photoluminescence (PL) spectroscopy with the illumination mode, another problem originates from the reduction of the spatial resolution due to the carrier diffusion prior to the recombination. It is indispensable to combine with the collection-mode operation to achieve high spatial resolution. Second, in the near-field spectroscopy, we need to detect weak signals, such as PL, Raman scattering, and so on. The standard near-field probe with the throughput of 10^{-4}-10^{-5} is not suitable for such measurement requiring high sensitivity. In order to solve these difficulties, we must decide to establish the illumination-collection hybrid-mode operation with high detection efficiency.

The optimization of the structure and the aperture diameter of the near-field probe is the most essential work for its application to the novel spectroscopy. So far, we have been emphasizing the advantage of the double-tapered structure for the enhancement of the illumination and collection efficiency [1, 2]. In this report, we describe the simultaneous achievement of high spatial resolution and high detection sensitivity through the optimization of the aperture size of the double-tapered probe. PL spectroscopy of single InGaAs quantum dots (QDs) is successfully performed at room temperature for the first time.

2. EXPERIMENTAL

Figure 1 shows the experimental configuration and block diagram of the measurement. The near-field probes investigated are fabricated by chemical etching technique. In order to shorten the strong optical loss region of narrow metal-cladding waveguide, the structure of the probe was optimized to have large cone angle at the apex. We prepared several probes with a various aperture diameter ranging from 200 nm to 800 nm (corresponding throughput of 0.5-20%). The sample was self-assembled InGaAs quantum dots with the diameter of 30 nm and the height of 15 nm. For the excitation of PL, the sample was illuminated with He-Ne laser (λ=633 nm) through the aperture. In order to achieve the high spatial resolution free

from the carrier diffusion effect, the resultant PL from QDs was collected by the same aperture. After rejecting the excitation light by means of the band-pass filter, the signal PL was detected by an avalanche photodiode.

3. RESULTS AND DISCUSSION

Figure 2 shows a PL image constructed by scanning the probe with the aperture diameter of around 300 nm. Each circular spot corresponds to a single QD with emission wavelength of 980 nm. The average spot size is estimated as 130 nm, which is almost equal to the resolution of this measurement since the size of QD is much smaller than the spot size. A significantly high spatial resolution of $\lambda/8$ is achieved with high sensitivity.

Figure 3 summarize the resolution and the sensitivity as a function of the throughput (aperture diameter) of the probe. With an increase of the aperture diameter, the spatial resolution is reduced gradually. It should be emphasized that the spot size (resolution) is much smaller than the aperture diameter. Even when we employ the 800-nm aperture, the resolution of 250 nm ($\lambda/4$) is attained. Furthermore, due to the use of large apertures, high detection sensitivity is also achieved simultaneously. We also evaluate the absolute value of the collection efficiency as high as 1-10%. Such high sensitivity contributes to the successful observation of PL from single QDs at room temperature.

4. ACKNOWLEDGMENT

The authors would like to thank Dr. K. Nishi (NEC Corporation) for providing us high-quality samples of InGaAs quantum dots.

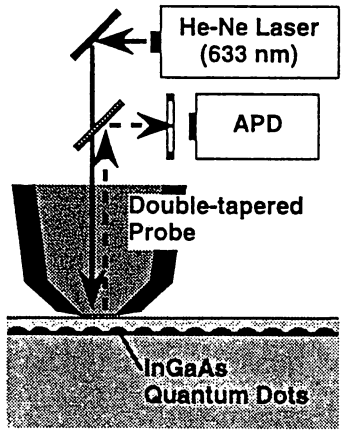

Fig. 1 Experimental configuration and block diagram of measurement.

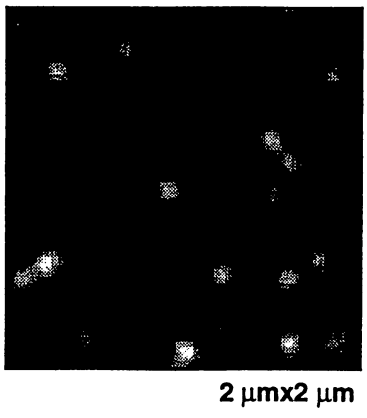

Fig. 2 Near-field PL image of single quantum dots.

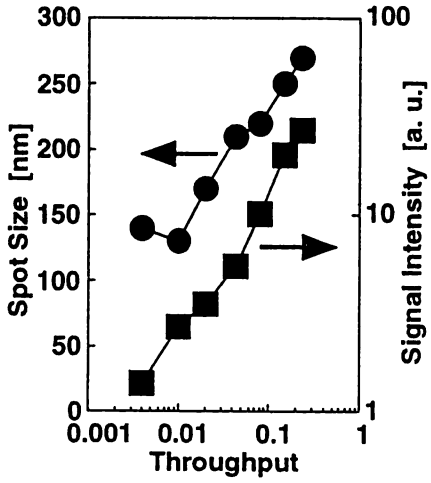

Fig. 3 Resolution and sensitivity as a function of throughput.

5. REFERENCES

[1] T. Saiki; S. Mononobe, M. Ohtsu, N. Saito, and J. Kusano, "Tailoring a high-transmission fiber probe for photon scanning tunneling microscope", *Appl. Phys. Lett.* **68**, 2612-2614 (1996).
[2] T. Saiki; K. Nishi, and M. Ohtsu, "Low temperature near-field photoluminescence spectroscopy of single quantum dots", *Jpn. J. Appl. Phys.* **37**, 1638-1642 (1998).

PE10

OBSERVATION OF POLYSILANE AGGREGATES WITH SCANNING OPTICAL NEAR-FIELD MICROSCOPE

Toshihiro Suzuki[a], Shin-ya Koshihara[a,b], Mamoru Yoshimoto[c],
Toshiharu Saiki[b], Shuji Mononobe[b], Motoichi Ohtsu[b,d],
Takashi Miyazawa[b] and Mitsuo Kira[e,f]

a:Department of Applied Physics, Tokyo Institute of Technology
2-12-1 Oh-okayama, Meguro-ku, Tokyo 152-8551, Japan
phone : +81-3-5734-2449 fax: +81-3-5734-2751
e-mail: skoshi@ap.titech.ac.jp
b:Kanagawa Academy of Science and Technology
c:Materials and Structures Laboratory, Tokyo Institute of Technology
d:Department of Applied Electronics, Tokyo Institute of Technology
e:Photodynamics Research Center, Institute of Physical and Chemical Research
f:Department of Chemistry, Tohoku University

KEY WORDS: polysilane, near-field microscope, ultra-violet (UV) region, atomically flat sapphire plate.

Poster Tuesday, December 8

1. INTRODUCTION

Obtaining an accurate image of the actual conformation of semiconducting polymer chains is vital in utilizing and controlling their inherent opto-electronic properties. Because, the structural changes in global and local molecular conformations will greatly affect various opto-electronic properties of conjugated polymers[1]. Especially, the progress in the near-field microscopic technique in the blue and ultra-violet (UV) region will play a key role for achieving various attractive molecular functionalities such as high density optical memory, linear and nonlinear optical devices which can be controlled by blue light. In this study, we report the photo-luminescence image of poly dihexylsilane (PDHS) in UV-region. Polysilane is an organic-inorganic hybrid material with a silicon quantum wire structure as shown in Fig.1. Spectroscopic studies have shown that PDHS has a direct-type band structure with a large gap energy (about 4.5 eV) due to the one-dimensional confinement effect of σ-electrons[2]. In addition, various attractive ideas for the applicational use in opto-electronic devices in blue and UV-regions have been proposed. The progress of the near-field microscopic technique in blue and UV-regions is important to make clear the relation between polysilane structure and electronic properties of it. We also make a report about a scanning near-field optical microscope in UV region by virtue of a triple tapered probe [3] and atomically flat sapphire plate [4].

2.EXPERIMENTALS

We prepared highly purified PDHS with a molecular weight of 300,000 by polymerization of n-dichlorodihexylsilane. The preparation methods for the triple tapered probe and atomically flat sapphire plate have been reported previously [3,4]. To increase the transmission efficiency of the fiber probe in UV-region, a multistep index fiber made of GeO_2 silica, non-doped silica and fluorine doped silica has been used. PDHS was cast on the substrate from a very dilute toluene solution of about 10^{-8} (Si-unit)/L. The sapphire plate is transparent to UV-light and its atomically flat surface with only atomic layer steps is hydrophobic. This is the reason why the sapphire plate is suitable for the observation of hydrophobic PDHS molecule using UV-light.

3.RESULTS

Figs.2(a) and (b) show the AFM and photoluminescence images of PDHS. As shown in this figure, PDHS molecules dispersed on the plate is forming the aggregate structure with the size of about 0.5 μm. From the results of light scattering and viscosity measurement, it has been conjectured that PDHS does not take a rigid rodlike helix structure. The obtained result seems to be well consistent with this expectation. The observation by near-field microscope of [n-decyl-(S)-2-methylbutyl silane] molecules which will take the rigid rod-like structure even on the sapphire plate [5] is now in progress.

4.REFERENCES

[1] K.Yokoyama and M.Yokoyama, Philos. Mag. **B61**, 59 (1990).
[2]H.Tachibana et.al. Phys. Rev. **B47**, 4363 (1993).
[3]S. Mononobe et.al. Opt. Commun. **146**, 45-48 (1998).
[4]M.Yoshimoto et.al. Appl. Phys. Lett. **67**, 2615-2618 (1995).
[5] K.Ebihara et.al. Jpn.J.Appl.Phys. **36**, L1211-1213 (1997).

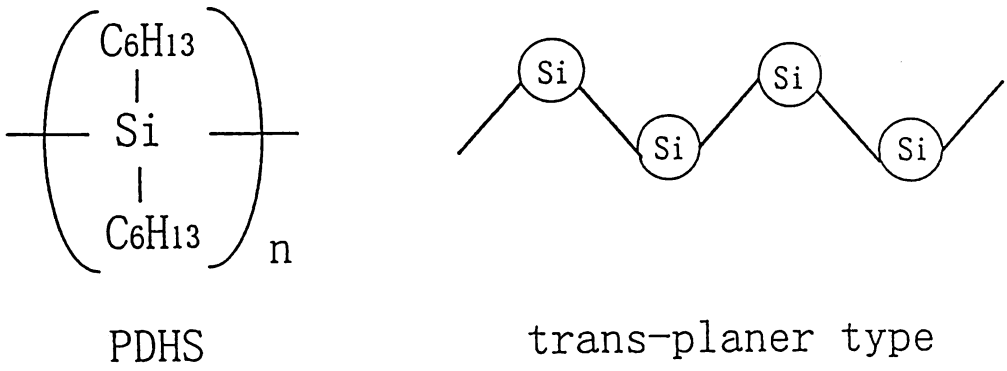

Fig.1 Chemical and schematical structures of PDHS

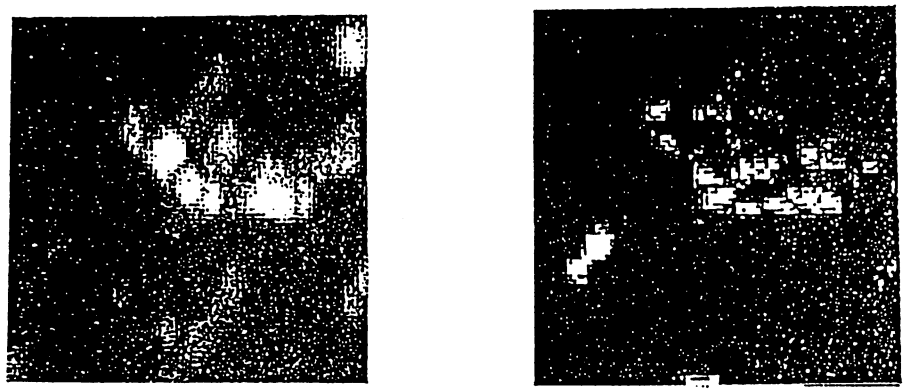

Fig.2 AFM (left-hand side) and near-field microscope (right-hand side) images of PDHS at room temperature (6μmx6μm).

I1

PHOTOCHEMICAL VAPOR DEPOSITION OF Zn BY OPTICAL NEAR-FIELD

Vitali Polonski, Yoh Yamamoto, and Motoichi Ohtsu
Department of Applied Electronics, Ohtsu laboratory
Tokyo Institute of Technology
4259 Nagatsuta-cho, Midori-ku
Yokohama 226-8502, Japan
Phone: +81-45-924-5476 fax: +81-45-924-5487
e-mail: vitali@ae.titech.ac.jp

KEY WORDS: Near-field optics, photochemical vapour deposition, patterned prenucleation

1. INTRODUCTION

We demonstrate for the first time the photochemical vapor deposition of metal by near-field optical technology (NFO-PCVD).Patterning of thin films has been traditionally performed by photolithography. Though several works of near-field optical lithography on the photo-resist films has been reported recently [1], it is unlikely to be employed by industry because conventional photo-lithography has been well established and matured. Apart from being complicated multistep method, it presents an etch-damaging threat to the substrate. On the other hand, nobody has ever succeeded in the subwavelength deposition of metals, oxides, and semiconductors even by using STM, e-beam, FIB, and MBE. However, this technique is required for photomask repair of DRAM, nano-photonic devices, and in-situ fabrication for the needs of microelectronics and for nanoscale electrochemical studies. These trends signify NFO–PCVD as a means of overcoming diffraction limitations and etch-damaging of the substrates. Expected reproducibility of NFO–PCVD for fabricating nanometric stripes and dots at desired positions is much higher than, e.g., the conventional self organized growth technique of semiconductor quantum dots. Moreover, by varying a light wavelength and appropriate parent gases selective growth can be accomplished.

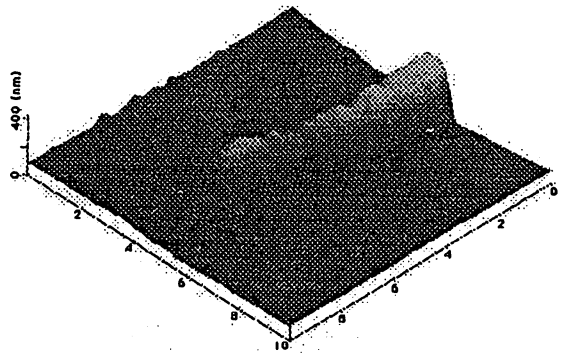

Fig.1 Zn deposit (1 μm width) obtained by prenucleation of DmZn by using an optical fiber instead of diffraction limited objective for UV light delivery

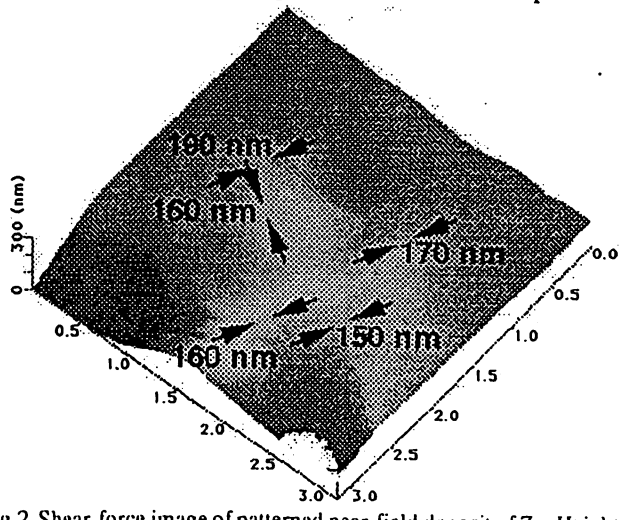

Fig.2 Shear-force image of patterned near-field deposit of Zn. Height of deposited lines corresponds to ~300 atomic layers. Cross sections with sub-200 nm half-width of few stripes are shown with arrows.

2. EXPERIMENTAL

The core of the experimental setup is an Illumination mode NOM placed inside the reaction chamber. 244 nm UV light from frequency doubled Ar-ion laser was coupled into the optical fiber in order to be used for patterned prenucleation stage. For near-field deposition we used aluminium coated tip with ~100 nm aperture. The fiber tip was fabricated by a 10 μm pure silica core multimode UV fiber [2]. Transmission loss at 244 nm for such fibers is 1.1 dB/m, which means the throughput of used tip is as high as 1 x 10^{-4}, and the power density is 1 kW/cm^2. Dimethylzinc (DmZn) was chosen as a parent gas. Earlier reports of the far-field prenucleated deposition of Zn [3] from this precursor and its well established characteristics [4] for UV light assisted deposition enabled us to expect similar behaviour of the film growth in the near-field using a UV fiber tip for light delivery. We used the same fiber tip to obtain shear-force image of deposited Zn patterns. Prior to the patterning stage the reaction chamber was evacuated to the pressure 10^{-4} Torr and filled with Ar buffered DmZn. After keeping 15 Torr pressure for 14 minutes the chamber was thoroughly reevacuated with turbomolecular pump. Such procedure produces a chemisorbed molecular layer with a thickness of few monolayers on the substrate. Patterning was performed in 10^{-4} Torr vacuum by shining the area beneath the aperture while keeping the tip in the near-field region and moving it across the substrate. As a result surface molecules of DmZn were decomposed selectively forming Zn nucleation centers. Fig.1 demonstrates 1 μm width deposit of Zn as a preliminary result of such approach. It was deposited on a corning glass (# 7059). Second stage of final deposition was performed using unfocused UV light (193 nm) of a pulsed excimer laser. After reaction chamber was refilled with 1 Torr of DmZn, the prenucleated area was irradiated from the optical far-field. Due to the presence of constant atom flux in the vicinity of the surface, the Zn around previously prenucleated centers is deposited and pattern is grown. Fig.2 shows shear-force image of successfully written pattern with sub 200-nm Zn stripes. We have chosen a carefully cleaned hydrophilic quartz coverslip with placed for 15 minutes and then washed off drops of poly-L-resine (1 mg/ml) as a substrate to mark up the area as well as to show the applicability of near-field deposition on the surfaces with complicated topography. Produced branch lines of the pattern can easily be seen on the image (threshold: 65 nm). Quantitative verification gave us an average height of the deposited Zn to be ~300 atomic layers, which corresponds well to the expected amount of atoms considering absorption cross section of DmZn at used wavelength and the total energy of laser pulses on the pattern area.

3. SUMMARY

As a result of NFO-PCVD experiments we achieved sub-200 nm width of deposited Zn lines. To the best of our knowledge our experiment is the first successful deposition of metal lines with subwavelength size. By a minor modification of the instrument, depositions of Al, W, etc. are expected. Described method seems to be a promising tool for a wide range of applications.

4. REFERENCES

[1] John A. Rogers, Kateri E.Paul, Rebecca J. Jackman, and George M. Whitesides, "Using an elastometric phase mask for sub-100 nm photolithography in the optical near field," *Appl. Phys. Lett.* **70** (20), 2658-2660 (1997)

[2] S.Mononobe, T.Saiki, T.Suzuki, S.Koshihara, M.Ohtsu, "Fabrication of triple tapered probe for near-field optical spectroscopy in UV region based on selective etching of a multistep index fiber," *Optics Communications* **146**, 45-48 (1998)

[3] D.J. Ehrlich, R.M. Osgood, Jr., and T.F. Deutsch, "Spatially delineated growth of metal films via photochemical prenucleation," *Appl. Phys. Lett.* **38** (11), 946-948 (1981)

[4] J. G. Eden, Photochemical vapor deposition, Chapter 4. John Wiley & sons, Inc., New York, 1992

NEAR FIELD OPTICS - 5, Technical Digest of the 5th International Conference
on Near Field Optics and Related Techniques, December 6-10, 1998

I6

THERMAL AND OPTICAL EFFECTS IN THE ANALYSIS OF SUBMICRON ALUMINUM AND TITANIUM-SILICIDE LINES BY NEAR-FIELD-OPTICAL-PROBE-INDUCED RESISTANCE-CHANGE

Kiyoshi Nikawa, Toshiharu Saiki*, Shoji Inoue** and Motoichi Ohtsu***

Device Analysis Technology Labs., NEC
1753 Shimonumabe, Nakahara-ku, Kawasaki, 211-8666 Japan
phone: +81-44-435-1682, fax: +81-44-435-1867, e-mail: nikawa@dret.cl.nec.co.jp
*,***Kanagawa Academy of Science and Technology (KAST), Kawasaki, Japan
**T.D.I., Co.,Ltd. (Technological Development of Information processing), Kawasaki, Japan
***Tokyo Institute of Technology, Yokohama, Japan

KEYWORDS: Near-field optical probe, resistance change, thermal effect, OBIRCH, optical effect, OBIC, submicron line, TiSi, Al, defect

1. INTRODUCTION

The identification of voids and other defects in the Al and silicide interconnects of integrated-circuit-device chips is a key part of failure analysis and process monitoring in the semiconductor industry. The optical-beam-induced resistance-change-detection (OBIRCH) method (first proposed by Nikawa et al. [1]) has been shown to be, in some respects, more useful in void detection than other conventional methods. The OBIRCH method uses two main simultaneous processes: laser-beam heating and resistance-change detection. We have modified the OBIRCH method to use a near-field optical probe [2] as the heat source instead of a laser beam. Testing of this NF-OBIRCH (Near-Field Optical proBe Induced Resistance CHange) method showed that it is superior not only to the conventional OBIRCH method but also to a conventional optical beam induced current (OBIC) method.

2. EXPERIMENTAL SETUP

To test our NF-OBIRCH method, we introduced an Ar laser (a mixture of 488 nm and 514.5 nm) into a near-field optical probe. The near-field optical probe we used were both apertured and metallized. The probe was scanned in the area of interest, using a shear force feedback technique. For amplifying the resistance change signals, we used a combination of a modulated-laser-beam and a lock-in amplifier. The voltage changes during scanning are introduced into an

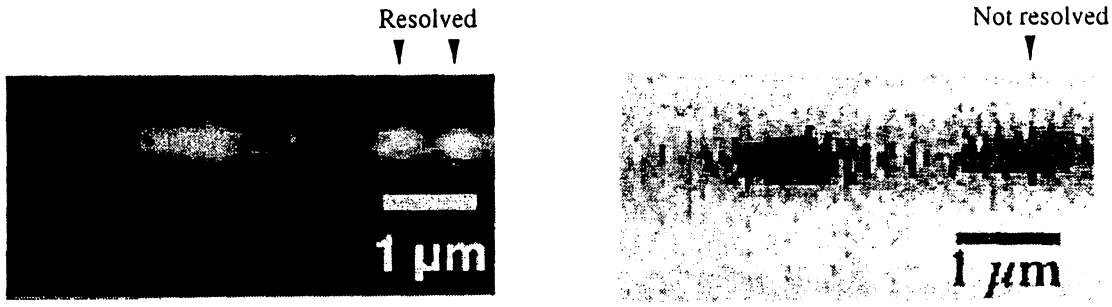

(a) NF-OBIRCH image: bright contrast is caused by OBIRCH effect

(b) Conventional OBIRCH image: dark contrast is caused by OBIRCH effect

Fig. 1. 0.3 μm wide Al line observation results

external input terminal of a typical scanning probe microscope system so as to produce an image of resistance changes.

The voltage change is simply described as:

$$\Delta V = I \Delta R \qquad (1)$$

where ΔV is a voltage change when a laser beam is irradiated, I is a current applied by a constant current source, and ΔR is a resistance change when a laser beam is irradiated. From the term of I, current paths can be observed , and from the term of ΔR, various defects can be observed .

3. OBSERVED RESULTS

Figure 1 shows the results of 0.3 μm wide Al line observations. Figure 1(a) shows the NF-OBIRCH image where the apex aperture size of the probe was 400 nm. Figure 1(b) shows the conventional OBIRCH image using 633 nm laser. The separation of a void are resolved in the NF-OBIRCH image (Fig. 1(a)) but not resolved in the conventional OBIRCH image (Fig. 1(b)).

0.2 μm wide TiSi line observation results showed: (1) The OBIRCH effect caused by heating can be observed using the metallized probe without interference from an OBIC effect. In the conventional OBIRCH method, the laser beam creates not only the OBIRCH effect, but also an OBIC effect that can mask the OBIRCH effect. (2) The OBIC can be observed using the apertured probe, in a higher spatial resolution than a conventional OBIC method.

4. REFERENCES

[1] K.Nikawa, C.Matsumoto and S.Inoue, "Novel method for void detection in Al stripes by means of laser beam heating and detection of changes in electrical resistance," *Jpn. J. A. P.*, **34**, Part1, no. 5, 2260-2265 (1995).

[2] T. Saiki, S. Mononobe, M. Ohtsu, N. Saito and J. Kusano, "Tailoring a high-transmission fiber probe for photon scanning tunneling microscope,"*Appl. Phys. Lett.*, **68**, 2612-2614 (1996).

I8

Characterization of *p-n* junction on Si substrate by multiwavelength near-field photocurrent measurement

Hiroaki FUKUDA[1,2], Yasushi KADOTA[2], and Motoichi OHTSU[1]

Interdisciplinary Graduate School of Science and Engineering
Tokyo Institute of Technology[1]
RICOH Co.LTD.,[2]
4259, Nagatsuda, Midoriku-ku, Yokohama, Kanagawa 213,Japan
phone : +(81)-45-590-1771 fax : +(81)-45-590-1894
e-mail : fukuda@rdc.ricoh.co.jp

KEY WORDS : Near-field optical microscope, near-filed photocurrent, *p-n* junction ,minority carrier, diffusion length , Si device , fiber probe

1. INTRODUCTION

Recently , near-field photocurrent measurement by using a near-field optical microscope (NOM) has been shown to be especially useful tool for the investigation of *p-n* junction on a semiconductor devices [1, 2] . In the present work , near-field photocurrent measurements with multiwavelength excitation sources are applied to the investigation of a *p-n* junction on Si substrate. We have measured the diffusion length of minority carriers by using the near-field photocurrent signals .

2. EXPERIMENTAL

A schematics of experimental set-up and sample structure is shown in Fig.1 . A fiber probe with 100nm tip diameter which has pure SiO_2 core is sharpened by using the selective chemical etching in buffered hydrofluoric acid [3] . To fabricate the aperture with sub-wavelength diameter (~100 nm) , the sharpened fiber probe is coated with Al (200 nm). As multiwavelength excitation light source , Ar^+ laser (λ = 351 , 458 , and 515 nm) are coupled into the fiber probe by using these lights, the penetration depth in Si substrate can be tuned from 10 nm to 250 nm . The photocurrent induced by the excitation light through the aperture is collected at electrode and amplified with current injection preamplifier. The signal is synchronously detected with a lock-in amplifier. In order to keep near-field excitation , the distance between fiber probe and sample is controlled by applying the shear-force technique. The surface of *p-n* junction is exposure by the etching of a passivation layer and a field oxide with reactive ion etching.

3. RESULTS

Fig. 2 shows cross-sectional profiles of the near-field photocurrent signals at the excitation wavelength (λ =351 , 458 , and 515nm) . The full width at the half of maximum of the cross sectional profile are 748 , 834 , and 1495 nm at λ =351 , 458 , and 515 nm, respectively . Since the penetration depth at λ =351 , 458 , and 515nm are 10 , 277 , and 685 nm respectively [4] , the increase of penetration depth results in the decrease of

Room B
Wednesday, December 9

the resolving power . At the ultraviolet wavelength excitation (λ =351 nm).the resolution is determined by aperture size and the diffusion length of minority carriers . The minority carrier diffusion length for electron *Ln* and hole *Lp* are estimated as 374 and 466 nm . This difference of the diffusion length between electron and hole can be observed through the slower rise of photocurrent in the *p* region than in the *n* region .

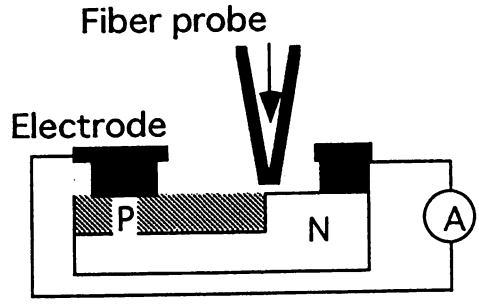

Fig.1 Schematic of experimental setup and sample structure.

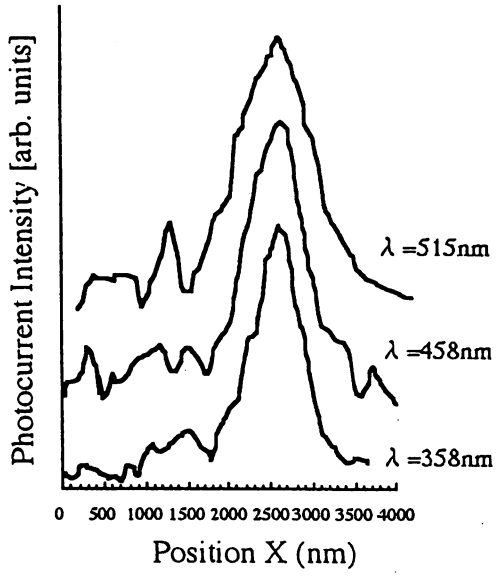

Fig. 2 Cross-sectional profiles of the near-field photocurrent signals at the excitation wavelength λ =351 , 458 , and 515nm .

4. SUMMARY

We demonstrate the near-field photocurrent measurements with multiwavelength excitation sources applied to the investigation of a *p-n* junction on Si substrate. By using 351 , 458 , and 515 nm wavelength light source , the penetration depth into Si substrate are varied from 10nm to 685 nm . The increase of penetration depth results in the decrease of the resolving power . The minority carrier diffusion length for electron *Ln* and hole *Lp* are estimated as 374 and 466 nm from the near-field photocurrent signals.

5. REFERENCE

[1] T.Saiki、N.Saito、J.Kusano、and M.Ohtsu : "Determination of slant angle of *p-n* interface by multiwavelength near-field photocurrent measurement" , *Appl. Phys. Lett.*, **69** (5), 644-646 (1996)

[2] K.Karrai、G.Kolb、G.Abstreiter、A.Schmeller: "Optical near-field current microscopy" , *Ultamicroscopy* , **61** , 299-304 (1995)

[3] T.PANGARIBUAN, K.Yamada , S.Jiang, H. Ohsawa , and M.Ohtsu : "Reproducible fabrication technique of nanometric tip diameter fiber probe for photon scanning tunneling microscope" , *Jpn. J. Appl. Phys.* , **31**, (9A) , L1302-367L1304 (1992)

[4] E. D. Palik : Handbook of Optical Constants of Solids , Academic Press , (1985)

I15

READ OUT CAPABILITY OF A PLANAR APERTURED PROBE FOR OPTICAL NEAR-FIELD MEMORY

T. Yatsui[1], M. Kourogi[1),2),3)], K. Tsutsui[1),3)], and M. Ohtsu[1),2),3)]
1) Tokyo Institute of Technology
4259 Nagatsuta, Midori-ku, Yokohama, Kanagawa 226-8502, Japan.
phone:+81-45-924-5476, fax: +81-045-924-5487
e-mail: yatsui@ae.titech.ac.jp
2) Kanagawa Academy of Science and Technology
3-2-1 Sakado, Takatsu-ku, Kawasaki, Kanagawa 213-0012, Japan.
3) National Institute for Advanced Interdisciplinary Research
1-1-4 Higashi, Tsukuba, Ibaragi 305-8562, Japan.

KEYWORDS: Near-field optical storage, optical near-field memory, planar apertured probe array, photolithography, anisotropical wet etching.

1. INTRODUCTION

For realization of high density and high speed near-field optical recording/read-out, we have proposed and demonstrated a novel silicon planar apertured probe array as a near-field optical head for optical memory.[1] In comparison with the conventional fiber probe, the planar probe array has durability because of its planar structure. Data transmission rate decreases in proportion to the number of array. Furthermore, since it can be used for reading data as a surface information, it allows us to overcome difficulty of precise mechanical tracking.

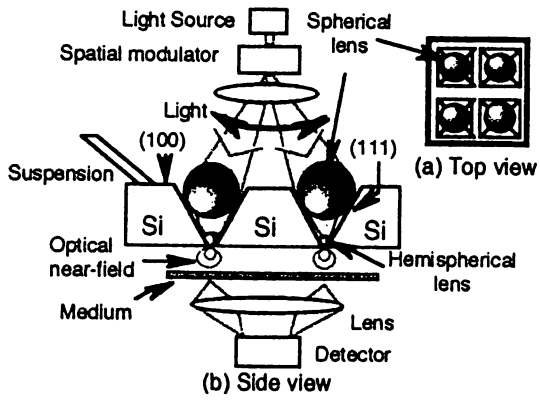

Fig. 1. Schematic explanation of the data storage system with planer probe array.

2. DEMONSTRATION OF A PLANAR APERTURED PROBE

The probe array was fabricated by utilizing photolithography and anisotropical etching of a silicon wafer. Inverted pyramids were formed on the silicon plate, and apertures were fabricated at the tops of the inverted pyramids. An aperture with a size less than 100 nm was realized. We observed the near-field image of a sample with the one of the apertures of the probe array. The probe array was glued to a suspension. Thin lubricant (FOMBLIN) film was coated on the sample. The line and space of aluminum film (width = 100 nm, space = 1 μm, thickness = 100 nm) on the glass plate was used as a sample. A laser beam (λ = 512 nm) was focused on one of the groove on the probe array whose aperture size of the probe was less than 100 nm. Then the transmitted light through the probe array and the sample was detected with a photo detector. Figure 2 shows the cross-sectional distribution of the transmitted light intensity. Dashed and solid lines are represent the result obtained without and with probe, respectively. One can find that the full width at half maximum of curve is 250 nm, which is more than twice that of the line width (= 100 nm). Major reason is light transmission through Si, because of no metal coating over the Si probe. That is the light might be transmitted into the Si and then the aperture size for the light become wider than the aperture size.

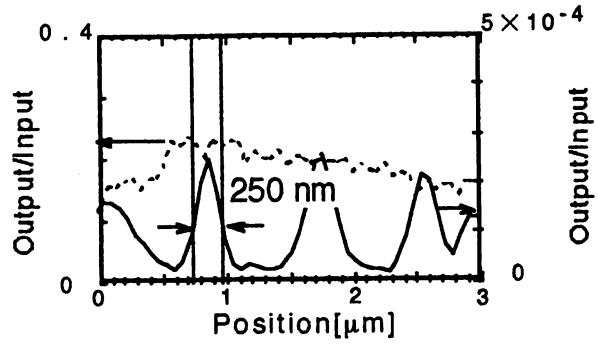

Fig. 2 The cross-sectional distribution of the transmitted light. Dashed line and solid line is for without and with probe, respectively.

2. ACKNOWLEDGMENT

The authors would like to express their thanks to Dr. M. B. Lee of National Institute for Advanced Interdisciplinary Research, Prof. H. Ishiwara and Prof. E. Tokumitsu of Tokyo Institute of Technology for their supports and useful suggestions in the fabrication process.

3. REFERENCE

[1] M. B. Lee *et al.* CLEO Pacific Rim '97 WL2

Nano/Atom Fabrication and Manipulation by Near-Field Optics

M. OHTSU[1,2,3]
(1) Tokyo Institute of Technology, 4259 Nagatsuta, Midori-ku, Yokohama, Kanagawa 226-8502 (e-mail: ohtsu@ae.titech.ac.jp)
(2) Kanagawa Academy of Science and Technology
(3) Ohtsu Localized Photon Project, ERATO, JST

We review recent progress of our works on near field optics. Main results are[1,2]:

1. Probe fabrication: (a) High throughput fiber probe with a triple tapered structure: Throughput as high as 10^{2} @ aperture diameter≦50 nm. (b) UV fiber probe:Throughput as high as 10^{-4} and transmission loss as low as 1dB/m. (c) Metal coated sharpened fiber probe with surface plasmon effect. (d) Apertured and protruded fiber probe with a metallized tip on its apex. (e) Planar apertured array on a Silicon substrate. (f) Functional probe for Na^{+}-selective optodes based on a tailed neutral ionophore.
2. Imaging experiments: (a) Imaging DNA single strand with 4 nm width (@ 2 nm x 2 nm pixel size) by optical feedback, without using shear-force technique.
3. Photoluminescence and raman spectroscopy:
(a) Photoluminescence and pump-probe spectroscopy of an InGaAs single quantum dot by illumination-collection mode at 5K. (b) UV photoluminescence spectroscopy of polysilanes quantum wires. (c) Raman spectroscopy of Polydiacetylene, Si, and β-carotene.
4. Industrial application: (a) Near field optical chemical vapor depositon of Zn: sub-micron sized dots and stripes by UV-optical near field(cf.1.(b)). (b) Diagnostics of Al stripes in an integrated circuits. (c) Optical storage and read-out by planar apertured sliding head (cf. 1.(e)) on a phase-change medium.
5. Atom manipulatoin: (a) Atomic funnel for preparing cold atoms to be coupled into a hollow optical fiber. (b) Depositon of atoms guided through a hollow optical fiber. (c) Design of a fiber probe for a single atom trapping.

Among these results, I focus on presenting 4(a) and 5 at the session for future nano/atom photonic functional devices and integrated circuits.

References

1. M. Ohtsu, *Near-Field Nano/Atom Optics and Technology*, Springer-Verlag, Tokyo, Berlin, Heidelberg, 1998
2. M. Ohtsu and H. Hori, *Near-Field Nano Optics*, Plenum, New York, 1998, in press.

Th-O-02
(Invited)

A Nearfield planar apertured probe array for optical near field memory

Motonobu Kourogi [1),2),3)], Takashi Yatsui [1)], Shigeru Ishimura[1)],
M. B. Lee [3)], N.Atoda [3)], Kazumasa Tsutsui[1)] and Motoichi Ohtsu[1),2),3)].

1)Tokyo Institute of Technology4259 Nagatsuta, Midori-ku, Yokohama, Kanagawa 226-8502,Japan.
phone:+81-45-924-5476, fax: +81-045-924-5487 e-mail : kourogi@ae.titech.ac.jp
2)Kanagawa Academy of Science and Technology 3-2-1 Sakado, Takatsu-ku, Kawasaki,
Kanagawa 213-0012,Japan.
3)National Institute for Advanced Interdisciplinary Research1-1-4Higashi, Tsukuba, Ibaraki305-8562, Japan.

For realization of high density and high speed near-field optical recording/read-out,we have proposed and demonstrated a novel silicon planar apertured probe array as a near-field optical head. [1] The planar apertured probe array is more durable than a conventional fiber probe. Furthermore it allows us to overcome difficulty of precise mechanical tracking of the single fiber probe because it can be used for reading data as a surface information.

A probe array was fabricated by utilizing photolithography and anisotropical etching of a silicon wafer. Inverted pyramids were formed on the silicon plate, and apertures were fabricated at the tops of the inverted pyramids. An aperture with a size less than 100 nm was realized. We observed the near-field image of a sample with the one of the apertures of the probe array. The probe array was glued to a suspension. Thin lubricant (FOMBLIN) film was coated on the sample. The line and space of aluminum film (width = 100 nm, space = 1 μm, thickness = 100 nm) on the glass plate was used as a sample. A laser beam (λ = 512 nm) was focused on one of the groove on the probe array whose aperture size of the probe was less than 100 nm. Then the transmitted light through the probe array and the sample was detected with a photo detector. Figure 2 shows the cross-sectional distribution of the transmitted light intensity. Dashed and solid lines are represent the result obtained without and with probe, respectively. One can find that the full width at half maximum of curve is 250 nm, which is more than twice that of the line width (= 100 nm).

A reference

[1] M. B. Lee *et al.* CLEO Pacific Rim '97 WL2

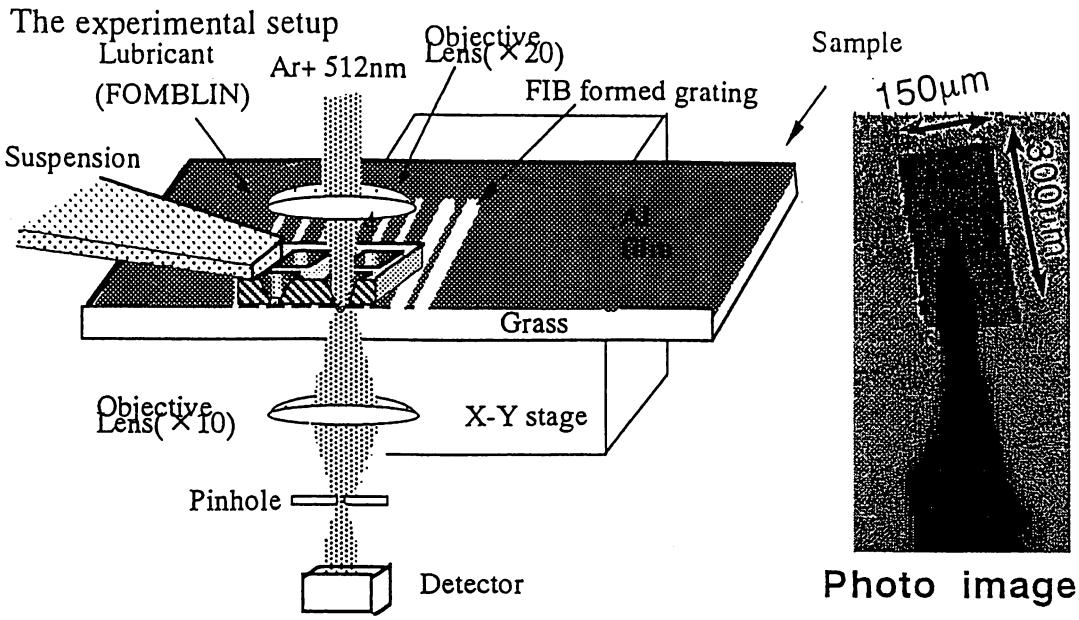

Fig. 1.Experimental setup.

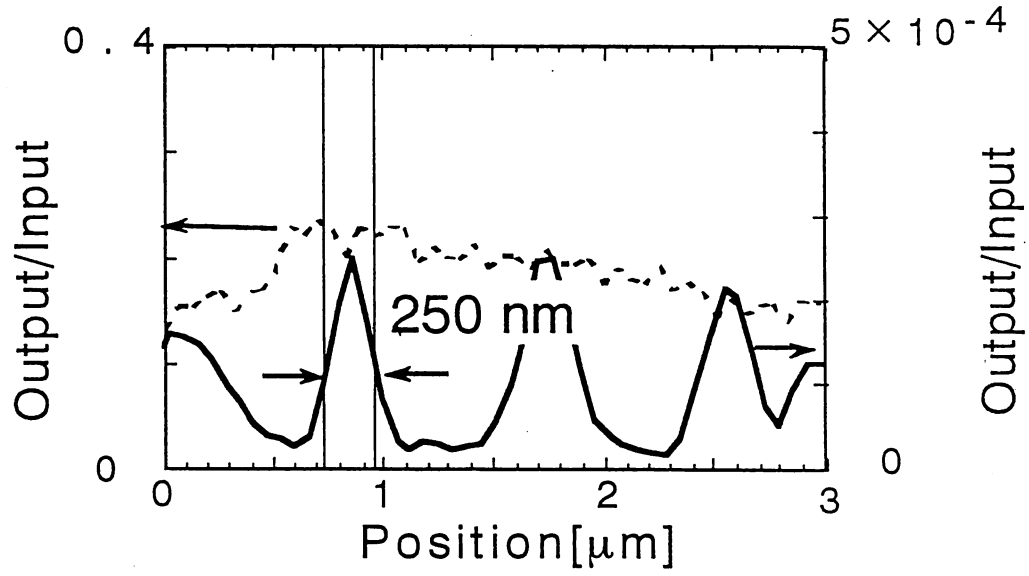

Fig. 2 The cross-sectional distribution of the transmitted light. Dashed line and solid line is for without and with probe, respectively.

Enhancing throughput over 100 times by a triple-tapered structure for near-field optical fiber probe

T. Yatsui [a], M. Kourogi [a,b], K. Tsutsui [a], and M. Ohtsu [a,b]

[a]Interdisciplinary Graduate School of Science and Engineering, Tokyo Institute of Technology,
4259 Nagatsuta, Midori-ku, Yokohama 226-8502, Japan.
[b]Kanagawa Academy of Science and Technology,
3-2-1 Sakado, Takatsu-ku, Kawasaki 213-0012, Japan.

ABSTRACT

We have successfully fabricated an extremely high throughput probe for near-field optics introducing a triple-tapered structure to reduce the loss in a tapered core, to focus the light, and to excite effectively the HE_{11} mode. A focused ion beam and selective chemical etching were used for fabrication. Over 100 times increase in the throughput of the triple-tapered probe with the aperture diameter D < 100 nm was realized in comparison with the conventional single-tapered probe. Furthermore, due to the third taper with a small cone angle, the localized optical near-field on the triple-tapered apertured probe with D = 60 nm has been confirmed.

Keywords: near-field, throughput, chemical etching, focused ion beam

1. INTRODUCTION

For studying optical properties of various surfaces in a nanometer scale, a near-field optical microscope has made a remarkable contribution to subwavelength-resolution imaging and spectroscopy by scanning a metallic fiber probe with a subwavelength aperture.[1,2] However, the most serious problem of using the metallic fiber probe is its low throughput, which rapidly decreases by decreasing the aperture diameter (D).[3,4] It is less than 1×10^{-5} with D < 100 nm in the conventional single-tapered probe.[5] Furthermore, since the input power is limited by thermal damage of probe tip,[6] signal-to-noise ratio is extremely low.

The conventional single-tapered probe with a protruded apex (Fig. 1(a)) have been fabricated by selective chemical etching,[7] followed by selective resin coating (SRC).[8] However, since this sharpened probe has a long (> 5 μm) loss region in the metallic tapered core,[9] the probe with an aperture at the flat end of the fiber (Fig. 1(b)) is expected to be optimum with regard to the lowest propagation loss.[10] However, since the aperture diameter D is much smaller than beam spot size that is nearly equal to the core

Part of the SPIE Conference on Far- and Near-Field Optics: Physics and Information Processing
San Diego, California • July 1998
SPIE Vol. 3467 • 0277-786X/98/$10.00

diameter (3 μm), the coupling efficiency from the guided mode in the optical fiber to the mode in the aperture might be extremely low. Recently, Saiki *et al.* have reported that the sharpened probe with large cone angle functions as a convex lens,[11] implying that the throughput might be increased if the aperture is fabricated at the focal point of this lens. Based on this consideration, we propose "a steeple-on-mesa" probe as shown in Fig. 1(c), where D_m is the mesa diameter. The mesa works as a convex lens, where the focal point is at the center of the plateau of the mesa. The propagation loss can be decreased by a short tip length. Furthermore, highly resolved images can be obtained by the steeple with a small cone angle on the mesa which is protruded from the metallic aperture. Figure. 1(d) shows the shape of the fabricated apertured probe with a triple-tapered core, which will be described later.

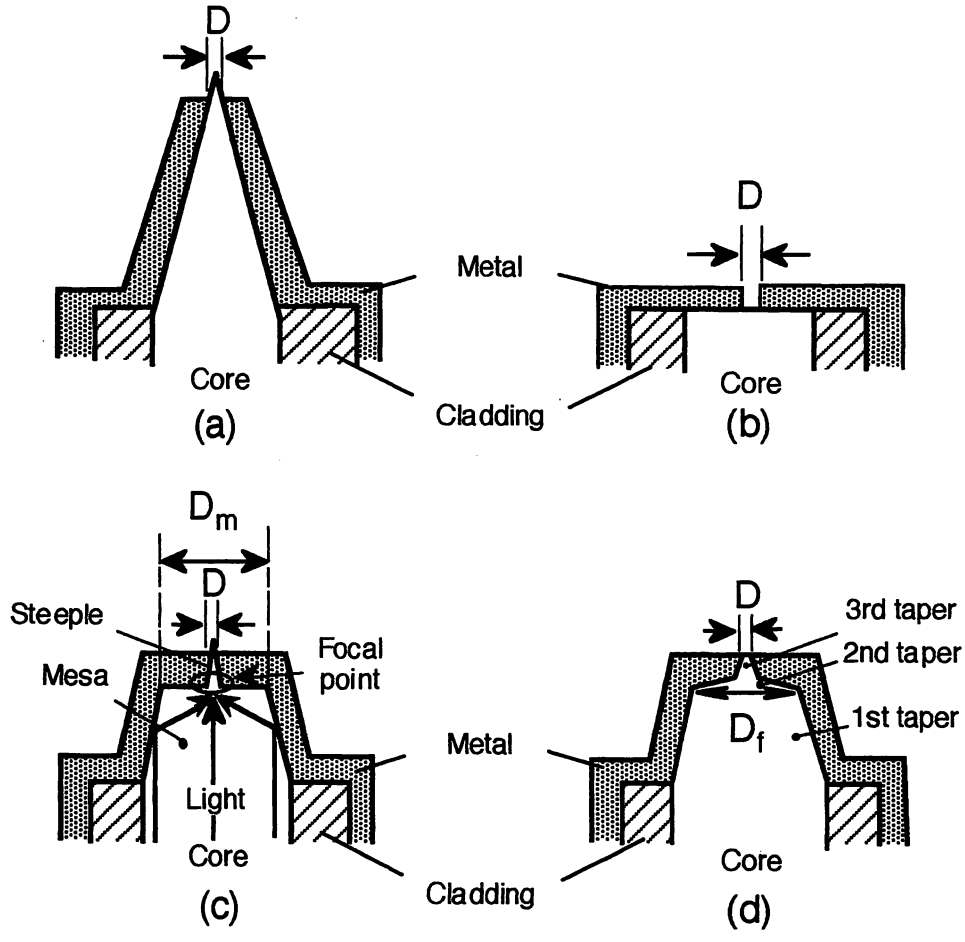

Figure. 1: A schematic of a metal-coated fiber probe. D : aperture diameter. (a) Conventional single-tapered probe, (b) probe with a small aperture at the flat end of the fiber, (c) proposed steeple-on-mesa probe. D_m : the mesa diameter, (d) fabricated triple-tapered apertured probe. D_f : foot diameter of the second taper.

Here, we determined the tip parameters which are required to focus light at the plateau of the mesa. By preparing single-tapered apertured probes with different D, the spatial distribution of the optical near-field intensity on the aperture was observed. On the basis of these results, we optimized the shape of the probe tip. To confirm the high resolution capability of the probe, the spatial distribution of the optical near-field intensity on the aperture was observed by scanning another sharpened probe over the aperture to scatter and detect the optical near-field.

2. EXPERIMENT

Figure 2 shows an experimental setup ,i.e. probe-to-probe method, to measure the spatial distribution of the optical near-field intensity on the apertured probe. Linearly polarized light from a laser diode (λ = 830 nm) was coupled into the single-mode fiber. The direction of incident light polarization was changed by a half wave plate to examine the dependence of the image on the direction of incident light polarization. The optical near-field generated on the apertured probe (probe A) was observed by scanning another probe (probe B) and detecting the scattered light with a photo-multiplier, while the separation between the two probes was maintained within several nanometers with shear-force technique.

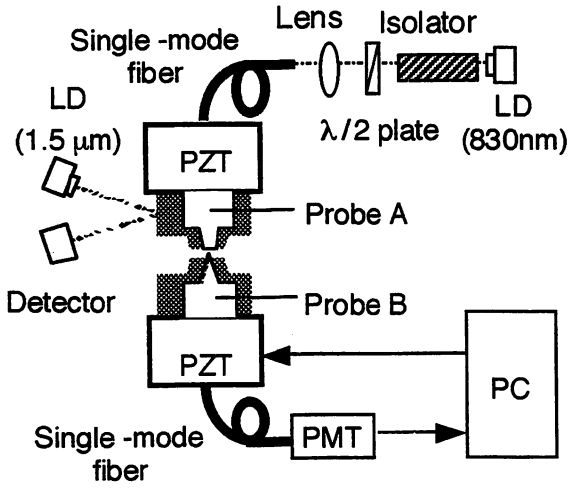

Figure. 2 : Experimental setup. Probe A: apertured probe, Probe B: scanning probe for scattering the optical near-field on the Probe A.

First, we checked whether light is focused in the single-tapered apertured probe. We used an apertured probe with D = 100 nm as probe B. The single-tapered apertured probe was fabricated by following three steps:

(i) The GeO_2 doped core of the fiber was tapered by selective chemical etching, where the core diameter and cone angle were 3 μm and 20°, respectively.[7]

(ii) The core was coated with 500-nm-thick gold film.

(iii) The top of the core was removed to form an aperture with focused ion beam (FIB).

Figures 3(a), (b), (c), and (d) show the observed spatial distribution of the optical near-field intensity on the aperture for D = 2 μm, D = 1.4 μm, D = 1 μm, and D = 550 nm, respectively. In Fig. 3(e), curves A, B, C, and D show the cross-sectional distribution along the white dashed line in Figs. 3(a), (b), (c), and (d), respectively. One can find in Fig. 3(e) that the spatial distribution of the optical near-field on the aperture is not monotonously narrowed by decreasing D and that the optical near-field intensity at the center of the core takes the maximum at D = 1 μm. It implies that there is a focal point in the metallic tapered core. Note that full width at half maximum (FWHM) of the central part of the curve C was as small as 150 nm, which is less than λ/5.

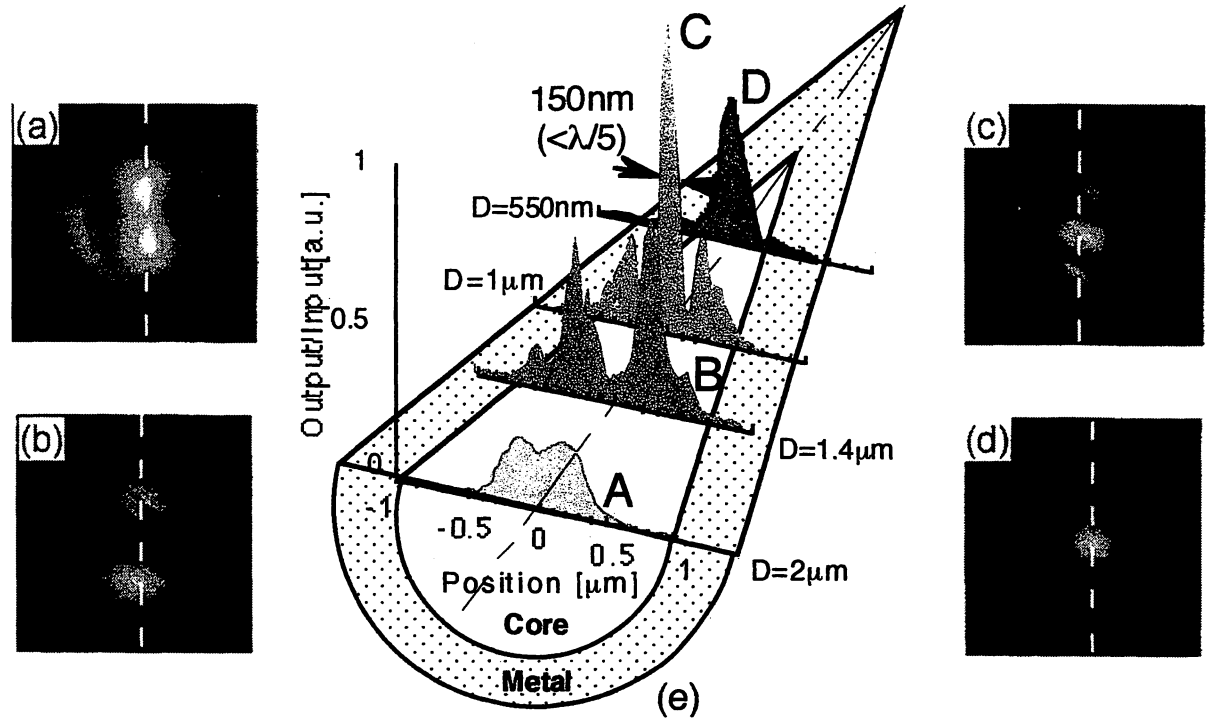

Figure. 3 : Spatial distribution of the optical near-field intensity on the conventional single-taped probe at λ = 830 nm. (a), (b), (c), (d) are for the single-tapered probe with D = 2 μm, 1.4 μm, 1 μm, and 550 nm, respectively. The image size is 1.5×1.5 μm^2. Curves A, B, C, and D in (e) are the cross-sectional profile along the white dashed line in (a), (b), (c), and (d), respectively.

Now let us compare the observed spatial distribution with the theoretical calculation based on following assumptions;

(i) The cladding is an ideal metal.

(ii) Spatial distribution on the aperture is summation of several modes with same symmetry in the core surrounded by an infinitely thick metal cladding so as that sidelobe the intensity is 30 %.

Figure 4 shows the spatial distribution on the apertured probe with D = 1 μm, where FWHM of calculated result is ~ 180 nm with 30 % sidelobe intensity, which is comparable to that of the curve C in Fig. 3(e).

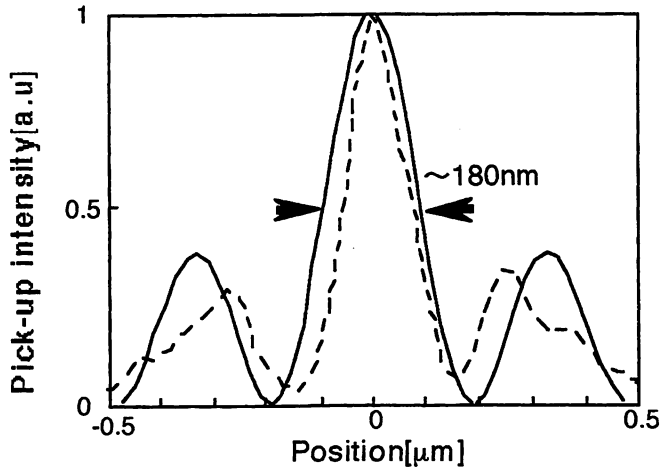

Figure. 4 : Spatial distribution on the apertured probe with D = 1 μm at λ = 830 nm. Solid curve ; calculated, dashed curve ; observed (curve C in Fig. 3(e)).

Second, we fabricated the steeple-on-mesa probe by the following five steps. However, due to several technical restrictions, fabricated probe had a triple-tapered core with an aperture, as is schematically explained by Fig. 1(d);

(i) The GeO_2 doped core of the fiber was tapered by selective chemical etching, where the cone angle was 20°.[7]

(ii) Irradiating the FIB over the sharpened core to reduce the core diameter, where the core diameter was reduced to 40 nm. (Fig. 5(a))

(iii) The first and second tapers of the core was formed by chemical etching. The foot diameter of second taper D_f is 1.6 μm. (Fig. 5(b.1)) The length and apex diameter of the third tapers are 350 nm, and 25 nm, respectively. (Fig. 5(b.2)) The cone angles of the second and third tapers are 30° and 150°, respectively.

(iv) The core was coated with 300-nm-thick gold film.

(v) The top of the third taper was removed by FIB to form an aperture.

In this work, the small apex of the third taper was removed for forming a flattened-aperture surface to observe spatial distribution of the optical near-field intensity on the aperture. However, protruded structure can be fabricated by the process developed here if the SRC method is employed.[8] Figures 5(c.1) and (c.2) show scanning electron microscopic images of a fabricated triple-tapered apertured probe with D = 60 nm. Since the third taper has a small cone angle, highly resolved images can be obtained

if it is used for a near-field optical microscope. Furthermore, since the length of the third taper (350 nm) is much shorter than the length of the single-tapered probe (5 μm), the decrease in the propagation loss is expected.

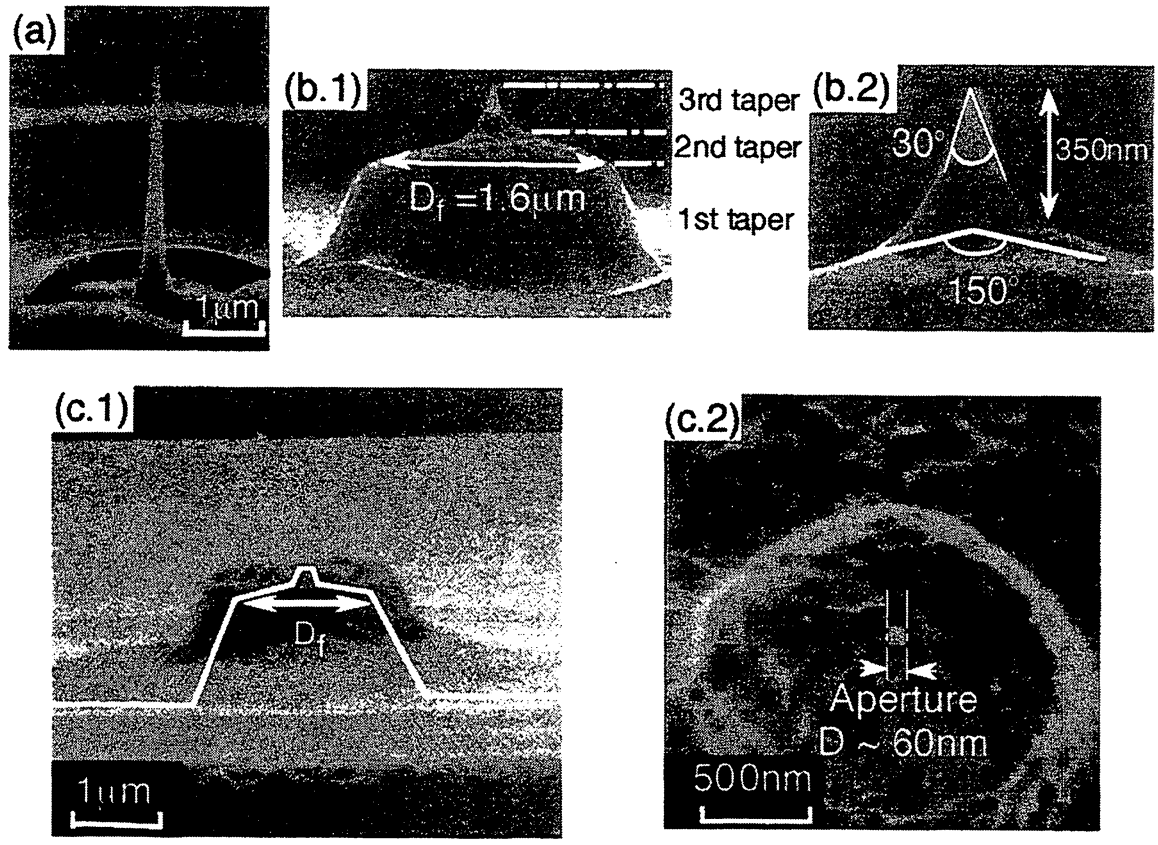

Figure. 5: SEM images of a triple-tapered probe. (a) Results of step (ii). (b.1), (b.2) The triple-tapered probe formed by step (iii) and a magnified image of the third taper. (c.1), (c.2) Side and top views of the probe by the steps (iv) and (v). D_f: the foot diameter of second taper.

Third, since the shape of the fabricated triple-tapered apertured probe differs from that of the proposed steeple-on-mesa probe due to the presence of the second taper, we compared the throughput of two triple-tapered apertured probes with D_f = 1.2 μm and 1.6 μm, single-tapered apertured probe with cone angle of 20°, and edged apertured probe[12] in order to optimize the shape. For estimating of the throughput, light from laser diode (λ = 830 nm) was coupled into the fiber, and the output light power ejected from the aperture was measured with a broad area optical power meter placed in the proximity of the aperture. The throughput is defined as the ratio of the measured output power to the input power coupled into the fiber.

In Fig. 6, the throughput is plotted as a function of the aperture diameter D for the triple-tapered apertured probe with D_f =1.2 μm (open circles) and D_f = 1.6 μm (closed circles), the single-tapered apertured probe (open squares), and the edged apertured probe (closed triangles). This figure shows that the triple-tapered apertured probes with D_f = 1.2 μm and that with D_f = 1.6 μm have the throughput 10 and 100 times higher than that of the single-tapered apertured probe for D < 100 nm, respectively. Since this figure also shows that the throughput of single-tapered apertured probe with D = 1.2 μm is as high as that with D= 1.6 μm, the large difference of the throughput between the two triple-tapered apertured probes implies that focused light at the foot of the third taper increases the throughput for the triple-tapered apertured probe with D_f = 1.6 μm. The difference between the optimum mesa diameter D_m (Fig. 1(c)) and a optimum foot diameter D_f (Fig. 1(d)) is due to the presence of the second taper, which suggests that further increase in the throughput can be expected by improving the shape of fabricated probe.

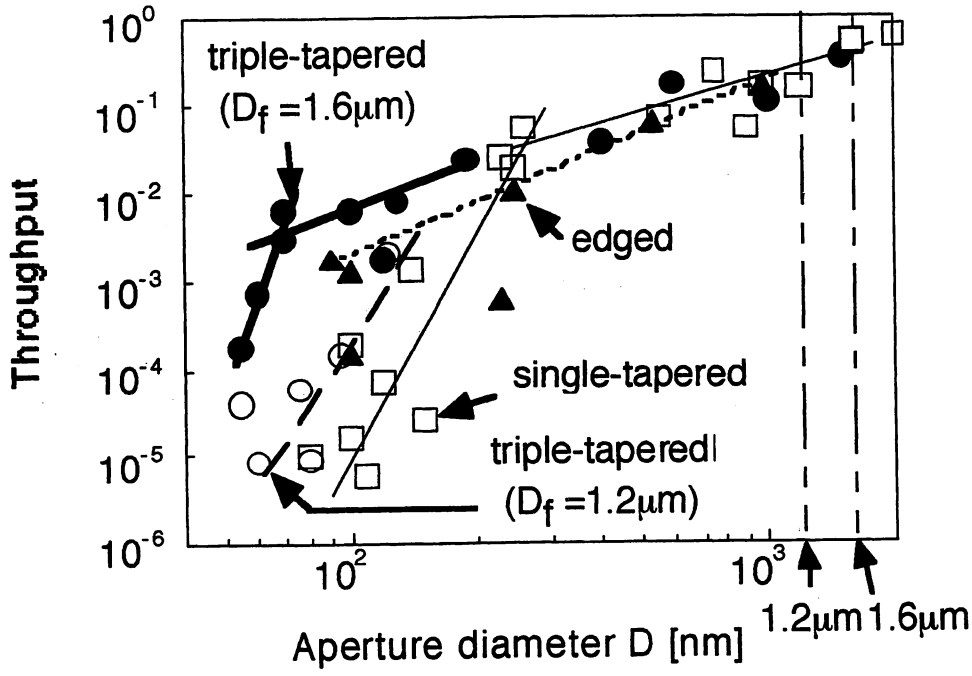

Figure. 6 : Throughput as a function of the aperture diameter: the triple-tapered probe with D_f =1.2 μm (open circles) and D_f = 1.6 μm (closed circles), conventional single-tapered probe (open squares), and the edged probe (closed triangles).

Drastic increase in the throughput of the triple-tapered probe can be also attributed to effective excitation of an HE_{11} mode. Since the dependence of the throughput on D for one of the triple-tapered apertured probe (D_f = 1.6 μm) is similar to that of the edged apertured probe in the region of 50 nm < D < 200 nm (see Fig. 6), the HE_{11} mode should be excited in the triple-tapered probe. The efficient excitation of the HE_{11} mode can be attributed to the scattering coupling at the foot of the third taper.[13]

Rapid decrease in throughput of the triple-tapered apertured probe with D < 60 nm in Fig. 6, where D is nearly equal to the cutoff diameter of the HE_{11} mode (30 nm), can be attributed to the extremely high propagation loss of the HE_{11} mode.[9]

Fourth, we checked whether the light is focused in the triple-tapered probe. We observed spatial distribution of optical near-field intensity on the aperture in the second taper of the triple-tapered probe with D_f = 1.6 μm. We used the apertured probe with D = 100 nm as probe B. Figures 7(a), (b), and (c) show the observed spatial distribution of the optical near-field intensity on the aperture for D = 1.5 μm, D = 1 μm, and D = 400 nm, respectively. In Fig.7(d), curves A, B, and C show the cross-sectional distribution along the white dashed line in Figs. 7(a), (b), and (c), respectively. One can find in this figure that the spatial distribution of the optical near-field intensity on the aperture is monotonously narrowed by decreasing D and that the optical near-field intensity at the center of the core takes the maximum at D = 400 nm, which suggests that there is a focal point at the foot of the third taper. These results indicate that the focusing light increases the throughput of the triple-tapered probe with D_f = 1.6 μm.

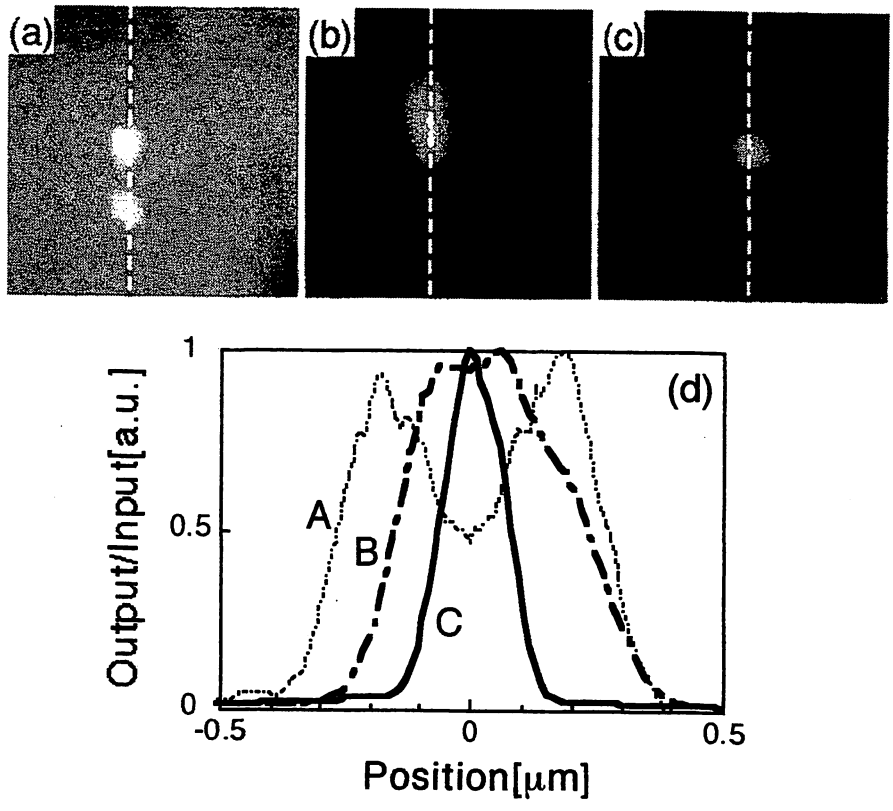

Figure. 7 : Spatial distribution of the optical near-field intensity on the aperture in the second taper of triple-tapered probe with D_f = 1.6 μm at λ = 830 nm. (a), (b), (c) are for D = 1.5 μm, 1 μm, and 400 nm, respectively. The image size is 1.5×1.5 μm². Curves A (dashed line), B (dashed-and-dot line), and C (solid line) in (d) are the cross-sectional profile along the white dashed line in (a), (b), and (c), respectively.

Finally, we checked whether the triple-tapered structure led high spatial resolution. For this purpose we observed the spatial distribution on the aperture of the triple-tapered probe with D_f = 1.6 μm and D = 60 nm. To enhance the efficiency of light scattering, we used a sharpened probe with 50-nm-thick gold as probe B.[12,14] Figure 8(a) shows the observed spatial distribution of the optical near-field intensity on the aperture. The cross-sectional distribution along the white dashed line in Fig. 8(a) is shown in Fig. 8(b). The FWHM of the spatial distribution is 160 nm which is considered to be due to the leakage of propagating far-field because of the thin coating of the metallic sharpened probe used for measurement. However, one can also find that a very sharp and narrow (80 nm) peak at the center of the curve, which is attributed to localization of the optical near-field due to the third taper with small cone angle.

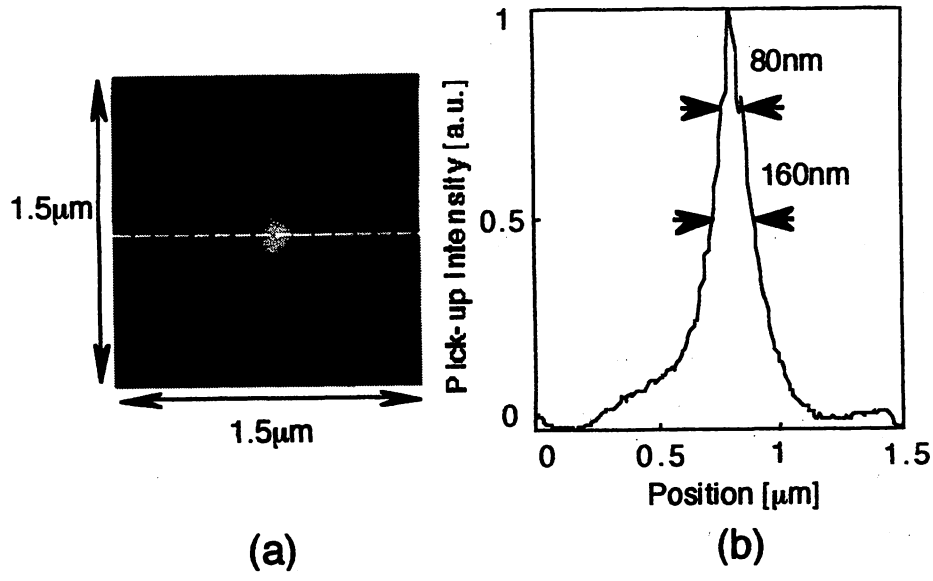

Figure. 8 : Spatial distribution of the near-field optical intensity on the triple-tapered apertured probe with D_f = 1.6 μm and D = 60 nm at λ = 830 nm. (a) Two-dimensional profile of the distribution. The image size is 1.5×1.5 μm². (b) Cross-sectional profile along the white dashed line in (a).

3. SUMMARY

We have proposed a steeple-on-mesa probe having high throughput and high resolution, and also estimated the optimum shape of the probe to focus the light at the plateau of the mesa. Further, we fabricated a triple-tapered apertured probe to demonstrate our proposal and have realized over 100 times increase of the throughput with D < 100 nm in comparison with the conventional single-tapered probe. This increase can be attributed to focusing light, the reduction of the propagation loss, and effective excitation of an HE_{11} mode. Further, the localized optical near-field on the apertured triple-tapered probe with D = 60 nm was

observed which is due to the third taper with small cone angle. It can be expected that such a high throughput triple-tapered probe is advantageously used for highly sensitive photo-emission spectroscopy, the ultra high speed and high density optical recording/readout, and so on.

4. ACKNOWLEDGMENT

The authors would like to express their thanks to Mr. K. Yoshida of Tokyo Institute of Technology with his valuable discussions.

5. REFERENCES

[1] *Near Field Optics*, edited by D. W. Pohl and D. Courjon (Kluwer, Dordrecht, 1993)

[2] M. Ohtsu, J. Light. Tech. **13**, 1200 (1995)

[3] U. Dürig, D. W. Pohl, and F. Rohner, J. Appl. Phys. 59, 3318 (1986)

[4] L. Novotony, D. W. Pohl, and B. Hecht, Opt. Lett. 20, 970 (1995)

[5] G. A. Valaskovic, M. Holton, and G.H. Morrison, Appl. Opt. 34, 1215 (1995)

[6] M. Stahelin, M. A. Bopp, G. Tarrach, A. J. Meixner, and I. Z. Granacher, Appl. Phys. Lett. 68, 2603 (1996).

[7] T. Pangaribun, K. Yamada, S. Jiang, H. Ohsawa, and M. Ohtsu, Jpn. J. Appl. Phys. 31, L1302 (1992)

[8] S. Mononobe, M. Naya, T. Saiki, and M. Ohtsu, Appl. Opt. 36, 1496 (1997)

[9] L. Novotony and C. Hafner, Phys. Rev. E50, 4094 (1994)

[10] T. Saiki, S. Mononobe, M. Ohtsu, N. Saito, and J. Kusano, Appl. Phys. Lett. 68, 2612 (1996)

[11] T. Saiki, K. Nishi, and M. Ohtsu, Jpn. J. Appl. Phys. 37, 1638 (1998)

[12] T. Yatsui, M. Kourogi, and M. Ohtsu, Appl. Phys. Lett. 71, 1756 (1997)

[13] A. Sommerfeld, *Optics*, (Academic Press, New York, 1954) Chap. 10

[14] Y. Inoue and S. Kawata, Opt. Lett. 19, 159 (1994)

Further author information -
T.Y.(correspondence): Email: yatsui@ae.titech.ac.jp; Telephone: +81-45-924-5476; Fax: +81-45-924-5487
M.K. : Email: kourogi@ae.titech.ac.jp
K.T. : Email: ktsutsui@ae.titech.ac.jp
M.O. : Email: ohtsu@ae.titech.ac.jp

A Near-field planar apertured probe array for optical near-field memory

M. Kourogi [1),2),3)], T. Yatsui [1)],S. Ishimura[1)], M. B. Lee [3)],N.Atoda [3)],K. Tsutsui[1)] and M. Ohtsu[1),2),3)]

1)Tokyo Institute of Technology, 4259 Nagatsuta, Midori-ku, Yokohama, 226,Japan.

2)Kanagawa Academy of Science and Technology, 3-2-1 Sakado, Takatsu-ku,213,Japan.

3)National Institute for Advanced Interdisciplinary Research, 1-1-4 Higashi, Tsukuba, 305, Japan.

ABSTRACT

We proposed and demonstrated a novel silicon planar apertured probe array as a near-field optical head for optical memory. In comparison with the conventional fiber probe, the apertured probe array has durability, higher read-out data transmission rate and it allows us to overcome difficulty of precise mechanical tracking of the single fiber probe because it can be used for reading data as a surface information. The probe array was fabricated by utilizing wet etching technique of a silicon wafer. Inverted pyramids were formed on the silicon plate, and apertures were fabricated at the tops of the inverted pyramids. An aperture with a size less than 100nm was realized. By scanning the probe array we obtained resolved images of the lines in corrugation which was made on a metal thin film. The observed line width was 250nm. Furthermore, we put spherical lens inside the inverted pyramids to focus the propagating light at the apertures automatically. The near-field intensity at an aperture was 16 times larger than that without a spherical lens.

Keywords: Near-field optical storage, Near-field optical memory, fiber probe, planar apertured probe array, photolithography, anisotropic wet etching, spherical lens.

1. INTRODUCTION

In conventional optical storage system, the data density is governed by the spot size of the focused laser beam, which is limited by the diffraction of light. For higher density, use of a shorter wavelength light source, e.g., a blue-violet semiconductor laser, and a solid immersion lens[1] have been proposed. On the other hand, near-field optics attracts great attention as a ultrahigh density optical recording method since the spot size inherently does not depend on the diffraction limit of light. Preliminary demonstrations of the near-field optical recording have been carried out on various medium surfaces such as magneto-optic[2],

Further author infomation -
M.K.: Email:kourogi@ae.titech.ac.jp; Telephone: +81-45-924-5476; Fax: +81-45-924-5487
T.Y.: Email:yatsui@ae.titech.ac.jp; Telephone: +81-45-924-5476; Fax: +81-45-924-5487
M.B.L.: Email:mblee@wwpost.nair.go.jp; Telephone: +81-298-54-2912; Fax: +81-298-54-2919
N.A.: Email:atoda@wwpost.nair.go.jp; Telephone: +81-298-54-2912; Fax: +81-298-54-2919
K.T.: Email:tsutsui@ae.titech.ac.jp; Telephone: +81-45-924-5476; Fax: +81-45-924-5487
M.O.: Email:ohtsu@ae.titech.ac.jp; Telephone: +81-45-924-5476; Fax: +81-45-924-5487

Part of the SPIE Conference on Far- and Near-Field Optics: Physics and Information Processing
San Diego, California • July 1998
SPIE Vol. 3467 • 0277-786X/98/$10.00

photochromic materials [3], and phase-change [4]. A sharpened and metal-coated optical fiber with a subwavelength aperture on its end has been employed as a probe in those experiments.

The fiber probe, however, has several drawbacks. First, it is mechanically weak in a near-field scanning scheme. It is impractical to scan the probe by conventional piezoelectric actuator at a high speed, e.g., v =1 m/sec, while maintaining the tip-medium separation as close as order of ten nanometers. Second, the transmission efficiency of light power is usually low, typically 10^{-5} when the aperture diameter is 100 nm [5]. This low efficiency of the near-field excitation of a fiber probe limits the scanning speed of the probe to be low. To obtain high enough scan speed, high laser power should be used, which often leads to the thermal damage of probe tip [6]. Recently several fabrication methods of high-efficiency probes were reported [5, 7]. The detected light power by these probes, originated due to reflection from the surface of the storage medium, has become as high as 1 mW. According to our estimation, the data transmission rate for read-out, limited by the shot noise associated with the detected photon number, can reach as high or even higher than 100 Mb/sec [8]. It is promising to have such a high data transmission rate in order to realize a fast read-out. However, the problem is how to scan the read-out head. Third, there is a difficulty of precise mechanical tracking of the single fiber probe to maintain it within the range of several 10nm.

To overcome this difficulty, we propose to adopt a two-dimensional planer probe array for near-field optical storage, demonstrate to fabricate the probe array by the micromachining process of a Si wafer, and demonstrate the data storage readout.

Advantages of the planar apertured probe array are :

(1)The appearance is a plane-shaped, and there is no projection which breaks easily in it.

(2)When the probe array with **n** elements is used, the scanning speed required for the same data transmission rate can be reduced to1/**n**. The optical power required for the same data transmission rate can also be reduced.

(3)Because it can read data as a surface information, it allows us to use a software tracking, i.e., it allows us to overcome difficulty of precise mechanical tracking of the single fiber probe.

(4) The separation between the array and the storage medium surface can be maintained constant due to a flat bottom surface of the array. The array can be smoothly scanned on the storage medium while maintaining a narrow gap, e.g., through the use of a coated lubricant oil film of nanometric thickness, as is the case of a contact-type hard disk.

2. A PLANAR APERTURED PROBE ARRAY

Schematic of the probe structure and the data storage system are illustrated in Figs. 1(a) and (b). The probe array fabricated with a silicon plate has concave pyramidal shaped grooves with nanometric apertures on their bottom ends. The laser beam from a light source propagates free space and enters into the grooves to generate the optical near field on the apertures to record the bits. The probe array was slightly tilted with respect to the direction of rotation of the medium as shown in Fig.1(a), thus each aperture passes through the neighboring line on which recorded bit are aligned. The distance between each probe is not necessary to be smaller than the optical wavelength. The light intensity incidents into each aperture of the array can be modulated depending on the information to be stored by inserting a planar spatial modulator into the light path. In readout, the scattered near-field light on the medium by the aperture array converts into the propagating light and detected by a photodetector located at a far field region. Thus, we can process the data simultaneously by recording or reading out the pits as a two-dimensional surface information. This

procedure greatly reduces the expected difficulty of precise tracking on nanometer-sized small pits of terabit-class high density storage.

For the spatial modulation of the laser in this system, there can be several some methods. First is a method using a liquid crystal light shutter. However, its long response time is not for the high-speed modulation. Second is a method using some lasers, i.e., one laser is associated in one aperture, and each is modulated independently. However, as a promising method we propose the one using a laser deflector by which a laser beam is scanned on the probe array. The high-speed deflection of the light is possible with the electro-optical technique. When this method is applied for the spatial modulation of the laser, the scattered light in a different aperture can be read by time series. Therefore, the system configuration is possible with one light source and one photodetector. This method has an additional advantage that the interference between the light scattered from neighboring apertures can be decreased.

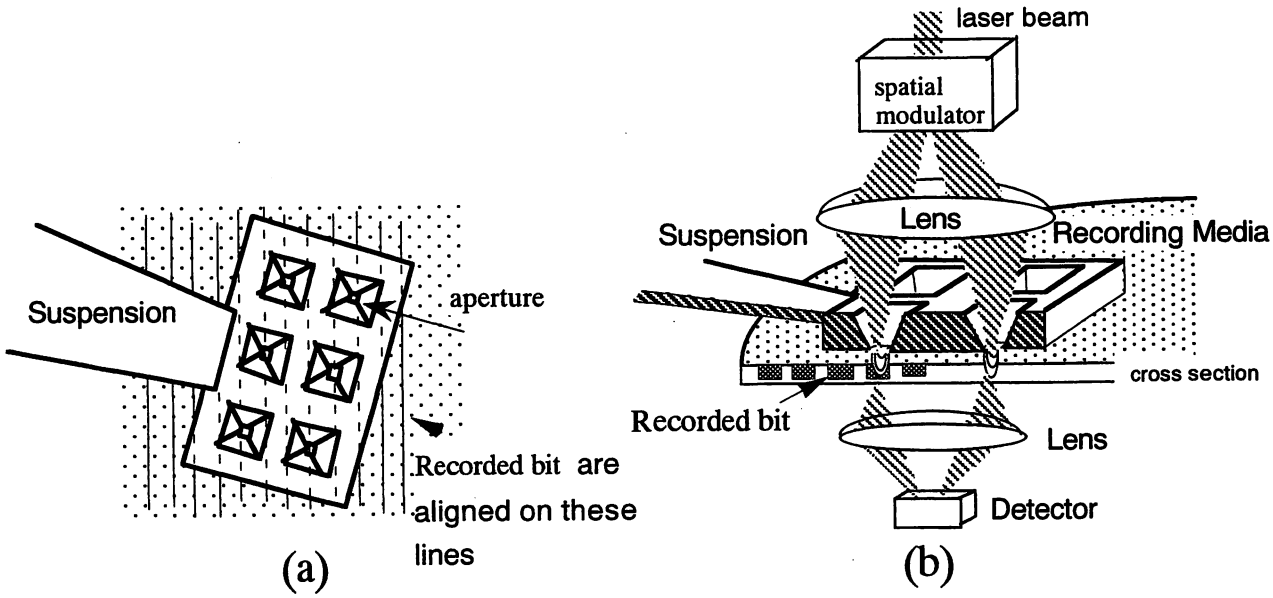

Fig. 1. Schematic explanation of the data storage system with planer probe array.
(a) top view (b) cross-sectional view.

3. FABRICATION OF THE PROBE ARRAY

The probe is fabricated by the micromachining process of a Si(100) wafer consisting of lithography and anisotropic wet etching. The concave pyramids of the probe array are formed by utilizing the difference in the etching rates along the (100) and (111) axes of the crystal. As a block layer for further etching, we used the buried oxide of a silicon-on-insulator (SOI) wafer. Figure 2 shows the fabrication process of our probe array. A wafer with SOI thickness of 10 μm is thermally oxidized to form 1.5 μm-thick SiO_2 film. Window regions with 1-2 mm^2 area are photolithographically defined on the back side of the wafer.

After removal of the SiO_2 with a buffered hydrofluoric acid (BHF) solution, the back side is anisotropically etched with 10 weight percents potassium hydroxide (KOH) aqueous solution at 80 °C until the etching stops to expose the buried oxide layer. The etching condition was preliminarily determined to maximize the etching rate ratio of Si(100) to (111) plane as well as that of Si to SiO_2. The thin Si membrane in the window region in Fig. 2(b) usually bulges out due to the stress unbalance. Therefore we strip away the oxides with BHF and reoxidize the wafer to form 0.1 μm-thick SiO_2 film. The formation of the new thin oxide film makes the surface flat and clean to increase the wettability of the photoresist. The thin oxide layer on the front side surface is patterned in a array of squares with the photolithography. Again the wafer is etched anisotropically. Following the formation of the concave pyramidal shaped grooves which are faceted with (111) planes of Si constrained by the oxide mask, the grooves slowly expands in the (111) direction. The etching is stopped when the buried oxide appears. Oxides are again stripped away with BHF to form small apertures in the bottom of concave pyramids, and if necessary a metallic film is sputter-deposited from the back side to block the transmission of far-field light. Finally edge part of the Si bulk is removed by cutting-off.

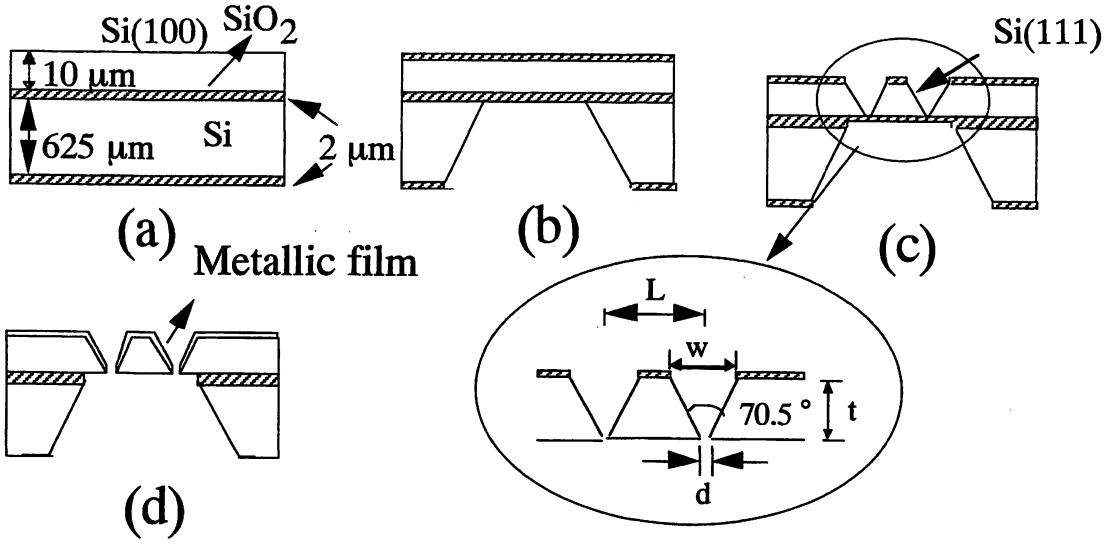

Fig. 2. Fabrication process for the planar apertured probe array. (a) initial wafer, (b) formation of window regions, (c) formation of grooves, and (d) oxide removal and metallic film deposition. The inset shows that aperture size **d** is determined by the pattern size **w** and SOI thickness **t**.

Figures 3(a) to 3(b) show the typical scanning electron microscopic (SEM) images of the fabricated aperture arrays. The lateral aperture sizes in the Fig.3(a) were 200 nm after 50-nm thick gold deposition. We confirmed that minimum aperture size as small as 80 nm could be obtained by this process among the fabricated several arrays, as shown in Fig. 3(b). This dimension is far beyond the wavelength of light which was not ever achieved, to the best of our knowledge, in conventional micromachined structures based on the anisotropic wet etching of Si. As is shown in the inset of Fig. 2, the apex angle (i.e., 70.5°) of the pyramid is governed by the crystallographic orientation of (111) plane. The aperture size **d** is determined by the thickness t of the substrate and the size of the upper surface of the concave pyramid **w**, which is given by $\mathbf{d} = \mathbf{w} - \sqrt{2}\mathbf{t}$. The accuracy of **w**

depends on that of lithography. The use of a SOI wafer provides high enough homogeneity and accuracy of **t**. The aperture size **d** is determined also by the thickness of the coated gold film. Advantage of this process is that the aperture array is fabricated effectively and homogeneously by using only the established technique of lithography for silicon planar process even though the size of aperture is smaller than the resolution limit of photolithography. Fluctuations of the aperture size **d** may induce fluctuations of the scattered light intensity from each aperture, which may decrease signal-to-noise ratio for signal detection. However, this decrease can be avoided by appropriately adjusting a threshold level for discriminating the temporal signal sequence. The separation **L** between the adjacent apertures, rather than the fluctuations of the aperture size, must be regulated for the read-out process. Conventional technique of photomask can maintain the accuracy of **L** sufficiently high because the value of **L** is set to be larger than the optical wavelength to prevent the interference of signal.

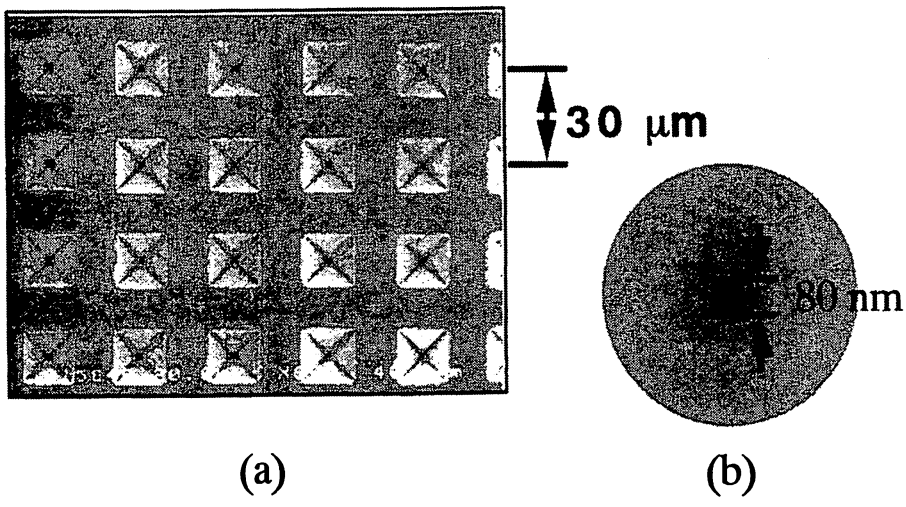

Fig. 3. SEM images of the fabricated aperture arrays (a) front side view,
(b) magnified image of one aperture with minimum size obtained : back side view.

4. DEMONSTRATION OF THE READOUT

In order to demonstrate the near-field readout using the probe array as a near-field optical head, we observed the near-field image of a sample with the one of the apertures of the probe array.

The experimental setup is shown in Fig.4. The probe array was detached from the wafer by using focused ion beam (FIB), and glued at the top of a beryllium copper suspension as shown in the upper photograph of Fig.4. Then the probe array was put on a sample which is fixed on the scanning X-Y stage. Thin lubricant (FOMBLIN) film was coated on the sample. The sample is a glass plate covered with 100nm thin film of aluminum. On the glass plate, several lines were drawn by using a FIB. The lower photograph of Fig.4 is the SEM image of the sample. The width of line on which film of aluminum being scraped was 100nm. The separation between each line was 1μm. A laser beam of wavelength 512 nm was focused on one of the groove on the probe array whose aperture size of the probe was less than 100nm. Then the transmitted light through the probe array and the sample was detected with a photomultiplier.

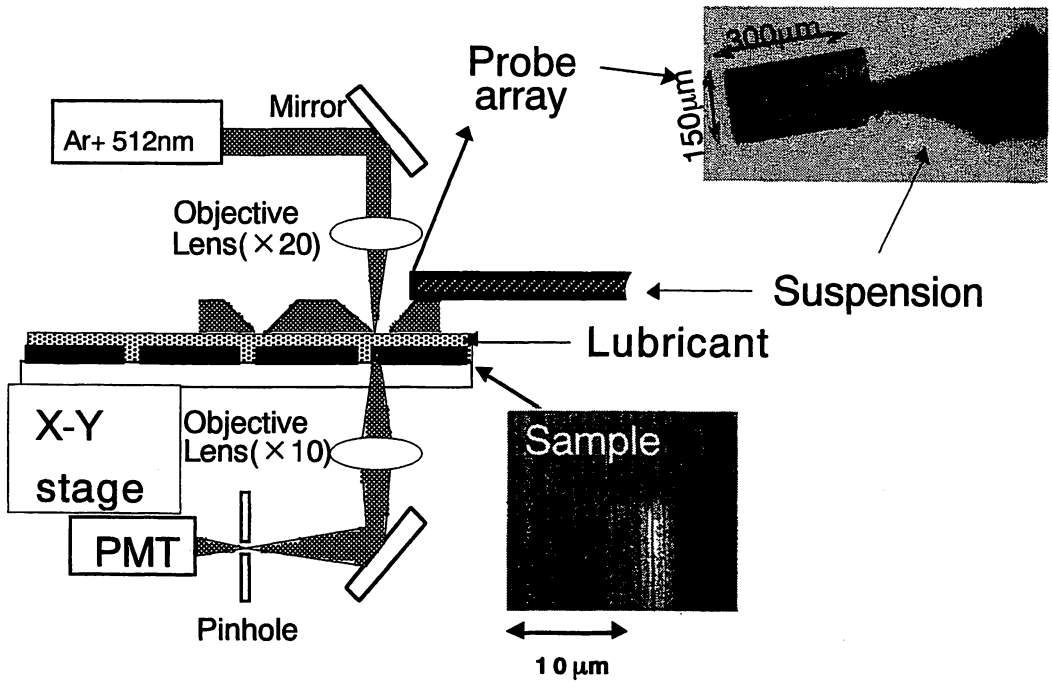

Fig.4 The experimental setup.

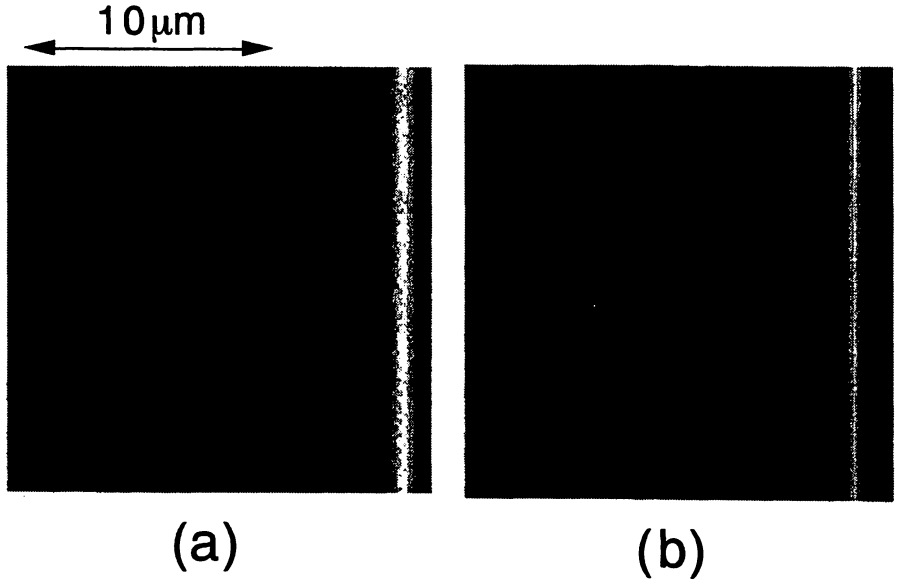

Fig.5 Images of the transmitted light intensity detected by the photomultiplier. (a) obtained without probe, i.e., laser light was directly focused on the sample. (b) obtained with probe.

Figures 5(a) and (b) show the image of transmitted light intensity detected by the photomultiplier. Figures 5(a) is obtained without probe, i.e., laser light was directly focused on the sample. Figures 5(b)is obtained with probe. Since the focused spot size was estimated to be 1μm, no line can be resolved in Fig.5(a), but lines are clearly separated in the case of measurement with probe as shown in Fig.5(b).

Figure 6 shows the cross-sectional distribution of the transmitted light. Curves A and B are represent the result obtained without and with probe, respectively. Vertical axis is detected optical power normalized to the peak power of the light detected without the probe. From the comparison between the carves A and B, it is seen that the transmitted light decreases to 1/1000. However it is 10 times larger than the transmission efficiency of light power of the typical near-field fiber probe whose aperture diameter is 100 nm. From the magnified profile shown in the inset, the full width at half maximum of curve is 250nm, which is more than twice that of the line (i.e.100nm). Major reason is light transmission through Si, because of no coating over the Si probe. That is the light might be transmitted into the Si and then the aperture size for the light become wider than the aperture size.

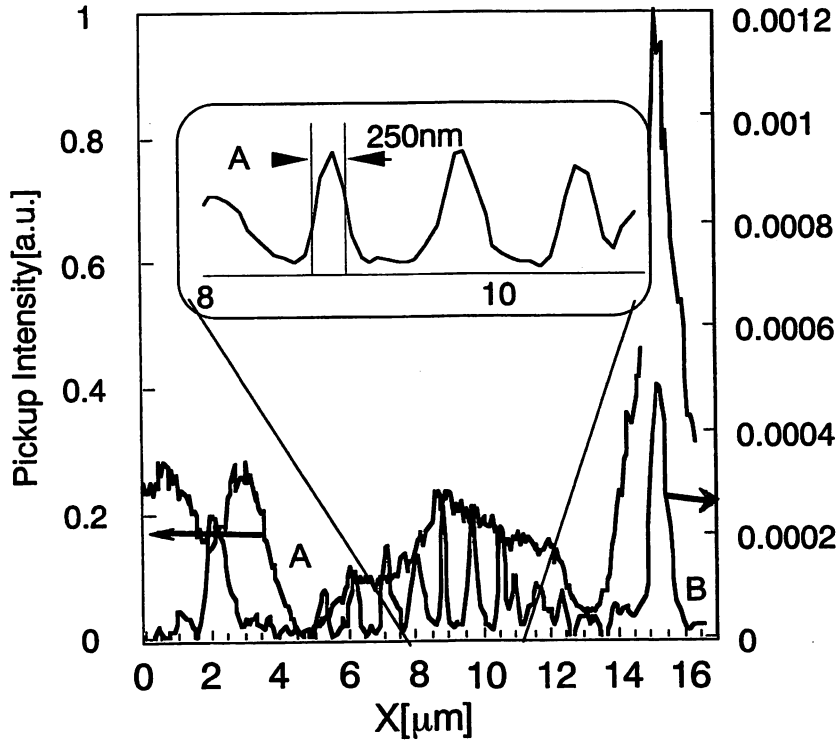

Fig.6 The cross-sectional distribution of the transmitted light. Curve A and curve B is for without and with probe, respectively. Vertical axis is detected optical power normalized to the peak power of the light detected without probe.

5. THE PROBE ARRAY WITH MICROLENSES

In the section 4, laser light was focused on the aperture in order to get large light transmission efficiency. However it is difficult to adjust the position of the laser spot at the aperture with the actual device. Therefore, it is necessary to focus the laser light automatically set at the aperture. Here we demonstrate putting microlenses to focus the propagating light on the surface of apertures. We have installed glass spherical lenses onto each aperture. The powder of glass spheres (refractive index : ~1.5) with 10 μm in diameter was suspended in isopropyl alcohol to form a colloidal solution. The Si wafer with fabricated probe array as in Fig. 2(d) was spin-coated with the solution. The glass spheres put on each aperture simply by the suctimg force through the aperture due to the evacuation applied to fix the wafer in the spinning process. Figure 7 shows the SEM image of the sphere lens array which was installed successfully by the simple method described above.

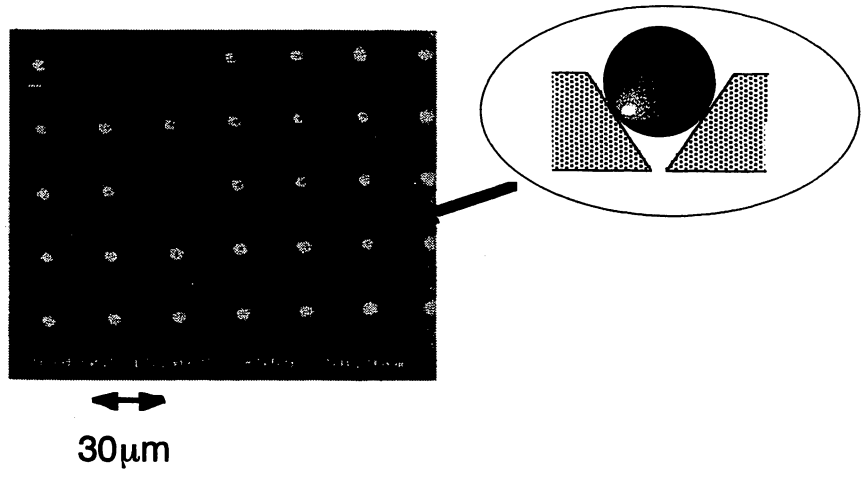

Fig.7 Probe array in which the spherical lens was installed.

The spatial distribution of the optical near-field intensity generated on the aperture with a aperture size of 500nm was measured by using collection-mode near-field optical microscopy (NOM) as shown in Fig.8. The laser light (λ=512 nm) was introduced from the front side of the probe without objective lens. Optical near field generated on the aperture was detected by a fiber probe tip fabricated with selective chemical etching and subsequent 30-nm thick gold deposition as shown in inset of Fig.8. The tip-sample separation was regulated by a shear force feedback method [9]. The comparison between the two types of probe shows that the use of sphere lens increases the light intensity as high as 16 times as shown in Fig.9. Much higher increase of the light intensity is expected by optimization of the refractive index of the spherical lenses.

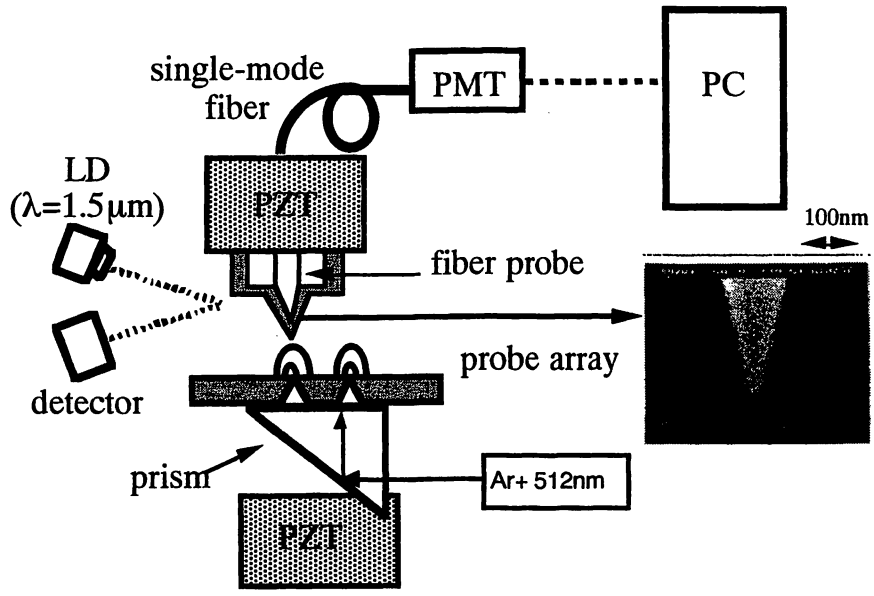

Fig. 8. Experimental setup of the scanning near-field optical microscopy for the evaluation of the probe. Inset: SEM image of the fiber probe tip used for the scanning.

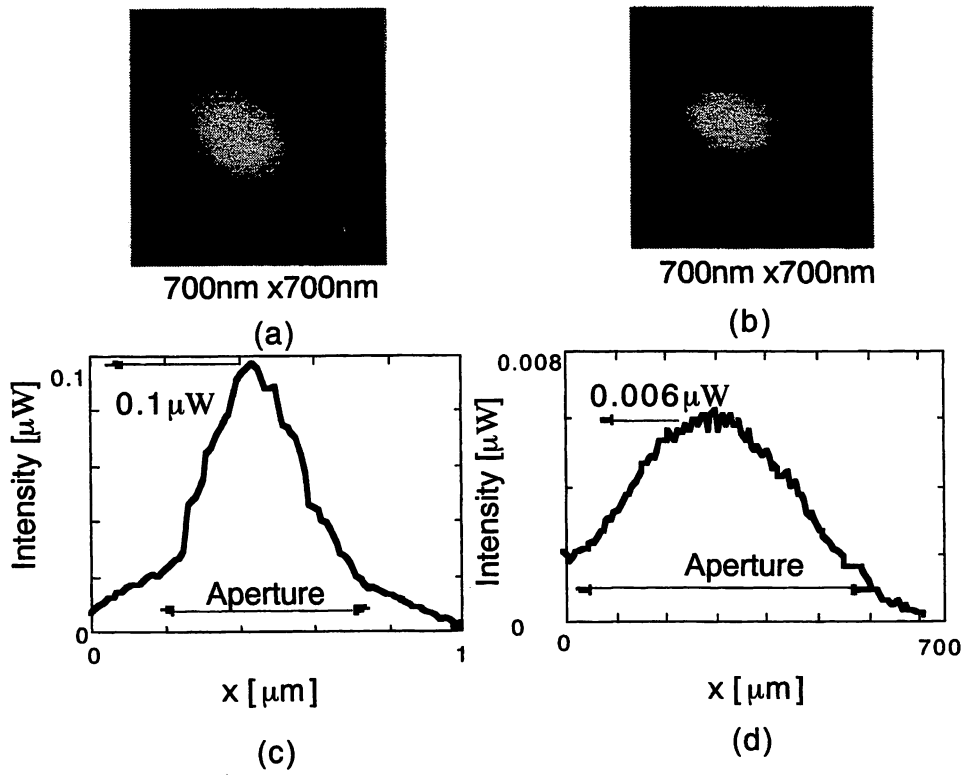

Fig. 9. Near-field image of the scanning near-field optical microscopy. (a)with spherical lens. (b) without spherical lens. (c) and (d) are cross sectional distribution of (a) and (b), respectively.

6. SUMMARY

We proposed and demonstrated a novel silicon planar apertured probe array as a near-field optical head for optical memory. The apertured array was fabricated by utilizing wet etching technique of a silicon wafer. Inverted pyramids were formed on the silicon plate, and apertures were fabricated at the tops of the inverted pyramids. An aperture with a size less than 100nm was realized. By scanning the probe array, we obtained resolved image of the lines in the corrugation which was made on a metal thin film. The observed line width was 250nm. Further, we put micro glass spheres in the inverted pyramids to focus the propagating light at the apertures automatically. The near-field intensity at the aperture was 16 times larger than that without a glass sphere.

7.ACKNOWLEDGMENT

We would like to thank Prof. H. Ishiwara and Prof. E.Tokumitsu (Tokyo Institute of Technology) for their supports and useful suggestions in the fabrication process.

8.REFERENCES

[1] B. D. Terris, H. J. Mamin, D. Rugar, W. R. Studenmund, and G. S. Kino, "Near-field optical data storage using a solid immersion lens," *Appl. Phys . Lett.*, vol. 65, pp. 388-390, 1994.

[2] E. Betzig, J. K. Trautman, R. Wolfe, E. M. Gyorgy, P. L. Finn, M. H. Kryder, and C.-H. Chang, "Near-field magneto-optics and high density data s torage," *Appl. Phys. Lett.*, vol. 61, pp. 142-144, 1992.

[3] S. Jiang, J. Ichihashi, H. Monobe, M. Fujihira, and M. Ohtsu, "High loc alized photochemical processes in LB films of photochromic material by using a photon scanning tunneling microscope," *Opt. Commun.*, vol. 106, pp. 173-177, 1994.

[4] S. Hosaka, T. Shintani, M. Miyamoto, A. Hirotsune, M. Terao, M. Yoshida, K. Fujita, and S. Kammer, "Nanometer-sized phase-change recording using a scanning near-field optical microscope with a laser diode," *Jpn. J. Appl. Phys.*, vol. 35, pp. 443-447, 1996.

[5] T. Saiki, S. Mononobe, M. Ohtsu, N. Saito, and J. Kusano, "Tailoring a high-transmission fiber probe for photon scanning tunneling microscope," *Appl. Phys.* Lett., vol. 68, pp. 2612-2614, 1996.

[6] M. Stahelin, M. A. Bopp, G. Tarrach, A. J. Meixner, and I. Zschokke-Granacher, "Temperature profile of fiber tips used in scanning nea r-field optical microscopy," *Appl. Phys. Lett.*, vol. 68, pp. 2603-2605, 199 6.

[7] T. Yatsui, M. Kourogi, and M. Ohtsu, "Highly efficient excitation of op tical near-field on an apertured fiber probe with an asymmetric structure," *Appl. Phys. Lett.*, vol. 71, pp. 1756-1758, 1997.

[8] M. Ohtsu, "High speed near-field optical technology for ultrahigh densi ty storage," *Tech. Digest of the Joint MORIS/ISOM Symp.*, pp. 180-181, 1997.

[9] E. Betzig, P. L. Finn, and J. S. Weiner, "Combined shear force and near -field scanning optical microscopy," *Appl. Phys. Lett.*, vol. 60, pp. 2484-24 86, 1992.

[I-3] REVIEW PAPERS

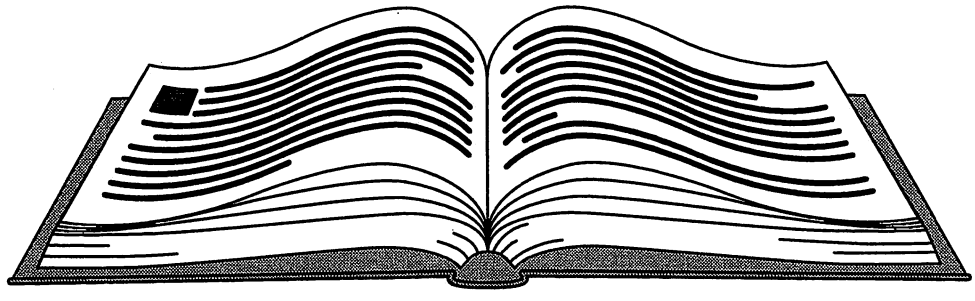

〈基礎編〉

基　礎　講　座

〈ナノ領域の光〉

ナノ領域の光加工とその応用

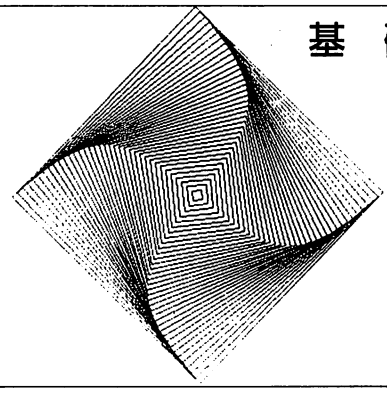

大　津　元　一

近接場光学技術の微細加工への応用について述べた．その例としてナノ寸法物質の堆積とその将来展望、さらには加工の応用としての超高密度光メモリーの実現のための問題点とその解決策の現状について概説した．

Keywords: optical near field, probe, deposition, atom manipulation, optical memory

1. まえがき

微粒子表面に発生した近接場光を測定するためには，プローブを近づけて近接場光を散乱させる必要がある（第1回目の講座参照）．このことはプローブにより近接場光のエネルギーの空間分布が乱されること，言い換えると場の分布が破壊されることを意味する．さらに近接場光を強く乱せば，入射光により微粒子中に誘起された双極子の空間分布の様子が変わる．さらに強く乱すと微粒子の一部がへこんだり，その構造や組成が変化することも考えられる．このように測定に付随する破壊性に着目すると，近接場光の利用は単に光学顕微鏡のような測定器としてのみではなく，むしろ加工機が本質的であるといえる．近接場光を加工に用いると商用エレクトロニクスをはじめとする広い範囲に対してインパクトを与える可能性がある．

欧米諸国における近接場光の研究は測定器としての顕微鏡への応用を主体に生物，有機化学への展開をみせている．一方，わが国では測定に関して単なる光学顕微鏡のみではなく，半導体微粒子の構造を評価できる分光分析機への応用が進んでおり[1]，さらには加工機としての応用が展開されている．また，近接場光を利用するためのプローブの加工自身も盛んである．また，加工の応用の一例として，1 Tbit/in^2 に達する記録密度が可能となる超高密度光メモリーの開発が産業界からの大きな興味を引いている．

さらに最近では，近接場光学の産業化へ向けて細部にわたる問題が検討されるにいたっており，近接場光学が将来の基盤技術として認知されつつある．本稿では，近接場光学について応用上の急展開を背景とし，ナノ寸法の光加工，および光メモリーへの応用について解説する．

2. 近接場光によるナノ加工

微細加工は半導体産業などに広く用いられているが，近接場光学の応用としてのナノ加工は既存の微細加工技術に対して次のような特長を有する：加工は物質を削ること（エッチング）と物質を積み上げること（堆積）に大別できる．近接場光を用いればいずれのプロセスも原理的に可能であるが，ナノ寸法のデバイスなどの構造を形成することを目標とするのであれば，あらかじめ堆積した物質を周囲から削り出す方法よりも，直接微細な物質を堆積する方が単純で効率もよい．さらに光を使うと，物質との共鳴相互作用を利用して特定の物質を選択的に堆積することが可能であること（すなわち不純物が混入しないこと），基板への損傷や汚染が少ないことなどの利点がある．ここで従来使われている伝搬光ビームの代わりに近接場光を用いると，微細なパターンの形成が可能となるので，将来のナノ寸法の光機能材料やデバイスの製作の際に威力を発揮する．

堆積の試みの例として，すでに実証されている亜鉛(Zn)金属の光化学気相堆積（光CVD）を紹介する[2]．これは図1に示すようにジメチル亜鉛 ($Zn(CH_3)_2$) などの有機金属蒸気に近接場光を照射し，光化学反応により Zn 原子とメチル基(CH_3)とを解離させ Zn を基板に堆積させる方法である．プローブ先端にしみ出す近接場光の存在する微小領域内でのみ解離が起こるので，基板上で Zn の微細なパターンが形成される．ただし，これを実現するために解決すべき問題としては次のようなものがある．すなわち，（1）ファイバープローブを用いる場合，解離エネルギー(3.76 eV)以上のフォトンエネルギーを有し十分なパワー密度をもつ波長 338 nm 以下の紫外域の近接場光が発生可能か．（2）基板上ではなく，近接場光を発生するファイバープローブ先端表面への堆積が強く起こり，最後にはプローブ表面が Zn 薄膜で覆われ近接場光が発生しなくなるのではないか，などである．

（1）を解決するために，紫外光に対して非常に小さな伝送損失（その値は 1 dB/m，これに対し従来用いられていたファイバーの伝送損失は 96 dB/m）をもつファイバーを用いてプローブを作成する技術が開発された[3]．ここで用い

東京工業大学大学院総合理工学研究科　〒226-8502　横浜市緑区長津田町 4259.
分類番号　7.9, 11.2
Nanometric fabrication by light and its applications. Motoichi OHTSU. Interdisciplinary Graduate School of Science and Engineering, Tokyo Institute of Technology (4259 Nagatsuta-cho, Midori-ku, Yokohama 226-8502)

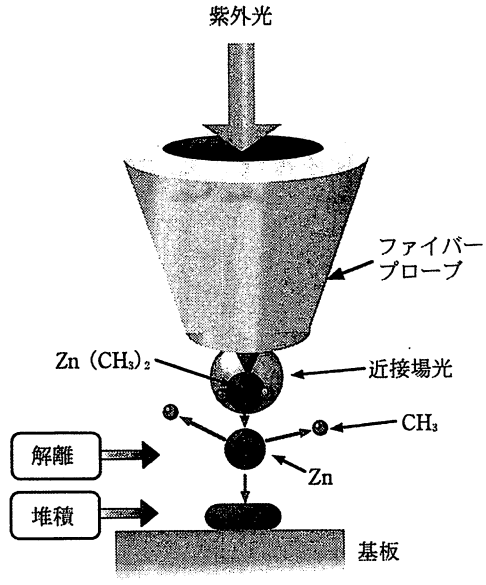

図1　ファイバープローブ先端の紫外域近接場光によるジメチル亜鉛($Zn(CH_3)_2$)の解離，Zn の堆積の原理．

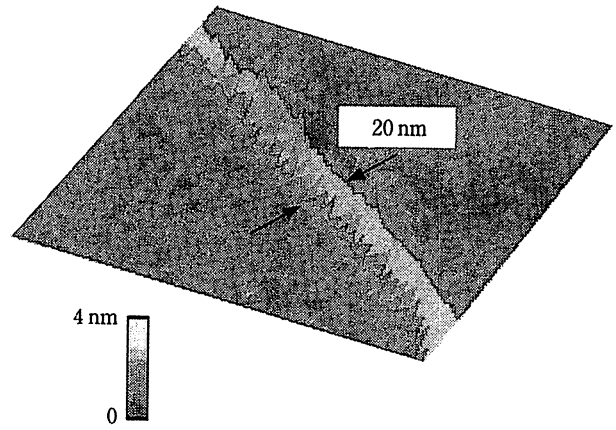

図2　ガラス基板の上に堆積した亜鉛の微細な楕円曲線のパターンの一部の形状測定結果．画像の一辺は 400 nm．

る紫外域（波長 244 nm）の近接場光のパワー密度の測定値は 1 kW/cm² に達しており，十分大きな値が得られている．(2)についてはプローブ表面が Zn 薄膜で覆われるのには 2～3 時間要するが，ナノメートル寸法の微細パターンの堆積に要する時間は数分以内なので問題はない．しかし念のために，この問題を回避するために，光ビームを用いた従来の光 CVD 用に提案されている前期核形成法[4]が採用されている．この工程は次のとおりである．(1)堆積用基板の置かれた反応容器中に $Zn(CH_3)_2$ 蒸気を満たして基板表面に $Zn(CH_3)_2$ 分子層を吸着させる．(2)排気後，ファイバープローブを走査し，近接場光により基板上の吸着分子層を解離して堆積の核となる Zn を析出する．(3)プローブを退避させた後，再度蒸気を満たし，ArF エキシマレーザーの紫外光ビームをファイバープローブを通さずに直接基板に照射して核の上に Zn を堆積，成長させる．

図2にはこの方法により堆積した Zn の細線パターンの形状計測結果を示す．この図は堆積に用いたファイバープローブを原子間力顕微鏡用プローブとして再び用い，堆積直後に測定したものである．基板はコーニングガラス(7092番)である．工程(2)の光源には Ar レーザーの第二高調波(波長 244 nm)を用いた．プローブ走査により任意の曲線・点などのパターンが描け，これが近接場光を用いる場合の利点であるが，図 2 はそのように描かれた楕円曲線（長径約 700 nm，短径約 300 nm）[2]のうちの一部を表示したものである．プローブ走査の全時間は約 2 分であり，この間，プローブ先端への Zn 薄膜の付着は無視できる．図 2 の矢印で示した部分の細線パターンの幅は 20 nm であるが，これは原子間力顕微鏡のために用いたファイバープローブの形状によって決まる分解能が含まれている．より高分解能の測定をすれば，さらに狭い幅をもつ像となるはずである．同じ光源からの伝搬光ビームを用いて行われた従来の光 CVD による Zn のパターンの幅の最小値は 2～3 μm なので[4]，図 2 ではこれに比べ 1/100 以下の値が実現している．図中のパターンの高さは約 3 nm であるが，これは 50 層の Zn 原子に相当する．なお，本ファイバープローブで観測可能な高さの最小値は 0.5 nm，すなわち約 8 原子層に達している．今後，実験条件の改良により，パターンのいっそうの微細化，パターン断面のアスペクト比の増加，堆積時間の短縮，などが期待される．

微細なパターンを作成することが目的の場合，その堆積時間は短いので，実際には上記の問題(2)はほぼ無視できる．したがって最近では，前期核形成の方法をとらず図 1 に示す基本的方法をそのまま用い，蒸気にファイバープローブを直接さらし，先端の近接場光で直接に解離，堆積が可能であることがわかってきた．この方法では単一工程なので再現性が高いことなどの利点を有する．この方法によりT字型の微細パターンが数分の時間以内で堆積されている[5]．上記の方法によれば Zn のほかに，Al，Cr，W などの金属パターンがガラスや Si 基板上に堆積可能である．

堆積速度はファイバープローブの走査速度に依存し，これは既存の堆積方法に比べ低速であることが実用化の際の問題となりうるが，次章の光メモリー記録再生用の高速走査可能なヘッドの例に見られるように，堆積用の新しいヘッド開発により高速化が可能である．なお，現状の速度でも集積回路のフォトマスクの修正，特に断線部分の結線に使える可能性が高い．なぜなら，フォトマスクの修正は正確さが要求されるが作業件数は少ないので，速度は必ずしも重要な要件ではないからである．LSI 製品技術の進歩に伴い，現在 256 M DRAM のレクチル(縮小投影方式のステッパーで用いられているフォトマスクのこと)の設計ルールは最小線幅 1 μm となり，欠陥の修正精度は ±1 μm が要求されている．これにはレーザーを用いたレーザーリペア法などが用いられているが[6]，それ以上の集積度に対応するために本方法への期待が高まっている．なお，近接場光による堆積は上記の金属のみでなく，絶縁体，半導体の堆積も可能と試算されており[7]，今後の発展が期待される．さらに，以上の堆積の極限技術として，近接場光による原子操作の応用としての単原子レベルでの堆積が検討されている[8]．

3. 近接場光による光メモリー

光メモリーは大きな産業規模の商用エレクトロニクスの一つであり，記録媒体，ヘッド，精密機構など，多数の要因からなる統合システムとしての加工の応用例といえる．従来の光メモリーの記録再生には伝搬光ビームをレンズで集光して用いているので，近い将来に記録寸法が光の回折限界に到達する．

一方最近，(財)光産業技術振興協会により2010年の高度情報化社会からの要求を想定し，光メモリー産業の進む方向を検討する手がかりとしてのロードマップが作成された[9]．これによると情報量の増大に伴うファイルの高密度化が必要で，光メモリーの記録密度として1 Tbit/in^2，また再生速度として100 Mbit/sが要求されると推定している．これらの値を実現するために近接場光による方法が検討され始めた．これは光磁気材料を用いた熱モード記録・再生[10]，フォトクロミック材料を用いたフォトンモード記録再生[11]の原理実験に端を発する．すなわち，ファイバープローブからの近接場光を記録材料に照射して材料表面の構造変化，形状変化を誘起し記録する方法である．再生には近接場光学顕微鏡と同様の計測を行う．方法は単純であるが，実際には上記の目標値を達成するための廉価性，信頼性を完備した商用システムを実現するため多くの技術的問題を解決する必要がある．

近接場光による記録密度および記録ピットの最小寸法はプローブ先端寸法によって決まる．記録密度1 Tbit/in^{2}に相当する記録ピット寸法(30 nm)を実現することは原理的にはすでに可能となっているが，記録・再生速度，記録・再生ヘッドの安定走査，記録材料の開発など，多くの技術的問題点を解決する必要がある．最近になって問題解決のための考察や実験が急速に活発化している．実用化の際の形態としては密閉型（従来のハードディスクドライブと同様の装置外形を有し，薄型・小型化により据置型の端末や携帯端末など広範囲の端末機器に使用），パッケージ型(従来のパッケージ型光ディスクの発展型としてテラバイト級の廉価な脱着可能な記録媒体を提供）の二つが考えられており，両型ともROM, WORMを経てRAMの実現にいたるべく，開発が始まっている．

以上のような光メモリーを実用化するために解決するための問題点はソフトウエアとハードウエアにかかわっており，かつこれらは相互に関連している．さらにハードウエアに関してはシステム，デバイス，記録媒体などの問題がある．これらの問題の詳細は文献[12]に列挙されているが，これらのうちのいくつかを解決するための著者らの試みを紹介する．

筆者らが開発した高効率型ファイバープローブ[13]では近接場光発生効率は1×10^{-2}に達しており，これを用いれば光のショット雑音によって決まる再生の際のデータ伝送速度は100 Mbit/s以上となることがわかっている．しかし，この場合プローブ記録媒体面の数10 nmの上空を10 m/s以上の速度で走査すること，記録媒体上での横揺れを防ぐトラッキング制御を施すこと，などの問題を有する．

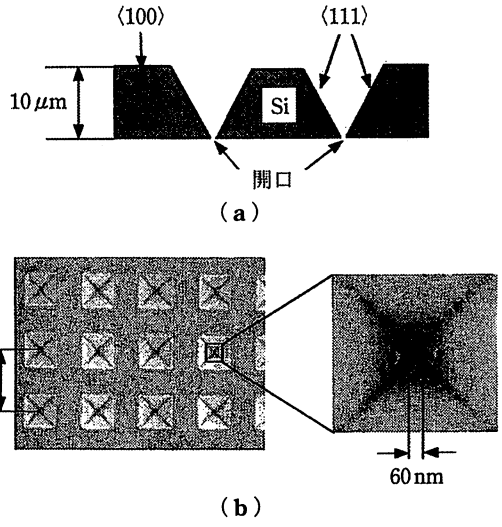

図3 (a)シリコン基板に形成された微小開口アレイの断面説明図．(b)作成された微小開口アレイの上面からの走査電子顕微鏡写真．

これらを解決するために半導体平面加工プロセス技術を用いてシリコン基板に図3(a)に示すような二次元の微小な開口アレイを作り，上面から照射した光によって微小開口に近接場光を発生させる記録・再生ヘッドが提案されている．これは次の利点をもつ：(1)アレイ中の全開口(個数をNと記す)を用いて記録・再生を行うので，走査速度は上記の値の$1/N$となる．たとえば$N=1\times10^2$，1×10^4のとき，おのおの10 cm/s, 0.1 mm/sとなり高速走査が不要となることがわかる．(2)底面が平坦なので記録媒体との間の距離をアレイ全体にわたって一定に保つことができる．(3)コンタクト型のハードディスクの走査と同様，記録媒体に塗布した潤滑剤薄膜[14]を介して滑らせ，記録媒体との距離を一定に保ったまま(1)に示した走査速度を実現することができる．(4)スラブ導波路および光検出器アレイなどとの集積化が可能である．さらに，アレイの配列軸を記録媒体のピット列の方向と傾けて走査すれば，横揺れ防止のための精密なトラッキング制御が不要になることが指摘されている[12]．

アレイはシリコン基板の異方性エッチングにより製作されている．均一性と精度を確保するためにSiO_2層が埋め込まれたSOI(Silicon on Insulator)基板が使われている．埋め込みSiO_2層を裏面からのエッチングの停止層として利用して表面Si層を残し，ここに凹部形成の窓開けパターンを形成する．そして開口形成後に凹部の斜面に金属膜を蒸着し，光を遮断する．最終的な開口寸法はこの蒸着膜厚に応じてしぼられる．

実際には，最適な製作条件を見い出す目的も兼ね，隣り合う開口間隔は30 μmとして製作された．図3(b)の走査電子顕微鏡写真からもわかるように正方形状の開口が再現性よく形成され，一辺の最小値として60 nmが実現している[15]．作製したアレイからの近接場光発生効率は約1×10^{-3}であった．さらに微小な球レンズを図3(b)の断面図中の凹部に設置し，開口部に入射光を集中させ，高効率ファイ

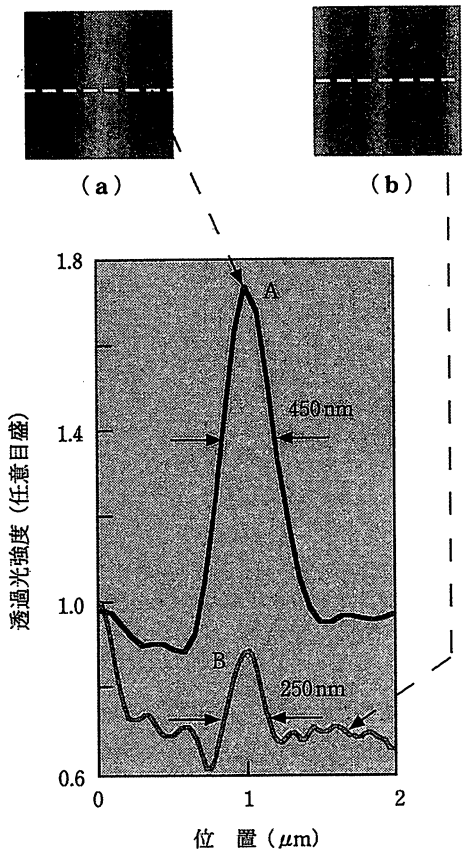

図4 $AgInTe_2$ への光記録・再生結果．光源の波長 514 nm，ここで使用したアレイ中の一つの開口の一辺は 150 nm．その走査速度 30 μm/s．(a) 記録は伝搬光ビーム，再生は近接場光による．(b) 記録・再生ともに近接場光による．(a)，(b) の図ともに一辺 2 μm．(c) 曲線 A，B：おのおの (a)(b) 中の破線に沿った信号強度の断面分布．

バープローブ[13]と同等以上の効率が得られている[12,15]．

予備実験としてこのアレイのうちの一つの開口を通して近接場光を発生させ，これにより $AgInTe_2$ のアモルファス相と結晶相との間の相変化を利用した記録媒体を用いて記録・再生が行われた．プローブ走査にはコンタクト型ハードディスクドライブで採用されている方法を採用した．すなわち，基板を BeCu 製のサスペンションに固定し，表面に潤滑剤の薄膜を塗布した記録媒体上を接触して滑らせることにより走査した．図4は直線状の記録パターンを再生した結果である．再生は記録材料を透過した光の強度測定により行った．(a) では従来の方法と同じく伝搬光ビームを集光して記録し，その後上記のアレイ中の一つの開口に発生した近接場光で再生した結果が示されている．(b) は記録・再生ともにアレイ中の一つの開口からの近接場光を用いた結果である．(c) は透過光強度の断面分布であるが，両曲線の比較から記録・再生とも近接場光を使った場合に狭い幅が記録・再生されたことが確認される．潤滑剤の薄膜厚，開口径，媒体の選定，などの改良により，より小さなパターンの記録再生が期待できる．

なお，同様のプローブのアレイ化については面発光レーザーのアレイを用いる方法[16]が提案されている．

4. むすび

近接場光をナノ寸法の微細加工に応用する可能性について概説したが，本文中にも示したように，今後は近接場光でなくてはできない応用の探索がいっそう重要となろう†．また，近接場光による加工のみでなく，この加工技術を進歩させるのに必要なナノ光デバイスの開発，すなわち近接場光のための加工が必須である．幸いなことに，これらの関連技術については日本の研究開発が世界をリードしている部分が多いが，例えば光メモリーの記録密度の飛躍的向上は既存技術の延長では不可能となっている現在，近接場光方式が唯一の救いであることに鑑み，さらに独創的な研究開発の推進が必要と思われる．

文献

1) M. Ohtsu (ed.): *Near-Field Nano/Atom Optics and Technology* (Springer-Verlag, Tokyo, Berlin, 1998)
2) V. V. Polonski, Y. Yamamoto, M. Kourogi, H. Fukuda and M. Ohtsu: J. Microscopy, to be published (1999).
3) S. Mononobe, T. Saiki, T. Suzuki, S. Koshihara and M. Ohtsu: Opt. Commun. **146**, 45 (1998).
4) D. J. Ehrlich, R. M. Osgood and T.F. Deutsch: Appl. Phys. Lett. **38**, 946 (1981).
5) 山本 洋, V. Polonski, 李 謹炯, 興梠元伸, 大津元一: 1998 年秋季第 59 回応用物理学会学術講演会, 15 pD 12 (1998).
6) 鷲尾邦彦: レーザ熱加工研究会誌 **5**, 1 (1998).
7) M. Ohtsu: *Abstract of Optical Probing and Creation of Advanced Photoactive Materials*--- 1998 Asian-Pacific Forum on Science and Technology--- p. 28. (November 1998, Ishikawa).
8) H. Ito, K. Sakaki and M. Ohtsu: Appl. Phys. Lett. **70**, 2496 (1997).
9) (財)光産業技術振興協会編: オプトニューズ **105**, 24 (1998).
10) E. Betzig, J. K. Trautman, R. Wolfe, EM. Gyorgy, P. L. Finn, M. H. Kryder and C.-H. Chang: Appl. Phys. Lett. **61**, 142 (1992).
11) S. Jiang, J. Ichihashi, H. Monobe, M. Fujihira and M. Ohtsu: Opt. Commun. **106**, 173 (1994).
12) 大津元一, 筒井一生, 興梠元伸, 李 明馥: 電子情報通信学会論文誌, J 81−C− I, 119 (1998).
13) T. Yatsui, M. Kourogi and M. Ohtsu: Appl. Phys. Lett. **73**, 2090 (1998).
14) 佐藤明伸, 安食 賢, 柳沢雅広: 第 20 回応用磁気学会学術講演会, 22 aA-12 (1996).
15) M. Kourogi, T. Yatsui, S. Ishimura, M.B. Lee, N. Atoda, K. Tsutsui and M. Ohtsu: *Proceedings of the SPIE Conference on Far-and Near-Field Optics*, p.258 (San Diego California, July 1998).
16) K. Goto: *Proc. International Joint Symposium on Magneto-Optical Recording and Optical Memory*, Th-L-03, p. 184 (1997).

(1998 年 12 月 28 日 受理)

† 読者がナノ加工，メモリーへの応用を含め，近接場光学についての最近の動向を調査をするためには，昨年 12 月南紀白浜にて開催された第 5 回近接場光学国際会議（発表件数は 276 件で過去の同会議中最高）での発表のうちのいくつかが掲載される英国の学術誌 Journal of Microscopy の特集号（本年発行予定）をご一読いただくことをお勧めする．なお，国内研究者による発表のうちいくつかは応用物理学会・日本光学会発行の Optical Review 誌の一般号からも順次掲載される．

近接場光学とは

—パラダイム・シフトのための初歩的Q&A—

東京工業大学　大学院　総合理工学研究科
大津　元一

1. はじめに

従来の光エレクトロニクスでは，伝搬光の示す回折現象により微小化の限界が課せられている。これに対し，近接場光学とその応用は，この限界を打破するナノテクノロジーを実現するための切り札として1990年代に入り急進展を見せている。特にそれは計測，分光分析，ナノ加工，光メモリーなどの分野で威力を発揮し，光技術のパラダイム・シフトを実現しうる。しかしながら，革新的技術であるために伝搬光を使う従来の技術とは一線を画しており，このために従来より疑問，誤解を抱く人が少なくない。近接場光学についての解説書も出版されているが[1),2)]，その内容は近接場光学の正しい理解に十分な物理的描像を与えているとはいえず，かえって新しい疑問，誤解を生じている。最近になって筆者らはこれらの問題を解決し，正しい理解に供するための英文モノグラフを上梓したが[3)]，本稿ではこの内容をもとに，従来からよくある疑問を列挙してそれに答えたい。

2. 近接場光の発生と検出の原理

本節では近接場光の発生と検出の原理を概説する。これは次節に列挙する疑問に答える根拠を提示するためである。**図1**に示すように，直径aの球（ここでaは入射光の波長に比べずっと小さいとする）に光があたった場合を考えよう。このとき，球内の原子・分子のなかの電子が励振され，無数の小さな振動双極子ができる。双極子は全体として直径aの球形の表面をもっているという制約を満足するため，相互の電気的相互作用によっておのおの適当に向きを変え，その結果，球全体が入射光に応答する大きな振動電気双極子となるように配列する。この図では，この直径aの球を，双極子の向きがおよそ揃った微小球（直径a_1：$a_1 \ll a$）の集まりとして表わしている。直径aの球全体からの光の放射は，個々の微小球の双極子から生ずるというよりも，そのような微小な双極子の間の相互作用の結果，それらが全体として作る大きな双極子がアンテナとなって生ずると考えてよい。それらの総和は直径aの球による散乱光である。

ところで，ここで考えている直径a_1の微小球は一様な双極子をもつと見なせる程度に小さい原

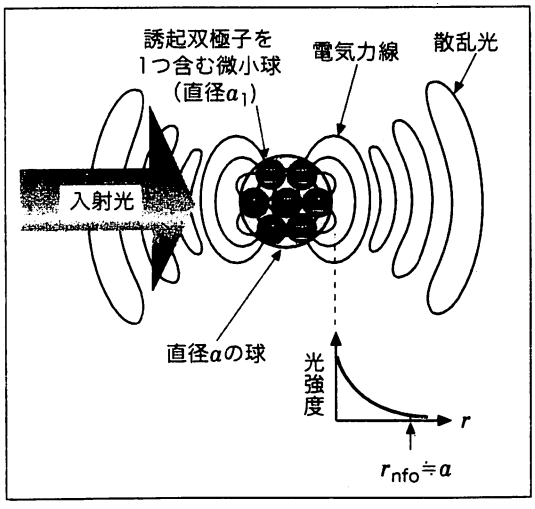

図1　近接場光の発生の原理

子・分子のかたまりであればよい(注1)。そのような微小球にできた双極子は，近隣の双極子とそれぞれ反発したり引き合ったりしながら光を発生する直径aの大きな双極子を作っている。図1ではこのような近隣の電気的相互作用の様子を，特徴的なある瞬間の電気の力の大きさと方向とを表わす電気力線によって示している。

さて，その電気力線と光の発生とについて考えてみよう。球表面近くにある振動双極子間の相互作用を表わす電気力線の一部は球表面から外に飛び出すが，このように外に飛び出した電気力線を全て足し合わせたものが近接場光である。外に飛び出しているとはいっても各電気力線の端は内部の双極子につながっていて表面の近くにあるから，近接場光の強度は表面から遠ざかるにしたがい急激に減少する。したがって近接場光は球表面にしみだした光の薄い膜といえる。計算や実験の結果，その膜の厚みは入射光の波長にはよらず，球の直径a程度の値となることが分かっている[3]。aが入射光の波長よりずっと小さいので非常に薄い光の膜ができる。

このような薄い近接場光の膜の外側では，双極子の向きが時間的に変動することによって図1に示したように，電気力線がちぎれてしまう。このようなちぎれたループ状の電気力線は光となって遠方に伝わっていく横波の電磁波であり，これは入射光によって発生する散乱光にほかならない。ここで，近接場光および散乱光の特性はおのおの散乱体形状および双極子全体がつくるアンテナに依存することに注意したい。

さらに近接場光に注目すると，その電気力線は一方の双極子から他方の双極子へ向かい，そこで終わっているから，遠方には出て行かない。このことはこのような電気力線や近接場光を遠方で測定することができないことを意味する。そこで，測定のためには**図2**のように第2の球を図1の第1の球に近づける。すると第1の球の表面の近接場光の電気力線の1部が第2の球に向かって伸び，これによって第2の球の表面に双極子が発生する。その双極子が同時に第2の球全体として作る大きなアンテナとなり，遠くまで飛んでいく散乱光成分を発生するので，これを遠くから測定することができる。つまり第1の球の近接場光が第2の球との相互作用を通じて伝搬光に変わったのである。なお，第2の球に発生した双極子は球表面に近接場光を発生したり，さらに第1の球に新たな双極子を発生することもある。これは2つの球が近接場光を多重散乱することに対応する。第2の球から遠くへ飛んでいく散乱光は，この多重散乱の結果できた大きなアンテナから生じたものである。

このように第1の球表面に第2の球を近づけると電気力線の分布はもはや第1の球のみの場合とは異なってしまう（その結果，第2の球から散乱光が発生するから第1の球表面の近接場光を間接的に測定できるのである）。この意味で近接場光は原理的に図1に示した当初の空間分布を乱すことにより（いいかえると「破壊」することにより），遠方から測定される。破壊のされかたは2つの球の位置関係によって決まる。第1の球の形や構造自体を破壊する可能性は少ないので，第2の球から発生する散乱光強度を第2の球の位置の関数として測定すると，近接場光の強度の空間分布，ひいては第1の球の表面の形状が測定できる。これが近接場光学顕微鏡である。このとき，空間的な

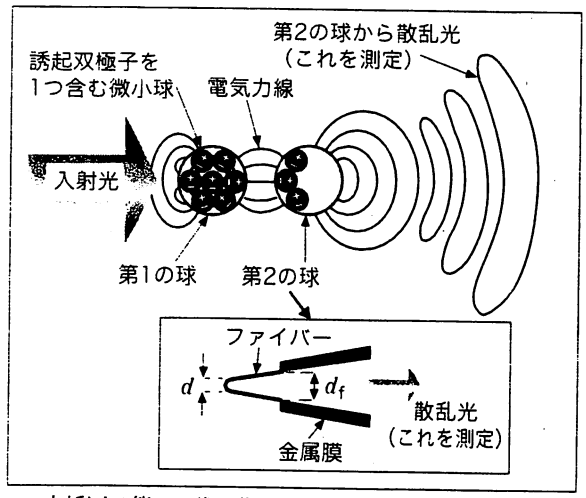

内挿図は第2の球の代わりに用いられるファイバープローブの構造

図2 近接場光検出の原理

測定精度は近接場光の空間分布，第2の球の大きさ，によって決まるから入射光の波長の値とは無関係である。したがって入射光の波長より小さな球を使えば，従来の光学顕微鏡よりもずっと小さいものを見ることができる。

なお，実際には第2の球の代わりに，図2の内挿図にあるように先端を尖らせたファイバーからなるファイバープローブがよく使われている。その際，図2の配置では第2の球，すなわちファイバープローブにも入射光が当たり，それにより散乱光も同時に発生するので，それを測定しないようにするために（すなわち測定のバックグラウンドを除去するために）ファイバープローブ根元に金属膜が塗布されている（根元直径d_f）。一方，第2の球によって近接場光を散乱光に変換する効率（すなわち近接場光の測定感度）は2つの球の直径が等しいときに最高になることが分かっている[3]。このことは近接場光を介した相互作用で第2の球に作られる双極子分布が如何に有効に伝搬光を放射する大きなアンテナを作ることができるかを考えれば容易に理解できる。そこで図1，図2の第1の球の表面の近接場光をもっとも効率よく測定するために，ファイバープローブ先端は第1の球の寸法と同等の曲率をもつように尖らせている。以上のようにして，近接場光学顕微鏡は図2の内挿図中のファイバープローブの金属膜から突出している部分の根元直径d_fと先端曲率の直径dとによって決まる範囲，すなわち$d \sim d_f$の寸法をもつ近接場光を測定する空間的「バンドパスフィルター」となっている。

（注1）微小球の直径a_1の設定には任意性がある。ただしその微小球が1つの双極子を含む程度小さいとしている。もし，この微小球にさらに近づいて観測する必要がある場合には，より細かく変化する複雑な電磁場を見ることになり，この微小球に近づく程度に応じて，さらに小さな多数の微小球（その直径をa_2と書く：$a_2 \ll a_1$）に分けて考える必要がある。その場合には直径a_1の微小球の表面で観測される近接場光のしみ出しの厚みはa_1となる。さらにそのなかの直径a_2の微小球に近づいて近接場光を観測する必要がある場合，その球をさらに小さな多数の微小球に分けて考える。このように必要な観測の寸法に応じて，対象となる球を順次微小球に分けて考えると，図1と同様の議論ができる。すなわち観測する寸法に対応して使うモデルの「階層性」がある。

ところでここで注意が必要なのはこのような分割を繰り返して，より小さなしかし性質がほぼ同様の双極子に分けられるという階層性は，無制限に続くわけではないということである。物体がある程度小さくなってくると，その寸法独特の効果がでてくることがある。

たとえば誘電体の光学的，電気的性質を測定するのであれば，上記のように分割を繰り返し行って，構成要素が元とほぼ同じ誘電体の性質を保つことができる限界があり，これは原子の寸法よりも大きいナノメートルの程度であると考えられる。これよりも小さい物質では，それを構成する多くの原子中の振る舞いがかなり変わったものになると予想される。それは個々の原子の性質ともまた異なっており，そのような領域は一般にメゾスコピックと呼ばれ，最近の科学技術の重要な1つの話題になっている。

なお，メゾスコピックという概念から考えると，実際には第1の球，第2の球という分け方をしても，それらが近づくと電磁気学的に見て外場に対しおのおのが独立である場合と異なる応答をしていることに気付くであろう。すなわち物質としては分かれているが，応答としては一体に見える。つまり光から見ればメゾスコピックな状態になっている。

以上で説明した階層性は現代科学に共通の概念であり，「何を観測するか」に応じて「巨視的古典論から素粒子論に至る理論モデルのうちどれを採用するか」に注意をはらう必要があることを意味している。このような考え方の起源をデモクリトスに見ることができよう。デモクリトスは，物質を小さく切り刻んでいったとき，それ以上小さく分割できない最小単位があると考え，これを「アトム」と呼び，これが「原子」の語源になったことはよく知られている。現代の科学の知識からすると，アトムもまた原子核や電子といった構成要素からできているということであるが，原子という性質を適用できる最小限界はやはり原子なのである。それ以上分割すれば，もはや原子核や電子が見えるだけで，原子としての性質は失われてしまう。ここで逆の考え方をするとまた重要なことが分かる。原子という寸法よりも大きいスケールで見て原子の性質を調べようとするならば，それらの構成要素である原子核や電子の個々の振る舞いにまで気を配る必要はないということである。これがむしろ現代版の「アトム」の意味である。

3. パラダイム・シフトのための質疑応答

【質問その1】

光学の教科書によると平面境界で光が全反射す

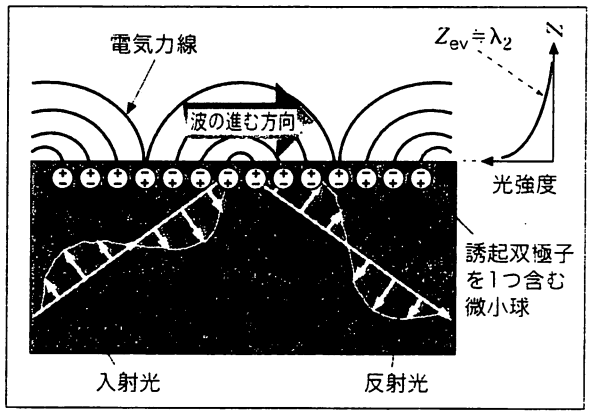

図3 無限平面状の表面のエバネッセント光の発生の原理

るときエバネッセント光が発生し，その厚みは波長程度であるが，図1では第1の球の直径程度である。両者の違いは何か？

【答え】

これは物質中およびその表面付近に発生する双極子の空間分布の違いに起因する。すなわち，平面の場合には**図3**に示すように無限に広い表面に入射光，反射光の位相に応じた向きの極性をもった双極子が多数誘起される。その結果，双極子間の電気的な相互作用を表わす電気力線は面内の広い範囲におよび，しかもそれらが完全な位相関係をもっていて，平面境界の外側にまったく伝搬光を生じない。これらの電気力線の総和としてのエバネッセント光のしみ出しの厚みは入射角で決まり，通常は光の波長程度となる。一方，図1の球の場合，直径aが光源の波長に比べずっと小さいので入射光の位相は球の内部ではほとんど一定である。したがって，双極子の配列は入射光の位相を反映することはできず，極性の揃った双極子が誘起される。これは全体としては大きなアンテナとなり伝搬光を生ずる。また，その範囲は球内部のみであり，分極を球の表面形状に合わせて配列させるための双極子間の電気的な相互作用はごく近隣に限られる。この部分が微小球の場合の近接場光であり，その電気力線が球表面にしみ出す範囲は小さく，その厚みはa程度となる。平面の場合がむしろ非常に特殊なケースなのである。

以上のように，近接場光は物質表面に誘起される双極子の間の電気的相互作用に起因するので，その空間分布はそれらの双極子の空間的分布に依存する。したがって近接場光のしみ出しの厚みは物質寸法に依存し，光源の光の波長には依存しない。これに対し，平面上のエバネッセント光はこの特徴をもたず，入射光振幅の空間的な位相変化の周期である波長の情報を担っているので，この点において依然として従来の光学の枠組み内に留まっている。したがって図1の近接場光は平面上のエバネッセント光とは一線を画されるべきである。

【質問その2】

近接場光学顕微鏡のプローブ先端を電子顕微鏡で観察した結果をもとに，しばしば**図4(a)**のような模式図が描かれている。このとき開口直径はd_fである。ということは近接場光学顕微鏡の分解能もd_fか？

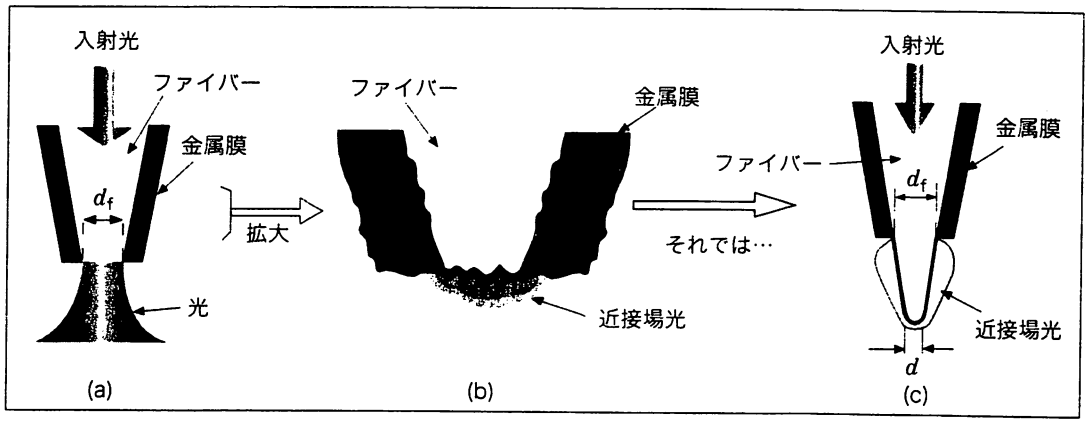

図4 (a)は金属膜が塗布された開口直径d_fのファイバープローブの構造，(b)は(a)の先端部分の拡大図，(c)は先端が金属膜から突出したファイバープローブの構造。先端曲率の直径はd。

【答え】

No! 電子顕微鏡像はプローブの光学的特性を表わしていない。実際には図4(a)の像のファイバー先端部にさらに近づいて観測すると図4(b)に示すように，さらに微小な凹凸をもつはずであり，【質問その1】の答えによればその凹凸の寸法に応じた空間的分布をもつ近接場光が生じている。したがって，プローブと試料との距離をこの凹凸の寸法まで近づけてこのような近接場光を測定すれば，凹凸の寸法程度の近接場光に至る成分までが観測にかかる。この考えを押し進めて，高い分解能を得るためのファイバープローブが図4(c)（および図2の内挿図）に示されている突出型プローブである。ファイバー先端部の曲率（直径d）が非常に小さくて，それが金属膜から突出しているので，より空間的に広がった近接場光成分に埋もれることなく高い分解能の画像が得られる。これは先端曲率程度の空間フーリエ周波数の成分をバンドパスフィルター的に選択して抽出する工夫である。また，根元の金属膜の開口（直径d_f）は伝搬光を遮断するために使っている。実際，これにより紐状のDNA 1本ずつの像が分離されて観測され，幅4nmが得られている[4]。なお，図4(a)の光はプローブから流れ出るように書かれているので，これは近接場光ではなく伝搬光である。近接場光らしく描くには図4(b)，(c)のように，あたかも水道の蛇口にぶら下がる水滴のようにしなければならない。

【質問その3】

近接場光の特性が入射光の波長とは無関係であるならば，近接場光は何色か？

【答え】

真空中（あるいは自由空間）の光でなければ波長は色とは関係ない。色に対応するのは光子エネルギーであるので，それは光の周波数である。したがって，図2中の2つの球を構成する物質の電子エネルギー変化をもたらす共鳴，発光などがない限り，第2の球からの散乱光は入射光と同じ周波数をもつので，同じ色に見える。

【質問その4】

分解能評価のための標準試料として回折格子を用いたいが，よろしいか？

【答え】

No! 近接場光の検出は図2にあるように2つの微粒子の間の二体散乱問題が基本である。回折格子は周期構造なので近接する複数の格子が検出に関与する多体の光散乱の問題となり，分解能評価などを複雑にする。

ところで従来の光学顕微鏡は空間フーリエ周波数軸上では回折限界を境としたローパスフィルター特性を有していたが，近接場光学技術はプローブ寸法によって決まるバンドパスフィルター特性を有する。したがって，分解能評価には従来とは異なる方法を用いるべきである。分解能を評価するにはまず画像のフーリエ解析で空間パワースペクトル密度を推定し，この高域遮断周波数を求め，この逆数を分解能の目安とするのが正しい[3]。このような測定に際し，空間的には白色雑音に対応する試料がよい。すなわち基板に降り積もった塵のようにランダムな寸法をもつ多数の微粒子が互いに自らの直径以上はなれて並んだようなものである。回折格子のような特性周波数をもつものは空間フーリエ周波数軸上で単に線スペクトルが得られるのみであり，装置の伝達関数の評価には不適当である。

また，近接場光の検出効率はプローブの特性によって決まるので，使用するプローブが決まった後に，そのプローブに対応する標準試料を検討すべきである。近接場光学顕微鏡一般に対する標準試料は存在しない。

【質問その5】

近接場光学用プローブ先端での近接場光発生効率(注2)が低くて使いにくいが…。

【答え】

確かに数年前までの効率は低く，1×10^{-6}程度であった。しかし現在ではファイバー中心部のコアの先鋭角を再現性よく制御加工し，効率を1×10^{-2}程度まで増加させることができるようになった。さらに，表面プラズモン効果などを併用す

ることもできるようになった。また，球レンズ付き平面開口プローブなども開発されており，現在ではプローブの効率が低いという常識は打破されつつある[3]。今後のいっそうの高効率化（同時にいっそうの高分解能化も）には再現性のよいプローブ作製技術の進歩が不可欠である。そのための再現性のよい量産技術としてはエッチング法がすぐれている。また，量産性はないが，試作用に自由度の高い加工を可能にするのが集束イオンビームを用いるドライプロセスである[3]。これらにより，紫外域（波長244nm）においても1kW/cm^{2}のパワー密度が得られるようになり，これを用いて金属や酸化物の微小パターンの光化学蒸気堆積法も実現している[5]。

（注2）発生効率≡（ファイバープローブ先端に発生する近接場光エネルギー）/（ファイバープローブ後端から入射させた伝搬光エネルギー）と定義するが，この測定の際，エネルギーではなくパワー比で求めている。特に定義式中の分子はファイバープローブ先端に発生する光全体のパワーを測定するので，ファイバープローブ根元直径d_fが十分に伝搬光を除去できる程度小さくない場合には，伝搬光のパワーも同時測定することになり，注意が必要である。

【質問その6】

せん断応力によりプローブ位置を制御する方法にはどのような問題があるか？

【答え】

虚像が見えてしまう。色々な説明の仕方があるが，そのうちの簡単なものを**図5**に示す。この図にあるように微小物質の表面に発生する近接場光の等エネルギー曲面とせん断応力の等ポテンシャル曲面とは互いに異なる。したがって，プローブがせん断応力の等ポテンシャル曲面を走査するとき，プローブは近接場光の等エネルギー曲面を横切る。この結果，光検出器に入る光パワーは変化するので，あたかも試料の凹凸が近接場光強度の変化として測られたような画像が得られる。例えば点A付近で観測される近接場光の強度変化はせん断応力の等ポテンシャル曲面の傾きが急であるからにほかならず，この近接場光学顕微鏡の分解能の高さを示しているのではなく，したがって虚像を見ていることになる。すなわちこれは光検出器を用いてせん断応力の空間的分布を測定しているに過ぎない。

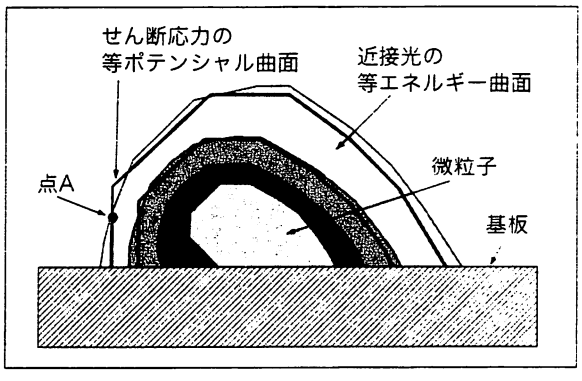

図5 微粒子表面の近接場光の等エネルギー曲面，およびせん断応力の等ポテンシャル曲面の比較

この虚像観測の可能性を排除するには，近接場光強度の測定値自身を制御信号として用いてプローブ位置を制御する。【質問その2】に対する答え中に記した幅4nmの紐状のDNAの像は，近接場光のみを用い，プローブを試料表面の1nm程度まで近づけて観測したものである。

【質問その7】

近接場光は顕微鏡に使われているが，そのほかの使い方はあるか？

【答え】

近接場光学顕微鏡は試料の形状を観測するものであり，このような観測は走査型トンネル顕微鏡，原子間力顕微鏡など，ほかの方法でも可能である。むしろ光の特徴を生かして，光源のフォトンエネルギーを掃引し，分光スペクトルを測定し，試料表面の構造解析をする方が有利である。

さらに，次のような原理により試料の加工が可能である：図2の第2の球を近づけると電気力線の分布ははじめの場合と異なるものになり，近接場光の空間的分布は壊されることになる。この破壊性の延長として，さらに球のなかの双極子の分布のようすが変わるほど強く近接場光を強く乱せば球の一部分がへこんだり，その構造や組成が変化することも考えられる。このように測定に付随

する破壊性に着目すると近接場光の利用は光学顕微鏡のような測定装置としてではなく，むしろ加工装置が本質的であることに気付く。実際に加工するためにはしばしば2つの球の役割を入れ替えて使う。すなわち，ファイバープローブの先端を第1の球とみなし，その後端から大きな強度の光を入れ，先端に近接場光を発生させる。これを第2の球表面に近づけるとその表面が窪んだり，構造変化する。このようにして第2の球を加工することができる。このような加工可能性こそがパラダイム・シフト実現可能性の根拠である。

【質問その8】

プローブ先端に近接場光を発生させ，それを試料に照射すれば，散乱光をプローブ外部の凸レンズで集めても高い分解能が得られるか？

【答え】

かならずしもそうとは言えない。たとえば半導体のフォトルミネッセンス測定の場合，プローブ先端の近接場光で局所的に半導体表面を励起しても，発生したキャリアーは1μm近くドリフトした後，再結合して発光する。したがってこの発光を凸レンズで集めてもその像の大きさはドリフト長程度あり，これはプローブ先端の寸法よりはるかに大きい。したがって，このような場合は発光もプローブを通して測定し，ドリフトの影響を除去しなければならない。このためには効率の高いプローブが必要であるが，すでにそれは開発されており，これを用いて半導体単一量子ドットのフォトルミネッセンス分光が行われている[3]。

4. まとめ

本稿冒頭に記したように近接場光技術は光学のパラダイム・シフトを実現する旗手として多くの方々が興味をもってくださるようになったが，従来の光学の手法と異なるので，素朴な疑問をもち，したがって参入に躊躇している方々も多い。本稿がその疑問解消の役にたち，多くの方々が参入するための心理的バリアーを取り払うことができれば幸いである。

参考文献

1) M. A. Paesler and P. J. Moyer: "Near field Optics", John Wiley & Sons, New York (1996)
2) J. P. Fillard: "Near Field Optics and Nanoscopy", World Scientific, Singuapore (1996)
3) M. Ohtsu (ed.): "Near-Field Nano/Atom Optics and Technology", Springer-Verlag, Tokyo/Berlin/Heidelberg/New York (1998)
4) S. Mononobe, R. UmaMaheswari, and M. Ohtsu: "Fabrication of a Nanometer-Level Resolving Probe with Metal-Dielectric-Metal Coat for Near-Field Imaging of Single Strand DNA Molecules", Technical Digest, The 5th International Conference on Near Field Optics and Related Techniques, Shirahama, Japan, PC6, pp.159～160 (December 6～10, 1998)
5) V. Polonski, Y. Yamamoto, M. Kourogi, H. Fukuda, and M. Ohtsu: "Nanometric Pattering of Zinc by Optical Near-Field Photochemical Vapour Deposition", J. Microscopy (May, 1999) 印刷中

Near-Field Optical Technology for Nano/Atom Photonics

M. OHTSU
Interdisciplinary Graduate School of Science and Engineering, Tokyo Institute of Technology, 4259 Nagatsuta, Midori-ku, Yokohama 226, Japan
(also with Kanagawa Academy of Science and Technology, KSP-East, Rm408, 3-2-1 Sakado, Takatsu-ku, Kawasaki 213, Japan)

ABSTRACT

In the workshop, requirements on near-field probe fabrication technology were presented to realize a new field of nano/atom photonics. As an example, fabrication of planar probe array for high density optical storage was demonstrated and related problems were presented for nano photonics. On atom photonics, progress of atom guidance by optical near-field was reviewed to realize an atomic-level deposition in forming the crystal surface.[1] Among these topics, this post-workshop report will focus on technical problems that have to be solved for realizing high density optical memory by optical near-field.

Experiments on the heat-mode[2] and the photo-mode[3]write/read-out(W/R) by optical near-field have revealed 1Tb/inch^2-class high density optical memory, where the limit on density is determined by the size of the optical near-field probe tip. However, there are a lot of problems to be solved to realize a practical optical memory, being compatible with the future commercial products which can be mass produced by industry. The problems are categorized to four. They are:

I SOFTWARE

What is the expected application software. For example, does it provide the information on personal health care, library data base, motion picture, weather forecasting, and so on? The form of the memory (e.g., read-only, erasable, etc.) strongly depends on these applications.

II SYSTEM

1. Fast driving mechanism should be developed, e.g., by following a flying head technology of hard disk drive.
2. Technique of precisely controlling the gap between the W/R head and the storage medium should be developed. The gap should be as narrow as 10-50 nm.
3. Accurate tracking or tracking-less drive should be developed to scan the W/R head.
4. In the case of the removable memory, the W/R head should also be removable with the disk. In this case, a low-cost W/R head with a reliable packaging should be developed, e.g., using a LED as a light source instead of using a LD.
5. Ultrasensitive photon detection technique should be developed.

III DEVICES

1. A probe with high throughput should be developed in order to realize a fast driving head.
2. Interface devices connecting light source, probe, and detector should be developed.
3. Flying head, actuator, and so on, should be developed for fast driving and scanning.

IV STORAGE MEDIA

1. It is essential to search for sensitive interaction mechanisms between the nano-particle and the optical near-field.
2. Novel media with small grain/domain size should be found.
3. Heat diffusion mechanism in nanometric volume should be studied.
4. An ultra-thin protection layer for storage media should be developed.

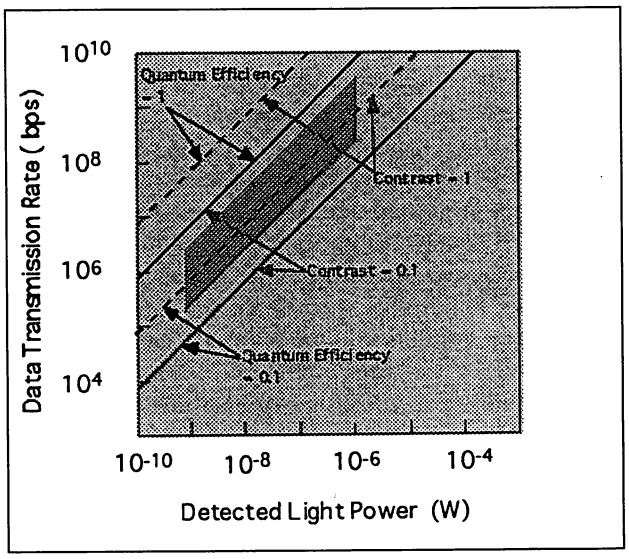

Figure 1: *Relation between the detected light power and the data transmission rate, which is limited by the shot noise. Shadowed area represents that the relation between power and rate to be realized by the present experimental condition. Contrast: ratio between the light reflected from the stored and non-stored part of the surface of the storage medium.*

Among the problems listed above, we have considered the problems on the devices. Since we have developed a precise and reproducible probe fabrication technique based on selective chemical etching of a fiber,[4,5] the detected light power by our probe, due to the reflection from the surface of the storage medium, has become as high as 1 μW. In this case, the data transmission rate for read-out, limited by the shot noise associated with the detected photon number, is estimated to be as high as or even higher than 100 Mb/s assuming that the contrast of the memory is 0.3, the quantum efficiency of the photodetector is 0.3, bit-error-rate is 10^{-9} (@PCM mode), and the optical frequency is 600 THz (Figure 1).

It is promising to have such a high data transmission rate in order to realize a fast read-out. However, the problem is how to scan the read-out head. If one uses a single probe tip to read-out the memory with the pit spacing of 10 nm, the scanning speed has to be as high as 1 m/s to realize the 100Mb/s data transmission rate. On the other hand, if the two-dimensional probe array with 100 x 100 elements is used, the scanning speed can be reduced to 100 μm/s, which can be easily realized by a conventional driving technology.

However, probe array with two-dimensional sharpened tip elements cannot be practical because the fluctuations in the tip lengths cannot be reduced to 10 nm by the existing micro/nano fabrication process. In order to avoid this difficulty, we have proposed a planar apertured

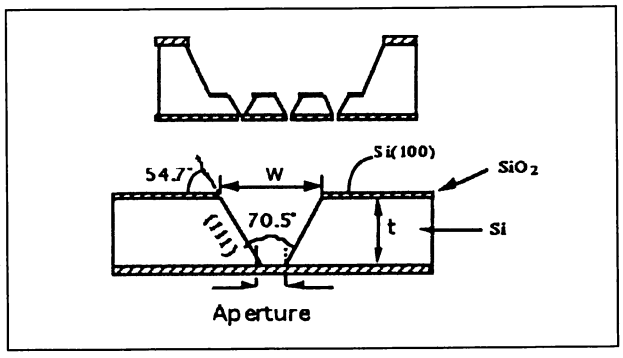

Figure 2: *Cross sectional profile of a planar apertured probe array.*

probe array fabricated by a silicon planar process (Figure 2). Advantages of this probe array are: (1) suitable for flying head technique of the hard disk drive, (2) precise gap control is possible by following the hard disk technique, (3) parallel information processing is possible, and more advantageously, the tracking-less read-out is possible,[6] and (4) compatible with integration of a slab waveguide and an array of photo-detectors.

Fabrication process includes oxidation, photolithography, removing SiO_2, anisotropic etching to form V-grooves and windows, and deposition of Au film. Figure 3 shows a SEM image of the fabricated probe array. Among the fabricated several arrays, the smallest aperture size was 80 nm.[7] It should be noted that the fluctuations of the size of each aperture in the array is not essential for tracking-less read-out. Instead, the separation between the adjacent aperture must be regulated, which can be assured by carefully designing a mask pattern for

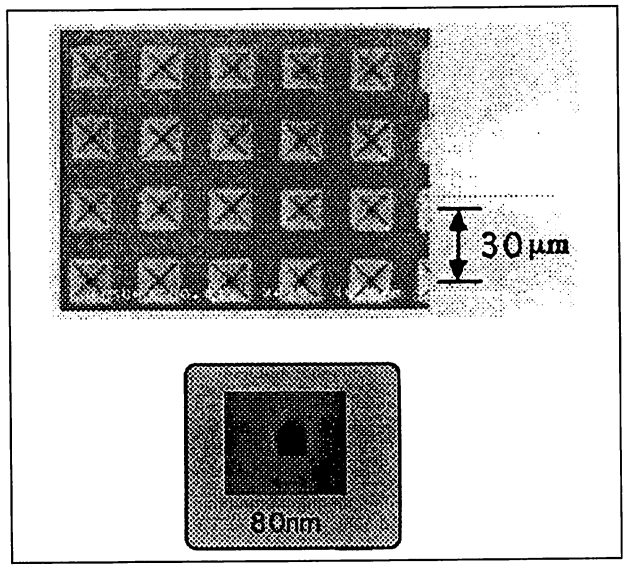

Figure 3: *SEM image of the fabricated planar apertured-probe array (upper) and that of the smallest size aperture (lower).*

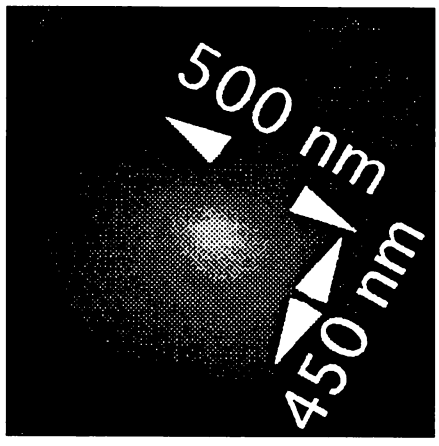

Figure 4: Measured spatial distribution of the optical near-field intensity on the aperture.

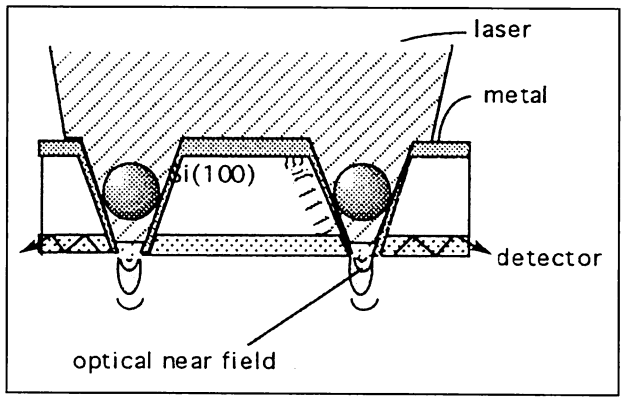

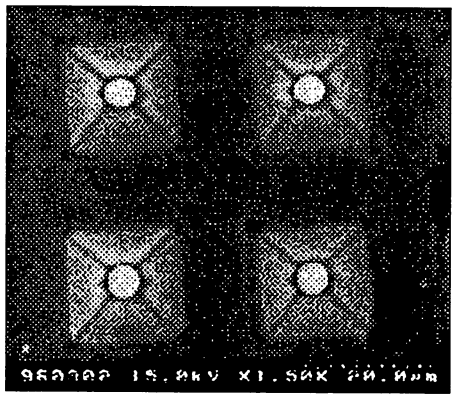

Figure 5: A schematic of the cross sectional profile of a planar apertured probe array with ball lenses and the SEM image of the fabricated array.

the photolithography in the present fabrication process.

Spatial distribution of the optical near-field intensity generated on the aperture was measured by scanning a conventional sharp fiber probe tip on the planar aperture. As is shown by Figure 4, a clear Gaussian profile of distribution was observed, from which a reliable operation of the probe array was confirmed. It was also confirmed semi-quantitatively that the throughput of this aperture is as high as, or even higher than that of our high throughput probe.[8] For further increase of the throughput, an array using a ball lens was proposed and fabricated (Figure 5).[6]

As a future outlook, it is expected that the conventional technology for optical disk and hard disk will be combined with the near-field optical technology to realize a 1Tb/inch^2-class high density near-field optical memory. This is because the driving mechanism is similar to that for the hard disk memory and a large amount of technology/know-how have been accumulated for conventional optical disk.

In summary, problems on software, system, devices, and storage media were presented to realize a high density near-field optical memory. Shot noise-limited data transmission rate, as high as 100 Mb/s, was estimated. Planar apertured probe array was proposed for trackingless and high-speed read-out. Fabrication of Si planar apertured probe array with the smallest aperture size of 80 nm was demonstrated. Possibility of increasing the throughput via the use of a ball lens was also demonstrated.

ACKNOWLEDGEMENT

We acknowledge Prof. K. Tsutui and Dr. M. Kourogi (TIT), Drs. S. Mononobe and R. Uma Maheswari (KAST), Drs. M.B. Lee and N. Atoda (NAIR) for their collaboration and discussions.

REFERENCES

1. M. Ohtsu(ed.), Near-Field Nano/Atom Optics and Technology, Springer-Verlag, Tokyo, Berlin, New York, 1998.
2. E. Betzig, et.al., *Appl. Phys. Lett.*, 61, p.142 (1992).
3. S.Jiang, et.al., *Opt. Commun.*, 106, p.173 (1994).
4. M. Ohtsu, *J. Lightwave Technol.*, 13 p.1200 (1995).
5. S. Mononobe, et.al., *J. Lightwave Technol.*, 14, p.2231 (1996).
6. M. Kougori, et.al.,The 6th Workshop on Near-field Optics, July 3, 1997, Osaka, Japan, *Tech. Digest*, p.73 (in Japanese).
7. M.B. Lee, et.al., The Pacific Rim Conference on Lasers and Electro-Optics (CLEO/PR'97), July 14-18, 1997, Makuhari, Japan, *Tech. Digest*, paper number WL2, p.91.
8. T. Saiki,et.al., *Appl. Phys. Lett*, 68, p.2612 (1996).

ISSN 0919-9195

電気学会技術報告 第715号

光と電子による
ナノメータ領域材料評価と制御

電子材料ナノメータ領域
評価技術調査専門委員会

1999年2月

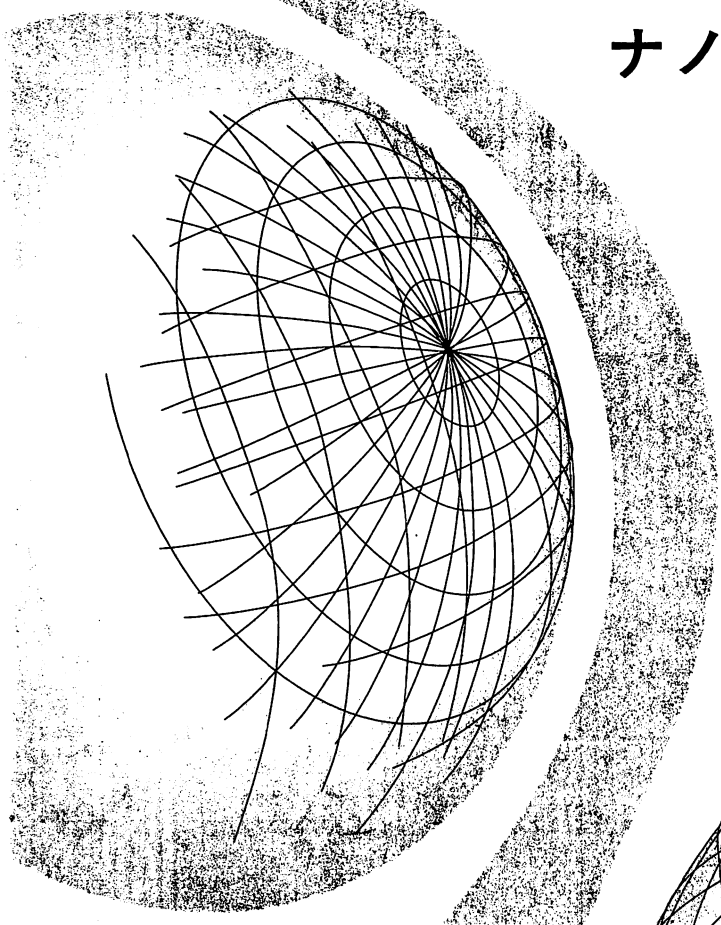

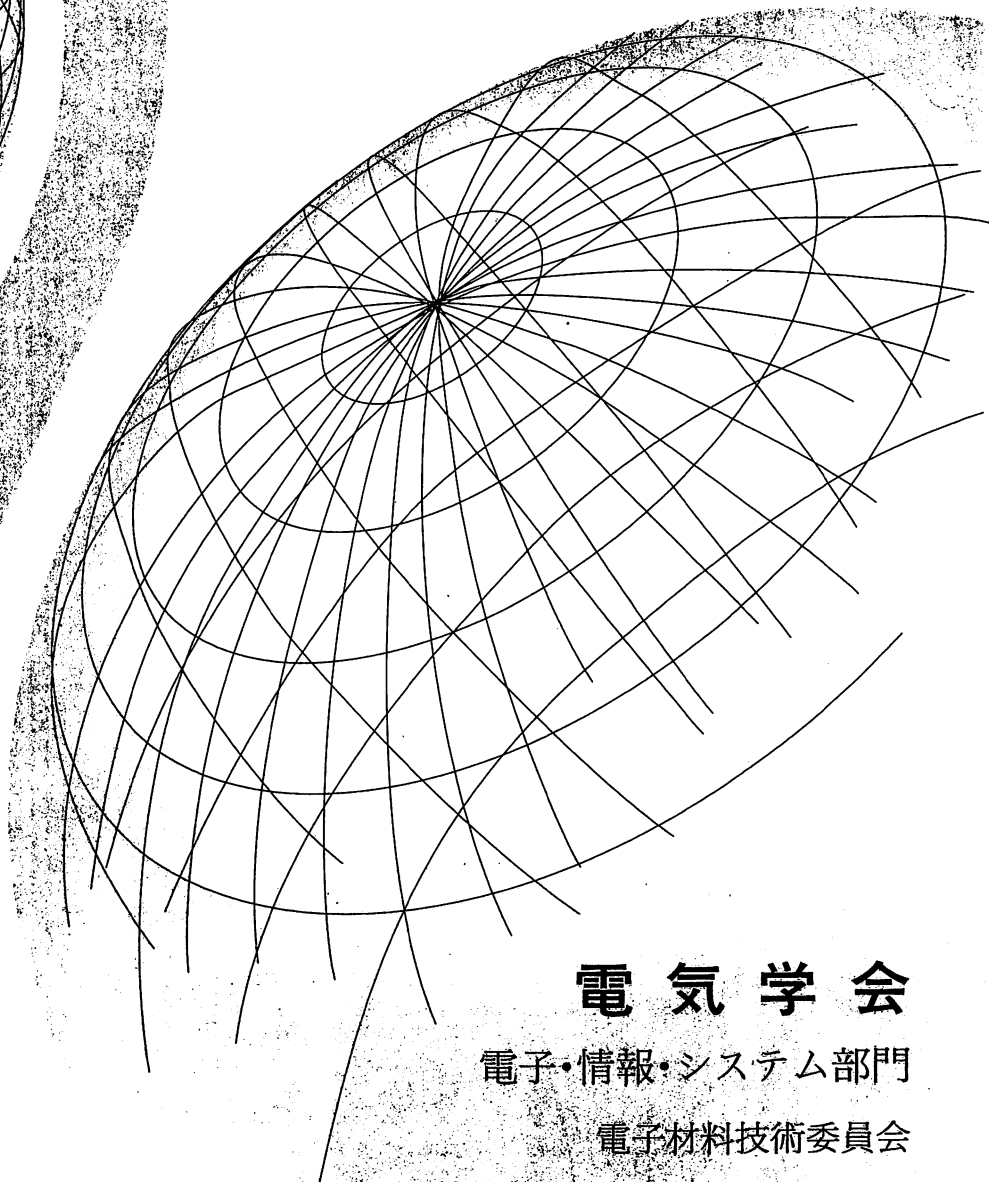

電 気 学 会
電子・情報・システム部門
電子材料技術委員会

光と電子によるナノメータ領域材料評価と制御

電子材料ナノメータ領域評価技術調査専門委員会編

目　　次

電子材料ナノメータ領域評価技術調査専門委員会委員

Subwavelength spatial resolution mapping measurement using near-field spectrometers

Yoshihito Narita, Toshiyasu Tadokoro, Teruki Ikeda, Toshiharu Saiki, Shuji Mononobe, and Motoichi Ohtsu

Recent advances in techniques used to integrate and manufacture semiconductors, metals, and organic materials may allow new materials as well as new devices, such as semiconductors, higher-density memories, and devices used in biotechnology, to be developed. However, these techniques require further study and development. In addition, products manufactured using such techniques will require nanometer-scale inspection.

Surface characterization of these semiconductors, metals, and organic materials can be performed using chemical analysis and various analytical methods, such as scanning electron microscopy (SEM) and transmission electron microscopy (TEM), X-ray microanalysis (XMA), scanning probe microscopy (atomic force microscopy [AFM] and scanning tunneling microscopy [STM]), and spectrometry (Raman, IR, UV-VIS, and photoluminescence). Topographic measurement methods have achieved submicron spatial resolution (SEM and AFM) and have been commonly used to perform nanometer-scale surface characterization. In contrast, although Raman and photoluminescence (PL) spectroscopy can be used to analyze important material characteristics, such as the molecular structure, quantum structure, and optical characteristics of a sample, the spatial resolutions of these methods are restricted to only 1 μm.

The present study proposes a new technique that provides the necessary spatial resolution, in which near-field optics are applied to conventional microspectroscopy. In the conventional lens imaging system, the spatial resolution is determined using the diffraction limit of the light. Thus, the minimum spot size on the sample surface is of the same scale as the wavelength of the light. However, the distribution of near-field light around the optical aperture depends not on the wavelength of light, but on the size of the aperture. Thus, the subwavelength spatial resolution is achieved using a subwavelength aperture. The concept of applying near-field optics to microscopes was originally introduced by Synge in 1928.[1] In the 1990s, researchers developed near-field optical microscopes (NOM) using optical fibers as probes.[2,3]

By combining the NOM with the spectrometer, two near-field spectrometers were developed: a near-field Raman spectrometer and a near-field PL spectrometer. Using near-field technology, a spatial resolution of less than 100 nm can be achieved for both Raman and PL spectroscopy, whereas conventional Raman and PL spectroscopy have spatial resolutions of over 1 μm. Furthermore, these systems enable the topographic and spectral mapping images of the sample surface to be measured simultaneously.

Mr. Narita, Mr. Tadokoro, and Dr. Ikeda are with ***JASCO Corp.****, 2967-5, Ishikawa-cho, Hachioji-shi, Tokyo 192-0032, Japan; tel.: 81-426-46-4118; fax: 81-426-46-4126. Dr. Saiki and Mr. Mononobe are with the Kanagawa Academy of Science and Technology, Kanagawa, Japan. Dr. Ohtsu is with the Interdisciplinary Graduate School of Science and Engineering, Tokyo Institute of Technology, Yokohama, Japan.*

Using near-field technology, a spatial resolution of less than 100 nm can be achieved for both Raman and PL spectroscopy, whereas conventional Raman and PL spectroscopy have spatial resolutions of over 1 μm.

The present study demonstrates near-field Raman mapping of polydiacetylene (PDA) single crystal and near-field PL mapping of InGaAs quantum dots (QDs).[4,5] PDA is an organic nonlinear optical material that has attracted great interest due to its optical properties.[6,7] The QD has a zero dimensional quantum structure, and potential applications as a laser source are being considered due to the unique energy-level structure of the QD.

Experimental

Schematic diagrams of the proposed near-field spectrometers are shown in *Figure 1*. The system consists of a probe, shear force feedback loop, and monochromator.

The excitation light is directed through the probe, which is fabricated using the chemical etching method.[8,9] This method of probe fabrication has very high reproducibility, and many different types of probe can be fabricated simply by changing the composition of the etching solution. The probe surface is coated using a metal such as gold or aluminum, and the metal at the top of the probe is removed to create an optical aperture. The size of the aperture is optimized at a diameter of 100–1000 nm, depending on the application.

The distribution of near-field light is several tens of nanometers around the probe aperture. Thus, a shear force feedback loop was used to maintain the probe–sample separation at 10 nm.[10] The probe is oscillated laterally at less than 1 nm amplitude at the first order resonance frequency (10–30 kHz) of the probe. The shear force interaction between a probe and a sample affects probe oscillation. Specifically, the amplitude of the oscillation varies according to the separation between the probe and the sample. Using a 1.3-μm laser diode and a PIN photodiode, the amplitude of the probe is monitored. The output of the photodiode is locked into the oscillation frequency and is fed back to the sample *Z* stage, which controls the separation between the sample and the probe. The topographic image of the sample surface is then measured by monitoring variations in the position of the sample *Z* stage. The wavelength of the excitation laser is selected according to the application. For PDA measurement using a near-field Raman spectrometer, the second harmonic (532-nm wavelength) of a Nd:YAG laser was used. After the mapping measurement, the aperture size was determined to be 150 nm, using SEM photography. A 633-nm He–Ne laser was used to measure the PL of the InGaAs QDs because PL is observed in the 900–1000 nm region. The size of the aperture was determined to be 1000 nm. Regardless of the wavelength of the excitation laser, a maximum power of 10 mW is coupled to the probe. For a 100-nm aperture, a power of approximately 10 μW is used to excite a sample through a probe because the optical throughput of probes is typically 10^{-3}.

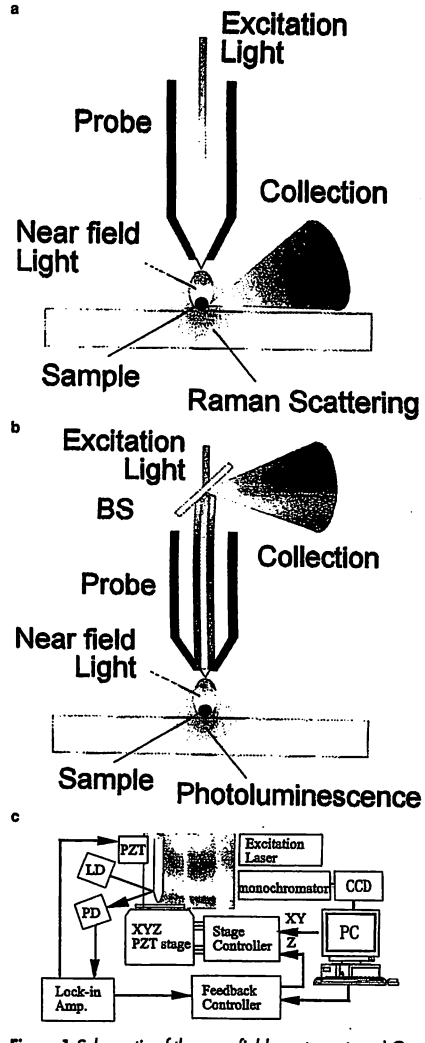

Figure 1 *Schematic of the near-field spectrometer. a) Optical arrangement of the near-field Raman spectrometer; b) optical arrangement of the near-field photoluminescence spectrometer; c) block diagram of the near-field spectrometers. The shadowed area shown in (c) represents either the near-field Raman spectrometer shown in (a) or the near-field photoluminescence spectrometer shown in (b).*

Raman scattering is collected in the direction perpendicular to the probe using a 100× objective lens. This optical arrangement is called the illumination mode.

In contrast, the illumination–collection mode is used in near-field PL spectroscopy. In the illumination–collection mode, PL is collected using a probe in order to achieve subwavelength spatial resolu-

tion because carrier diffusion results in PL from a 1-μm-diam area, even if an area of 100 nm is excited. Collected Raman scattering and PL light are introduced into a monochromator (NRS-2100 Raman spectrometer or CT-50C monochromator, JASCO Corp., Tokyo, Japan) through a notch filter or dichroic mirror, which attenuates the excitation light. The signal is detected using a liquid nitrogen cooled charge coupled device (CCD) detector. A probe having an aperture of 100 nm allows photon detection rates on the order of 10 photons/sec for PDA Raman measurement.

For low-temperature PL measurement, the sample stage and probe are set in a helium cryostat. Temperature is monitored at the side of sample stage and maintained at 5 K during measurement.

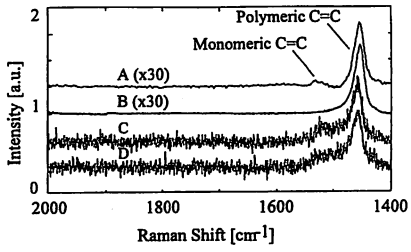

Figure 2 *Near-field Raman spectra of polydiacetylene. Spectra A and B, obtained using a commercial Raman spectrometer (NRS-2100), are reference Raman spectra of polydiacetylene. Spectra C and D, obtained using a near-field Raman spectrometer, are separated spatially by 100 nm. Spectra B, C, and D were obtained using the same polydiacetylene crystal. Spectrum A was obtained using another polydiacetylene crystal that shows more monomeric character.*

Results and discussion

A near-field Raman mapping result of the PDA surface is shown in *Figures 2* and *3*. The mapped area is 1 μm × 1 μm and contains 10 × 10 points. Note that this is almost identical to the spatial resolution of the conventional Raman spectrometer. It takes approximately 17 hr to measure this area, which corresponds to 5 min per point. The reference spectra of PDA (Figure 2, spectra A and B) have Raman peaks at 1457 cm^{-1} and 1520 cm^{-1}. These peaks are observed even in the near-field Raman spectra (Figure 2, spectra C and D). The topographic mapping image (Figure 3*a*) shows a maximum surface roughness of 870 nm. The intensity ratio mapping image of monomeric and polymeric Raman peaks (Figure 3*b*) shows a maximum difference in the scan area of 0.4.

The PDA crystal is composed of successive C-C, C=C, and C≡C bonds. When successive bonds are numerous, PDA indicates a polymeric optical character, and the C=C Raman peak is observed at 1457 cm^{-1}. When successive bonds are few, however, PDA indicates a monomeric optical character and the C=C Raman peak shifts to 1520 cm^{-1}. Therefore, the observed 1457 cm^{-1} and 1520 cm^{-1} peaks are assigned to polymeric and monomeric peaks, respectively. As shown by spectra C and D of Figure 2, the monomeric peaks separated spatially by 100 nm have different intensities. The spatial distribution of the intensity ratio of monomeric and polymeric peaks (Figure 3*b*) shows the two-dimensional distribution of polymeric and monomeric areas of the PDA surface.[4] The higher the intensity ratio, the more monomeric is the surface of PDA.

In addition, the intensity ratio of monomeric and polymeric peaks reveals the difference in optical character in subwavelength spatial resolution. The spatial resolution of the near-field Raman spectrometer is higher than the excitation wavelength (532 nm), which is half of the scanned area, and is much higher than the spatial resolution of the conventional Raman spectrometer.

Since the excitation power is restricted to 10 μW, the Raman spectra of samples having low Raman scattering efficiency are difficult to measure. However, the Raman scattering efficiency of PDA is very high due to the resonance Raman effect. Typically, the excitation and detection efficiencies of the near-field Raman spectrometer are three orders of magnitude lower than those of the conventional micro-Raman spectrometer. Near-field Raman spectra have been reported for samples having relatively high Raman scattering efficiency, such as silicon, polydiacetylene, diamond, Rd doped KTP (potassium titanyl phosphate), rhodamine 6G, 3-hydroxykynurenine, cobalt phthalocyanine, benzoic acid, CCl_4, and poly(phenylene vinylene).[11-18] However, expanding the applicability of this method requires detection efficiencies increased by at least two orders of magnitude. This might be achieved through improving the probe and the detection system in addition to increasing the efficiency of the Raman scattering collection.

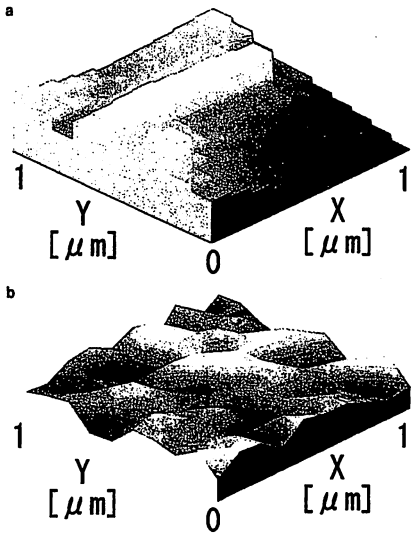

Figure 3 *Near-field Raman mapping of the polydiacetylene surface. a) Surface topography of polydiacetylene. The contrast variations reveal height changes in the 0–870 nm range. b) Mapping image of the ratio of polydiacetylene monomeric and polymeric Raman peaks. The contrast variations reveal ratio changes in the 0–0.4 range.*

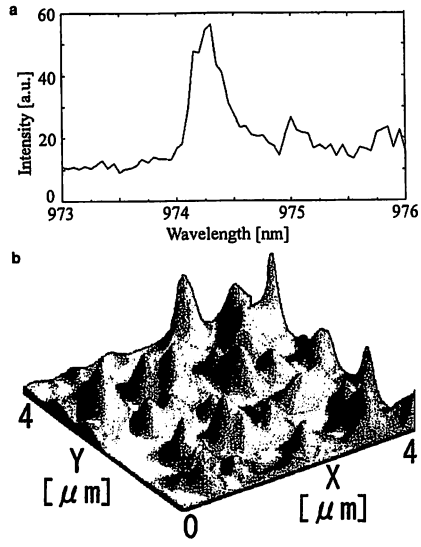

Figure 4 *Near-field photoluminescence mapping of quantum dots (courtesy Dr. K. Nishi, NEC Corp., Japan). a) Photoluminescence spectrum of a single quantum dot. The peak width is 0.5 meV. b) Spectral mapping image of quantum dots. The scans cover 4 μm.*

Figure 4 shows the mapping of the near-field PL spectra of QDs.[5] The typical dot diameter and height are approximately 30 nm and 15 nm, respectively. The dots are covered by 70-nm-thick GaAs and AlGaAs cap layers. Measurement was performed in the weak excitation region, i.e., 0.2 W/cm^2 at the aperture of the probe. A PL peak having a peak width of 0.5 meV can be clearly observed in Figure 4*a*. The PL peak corresponds to the emission from the ground states of a dot.

Figure 4*b* shows the spatial distribution of QDs having a PL wavelength of 975 nm. The diameter of the smallest QD observed is 160 nm. Although the 1000-nm aperture probe was used for the measurement, the near-field interaction between the probe and the QD allows higher spatial resolution. Investigation of the excitation power dependence of the PL intensity of each QD allows the origin of the PL to be clarified, i.e., a ground state excitation, a ground state excitonic molecule, or higher excited states.

The results of these investigations will clarify many of the optical characteristics of QDs and QD lasers. The proposed low-temperature near-field PL spectrometer is also useful for the qualitative analysis of GaAs impurities and the investigation of the optical properties of quantum wires.

References

1. Synge EH. A suggested method for extending microscopic resolution into ultra-microscopic resolution. Phil Mag 1928; 6:356–62.
2. Pohl DW, Courjon D. Near field optics. In: Pohl DW, Courjon D, eds. Dordrecht: Kluwer Academic Publishers, 1993, vol. 242 of NATO ASI Series E.
3. Ohtsu M. Progress of high-resolution photon scanning tunneling microscopy due to a nanometric fiber probe. J Lightwave Technol 1995; 13(7):1200–21.
4. Narita Y, Tadokoro T, Ikeda T, Saiki T, Mononobe S, Ohtsu M. Appl Spectrosc 1998; 52(9):1141–4.
5. Saiki T, Nishi K, Ohtsu M. Low temperature near-field photoluminescence spectroscopy of InGaAs single quantum dots. Jpn J Appl Phys 1998; 37, 3B:1638–42.
6. Exarbos GJ, Risen WM Jr, Baughman RH. Resonance Raman study of the thermochromic phase transition of a polydiacetylene. J Am Chem Soc 1976; 98(2): 481–7.
7. Kobayashi T, Yoshizawa M, Stamm U, Taiji M, Hasegawa M. Relaxation dynamics of photoexcitations in polydiacetylenes and polythiophene. J Opt Soc Am B 1990; 7(8):1558–78.
8. Mononobe S, Ohtsu M. Fabrication of a pencil-shaped fiber probe for near-field optics by selective chemical etching. J Lightwave Technol 1996; 14(10):2231–5.
9. Mononobe S, Saiki T, Suzuki T, Koshihara S, Ohtsu M. Fabrication of a triple tapered probe for near-field optical spectroscopy in UV region by selective etching of a multistep index fiber. Opt Commun 1998; 146:45–8.
10. Beztig E, Trautman JK. Near-field optics: microscopy, spectroscopy, and surface modification beyond the diffraction limit. Science 1992; 257:189–95.
11. Sharp SL, Warmack RJ, Goudonnet JP, Lee I, Ferrell TL. Spectroscopy and imaging using the photon scanning-tunneling microscope. Acc Chem Res 1993; 26(7):377–82.
12. Tsai DP, Othonos A, Moskovits M. Raman spectroscopy using a fiber optic probe with subwavelength aperture. Appl Phys Lett 1994; 64(14):1768–70.
13. Jahncke CL, Paesler MA, Hallen HD. Raman imaging with near-field scanning optical microscopy. Appl Phys Lett 1995; 67(17):2483–5.
14. Smith DA, Webster S, Ayad M, Evans SD, Fogherty D, Batchelder DN. Development of a scanning near-field optical probe for localized Raman spectroscopy. Ultramicroscopy 1995; 61:247–52.
15. Jahncke CL, Hallen HD, Paesler MA. Nano-Raman spectroscopy and imaging with a near-field scanning optical microscope. Raman Spectrosc 1996; 27: 579–86.
16. Grausem J, Humbert B, Burneau A, Oswalt J. Subwavelength Raman spectroscopy. Appl Phys Lett 1997; 70(13):1671–3.
17. Emory SR, Nie S. Near-field surface-enhanced Raman spectroscopy on single silver nanoparticles. Anal Chem 1997; 69(14):2631–5.
18. Webster S, Batchelder DN, Smith DA. Submicron resolution measurement of stress in silicon by near-field Raman spectroscopy. Appl Phys Lett 1998; 72(12): 1478–80.

実験室

近接場光学用プローブ

東京工業大学総合理工学研究科　大津元一

§1　まえがき

近接場光は微粒子表面に局在し，微粒子寸法程度の厚みをもつ非伝搬光であり，固体をはじめとする各種物質の極微形状計測，分光分析，加工，さらには原子操作などに使われている[1~3]．これを検出するには，**第1図**(a)に示すように第二の微粒子を近接場光内に挿入し伝搬光に変換する(すなわち非伝搬光を第二微粒子で散乱する)．この第二微粒子はプローブと呼ばれる．このとき，近接場光の寸法依存局在性の特徴を生かすために変換する体積はできるだけ小さい方がよいが，二つの微粒子の寸法が等しいときに変換効率が最大となるので[1,2]，プローブの寸法は第一微粒子の寸法と同等であることが有利である．したがって，プローブの特性は測定対象である第一微粒子の寸法，形状に依存する．さらに変換効率は二つの微粒子による近接場光の散乱効率によって決まるので，これらの微粒子の構造にも依存する．

以上のように近接場光の検出には，近接場光の散乱によって光学的に結合した状態にある二つ微粒子の近距離電磁相互作用の特性を勘案する必要がある．すなわち非伝搬光である近接場光のうちのいかに小さな体積をいかに効率よく伝搬光に変換するかにかかっている．

この二点を実現するために第1図(a)の基本形の第二微粒子のかわりに，より実際的に用いられるプローブを第1図(b)に示す．このような先鋭化されたプローブは各種誘電体材料をもとに作ることができるが，加工制御性の点でガラス製のファイバーがよく用いられる．ファイバーは伝搬光を伝送するコア部と，その支えのクラッド部からなるが，この図ではコア部が突出し，先鋭化されている場合を示す．これをさらに各部の役割に分けて模式的に表わすと第1図(c)のようになる．すなわち円錐形の最先端部①は第1図(a)の第二微粒子の役割をし，空間分解能，感度に寄与する．傾斜部の②はコントラストに寄与する．金属膜の被覆された傾斜部③は①,②で散乱され伝搬光に変換された光を，④の伝送線路の導波モードに結合する役割を果たす．根元部の④は伝搬光を従来のファイバーの機能を用いてファイバー後端まで伝送するための伝送線路である．

①~④の部分の性能を十分に高めるためには

①について：　できるだけ小さくし，検出の空間分解能を高くする．金属微粒子などを用い散乱

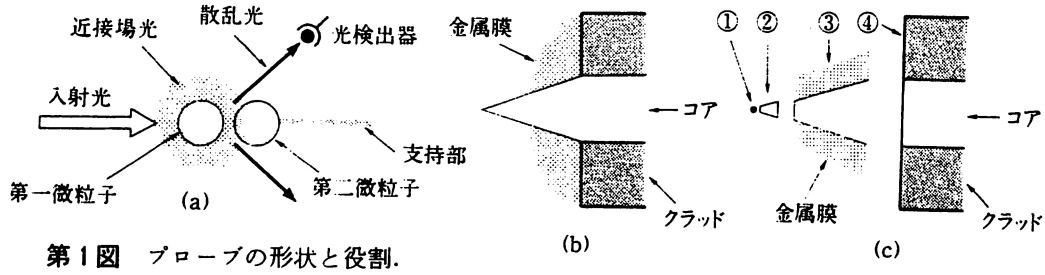

第1図　プローブの形状と役割．
(a) 第一微粒子表面の近接場光と，それを散乱するプローブとしての第二微粒子．
(b) ファイバープローブの断面形状．
(c) 役割別に分離したファイバープローブの概念図．

効率をあげる．

② について： 傾斜角をできるだけ小さくして低空間フーリエ周波数成分の検出効率を下げ，コントラストを上げる．傾斜形状を調節して導波モードへの結合効率をあげる．

③ について： 傾斜形状を調節して導波モードへの結合効率を上げる．

④ について： 伝送する光波長に対して損失の少ない材料を用いる．

これらの考慮のもとに目的に応じた各種プローブが考案されている．これら各種プローブの詳細を次節以下に記す．

§2 ファイバープローブ

標準的なプローブとしてシリカガラス製の光ファイバーを用いたプローブが広く使われている．先端微小化のための先鋭化の加工法として，ファイバーを加熱し引っ張る技術が開発されているが，加工精度，歩留まり，などの点で問題がある．特に前節の①～③の機能を引き出すことができない．これを打破する方法として緩衝フッ酸溶液による選択化学エッチングによる方法が発達しているので，本節ではこの方法を概説する．

選択化学エッチングの基本的方法は体積比が NH_4F(40重量%):HF(50重量%):$H_2O=X:1:1$ の緩衝ふっ酸溶液中にファイバーを約一時間浸し，クラッド端部を除去してコア部を選択的に先鋭化する[1]．たとえば $X=10$～30 のときのコアの先鋭角はコア中の GeO_2 濃度によって決まり，最小値をとる．このことは先鋭角がエッチング溶液の組成のばらつきによらず高い再現性で作成できることを示している．**第2図**は先鋭化されたコアの先端部の例を示す．前節の①の機能は先端部の曲率半径の寸法が対応するが，本方法ではそれは2 nm程度またはそれ以下が実現している．また，先鋭角の再現性が高いことは①～③部の寸法の最現性も高いことを意味している．先鋭角の最小値は14度であり，これはコア中の GeO_2 の濃度が23モル%のときに得られた．なお，先鋭化の素過程として，コア，クラッドの組成の違いにより，発生する反応生成物(それぞれ $(NH_4)_2GeF_6$, $(NH_4)_2SF_6$)が溶液へ溶解する速度の差に起因するといわれている．

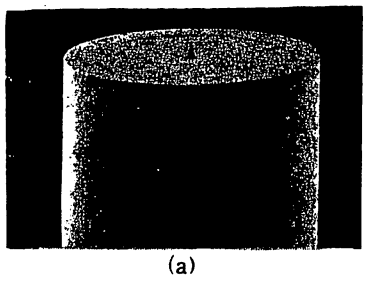

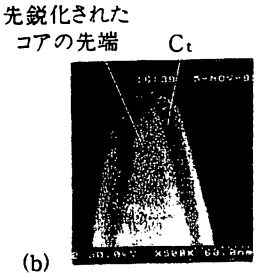

第2図
先鋭化されたコアをもつファイバーの電子顕微鏡写真．
(a) 全体像．
クラッド外径は90 μm．
(b) コア先端の拡大図．
C_t と記された表皮層は電子顕微鏡観察時に付着した汚染物の層．

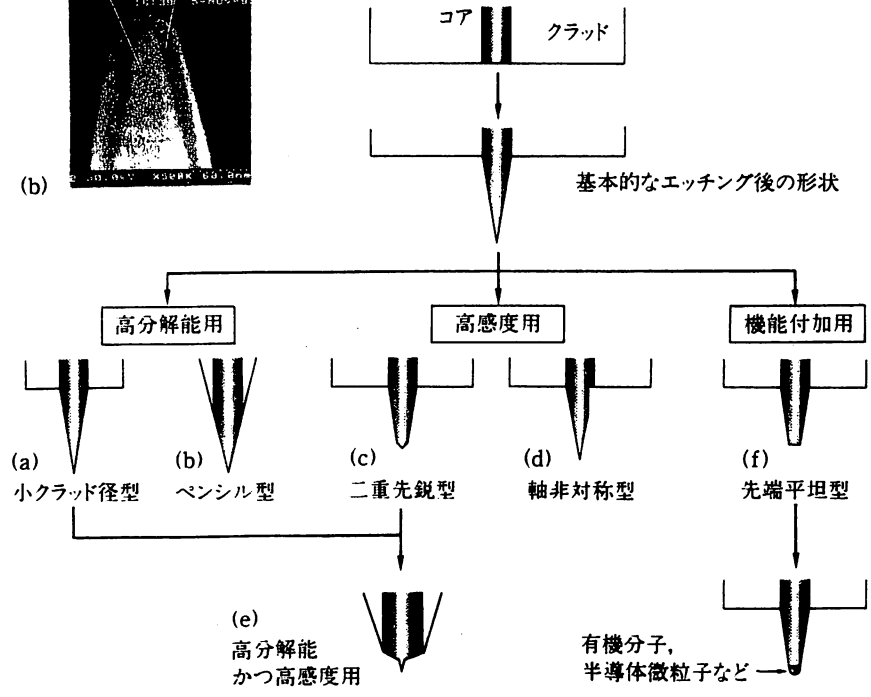

第3図 エッチング法で加工された各種ファイバーの断面形状の説明図．

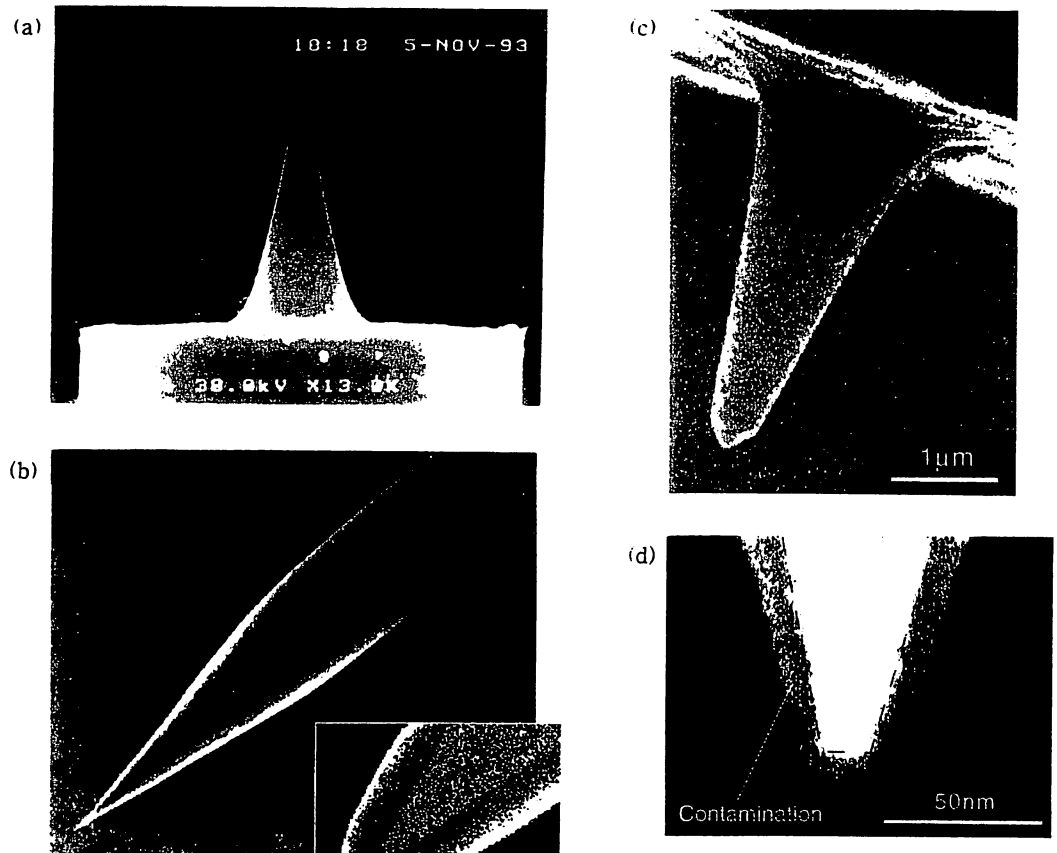

第4図 エッチング法で加工された各種ファイバーの電子顕微鏡写真.
(a) 小クラッド径型. クラッド径は8 μm.
(b) ペンシル型.
(c) 二重先鋭型.
(d) 先端平坦型.

前節で述べたようにプローブの形状は測定対象の光学的特性を勘案して最適化されるべきであるが，エッチング法ではそれが可能で，上記の基本的方法を修正して**第3図**に示す各種のファイバープローブが実現している．これらについて以下で示す.

(1) 高分解能用

上記の基本的方法で作成可能である．電子顕微鏡で観測した場合，第2図に示したように先端曲率半径約1 nmが確認されている．これは原子間力顕微鏡の市販カンチレバーの先端形状より小さい．これをもとに次の形状が考案されている.

(a) 小クラッド径型

通常のファイバーではクラッド外径が大きく(125 μm)，近接場光学顕微鏡用プローブとして用いるとき，クラッド端面の最外周の角部が試料表面に接するなどの問題がある．これを解決するために，あらかじめモル比Xの小さなエッチング液でクラッド外径を小さくしておき，その後上記の基本的エッチング溶液によりコア部を先鋭化する．これにより**第4図**(a)に示すように小クラッド径のプローブが実現する[5]．クラッド外径はコア径の2倍程度まで小さくできる.

なお，このような小クラッド径のプローブを用いると機械的振動の共振周波数が増大し，プローブ位置制御に援用されているせん断応力の検出感度を向上するのに有利である.

(b) ペンシル型

先鋭部の形状は第4図(a)と同様であるが，クラッド端面の最外周が角部を持たず，コア，クラッドあわせてペンシル形をしたものも実現できる(第4図(b))[6]．これは本節最後に示すように，

金属膜蒸着の際に先鋭部全体に均一に蒸着できる利点を有する．

(2) 高感度用

先鋭角が小さいとそれに従って先端曲率半径が小さくなり，(1)の目的に有利であるが，前節の③における変換効率が減少して感度が低くなる．分解能を犠牲にしても感度をあげる目的のために以下の形状が加工されている．

(a) 二重先鋭型

第4図(a)と同様エッチングを二段階にわけて第4図(c)のような二重先鋭型が考案されている[7]．ここではファイバー根元付近の先鋭角は(1)の場合と同等であるが，先鋭部のコア断面直径が光波長以下の部分で先鋭角を大きくし，先端部までの距離をできるだけ小さくして，先端で散乱された近接場光がコア根元に達する効率をあげている．これにより(1)の場合より10倍以上大きな検出効率が実現している．

(b) 軸非対称型

先鋭化コアをもつファイバーはすべて軸対称である．したがって，前節の②～④に励振される伝搬光は HE_{11} モードである．これに対し，本節最後に述べるように，③部に蒸着された金属膜を利用し，コアと金属膜との境界でプラズモンが関与する HE_{11} モードを励振すれば導波モードへの結合効率が向上する．すなわち③部に導波モード変換機能を作りつければよい．そのために再現性のよい方法として，③部を軸非対称にすることが考案されている[8]．加工には収束イオンビームが用いられている．これにより検出効率は10倍以上向上している．

(3) 高分解能かつ高感度用（および紫外用）

(2)の(a)ではコア先端付近の先鋭角を大きくするために空間分解能は低下する．分解能と感度の両方を高めるために，先鋭角の大きなコアの先端にさらに先鋭角の小さな突起部を実現する方法が考案されている[9]．これにはコア自身の動径方向屈折率分布が3段階になっているものをエッチングすることにより実現されている．

ところで従来のファイバーは近赤外領域において伝送損失が小さくなるように設計製作されているので，青色～近紫外領域での使用時には前節における④部の性能が低い．これに対しここで用いるファイバーではコア部に GeO_2 がドープされていないため波長350 nm程度の紫外域での使用が可能である．

なお，同様の形状のファイバープローブを集束イオンビームを援用して作成する方法も考案されている[10]．

(4) 機能付加用

次節の機能性プローブを作成するためには，有機分子，半導体微粒子などをプローブ先端に固定する必要がある．そのためにはエッチングを先鋭化途中で止めて第4図(d)のようにコア先端を平坦化する[11]．この平坦部は上記の物質を固定するのに有利である．なお，このように先端が平坦であると，生体微粒子のように柔らかい試料表面をプローブ走査時に損傷することを避けられる利点を有する．

なお，以上のファイバープローブはエッチングによる加工後，第1図(b)にも示したように根元部に金属膜を塗布する(**第5図**)．金属膜塗布部からは光が出入りしないので，大きな物体のまわりの近接場光，さらには伝搬光を散乱することを防ぐことができる．したがってこれを顕微鏡などの計測に用いる場合，ファイバープローブは先端の曲率半径の値と根元の金属膜塗布端におけるコア断面半径の値との間の空間局在寸法をもつ近接場光のみを選択的に散乱する空間バンドパスフィルターとして働く．

塗布する金属膜材料としてアルミや金が用いられている．アルミは短波長域における光のしみだし厚みが金に比べて小さいので有利である．しかし酸化し易いこと，真空蒸着用のボートを腐食しやすいなどの欠点を有する．金は酸化しにくく化学的に安定であり，比較的蒸着が容易であるが，可視･短波長域における吸収係数の低下や，ファ

イバー用ガラスとの密着性が低いなどの問題がある．密着性を改善することを目的として，しばしばクロム(Cr)との重ね膜の形で使用される[11]．

コア根元のみに金属膜を塗布するには真空蒸着やスパッタにより金属膜を塗布した後，樹脂などのレジストを塗って，KI溶液によりエッチングして先端の金属膜を除去する方法[12]，同様に金属膜塗布後，フォトレジストを塗ってフォトリソグラフィにより先端の金属膜を除去する方法[13]などがある．

§3 機能性プローブ

ファイバープローブ先端に異種物質微粒子を固定し，各種の光学応答特性を実現するものを機能性プローブと称する．下記の例がある．

(1) 金属膜塗布型

先端に金属膜を塗布し近接場光散乱効率を向上させるもの．さらに表面プラズモンを励起し，光強度を増強させるもの[14]．

(2) 発光型

半導体微粒子や色素分子を固定するもの．特に色素分子を固定したものは各種化学センサーとしての応用可能性が開かれている[2,15]．

§4 まとめ

近接場光学用プローブは，現在までのところ，光ファイバーの選択化学エッチングにより大きな成功をおさめた．特に我が国の光ファイバー技術の優越性に助けられ，プローブの性能は諸外国に比べ先行している．今後は，加工，メモリ，原子操作などへの展開に応じ，光ファイバー以外の素材を用いたプローブの開発が活発化するであろう．そのような兆しとしてシリコン平板の微細加工により微小開口をアレイ状に作りつけたプローブが開発され，超高密度光メモリへの応用に供されている[16]．

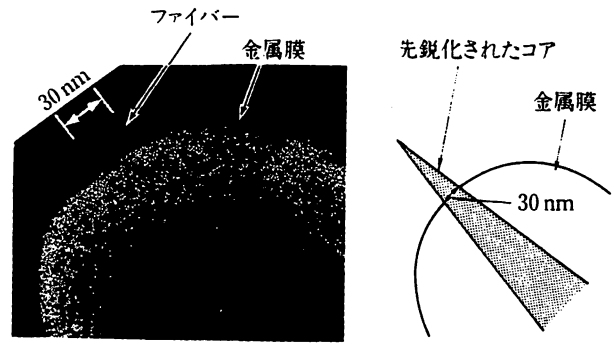

第5図 金属膜を蒸着し，コア先端が突出したファイバープローブ．
(a) 電子顕微鏡写真．(b) 断面形状説明図．

本稿の話題に関する研究を主に遂行し，また本稿の内容について議論いただいた㈶神奈川科学技術アカデミー研究員物部秀二氏に感謝します．

〔参考文献〕

1) M. Ohtsu and H. Hori: *Near-field nano-optics* (Plenum, New York, 1998).
2) M. Ohtsu (ed.): *Near Field Nano/Atom Optics and Technology* (Springer, Berlin, New York, Tokyo, 1998).
3) 斎木敏治，大津元一：固体物理 **33** (1998) 395.
4) T. Pangaribuan, K. Yamada, S. Jiang, H. Ohsawa and M. Ohtsu: Jpn. J. Appl. Phys., **31** (1992) L1302.
5) T. Pangaribuan and M. Ohtsu: Electron. Lett., **29** (1993) 1978.
6) S. Mononobe and M. Ohtsu: J. Lightwave Technol., **14** (1996) 2231.
7) T. Saiki, S. Mononobe, M. Ohtsu, N. Saito and J. Kusano: Appl. Phys. Lett., **68** (1996) 2612.
8) T. Yatsui, M. Kourogi and M. Ohtsu: Appl. Phys. Lett., **71**, (1997) 1756.
9) S. Mononobe, T. Saiki, T. Suzuki, S. Koshihara and M. Ohtsu: Opt. Commun., **146** (1998) 45.
10) 八井 崇，興梠元伸，筒井一生，大津元一：電気学会電子材料研究会資料，資料番号 EFM-97-11 (1997) 19.
11) R. UmaMaheswari, S. Mononobe and M. Ohtsu: J. Lightwave Technol., **13** (1995) 2308.
12) S. Mononobe, M. Naya, T. Saiki and M. Ohtsu: Appl. Opt., **36** (1996) 1496.
13) T. Matsumoto and M. Ohtsu: J. Lightwave Technol., **14** (1996) 2224.
14) M. Ashino and M. Ohtsu: Appl. Phys. Lett., **72** (1998) 1299.
15) 栗原一嘉，大津元一：応用物理学会・日本光学会・近接場光学研究グループ，第7回研究討論会予稿集(1998年7月，名古屋) 78.
16) 大津元一，筒井一生，興梠元伸，李 明馥：電子情報通信学会誌 C-I，J81-C-I (1998) 119.

（3）局在プラズモン共鳴プローブの開発と新しいニアフィールド顕微鏡

神奈川科学技術アカデミー　芦野　慎
現）アトムテクノロジー研究体
神奈川科学技術アカデミー
東工大院総理工　大津元一

1. まえがき

ニアフィールド顕微鏡[1]は，境界面に存在する“伝搬しない光”，すなわち近接場光を扱うため，光の回折限界をはるかに超えたナノメートル領域の光学的性質を探る強力なツールとして発明当初から注目されてきた[2]．ニアフィールド顕微鏡の特徴の1つに，高い空間分解能を有する分光を行える点がある．例えば近接場ラマン分光[3]は，ナノメートル領域の材料評価技術として今後非常に期待される．しかし現時点では，励起効率と検出感度が問題となっており，探針ー試料間の局在場の増強が得られれば，それらの問題が一気に解決されるとみられる．通常のラマン散乱分光においては増強剤として金属の微粒子や微小突起が用いられている[4]．これは微粒子や微小突起に局在した電子の集団振動である局在プラズモン[5]が励起され，それによる近接場の増強が得られるためとする説が有力である．この説が現れたころから，ニアフィールド顕微鏡の探針に局在プラズモンを励起する理論的・実験的研究が行われている．そして，探針先端部の局在場の増強は分光面への適用だけでなく，非線形効果を用いたナノメートル領域の機能性デバイスや単原子操作などへの応用も期待され始めている．いずれにせよ必要とされるのは，探針先端への局在プラズモンの共鳴的な励起であり，共鳴効果がもたらす空間的に局在化された近接場の莫大な増強効果である．しかし，多大な期待に反して探針先端への“共鳴的な”励起が実現されたという報告例はこれまでになかった．この「技術ノート」では，われわれがどのようなかたちではじめて探針先端への“共鳴的な”励起を達成した[6]かについて報告するとともに，探針先端の局在場の共鳴的な増強が空間分解能の飛躍的な向上に対しても有効であること，さらに共鳴効果を用いた新しいタイプの顕微鏡の可能性について報告する．

2. 金属化プローブの製作

局在プラズモンが可視光域で共鳴的に励起され，莫大な近接場の増強が得られる材料としては金と銀に限られるため，先端をそれらで覆った探針の製作が試みられている．われわれは光ファイバー製の探針先端への金蒸着を行った．基板となる光ファイバー製の探針は，NH_4F，HF，およびH_2Oの混合溶液に浸し，先端径を10 nm以下に尖鋭化させた[7]ものを用いた．問題となるのは先端がナノメートル寸法のテーパー状のガラス面に薄く滑らかで，しかも実際の測定に耐えられるだけの機械的強度をもった金蒸着膜をいかに形成させるかであった．

そこでわれわれはガラスと金薄膜との中間に両者を接合させる材料を極微量導入することを考えた．接合材料として注目したのは，ナノメートル領域で“金属的性質”と“半導体的性質”の両者を合わせもつ，ゲルマニウムである[8]．その有効性は，以下に示す実験等で確かめた．用意した試料は，約5×10^{-4} Paの真空下で平坦なガラス基板に約30 nmの金薄膜を蒸着したものと，同じ膜厚の金を蒸着する直前にゲルマニウムを1 nm蒸着したものである．蒸着速度は前者が金：50～60 nm/min，後者がゲルマニウム：2～3 nm/min，金：10～20 nm/minで，どちらも輻射熱で基板を200℃程度に加熱している．それら2つに対して，スクラッチ試験[9]から基板への付着力（Benjamin-Waever力）F_{BW}を求めた．前者では，F_{BW}が約4.5 MPaであったのに対して後者は約23 MPaであったことから，ゲルマニウムの導入により基板への密着性が非常に向上することがわかった．試料表面の構造をSTM，およびAFMで観察した結果では，ゲルマニウムを導入することでより結晶粒界が広がるとともに，表面の凹凸が減少する傾向がみられた．さらに，光学的性質の変化を分光エリプソメーター[10]とATR分光[5]から調べた．紙面の都合上結果だけを述べると，可視光領域での変化はほとんど得られなかった．

以上から，ゲルマニウムの有効性が確認できたので，ほぼ同じ条件で尖鋭化光ファイバーに金蒸着膜を形成させた．**図1**（**a**），（**b**）は作製した探針の電子顕微鏡写真である．下地の光ファイバーのテーパー角は約19°であり，金蒸着後の角度は約20°であった．さらに，先端曲率半径は約5 nm，金蒸着後は約30 nmであった．これより，蒸着膜厚は先端部で約25 nm，根本の部分で約80 nmであり，図1（**c**）に示したモデル図にほぼ等しい構造が得られている．これは，Novotnyらの計算モデル[11]に類似した構造である．

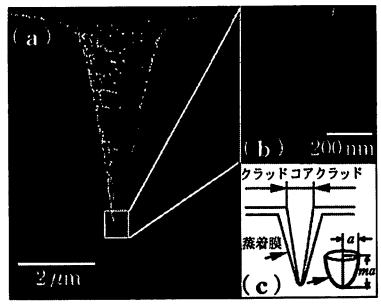

図1 作製した金属化プローブの電子顕微鏡写真（**a**）全体図．（**b**）探針先端の拡大図．（**c**）断面の模式図．

3. 局在表面プラズモンの共鳴励起

金属化プローブ先端への局在プラズモンの励起は，**図2**に示される実験配置で行った．励起光源に色素レーザー（R6G）を用い，単一波長の集光していないp偏光を全反射条件（入射角45±0.01°）でBK7製のプリズム面に入射し，特定の波数ベクトルをもつ近接場を誘起した．探針はシェアフォースによるフィードバック制御で，試料に対し約5 nmの位置まで近づけ，固定した．探針先端から得られる散乱光は光ファイバーを通じて末端の光電子増倍管で電気信号に変換させた．入射光強度はハーフミラーで分割した一方をモニターし，常に一定に保った．このような条件で色素レーザーの波長を約630 nm（1.97 eV）から約570 nm（2.18 eV）まで変化させ，散乱光強度を測定した（**図3a**）．同図**b**は，裸の光ファイバー製の探針の場合である．これとの比較から約2.11 eV（波長約588 nm）で検出光強度が最大となり，裸のファイバーに比べ約5.8倍の強度が得られている．

図3のc～eは，表面局所場理論[12]から求めたものである．入射電磁場E_0に対し局所場の増強因子E_{tip}/E_0は，

$$\frac{E_{tip}}{E_0}=\frac{\varepsilon_m/\varepsilon_s}{1+[(\varepsilon'_m/\varepsilon_s)-1]A+i(\varepsilon''_m/\varepsilon_s)A+R\varepsilon''_m\sqrt{\varepsilon_s}+iR(1-\varepsilon'_m)\sqrt{\varepsilon_s}} \quad (1)$$

ただし，

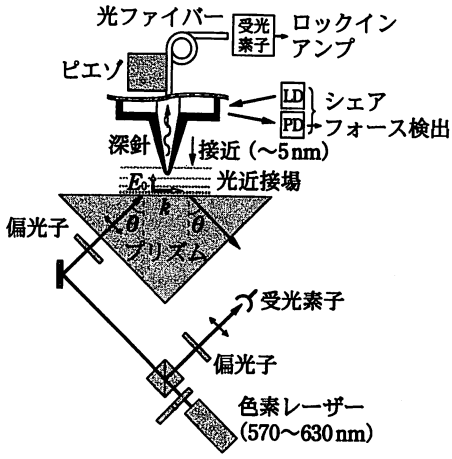

図2　探針への局在プラズモンの共鳴的な励起のために用いた装置の配置図.

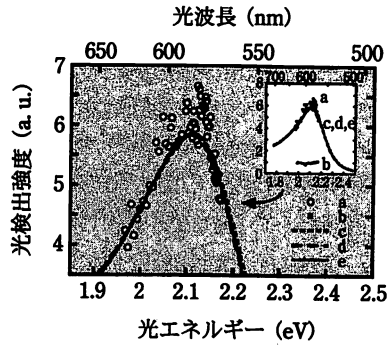

図3　探針より得られた光検出強度の励起光エネルギー，および，波長に対する依存性．a)作製した金属化プローブの場合．b)裸の光ファイバーの場合．c～e)表1に示される各パラメーターを用いて(1)式より求めた回帰曲線．縦軸は共鳴エネルギー(2.11eV)におけるbの値に対して規格化してある．

$$R=\frac{4\pi}{3}\frac{V}{\lambda^3}=\frac{16\pi^3 m}{9}\left(\frac{a}{\lambda}\right)^3,$$

$$A=\frac{1}{m^2-1}\left[\frac{m}{2\sqrt{m^2-1}}\ln\left(\frac{m+\sqrt{m^2-1}}{m-\sqrt{m^2-1}}\right)-1\right]$$

ここで，ε_m，および ε_s はそれぞれ半回転楕円体，および周囲の誘電率を表し，a，m は半回転楕円体の底面半径，それと長軸との軸比を表している．また，V は全体積を，λ は励起光波長を示している．実際に c～e を得る際に用いた各パラメーターを**表1**に示す．ただし，ε_m は文献[13]の値を用いた．表中の $|E_{tip}/E_0|^2$ は実験で得られた共鳴波長における局所場の増強度を表している．

作製した金属化プローブの電子顕微鏡写真から，m は1.5～2.0であるため，表1から ε_s は1ではなく，1.5～2.0の範囲にあることが示される．探針が基板の極近傍まで接近した場合，探針ー試料間の誘電率が増加することが指摘されており[14]，本研究結果はそれを指示している．その際の局所場の増強度は150～200倍となる．裸のファイバーとの比較では約5.8倍であるが，裸のファイバーの場合，探針ー試料間の多重散乱効果[15]や先端以外のテーパー部での散乱光の受光効果が含まれていると考えられ，入射光に対する金属化プローブ先端の局所場増強度としてはこの計算結果に近いものと考えられる．

4. 増強度の距離依存性と新しいタイプのニアフィールド顕微鏡の可能性

計算結果から，探針ー試料間距離がナノメートル寸法まで狭まることによる誘電率変化が共鳴条件に含まれていることが示された．これが事実であれば，検出光強度は非常に鋭い距離依存性を示すことになる．詳細はここでは省略するが，実際，励起光波長を固定し探針ー試料間距離を変化させた実験結果では，非常に鋭い距離依存性が得られている[16]．さらに励起光がs偏光の場合には近接場の増強は得られていない．鋭い距離依存性が得られる場合，試料表面の極微小な構造に起因する変調成分も検知できることから，空間分解能の飛躍的な向上が期待される．また，偏光成分に敏感なことから，試料上の近接場の方向に関する情報が得られる可能性がある．さらに，常に探針先端で共鳴が得られるように励起光の周波数（波長）を変調することが可能であれば，試料表面上でのナノメートル領域の極微小な誘電率変化を画像化できる可能性がある．

5. むすび

ニアフィールド顕微鏡で用いられている尖鋭化光ファイバー先端に，真空下で微量のゲルマニウムを蒸着した直後に金蒸着を行うことで，先端が非常に滑らかで機械的強度が高い金属化プローブが得られた．この金属化プローブ先端をp偏光のレーザー光により誘起させた近接場領域に固定し光波長を変化させた結果，検出光強度は鋭い波長依存性を示し，波長約588 nm (約2.11 eV) において共鳴が得られた．表面局所場理論によるシミュレーション結果では共鳴効果は探針ー試料間距離に強く依存し，さらに励起光の偏光に敏感であることが予想された．これより金属化プローブ，すなわち，局在プラズモン共鳴プローブにより，近接場分光やさまざまな応用への道が開かれると同時に，高い空間分解能をもち，試料表面のナノメートル寸法の極微小な領域の光学的性質を画像化する，新しいタイプのニアフィールド顕微鏡の実現の可能性が得られたことになる．

表1　図3の実験結果に対する計算シミュレーションにおいて用いたパラメーター．a は作製した金属化プローブの電子顕微鏡観察結果により固定した．

	ε_s	m	a(nm)	$\lvert E_{tip}/E_0\rvert^2$
curve c	1.00	2.61	31	385
curve d	1.53	1.92	31	202
curve e	2.07	1.52	31	128

1) D. W. Pohl and D. Courjon, eds: *Near Field Optics* (Kluwer, Dordrecht, 1993).
2) E. Betzig and J. K. Trautman: Science **257**, 189 (1992).
3) C. J. Jahncke, M. A. Peasler, and H. D. Hallen: Appl. Phys. Lett. **67**, 2483 (1995).
4) R. K. Chang and T. E. Furtak, eds: *Surface Enhanced Raman Scattering* (Plenum, New York, 1982).
5) H. Raether: *Surface Plasmons on Smooth and Rough Surfaces and on Gratings*, Springer Tract in Modern Physics Vol.111 (Springer - Verlag, Berlin, 1988).
6) M. Ashino and M. Ohtsu: Appl. Phys. Lett. **72**, 1299 (1998).
7) T. Pangaribuan, K. Yamada, S. Jiang, H. Osawa and M. Ohtsu: Jpn. J. Appl. Phys. **31**, L1302 (1992); T. Pangaribuan, S. Jiang, and M. Ohtsu: Scanning **16**, 362 (1994).
8) M. Ashino, M. Tomitori, and O. Nishikawa: Appl. Surf. Sci. **87-88**, 12 (1995).
9) S. Baba, A. Kikuchi and A. Kinbara: J. Vac. Sci. Technol. **A 4**, 3015 (1986); S. Baba, A. Kikuchi and A. Kinbara: J. Vac. Sci. Technol. **A 5**, 1860 (1987).
10) 田所利康，吉田裕：Jasco Rep. **35**, 20 (1993).
11) L. Novotny, D. W. Pohl, and B. Hecht: Ultramicroscopy **61**, 1 (1995).
12) G.T. Boyd, Th. Rasing, J.R.R. Leite, and Y.R. Shen: Phys. Rev. **B 30**, 519 (1984); A. Wakaun, J.P. Gordon, and P.F. Liao: Phys. Rev. Letts. **48**, 957 (1982).
13) P. B. Johnson and R. W. Christy: Phys. Rev. **B 6**, 4370 (1972).
14) U. Ch. Fischer and D. W. Pohl: Phys. Rev. Lett. **62**, 458 (1989).
15) H. Furukawa and S. Kawata: Opt. Commun. **148**, 221 (1998).
16) M. Ashino and M. Ohtsu: 投稿準備中.

分類番号　7.1, 7.10

(3) *Developement of localized plasmon resonance probe for novel near-field optical microscopy.* Makoto ASHINO*,† and Motoichi OHTSU*,**.
*Kanagawa Academy of Science and Technology.
**Interdisciplinary Graduate School of Science and Engineering, Tokyo Institute of Technology. †Present address: Joint Research Center for Atom Technology.

Electronics and Communications in Japan, Part 2, Vol. 81, No. 8, 1998
Translated from Denshi Joho Tsushin Gakkai Ronbunshi, Vol. J81-C-I, No. 3, March 1998, pp. 119–126

Near Field Optics and Its Application to Optical Memory

Motoichi Ohtsu, Kazuo Tsutsui, and Motonobu Kourogi

Tokyo Institute of Technology, Yokohama, Japan 226-8502

Myung-Bok Lee

National Institute for Advanced Interdisciplinary Research, Tsukuba, Japan 305-0046

SUMMARY

This paper explains the principle of near field optics and lists the problem of high density optical memory for which a storage density of 1 Tbit/inch^2 is expected as an application. Furthermore, the possibility of tracking avoidance is introduced in storage and read out, especially the latter, by using a planar probe array. The present status of probe array fabrication discussed. © 1998 Scripta Technica, Electron Comm Jpn Pt 2, 81(8): 41–48, 1998

Key words: Optical memory; near field optics; fiber; tracking.

1. Introduction

Physical quantities for the characteristics of light propagating in free space include the power, wavelength, frequency, and polarization. They can be controlled. By using this controllability, light has widely been used for communication, information processing, and so on. However, due to diffraction, one of the properties of light, it has not been possible to localize the light within a space having dimensions less than a wavelength. Hence, the dimensions of an optical device cannot be less than the optical wavelength, and this presents a limit to the miniaturization of optical devices.

Near field optics is a powerful method for miniaturization beyond the diffraction limit. The optical near field treated in this subject is nonpropagating light generated on the surface of nanometric materials with energy localized on the material surface. Hence, in order to generate such light, it is necessary to process and fabricate nanometric materials smaller than the wavelength of light. Therefore, nanofabrication is an indispensable technique for near field optics.

Historically, the possibility of a high resolution optical microscope was suggested in 1928 [1]. At that time, no fundamental subjects, such as the localization of the optical field and the need for nanofabrication, were discussed. Experimental results were reported only in the 1980s when nanofabrication became possible [2, 3] and near field optics was initiated.

In the 1990s, near field optics advanced from measurement to fabrication and further to atomic manipulation [4] and atomic accumulation [5]. A new research area that may be called nano/atom photonics is now being explored. In this context, this paper explains the present status and future of optical memory as an application. In regard to the probe, a device that is needed in near field optics, and its fabrication method and measurement applications, the reader is referred to Refs. 3, 6, and 7.

CCC8756-663X/98/080041-08

2. The Optical Near Field and Its Characteristics

The optical near field involves short-range electromagnetic interactions between the induced polarizations adjacent to the surface when a material is illuminated with light. This is considered to involve surface excitations, such as surface plasmons and surface polaritons [8], and is nonpropagating light localized near the material surface. Under optical illumination, the optical near field is generated together with propagating light regardless of the dimensions and shapes of the material. It is shown by scattering theory that the volume in which the optical near field is localized is of the same order as the material dimension if the latter is shorter than the wavelength of the incident wave [9]. However, the optical near field cannot be detected in the far field, more than an optical wavelength away, since this is a nonpropagating wave. Therefore, a second nanometric material called a probe is inserted into the near field as shown in Fig. 1(a) so that the optical near field is converted to a propagating wave by scattering, thus allowing detection. If the dimension of the probe is equal to that of the material generating the optical near field, the scattering efficiency is maximized [9]. Therefore, fabrication of the probe by a nanofabrication technique is necessary for detection.

For measurement, the probe is scanned along the material surface and the power of the scattered light is measured as a function of position. In this way, the spatial distribution of the optical near field power, namely the shape of the material surface, can be measured, so that a microscopic image of the shape of the material can be obtained. Its resolution depends on the probe dimension and is independent of the wavelength of the light. Therefore, if a probe of size less than the optical wavelength is used, measurement exceeding the diffraction limit becomes possible.

It is also possible, as shown in Fig. 1(b), to generate an optical near field on a probe surface scattered by a nanometric material. The authors call Fig. 1(a) the collection mode and Fig. 1(b) the illumination mode. In case of either Fig. 1(a) or 1(b), the optical near field is multiply scattered. The optical power density related to the local optical scattering is not necessarily small. Sometimes, the material itself may be deformed and its structure may be altered. This is actually a fundamental property of optical near field allowing it to provide a new nanofabrication technique. In the case of such fabrication, the diffraction limit can be exceeded as in the case of the measurement described above.

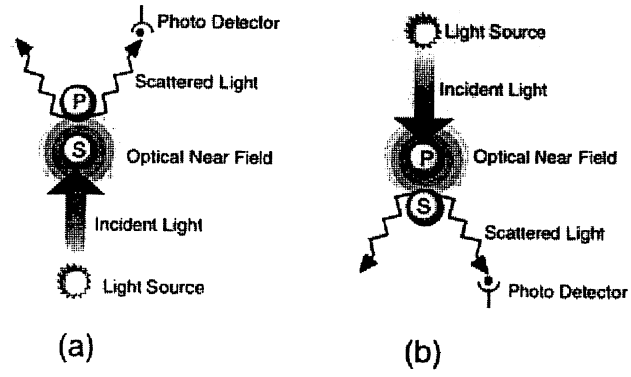

Fig. 1. Principle of generation and detection of optical near field. (a) Generating the optical near field on the surface of a sample (S) and scattering by the probe (P) for detection. (b) Generating the optical near field on the surface of a probe (P) and scattering by the sample (S) for detection.

3. Applications to Optical Memory

3.1. Present status of density enhancement of optical memory

Conventional optical memory is based on focusing propagating light with a lens. The average improvement of the storage density is said to be about 30% per year. For instance, in the case of DVD-RAM, the density reached about 2 Gbit/inch^2 in 1997 (where the track width is 0.74 μm and the wavelength of the laser diode source is 650 mn) [6]. However, in the near future, the storage dimension will reach the diffraction limit. In order to further increase the storage density, the use of shorter wavelengths, such as the blue-violet laser diode, volume holograms, and multivalued modulation recording, have been proposed. These are combinations of existing concepts and offer the technologies for the near future. A storage density of several tens of times greater than the present density is expected. On the other hand, the method of near field optics is a technology based on a new concept.

In contrast to the method of near field optics there is a method using a solid immersion lens (SIL) made of a material with a large index of refraction [10]. This is a source of some confusion. Since the SIL has a large numerical aperture (NA), the defocusing dimension due to diffraction is smaller than that in a conventional lens and hence provides a higher storage density. Since the focal length of this lens is short, the storage medium needs to be placed near the lens. Hence, this method is sometimes called near field optics technology. However, it is clear that propagat-

ing light is used in this technology, which is therefore within the conventional diffraction limit. By using this method, storage and read out areas about 350 nm in diameter have been achieved for TbFeCo, a typical magneto-optical recording medium [11]. It is known that the upper limit of the numerical aperture is necessarily restricted and the focal depth becomes demanding as the index of refraction of the SIL material is increased. The limit is reached sooner or later.

The method based on near field optics exceeds these diffraction limits, and the upper limit of the storage density is determined in principle by the dimension of the probe tip. The limit could possibly reach 1 Tbit/inch^2. By using the illumination mode corresponding to Fig. 1(b), storage and read out were first carried out for a magnetic domain with a diameter of about 60 nm for a Pt/Co multilayered film, one type of magneto-optical storage medium [12]. The corresponding storage density reaches 170 Gbit/inch^2. Since local heating by light is used, this method is called thermal mode storage according to the conventional classification of optical storage. At the same time, the authors carried out photon mode storage by illuminating an organic thin film of photochromic material with the optical near field and by inducing a structural change from a trans isomer to a cis isomer [13, 14]. It was demonstrated that read out can be done by measurement of the change in transmission coefficient of the thin film and that erasure is possible by illumination with long wavelength light. The recording dimension of 1 bit is about 50 nm, similar to that for thermal mode storage. An advantage of this method is that no local heating is needed.

More recently, an attempt has been made using the phase-change storage medium $Ge_2Sb_2Te_5$ to achieve recording at a lower temperature than in thermal mode recording [15, 16]. The minimum storage dimension is about 80 nm, corresponding to a storage density of 100 Gbit/inch^2. Also, photon mode storage using a more sensitive photochromic material is advancing [17].

The present situation, however, is such that storage and read out experiments are carried out with a probe made by sharpening a glass fiber (called the fiber probe) to attain a high storage density. It cannot be concluded that a useful approach for practical realization has been demonstrated.

3.2. Identification of problems

It is obvious that optical memories and their peripheral devices as commercial products can be attained after the problems of cost and reliability are resolved. In what follows, these problems are clarified and solution procedures are discussed. The following discussions are the outcome of studies by our group and are not necessarily general requirements. Nevertheless, this discussion may suggest future directions.

The problems for practical use of the optical memory based on near field optics are related to software and hardware, and are correlated with each other. The main problems are listed below.

A. For software: (1) Specification of the information provided to the user (individual medical information, literature information of library, weather information, dynamic images, and so on). By means of such settings, the memory format, such as ROM, and erasure ability can be determined. This format affects the hardware development. (2) A storage system that skips topographical singularities such as bumps and dips at nanometer scale on the surface of storage medium.

The next three points relate to hardware.

B. The system: (1) The shape of the storage medium (whether disk type, such as a CD, or linear, such as a magnetic tape). This depends on the type of recording information. (2) Scanning of the read-out head. (3) Distance control between the probe and the storage medium. (4) Tracking control of the read-out head. (5) Removal/installation of the storage medium, by which portability of the optical memory becomes possible. (6) High-speed detection of a weak light wave at read out.

C. The device: (1) Probe scannable at a high efficiency and necessary speed. (2) Interface device connecting the light source, probe, and photodetector. (3) Flying head and actuator for probe scanning.

D. The storage medium: (1) Search for a mechanism of highly sensitive interaction between fine particles at nanometer scale and the optical near field, and the necessary materials. (2) Material with a small particle radius and with magnetic domains. (3) Investigation of physical quantities and thermodynamic concepts in the nanometer region. Studies of the concepts of heat and temperature as statistical physical quantities and the applicability of theoretical models of their dissipation. (4) Protective film of nanometer thickness.

3.3. Toward solution of the problems

We describe the attempts we have made to address some of the problems listed above (related to the problems B (2)–(4) and C in the previous section).

A. On the configuration of the read-out head: First, the limit on the data transmission rate at read out is estimated. The light from the light source is incident on the probe. Consider the situation in which the optical near field generated at the probe tip illuminates the surface of the recording medium and the signal is restored by receiving the scattered light. The calculated results of the relationship between the optical near field generating efficiency of the

probe (defined as (power of generated optical near field)/(incident light power to the probe)) and the data transmission rate are plotted in Fig. 2 with a solid line [18]. In this case the assumptions used in the calculations are: (1) The read-out method is PCM. (2) The bit error rate is maintained at 1×10^{-12} [19]. (3) The error rate is dictated by the shot noise of the received light. (4) The incident power to the probe is less than the breakdown threshold of the fiber probe with an evaporated metal film [20, 21] and is 1 mW. (5) The wavelength of the light source is 600 nm. (6) The contrast (the ratio of the amount of reflected light for a "1" bit to that of a "0" bit) of the scattered light from the recording medium is 0.1. (This is based on the results of storage experiments in photon mode by the authors [13, 14]. This value can also be used in the case of thermal mode storage.)

In the case of the probe fabricated by the authors by sharpening a glass fiber by chemical etching and evaporating a metal film [20, 21], the value of the generating efficiency of the optical near field is 1×10^{-5} to 1×10^{-3} (the hatched region in Fig. 2). Therefore, from the solid line in this figure, a data transmission rate reaching about 50 Mbit/s can be expected. Corresponding to a storage density as high as 1 Tbit/inch^2, this transmission rate is further increased and a value of 1 Gbit/s is achieved. This is done by improving the probe. The first improvement measure is to develop a fiber probe with a higher generating efficiency

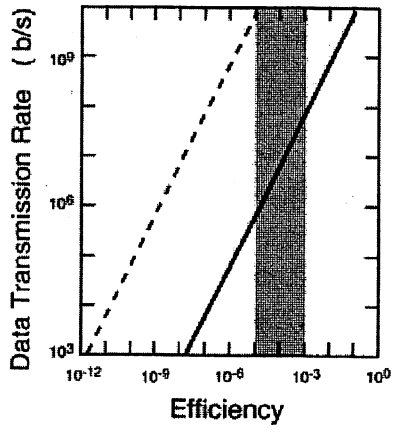

Fig. 2. Dependence of data transmission rate on the efficiency of generating the optical near field. The efficiency is defined as the ratio of the generated optical near field power to the incident light power to the probe. Meshed area represents the value of the efficiency realized by the existing fiber probe. A solid line represents the data transmission rate to maintain the shot noise-limited bit error rate as low as 1×10^{-12}. A broken line represents the probe array with 100×100 elements.

for the optical near field. The scanning capability is a problem in this case. When the target values (r = 1 Gbit/s and s = 25 nm) are substituted into the relationship $v = sr$ between the data transmission rate r, the spacing s of the stored bits, and the scanning speed v, we obtain v = 25 m/s. However, it is not easy to scan at this speed when the distance between the storage medium and the probe is maintained less than several tens nm of a conventional actuator such as PZT. As a second improvement method, read out by several probes in a two-dimensional array is promising. If the number of probes in the two-dimensional array is n, the scan speed of the array is $v = sr/n$. If a 100×100 probe array is used (where $n = 1 \times 10^4$), then v = 2.5 mm/s, which is a speed low enough to be attained by using conventional technology.

In order to obtain such a two-dimensional array, the authors have fabricated an array of two-dimensional apertures on a silicon substrate by means of the semiconductor planar process technology (see Fig. 3). The authors have proposed a device in which the optical near field is generated in the nanometric apertures by light incident from above. This device has the following advantages. (1) Since the bottom surface is flat, the distance to the storage medium can be held constant over the entire array. (2) As in scanning a contact-type hard disk, it is possible to slide on the storage medium coated with a lubricating thin film [22] so that the distance to the storage medium is held constant with the above scanning speed. (3) Scanning that does not require tracking (described below) is possible. (4) Integration with the slab waveguides and photodetector array is possible.

B. Storage by probe array: As the shape for the storage medium, a disk-type plane is used. As shown in Fig. 4(a), the light is incident on the upper surface of the probe array and the optical near field is generated in the aperture. Lubricant is used between the probe array and the storage

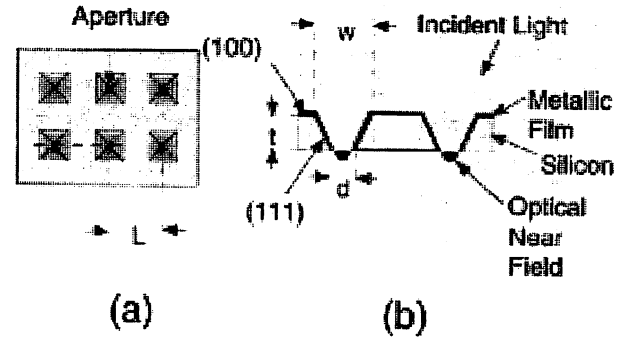

Fig. 3. Profile of the probe array with two-dimensional apertures fabricated on a silicon substrate. (a) Top view. (b) Cross-sectional view.

medium so that the sweep is carried out while the array and medium are held close together by surface tension (about 10 nm). After passing through the spatial modulator, the incident light illuminates the upper surface of the probe array. It is possible to perform storage by independently modulating the incident light intensity on each aperture according to the information to be stored. The transmission mode of the light is in free space from the source to the spatial modulator and to the upper surface of the probe, by which the weight reduction of the probe array as a read-out head is made possible. In order to prevent interference between the addresses, the distance L between adjacent apertures needs to exceed the optical wavelength. This is advantageous in the preparation of a photo mask for array fabrication since no special nanofabrication technology is needed.

C. Avoidance of tracking in playback: In conventional optical memory, control of the position of the read-out head in scanning over the stored bits or the tracking function is required. However, it is not necessary if the above probe array is used [18].

As shown in Fig. 4(b), the row of the probe array is scanned with a slant angle of θ with respect to the stored bit row. The probe array is scanned in the direction shown by the arrow. In this case, each aperture in the probe array passes through the broken lines with a spacing of D (= $L \sin \theta$ where L is the aperture spacing). If a conventional optical system is used, the scattered light on the storage medium can form an image of the aperture plane via a lens system on the photodetector array above the probe array. This is possible because the aperture spacing L is larger than the incident wavelength. If the intensity of the light detected in this manner is stored as a time-sequential electrical signal, the information represented by the scattered light intensity at an arbitrary position on the storage medium can be computed from the time elapsed since the sweep speed is known. Therefore, the stored bits with a spacing smaller than the aperture spacing L can be observed.

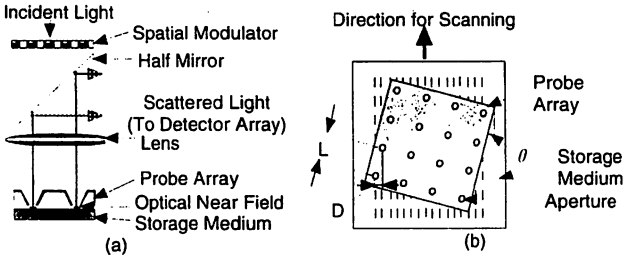

Fig. 4. Schematic explanation of storage and read out. (a) Storage by using a spatially modulated propagating light and a probe array. (b) Read out by scanning a probe array with the tilted angle of θ. Broken lines represent the trajectory of each aperture.

By using this method, continuous detection is possible in the scan direction of the probe array. Since the dimension d of each aperture of this probe array is less than the memory dimension d_M of the storage medium, all of the scattered light intensities at less than the spatial Fourier frequency component determined by $1/d_M$ can be observed by the probe array. Hence, the spatial distribution of the scattered light intensity from the storage medium in the scanning direction can be restored completely. The restoration is discrete in the scanning direction and the transverse direction. However, if $D \leq d_M/2$, perfect restoration is possible by the sampling theorem. A similar proposal is also made in a method in which the surface emitting laser array is used as the read-out head [23]. If the spacing of the stored bits is s = 25 nm and the number of apertures is n = 100 × 100 as in A, the dimensions of the probe array are 250 μm × 250 μm. It is possible in a conventional inexpensive system to achieve a mechanical positioning accuracy in scanning that is less than several tens of μm. Hence, if the position coordinate in the transverse direction is stored in auxiliary memory, it is possible to select the location again mechanically, even without the tracking control mechanism of the probe array for each bit on the storage medium. If error correcting codes are added in both the scanning direction and the transverse direction, and interleave is carried out at the same time, defects in the probe array and the storage medium can be dealt with.

D. Fabrication of probe array: The probe array proposed by the authors is fabricated by anisotropic etching of silicon substrate. By using the difference in etching speed along the (100) axis and the (111) axis of the silicon crystal, the concavity in Fig. 3 is formed and its bottom is used as the aperture. In this case, the taper angle of the concavity is determined by the direction of the (111) axis and is 70.5 degrees. The aperture dimension d is given in terms of the silicon thickness t and the upper surface dimension w of the concavity as $d = w - \sqrt{2}t$. Hence, the magnitude and accuracy of d are determined by w and t. On the other hand, to secure the uniformity and accuracy of t, the use of SOI (silicon on insulator) with a buried SiO_2 layer is effective. The buried SiO_2 layer is used as the stopping layer for the etching from the back surface so that a membrane of the surface Si layer is left where the window pattern of the concavity is formed. After the aperture is formed, metal films are evaporated on the slant surfaces of the concavity so that the light is shut off. Alternatively, evaporation can be applied to the back surface of the substrate. The final aperture dimensions are adjusted according to the evapo-

rated film thickness. The advantage of this fabrication method lies in the fact that a fine aperture structure exceeding the resolution limit of lithography can be formed both uniformly and effectively by means only of the well-established lithographic technique of the silicon planar technology. To avoid tracking, it is desirable that the accuracy of the distance L between the apertures be high. However, L has a value larger than the incident wavelength and can be achieved with the conventional photo mask technique. Fluctuations of the aperture dimensions cause fluctuations of the scattered light intensity from each stored bit and strongly affect the receiving sensitivity. However, this can be avoided by setting a discriminating threshold value after time sequencing the signal.

An example scanning electron microscope photograph of probe array that we fabricated is shown in Fig. 5 [24]. In this case, $L = 30\ \mu$m with a view to finding the optimum fabrication condition. Also, since there are cases in which the aperture may be buried by the evaporated metal film, the side of the square aperture is designed to be about 300 nm. After the aperture is formed, a metal film with a thickness of about 50 nm is evaporated. A square aperture with a side of about 200 nm is fabricated with high reproducibility. A probe array with a minimum side of 80 nm is realized as well.

In order to study generation of the optical near field of the probe array, the spatial distribution of the optical near field power on the aperture surface was measured with a near field optical microscope developed by the authors. A single peak characteristic was obtained, and a reproducible optical near field generation was confirmed. Also, the power density of the generated optical near field was almost equal to the power density on the upper surface of the probe array; hence the incidence plane of the light. From this fact,

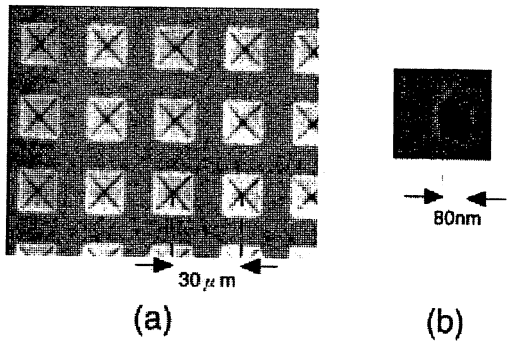

Fig. 5. Scanning electron micrograph of a fabricated probe array. (a) Top view. (b) Bottom view of the smallest aperture.

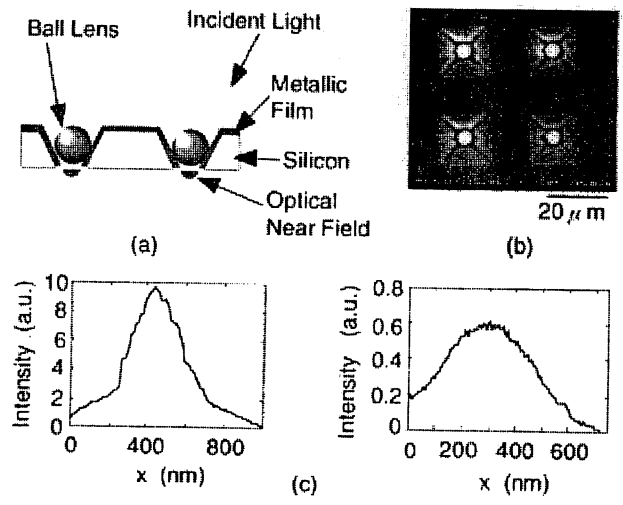

Fig. 6. A probe array with ball lenses and its near field optical performance. (a) Cross-sectional profile of the probe array with ball lenses. (b) Scanning electron micrograph of a fabricated probe array with ball lenses. (c) Measured cross-sectional spatial profile of an optical near field intensity generated on an aperture with (left) and without (right) the ball lens.

we found that the generating efficiency of the optical near field is equal to or higher than that in the probe developed by the authors. To further increase the generating efficiency, a glass spherical lens was installed in the concavity as shown in Fig. 6(a) and a probe array was fabricated such that the incident light was concentrated in the aperture [18, 25]. Figure 6(b) shows a scanning electron micrograph. The optical near field power values measured by the same method as above are presented in Fig. 6(c). From a comparison with the vertical axis for the results without a glass spherical lens we find that the power is increased by a factor of 16 with a glass spherical lens. Hence, high efficiency storage and read out at a high data transmission rate are expected.

4. Conclusions

In this paper, the principles of near field optics as a new nanofabrication technique and the present status of experiments are summarized. The problems of high density optical memory as a typical application, in which a storage density of 1 Tbit/inch^2 is expected, are presented. The possibility for tracking avoidance is introduced for storage and read out, particularly for read out, by a planar probe array. We report on the status of development of the probe array.

Presently, judging from the experimental results reported by research groups in several countries including Japan, confirmation of the principle of optical memory by the optical near field technique has been completed. The stage is now set for determining how low-cost and reliable techniques can be achieved.

Acknowledgments. Part of this work was a collaborative effort with Dr. N. Atoda, National Institute for Advanced Interdisciplinary Research, Ministry of International Trade and Industry, and Mr. T. Yatsui, a doctoral student at the Tokyo Institute of Technology.

REFERENCES

1. E.H. Synge. A suggested method for extending microscopic resolution into ultra-microscopic resolution. Phil. Mag., **6**, pp. 356–362 (1928).
2. D. Pohl and D. Courjon. Near Field Optics. Kluwer Academic Press, Dordrecht (1992).
3. M. Ohtsu. Progress of high-resolution photon scanning tunneling microscopy due to a nanometric fiber probe. J. Lightwave Technol., **13**, No. 7, pp. 1200–1221 (July 1995).
4. H. Ito et al. Laser spectroscopy of atoms guided by evanescent waves in micron-sized hollow optical fibers. Phys. Rev. Lett., **76**, No. 24, pp. 4500–4503 (June 1996).
5. H. Ito, K. Sakaki, M. Ohtsu, and W. Jhe. Evanescent-light guiding of atoms through hollow optical fiber for optically controlled atomic deposition. Appl. Phys. Lett., **70**, No. 19, pp. 2496–2498 (May 1997).
6. M. Ohtsu and S. Kawada. Near Field Nano Photonics Handbook. Optronics, Tokyo (1997). (in Japanese)
7. Special Issue on Near Field Optics, Optics, **26**, No. 10, pp. 509–540 (Oct. 1997). (in Japanese)
8. Y. Hori. Photon scanning tunneling microscope and its theoretical interpretation. Applied Physics, **61**, No. 6, pp. 612–616 (June 1992). (in Japanese)
9. K. Jang and W. Jhe. Nonglobal model for a near-field scanning optical microscope using diffraction of the optical near field. Opt. Lett., **21**, No. 4, pp. 236–238 (Feb. 1996).
10. S.M. Mansfield and G.S. Kino. Solid immersion microscope. Appl. Phys. Lett., **57**, No. 24, pp. 2615–2616 (Dec. 1990).
11. B.D. Terris et al. Near-field optical data storage using a solid immersion lens. Appl. Phys. Lett., **65**, No. 4, pp. 388–393 (July 1994).
12. E. Betzig et al. Near-field magneto-optics and high density data storage. Appl. Phys. Lett., **61**, No. 2, pp. 142–144 (July 1992).
13. J. Ichihashi et al. Attempt of high density optical recording by photon scanning tunneling microscope. Applied Physics Society, 11th Optical Sensing Technical Meeting, No. LST111-8, pp. 51–57 (June 1993).
14. S. Jiang et al. Highly localized photochemical process in LB films of photo-chromic material by using a photon scanning tunneling microscope. Opt. Commun., **106**, No. 4. pp. 173–177 (March 1994).
15. T. Shintani et al. Phase change writing in a GeSbTe film with scanning near-field optical microscope. Ultramicroscopy, **61**, No. 1, pp. 285–289 (Dec. 1995).
16. S. Hosaka et al. Phase change recording using a scanning near-field optical microscopy. J. Appl. Phys., **79**, No. 10, pp. 8082–8086 (May 1996).
17. M. Hamano and M. Irie. Rewritable near-field optical recording photochromic thin films. Jpn. J. Appl. Phys., **35**, No. 3, pp. 1764–1767 (March 1996).
18. M. Kourogi et al. Trackingless ultra high speed optical playback system with a planar probe array. Applied Physics Society, Japan Optical Society and Near Field Group, 6th Research Meeting, pp. 73–78 (June 1997). (in Japanese)
19. K. Yamamoto. Optical Fiber Communication Technologies. Nikkan Kogyo Shimbun, Tokyo, pp. 151–176 (1995). (in Japanese)
20. S. Mononobe, M. Naya, T. Saiki, and M. Ohtsu. Reproducible fabrication of a fiber probe with a nanometric protrusion for near-field optics. Appl. Opt., **36**, No. 7, pp. 1496–1500 (March 1997).
21. T. Saiki et al. Tailoring a high-transmission fiber probe for photon scanning tunneling microscope. Appl. Phys. Lett., **68**, No. 19, pp. 2612–2614 (May 1996).
22. A. Sato, K. Aziki, and M. Yanagisawa. Low jumping of contact recording system—New design slider. 20th Japan Applied Magnetics Society Scientific Meeting, No. 22aA-12, p. 220 (April 1996). (in Japanese)
23. K. Goto. Optical heads using VCL arrays with nanometer size output tip-windows for a tera byte optical disk. Proc. International Joint Symposium on Magneto-Optical Recording and Optical Memory, Yamagata, Japan, No. Th-L-03, pp. 184–185 (Oct. 1997).
24. M.B. Lee et al. Fabrication of Si planar apertured array for high speed near-field optical storage and readout. Technical digest of the Pacific Rim Conference on Lasers and Electro-Optics, Makuhari, Japan, No. WL2, pp. 91–92 (July 1997).

24. M. Kourogi et al. Fabrication of a planar aperture probe with a spherical lens for reading the ultra high density optical near field memory. 58th Applied Physics Scientific Meeting, **2**, No. 5aL1, p. 984 (Oct. 1997). (in Japanese)

AUTHORS (from left to right)


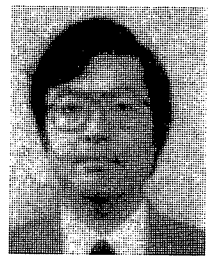
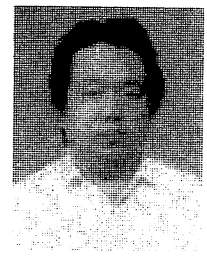
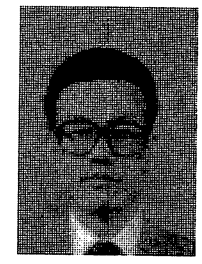

Motoichi Ohtsu (member) graduated from the Department of Electronics Engineering, Tokyo Institute of Technology, in 1973 and completed the doctoral course in 1978. He holds a D.Eng. degree. He later became a research associate and an associate professor at the same university. He became a professor in 1991. Since 1993, he has had a joint appointment as project leader for the Photon Control Project at Kanagawa Academy of Science and Technology. He has been engaged in research on quantum control engineering. He received a Koga Gold Medal from the International Scientific Radio Union, a Japan IBM scientific award, an Applied Physics Society award, and an Inoue academic award. He is a member of the Japan Society of Applied Physics, the Institute of Electronics, Information and Communication Engineers of Japan, the Institute of Electrical Engineers of Japan, the Optical Society of America, and the American Physical Society and a senior member of the Institute of Electrical and Electronics Engineering.

Kazuo Tsutsui graduated from the Department of Electrical and Electronic Engineering, Tokyo Institute of Technology, in 1981 and completed the M.S. course in 1983 and the doctoral course in 1986. He received a D.Eng. degree. He became a research associate at the same university in 1986. In 1990, he became an associate professor. He has been engaged in research on semiconductor/insulator heteroepitaxy, the dry process, and ultrafine fabrication process technology. He is a member of the Applied Physics Society.

Motonobu Kourogi graduated from the Department of Optical and Mechanical Engineering, Shizuoka University, in 1988 and completed the M.S. course at the Tokyo Institute of Technology in 1990. In 1993, he completed the doctoral course. He received a D.Eng. degree. He then became a research associate. He has a joint appointment as an adjunct researcher in the Photon Control Project at Kanagawa Academy of Science and Technology. He has been engaged in research on quantum optics and its applications, and laser control. He is a member of the Applied Physics Society.

Myung-Bok Lee graduated from the Department of Metallurgy, Seoul University, Korea, in 1993. In 1995, he completed the M.S. course at the Korea Advanced Institute of Science and Technology. He then became a research staff member. In 1996, he completed the doctoral course at the Tokyo Institute of Technology. He received a D.Eng. degree. Since then, he has been affiliated with the National Institute for Advanced Interdisciplinary Research, where he is involved in the ultra high-density optical recording project. He is a member of the Japan Applied Physics Society.

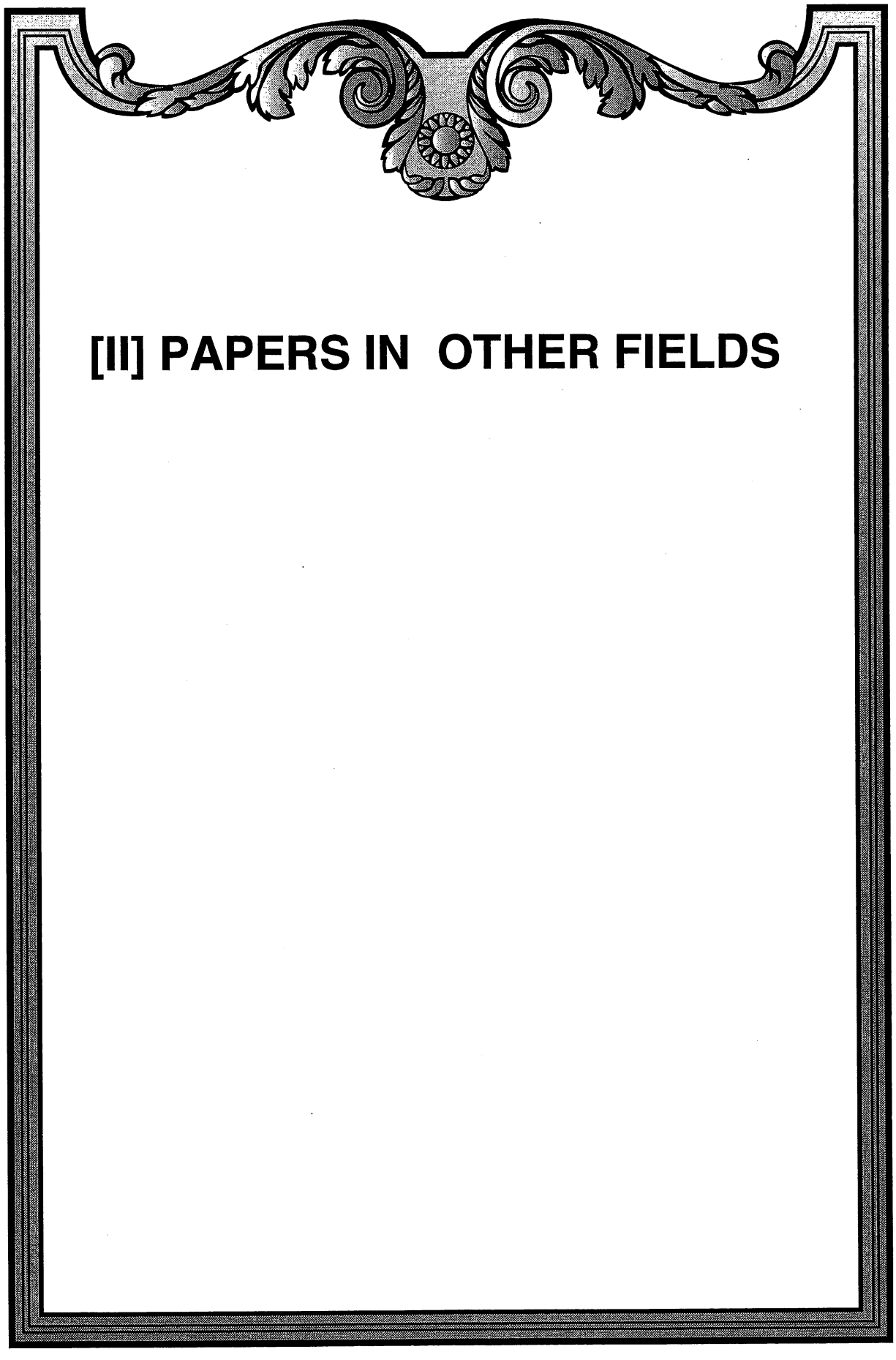

[II] PAPERS IN OTHER FIELDS

12-THz Frequency Difference Measurements and Noise Analysis of an Optical Frequency Comb in Optical Fibers

K. Imai, B. Widiyatmoko, Motonobu Kourogi, and Motoichi Ohtsu, *Senior Member, IEEE*

***Abstract*— A span up to 50 THz of optical frequency comb (OFC) has been obtained by self-phase modulation in an optical fiber. The coherent nature of the process was verified by heterodyne-detecting the sidebands offset by up to 12 THz from the carrier. The signal-to-noise ratio (SNR) of the beat signal between a sideband at 12 THz offset and another single-mode laser was 32 dB in a 1-MHz bandwidth. Although the linewidth of each beat signal was maintained within a few megahertz, phase noise pedestal power increased with the offset frequency.**

***Index Terms*—Electrooptic modulation, fiber optics, frequency conversion, frequency measurement, nonlinear optics, nonlinear wave propagation, phase modulation.**

I. Introduction

OPTICAL frequency comb (OFC) is essential to many applications which require precise optical frequency control, such as optical frequency measurements, synthesis, short pulse generation, and optical communications. The accuracy of difference frequency measurements using an OFC generator based on a Fabry–Perot (FP) electrooptic (EO) modulator [1]–[3] has reached about 6.8×10^{-14} [4]. Several efficient EO modulators, such as the FP-EO modulator and the quasi-velocity matched modulator [5], have been demonstrated, as has phase locking between combs generated from different lasers [6]. To realize these precise controls over the whole bandwidth of optical frequency, the span of the OFC has to be increased to several hundred terahertz, which requires a more efficient modulation process.

We have applied self-phase modulation (SPM), which has been used for ultrashort pulse generation, to realize a pulse train from a conventional OFC generator (OFCG) to further increase the OFC span. We obtained an OFC span up to 30 THz in the 1.55-μm region [7] by using a dispersion-flattened optical fiber (DFF) [8] as the SPM medium. Spectral broadening of a pulse train is a result of four-wave mixing (FWM) between the different modes; therefore, the mode separations of the generated sidebands are maintained.

However, the practical spectral broadening process is not ideal because of the existence of noise sources such as spontaneous emission from the optical amplifier and laser and microwave oscillator noise. Since a part of the noise increases the phase noise intensity through the intensity-dependent refractive index, the noise sources degrade the quality of the generated sidebands. In this paper, we describe the experimental results of beat signal measurements between the comb and other single-mode lasers. Applying a heterodyne detection method, we have investigated the contribution of these noise sources and, furthermore, proved the coherent nature of the nonlinear process.

Manuscript received August 14, 1998; revised November 30, 1998.

The authors are with the Interdisciplinary Graduate School of Science and Engineering, Tokyo Institute of Technology, Yokohama 226–8502, Japan.

Publisher Item Identifier S 0018-9197(99)02536-1.

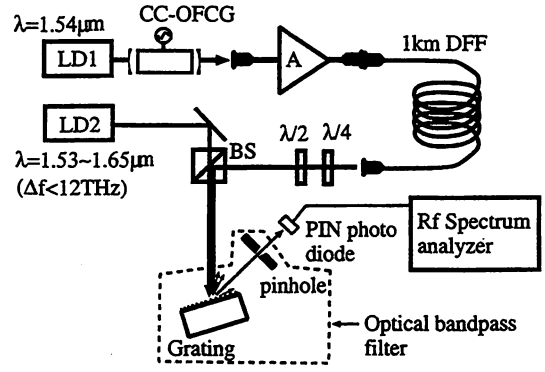

Fig. 1. Experimental setup. LD1: 1.54 μm laser diode; LD2: 1.6-μm or 1.55-μm tunable laser diode; CC-OFCG: a coupled-cavity optical frequency comb generator; A: optical fiber amplifier; DFF: 1-km length dispersion flattened optical fiber; $\lambda/4$: quarter-wave plate; $\lambda/2$: half-wave plate; BS: beam splitter.

II. Experiment

A. Experimental Setup

Fig. 1 shows the experimental setup for the beat signal measurement. LD1 is a single-frequency laser at 1.54 μm with an average output power of 4 mW. To increase the conversion efficiency of the laser light to the OFC, we used a coupled-cavity OFCG (CC-OFCG) [9]–[11]. The OFCG was fabricated by using an EO modulator with high reflection coatings on both facets ($LiNbO_3$ crystal $1\times1.2\times23$ mm^3, radius of curvature ∞ and 50 mm, mirror reflectivity of 99.6%). The finesse of the cavity was 600. The modulation frequency was 6.06 GHz and a modulation index of 0.75 rad was obtained when 20-W microwave power was fed to the resonator. Because the OFC span was limited by the group velocity dispersion (GVD) of the EO crystal [12], the frequency span of the OFC was limited to 7 THz at resonance. The OFCG generated a train of Lorentzian pulses with a

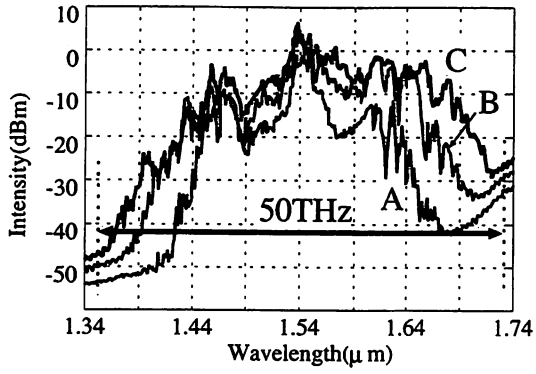

Fig. 2. The envelope spectra of the output of the DFF. The resolution bandwidth was 1 nm. The output powers for curves A, B, and C were 50, 100, and 200 mW, respectively. The OFC span was defined as the width where the intensity was more than −50 dBm. The OFC span was 30 THz for curve A and 50 THz for curve C.

repetition rate of twice the modulation frequency. Because of the crystal GVD, the measured pulsewidth was broadened to 1 ps compared to the expected value without GVD. Output power of the OFCG was increased by 80 times using the front coupling mirror, thus the transmittance of the CC-OFCG was about 20% of the input power. Part of the comb was used to control the monolithic cavity and half was lost at the fiber coupling. An average power of 0.2 mW was coupled into an erbium-doped fiber amplifier (EDFA). Its output was introduced to a 1-km length of DFF (anomalous dispersion 0.12 ps/km/nm @ 1550 nm) [8]. When the maximum output power of the amplifier was 200 mW, the peak power of the pulse train was estimated to be about 10 W.

The optical spectrum from the DFF in the vicinity of several sideband frequencies was heterodyne-detected using an additional laser diode (LD2) acting as a local oscillator (LO), a fast InGaAs pin photodiode (PD), and an RF spectrum analyzer. The LO field is combined with the comb using a beam splitter. A 1.6-μm LD and a 1.55-μm LD were used as LD2 for frequency difference measurements. The tunable range of the two lasers was between 1.51 and 1.64 μm in wavelength, and the maximum frequency offset from the LD1 was 12 THz. Because the comb power is much higher than the power of LD2, we used a grating and a pinhole as a filter to remove the amplitude noise of the comb. The spectral width of 1 nm around the sideband was coupled into the PD. The beat signal was amplified, and its spectrum was measured with an RF spectrum analyzer.

B. Experimental Result

The spectra of the DFF output were also investigated with the help of a monochromator. Fig. 2 shows the envelope spectra measured with 1-nm resolution. The output powers for curves A, B, and C were 50, 100, and 200 mW, respectively. The spectral broadening was observed when the average power of the EDFA output was more than 50 mW. The OFC span, which was defined as the width where the intensity of each measured point was more than −50 dBm, was 30 THz for the output power of 50 mW, and it increased to 50 THz when the output of the amplifier was 200 mW. Wavelengths

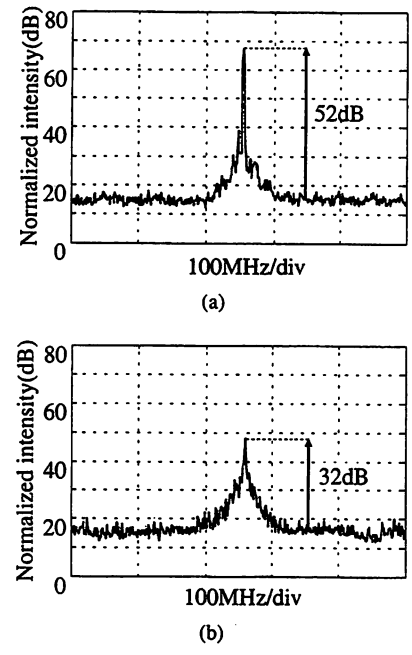

Fig. 3. RF spectra of beat signals between LD2 and the comb. The offset frequency from the carrier are (a) 1 THz and (b) 12 THz. The intensities are normalized to shot noise produced by LD2. The span and resolution bandwidth were 500 and 1 MHz, respectively.

longer than 1.7 μm were estimated by extrapolation. Even though the power increased to 260 mW, the spectrum was almost the same as curve C. The frequency span of 50 THz is as large as a quarter of the carrier frequency, and 8000 sidebands are included. To our knowledge, this is the widest sideband spectrum that has been obtained from a single-mode laser using only external modulation. SPM in the optical fiber is efficient, especially in the wavelength range from 1.3 to 1.6 μm. The material GVD of the optical fiber in this wavelength range can be compensated for by structural GVD in the DFF, which has a double cladding layer. Such a refractive index profile not only affects the GVD compensation but also enhances the nonlinearity, because this profile reduces the mode field diameter. However, spectral broadening became less efficient for the higher average powers because of the fourth-order dispersion of the DFF. Therefore, 50 THz was the limit of the spectral broadening due to fourth-order dispersion. To increase the broadening efficiency, we need optical fibers with a smaller dispersion of the higher order or a wider anomalous dispersion range, even if the GVD of the center wavelength may be larger than that of the DFF.

Fig. 3(a) and (b) shows the heterodyne-detected spectra of the beat signals when the frequency offset from the carrier was 1 THz (1.53 μm) and 12 THz (1.645 μm), respectively. The output power was 50 mW and the envelope spectrum of the comb was similar to curve A of Fig. 2. The beat signals were measured with a resolution bandwidth of 1 MHz and a span of 500 MHz. The intensities are normalized to the shot-noise limit produced by LD2. The SNR's were 52 dB for 1 THz and 32 dB for 12 THz in a 1-MHz resolution bandwidth. The floor of the beat spectra was due to beat noise between the second laser and the spontaneous emission noise around the sideband. The beat noise intensities were 16 dB higher

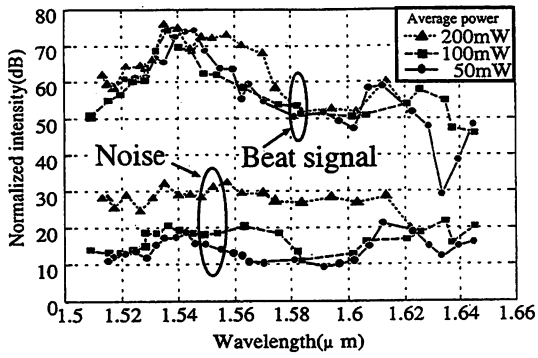

Fig. 4. Dependence of the beat signal intensity and the noise intensity on the wavelength of LD2 as a function of the average output power of the EDFA. Both the signal and noise intensities are normalized to shot noise produced by the photocurrent of LD2. The upper points show the wavelength dependence of the beat signal intensities and the lower points show that of the noise intensities.

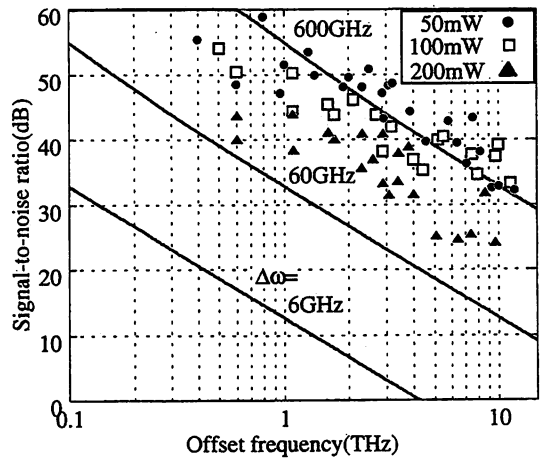

Fig. 5. Dependence of the SNR on offset frequency as a function of output power of the amplifier. Circles, squares, and triangles are the measured SNR for 50, 100, and 200 mW, respectively. Solid lines are the theoretical result showing the SNR decrease for large offset frequencies for $\Delta\omega = 6$, 60, and 600 GHz, respectively. The SNR for the initial two modes were assumed to be 60 dB.

than the shot-noise limit. Noise from the RF amplifier was not negligible at the second laser wavelength of 1.645 μm because the output power of the second laser decreased to 50 μW. The noise of the RF amplifier was comparable to the beat noise. The linewidths of the beat spectra were less than a few megahertz at the −3-dB point. Since the linewidth of the laser was 1 MHz, we could not observe the difference between the linewidth of the two beat signals. The measured beat spectra proved the coherent nature of this process. However, the noise floor of the beat signals within 100 MHz around the carrier increased with the offset frequency because of higher order multiplication of several additional noises.

Fig. 4 shows the dependence of the beat signal intensity and the noise intensity on the wavelength of LD2 for several average output powers of the EDFA. Both the signal and noise intensities are normalized to the shot-noise level of LD2. The upper points show the wavelength dependence of the beat signal intensities and the lower points show that of the noise intensities. Circles, squares, and triangles show the measured intensities for an EDFA power of 50, 100, and 200 mW, respectively. Since the spontaneous emission spectrum added in the amplifier is also broadened by the signal pulse intensity, the variation of the noise intensity was also similar to the measured spectral profile. Further, because of the noise characteristics, the decrease of the SNR with increases in the offset frequency was slower than that of a conventional OFCG, which has an exponentially decreasing sideband intensity. However, the SNR of the comb produced by SPM also gradually decreased with offset frequency, and the noise intensity increased with the average power. Fig. 5 shows the dependence of the SNR on offset frequency as a function of amplifier output power. Circles, squares, and triangles show the measured SNR of the beat signals that are shown in Fig. 4 for average powers of 50, 100, and 200 mW, respectively. The SNR for each power was 20 dB per decade.

III. Discussion

A. Discontinuity of the Sideband Spectrum

The sudden decrease of beat signal intensity at 1.63 μm for 50 mW was due to the discontinuity of the sideband spectrum. Theoretical calculations show that the spectral envelope after broadening has large intensity variations between odd and even sidebands [7]. The variation appears to be due to the typical output of an OFCG which consists of two pulses in a period of sinusoidal modulation: a positive pulse and a negative pulse. The spectral range is above the carrier frequency for one pulse and below the carrier frequency for the other. Therefore, the pulse repetition rate is f_m if we consider the difference between the two pulses. As indicated in [6], all sidebands above the carrier and even sidebands below the carrier are in phase with the carrier, but the phase of odd sidebands below the carrier are π-shifted. The spectra of two pulses are independently broadened by SPM because the two pulses are separated by $1/2f_m$ in the time domain. The obtained comb is the result of the superposition of the two broadened spectra. Therefore, the power of each sideband is added destructively or constructively according to its order, and the intensity of the sidebands are discontinuous between odd and even order. This discontinuity indicates that the difference of the initial pulses becomes smaller after spectral broadening, and the characteristic of the pulse train was similar to a pulse train with a repetition rate of $2f_m$.

B. Noise Sources

The noise sources for the comb generated in the optical fiber were: 1) the amplified spontaneous emission (ASE) noise; 2) the noise of the modulation signal; 3) imperfect control of both the cavities in the CC-OFCG; 4) laser noise; 5) environmental perturbations such as acoustic pressure and temperature; and 6) spontaneous emission noise produced in the parametric amplification process. Although the spontaneous emission due to the parametric process will determine the limit of the SNR of the SPM sidebands, the contribution was negligible compared to the ASE from the EDFA. Phase noise introduced by acoustic pressure and temperature fluctuations around the optical fiber affects the longterm stability of the sideband frequencies. To compensate for these phase fluctuations, an ac-

curate cancellation technique has been demonstrated [13] that provides millihertz accuracy. This technique can be employed to stabilize an OFC.

1) ASE Noise: ASE noise was added to the amplified comb with 30 dB higher than the shot-noise limit, a gain of 23 dB, and a noise figure of dB for 50-mW output power. The noise spectrum is uniform over a wide frequency range. The contributions of ASE to the comb are phase noise, amplitude noise, and phase noise induced by amplitude noise through the intensity-dependent refractive index [14], [15]. The phase and amplitude noise of the initial modes impose fluctuations on each of the generated sidebands, so they have a flat distribution of noise, which is shown in Fig. 3. However, the SNR decreases with increasing sideband order. Because the fluctuations of the initial sidebands are not correlated to each other, they impose a sum effect on the mixing product. We estimate that the decrease of the SNR for large offset frequency sidebands is the multiplication factor of the fluctuations.

We assume that the initial comb consists of only two optical frequencies ω_0 and ω_1 with a frequency spacing of $\Delta\omega$ for simplicity. A small $\Delta\omega$ requires a large number of multiplications compared with a large $\Delta\omega$ to produce a sideband at the same offset frequency. A new frequency ω_n, which is $n\Delta\omega$ away from ω_0, is produced by the mixing process $n\omega_1 - (n-1)\omega_0$. This assumption is valid for large offset frequency sidebands when the modulation index due to SPM in the fiber is small. This assumption applies at the average power of 50 mW in our experimental results, since this power provides the lowest modulation index necessary to generate sidebands at an offset around 10 THz. The output of the OFCG has actually more than a thousand sidebands in the whole bandwidth. A number of different mixing processes produce sidebands at a given frequency with a high multiplication factor. However, the contribution of the higher multiplication factors can be ignored when the modulation index is small and sideband generation with the lowest multiplication factor is dominant. Therefore, FWM from the two initial modes represents the multiplication of phase noise and amplitude noise due to ASE. The phase fluctuation of the sideband is $n\Phi_1(t)-(n-1)\Phi_0(t)$, where $\Phi_0(t)$ and $\Phi_1(t)$ are phase fluctuations of the initial modes. $\Phi_0(t)$ and $\Phi_1(t)$ are supposed to be stationary Gaussian random process, and the temporal averages of the phase noise power for the two modes are assumed to be equal: $\langle\Phi_0(t)^2\rangle = \langle\Phi_1(t)^2\rangle$. The phase noise power of the sideband becomes $n^2 + (n-1)^2$ times larger than that of the initial modes. Amplitude fluctuations of the mixing product are also estimated from the initial amplitude $(1 + a_0(t)), (1 + a_1(t))$, where $a_0(t)$ and $a_1(t)$ are amplitude fluctuations of the initial modes ($|a_0(t)|, |a_1(t)| \ll 1$). Amplitude fluctuation of the mode ω_n is $(1 + a_1(t))^n(1 + a_0(t))^{n-1} \simeq 1 + na_1(t) + (n-1)a_0(t)$. If the temporal average of the amplitude noise power is assumed to be $\langle a_0(t)^2\rangle = \langle a_1(t)^2\rangle$, then the amplitude noise intensity of the sideband also becomes $n^2 + (n-1)^2$ times larger than that of the initial modes.

These simple considerations show that SNR's of sidebands decrease by approximately 20 dB per decade while the linewidth broadening due to carrier collapse is not significant. The solid lines of Fig. 5 show that the theoretical results of the SNR decrease with large offset frequencies for $\Delta\omega = 6$, 60, and 600 GHz, respectively. The SNR's for the initial two modes were assumed to be 60 dB from the experimental conditions. The mode separation of 600 GHz is close to the initial 3-dB bandwidth of the OFC after the amplifier. The measured SNR for 50 mW was in good agreement with the theoretical result of 600 GHz for large offset frequencies. Therefore, a large span and a high SNR of the initial comb is required for high-quality sideband generation. This agreement also indicates that the linewidth broadening due to the carrier collapse was not significant for offset frequencies less than 12 THz. Although theoretically several hundred terahertz is possible, the carrier collapse will be a major contribution to decreasing the SNR for offset frequencies of more than 100 THz. Further decrease of the SNR could result from the high-power pulses because it increases the phase noise induced by amplitude noise and also enables sideband generation with a high multiplication factor.

2) Phase Noise of the Modulation Signal: Carrier collapse is particularly important for higher order sidebands, because the noise amplitude is multiplied by the same factor as the sideband order. Noise sources which cause the carrier collapse are phase noise of the RF modulation signal and fluctuation of the cavity length. Since the kth sideband of the OFCG output has a phase deviation which is k times larger than the phase deviation of the RF signal, the power of the noise sidebands for the kth-order sideband increases by a factor of k^2 [16]. The mixing products between the sidebands in an optical fiber maintain the phase deviations in proportion to the order of the sideband. Since the 12-THz offset frequency is the 2000th sideband, the phase noise level increases 66 dB compared with the RF signal. The measured relative intensity in the noise sidebands of the 12-THz beat signal was larger than that of the 1-THz beat signal, showing that the phase noise around the beat signal indeed increased with the sideband order. In the measured beat signals, the intensity in the foot of the beat signals increased by 20 dB when the multiplication factor increased from 160 (1 THz) to 2000 (12 THz). The theoretical value of the multiplication factor, 22 (dB), is in good agreement with the experimental result. Although carrier collapse due to the phase noise of the modulation signal was not significant for the 12-THz offset frequency, a low noise oscillator will be required for larger offset frequencies.

3) Imperfect Control of OFCG Cavities: The imperfect control of the OFCG cavity make amplitude and phase noise at frequencies less than several tens of kilohertz. Also, the fluctuation of the front coupling cavity causes amplitude and phase fluctuations of the comb. We found that the measured beat signal included large amplitude fluctuations. Because spectral broadening depends on the output power, small input power fluctuations induce large fluctuations in the sideband power. When the power fluctuation at the output of the CC-OFCG was 20% of the average power, the sideband intensity at 7 THz offset from the carrier varied by more than 10 dB. The intensity fluctuation was reduced to less than 3 dB when the output power fluctuation was reduced to a few percent of the average power by stabilization of the front cavity. The error signal for stabilization of the monolithic cavity is

obtained as a mixing product between the modulation signal and a reference signal obtained by a fast photodiode detecting part of the comb. The amplitude of the error signal, which is the gain of a feedback loop at the same time, changes as the power fluctuates. When the monolithic cavity length is locked with the offset from the zero crossing of the error signal, the length of the monolithic cavity also changes with power fluctuations, which causes phase fluctuations in the sidebands. The phase deviation due to the cavity fluctuation becomes k/β times as large as the deviation for the kth sideband under the modulation index of β [12]. Since this phase deviation also increases in proportion to the order of the sideband, the instability of the OFCG affects the measured beat spectrum, especially with large offset frequency. Therefore, the cavity fluctuation of the M-OFCG also causes carrier collapse due to the large phase deviations. Although we observed the dependence of power in the phase noise pedestal on the offset of the cavity locking, the dependence on the locking point is under consideration.

4) Noise of the Laser: The amplitude noise of the laser is small compared with its phase noise, and phase noise produced by this amplitude noise is negligible. However, the phase noise of the laser is converted to amplitude noise by passing through the FP cavity of the OFCG. The amplitude noise increases phase noise of the sidebands by SPM. Compared with the previous measurements where a conventional OFCG was used, the noise in the foot of the beat signals was larger than that of a conventional OFCG, even around the carrier frequency. Therefore, the phase noise of the comb is increased in the combination of the OFCG using an FP modulator and SPM.

IV. Summary

We have demonstrated OFCG over a span of up to 50 THz using SPM in an optical fiber. Each sideband was investigated and the coherent nature of the process was proved by heterodyne detection with the help of an additional LD as a local oscillator. The SNR of the beat signal at the offset frequency of 12 THz was 32 dB when the resolution bandwidth was 1 MHz. Although the power in the foot of the beat signal increased with sideband order, the linewidth of the beat signal was less than a few megahertz.

Acknowledgment

The authors thank Dr. Onishi, Sumitomo Electric Industries, for the DFF and Dr. Zhao, University of Sydney, and Dr. Tiemann, University of Colorado, for helpful discussions.

References

[1] T. Kobayashi, T. Sueta, Y. Cho, and Y. Matsuo, "High-repetition-rate optical pulse generator using a Fabry-Perot electro-optic modulator," *Appl. Phys. Lett.*, vol. 21, no. 8, pp. 341–343, 1972.

[2] M. Kourogi, K. Nakagawa, and M. Ohtsu, "Wide-span optical frequency comb generator for accurate optical frequency difference measurement," *IEEE J. Quantum Electron.*, vol. 29, pp. 2693–2701, Oct. 1993.

[3] A. Morimoto, A. Shibagaki, and T. Kobayashi, "Efficient ultrashort optical pulse generator using a modified fabry-perot modulator," in *CLEO'93, 1993 OSA Tech. Dig.*, 1993, vol. 11, pp. 558–559, paper CThS84.

[4] Th. Udem, M. Kourogi, J. Reichert, and T. W. Hänsch, "Accuracy of optical frequency comb generators and optical frequency interval divider chains," *Opt. Lett.*, vol. 23, no. 17, pp. 1387–1389, 1998.

[5] D-S. Kim, M. Arisawa, A. Morimoto, and T. Kobayashi, "Femtosecond optical pulse generation using quasivelocity-matched electrooptic phase modulator," *IEEE J. Select. Topics Quantum Electron.*, vol. 2, pp. 493–499, May/June 1996.

[6] M. Kourogi, B. Widiyatmoko, and M. Ohtsu, "3.17-THz frequency-difference measurement between lasers using two optical frequency combs," *IEEE Photon. Technol. Lett.*, vol. 8, pp. 560–562, Apr. 1996.

[7] K. Imai, M. Kourogi, and M. Ohtsu, "30-THz span optical frequency comb generation by self-phase modulation in an optical fiber," *IEEE J. Quantum Electron.*, vol. 34, pp. 54–60, Jan. 1998.

[8] Y. Kubo, H. Kanamori, H. Yokota, and S. Tanaka, "Dispersion flattened single-mode fiber for 10,000 km transmission system," in *Conf. Proc. ECOC'90*, 1990, pp. 505–508.

[9] M. Kourogi, T. Enami, and M. Ohtsu, "A coupled-cavity monolithic optical frequency comb generator," *IEEE Photon. Technol. Lett.*, vol. 8, pp. 1698–1700, Dec. 1996.

[10] A. S. Bell, G. M. Macfarlane, E. Riis, and A. I. Ferguson, "Efficient optical frequency-comb generator," *Opt. Lett.*, vol. 20, no. 12, pp. 1435–1437, 1995.

[11] M. Kourogi, T. Enami, and M. Ohtsu, "A monolithic optical frequency comb generator," *IEEE Photon. Technol. Lett.*, vol. 6, pp. 214–217, Feb. 1994.

[12] M. Kourogi, B. Widiyatomoko, Y. Takeuchi, and M. Ohtsu, "Limit of optical-frequency comb generation due to material dispersion," *IEEE J. Quantum Electron.*, vol. 31, pp. 2120–2126, Dec. 1995.

[13] L.-S. Ma, P. Jungner, J. Ye, and J. L. Hall, "Delivering the same optical frequency at two places:accurate cancellation of phase noise introduced by an optical fiber or other time-varying path," *Opt. Lett.*, vol. 19, no. 21, pp. 1777–1779, 1994.

[14] J. P. Gordon and L. F. Mollenauer, "Phase noise in photonic communications systems using linear amplifiers," *Opt. Lett.*, vol. 15, no. 23, pp. 1351–1353, 1990.

[15] M. Murakami and S. Saito, "Evolution of field spectrum due to fiber-nonlinearity-induced phase noise in in-line optical amplifier systems," *IEEE Photon. Technol. Lett.*, vol. 4, pp. 1269–1272, Nov. 1992.

[16] F. L. Walls and A. DeMar.i, "RF spectrum of a signal after frequency multiplication; measurement and comparison with a simple calculation," *IEEE Trans. Instrum. Meas.*, vol. IM-24, pp. 210–217, June 1975.

K. Imai was born in Tokyo, Japan, in 1971. He received the B.S. and M.S degrees from Tokyo Institute of Technology, Tokyo, Japan, in 1994 and 1996, respectively. He is currently working toward the Ph.D. degree in applied electronics at the same institution.

Mr. Imai is a student member of the Japan Society of Applied Physics.

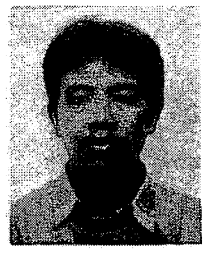

B. Widiyatmoko was born in Boyolali, Indonesia, in 1962. He received a degree in physics from Gadjahmada University, Yogyakarta, Indonesia, in 1987 and received the M.S. degree in applied electronics from Tokyo Institute of Technology, Tokyo, Japan, in 1995. He is currently working toward the Ph.D degree in applied electronics at the Tokyo Institute of Technology.

Since 1987, he has been with Research and Development for Applied Physics, Indonesia Institute of Science, as a Member of the Research Staff.

Mr. Widiyatmoko is s student member of the Japan Society of Applied Physics.

Motonobu Kourogi was born in Shiga, Japan, 1966. He received the B.S. degree from Shizuoka University, Shizuoka, Japan, in 1988, and the M.S. and Ph.D. degrees from the Tokyo Institute of Technology, Tokyo, Japan, in 1990 and 1993, respectively.

Since 1993, he has been with Tokyo Institute of Technology as a Research Associate. His current research interests are frequency synthesis of semiconductor lasers.

Dr. Kourogi is a member of the Japan Society of Applied Physics.

Motoichi Ohtsu (M'88–SM'90) received the B.E., M.E., and Dr.E. degrees in electronics engineering from the Tokyo Institute of Technology, Tokyo, Japan, in 1973, 1975, and 1978, respectively.

In 1978, he was appointed a Research Associate, and in 1982, he became Associate Professor at the Tokyo Institute of Technology. From 1986 to 1987, while on leave from Tokyo Institute of Technology, he joined the Crawford Hill Laboratory, AT&T Bell Laboratories, Holmdel, NJ. In 1991, he became a Professor at Tokyo Institute of Technology. Since April 1993, he has been concurrently the leader of the "PHOTON CONTROL" project of Kanagawa Academy of Science and Technology, Kanagawa, Japan. His main field of interests are photon scanning tunneling microscopy, its application to nanoscale photonics and quantum optics, and laser frequency control. He has written over 150 papers and received a number of patents. He is the author and co-author of 13 books, including two in English, entitled *Highly Coherent Semiconductor Lasers* (Boston, MA: Artech House, 1991) and *Coherent Quantum Optics and Technology* (Dordrecht, The Netherlands: Kluwer, 1993). He has been a tutorial lecture of the SPIE and the Optical Society of America.

Dr. Ohtsu is a member of the Japan Society of Applied Physics, the Institute of Electronics, Information and Communication Engineering of Japan, the Institute of Electrical Engineering of Japan, and the Optical Society of America. He has been awarded eight prizes from academic institutions including the Issac Koga Gold Medal of URSI, the Japan IBM Science Award, and two awards of the Japan Society of Applied Physics.

Linking Two Optical Frequency Combs by Heterodyne Optical Phase Locking Between Diode Lasers at 2.6-THz Frequency-Difference

B. Widiyatmoko, M. Kourogi, and M. Ohtsu, *Senior Member, IEEE*

***Abstract*—Two optical frequency combs (OFC) with total span of 8 THz have been realized and linked by injecting two laser beams into one OFC generator. Two lasers whose frequencies were separated by 2.6 THz were heterodyne phase-locked to link the two combs. The phase-locked loop bandwidth was 1 MHz and the phase error variance was estimated to be 0.08 rad^2.**

***Index Terms*— Electrooptic modulation, optical phase-locked loops, phase noise, optical pulse generation, laser stability.**

HIGHLY accurate laser frequency measurement is indispensable for the development of coherent optical communication systems and precise measurements of physical constants. An optical frequency-synthesis chain which connects the optical laser frequency to infrared frequency standards or to a microwave atomic clock based on optical frequency difference divider has been proposed [1]–[3] and realized [4]. Its basic concept is the large frequency difference is coherently bridged using an optical frequency divider which can divide the frequency difference between lasers by using phase locking via beat signal of their harmonics and sum frequency [2]. A similar method has also been proposed using an optical parametric oscillator as the frequency divider [3]. However, the chain becomes more complicated and requires several phase-locked laser sources because it needs many divider stages to measure directly the difference frequency between the harmonic frequency and sum frequency using a photodetector. To overcome these difficulties, a system for measuring large optical frequency difference with an optical frequency comb (OFC) generator consisting of an electrooptic (EO) modulator inside Fabry–Perot (FP) cavity has been proposed [5], [6].

In the frequency-difference measurement using an OFC generator, the highest measurable frequency difference depends on the power of the sideband. The limit of the span of the sidebands due to the material dispersion of the OFC has been experimentally studied [7]. Recently, an OFC with a span over the dispersion limit as wide as 30 THz has been realized by self-phase modulation (SPM) method using dispersion flattened optical fiber [8], but this method can only be applied in the 1.55-μm wavelength region because of the large dispersion of optical fiber in other regions. An OFC chain as shown in Fig. 1(a) can be used to expand the OFC in order to overcome the dispersion limit. Laser 1 is a master laser whose frequency could be stabilized to the molecular absorption line. The OFC is generated from laser 1. If another laser (laser 2) is locked to one sideband of the OFC by a phase-locking technique and the OFC can be generated from this laser, this process can be repeated to achieve a wide span of linked OFC's.

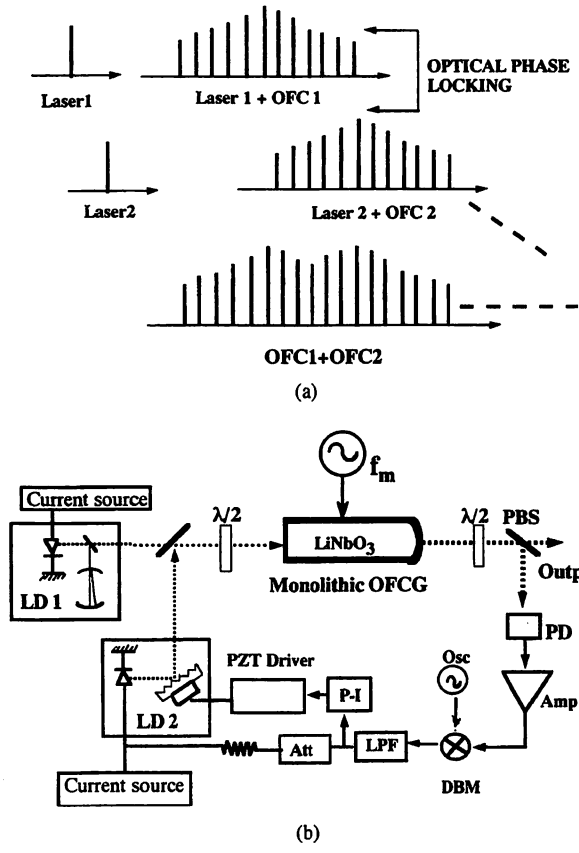

Fig. 1. Schematic explanation of (a) the optical frequency comb chain and (b) the experiment setup. LD: Laser diode. PBS: Polarized beam splitter. PD: Photodetector. DBM: Double balanced mixer. LPF: Lowpass filter. P-I: Proportional-integral control. ATT: Attenuator.

Manuscript received June 24, 1998; revised December 4, 1998.

B. Widiyatmoko is with the Interdisciplinary Graduate School of Science and Engineering, Tokyo Institute of Technology, Midori-ku, Yokohama 226, Japan. He is also with the Research and Development Center for Applied Physics, Indonesia Institute of Sciences, Komplek PUSPIPTEK, Serpong, Tangerang 15314, Indonesia.

M. Kourogi and M. Ohtsu are with the Interdisciplinary Graduate School of Science and Engineering, Tokyo Institute of Technology, Midori-ku, Yokohama 226, Japan. They are also with the Kanagawa Academy of Science and Technology, Takatsu-ku, Kawasaki-shi, Kanagawa 213-0012, Japan.

Publisher Item Identifier S 1041-1135(99)02512-4.

In this letter, we report an optical phase-locking experiment between two OFC's to form an OFC link, using two lasers with frequency difference of 2.6 THz.

The measurable frequency difference depends on the signal-to-noise ratio (SNR) of the beat signal. In a conventional method, i.e., frequency-difference measurement between two lasers with one laser forming the OFC, the SNR depends on the power of one sideband which contributes to beat generation. In this optical phase-locking experiment between two combs whose center frequencies are ν_1 and ν_2, respectively, the heterodyne signal results from the superposition of many sideband pairs of each comb sidebands so that the SNR can be increased by up to 20 dB [9]. In order to realize the high-efficiency beat generation, the beat signals generated by many sidebands must be in-phase. Note that the sidebands of the OFC is generated by phase modulation of laser light, so they have low-order sidebands ($k < 0$ and $k' < 0$, where k and k' are sideband order of laser 1 and laser 2, respectively) in accordance with Bessel function of $-j'$th order, and high-order sideband ($k > 0, k' > 0$) in accordance with Bessel function of $+j'$th order. In this experiment, the beat signal is generated by superposition of the beat between the pairs of the nearest modulation sidebands from two lasers which have the same sign, i.e., the $-k$ sideband and $-k'$ sideband or the $+k$ sideband and $+k'$ sideband. The beat between two sidebands with opposite sign will disappear by the interference between the beat of their neighborhing pair because they have the π-radian phase difference between each other. If the sideband powers of the two OFC's are identical, the shot noise limited SNR is given by [9]:

$$\mathrm{SNR}_k = \frac{\eta_{\mathrm{FP}}\eta_{\mathrm{PD}}P_1P_2\frac{\pi}{2\beta F}\exp\left(-\frac{K\pi}{\beta F}\right)}{(P_1+P_2)2h\nu B} \qquad (1)$$

where K is the number of the sidebands between the two lasers frequencies, η_{FP}, β, F, h are the efficiency of the FP cavity, modulation index, finesse of FP cavity and Planck's constant, respectively. $\nu = (\nu_1 + \nu_2)/2$ is the average of the two laser frequencies, η_{PD} is the quantum efficiency of the photodiode and B is its detection bandwidth.

Fig. 1(b) shows our experimental setup. Two semiconductor lasers of 0.78-μm wavelength were used. Laser 1 was stabilized using a resonant FP resonator, so that the laser linewidth was reduced to about 10 kHz. The other (Laser 2) was an extended-cavity semiconductor laser in order to tune the frequency-difference continuously. Two laser beams ware injected into one OFC generator then driven by a microwave frequency f_m. The OFC generator consisted of an EO crystal ($LiNbO_3$, $1.25 \times 1 \times 21$ mm^3) with high-reflection coating (99.5% at a wavelength of 0.83 μm of wavelength) on both ends, i.e., the EO crystal works as a monolithic FP cavity. Two ends of the crystal were polished to be flat and convex with a curvature radius of 50 mm. The value of finesse and $\eta_{\mathrm{F\text{-}P}}$ were 380 and 0.15, respectively. Its free-spectral range (FSR) and the modulation frequency f_m were 3.14 and 6.28 GHz (=2FSR), respectively. The maximum single pass modulation index β was 0.36π radian when the microwave power was 10 W.

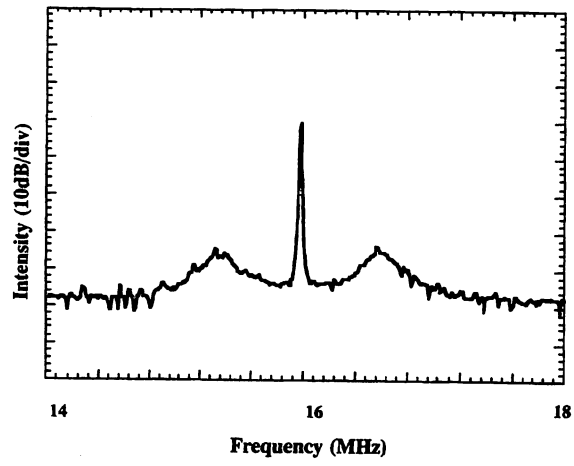

Fig. 2. Heterodyne signal under locked condition observed by RF spectrum analyzer with 3-kHz resolution bandwidth and 4-MHz span.

Since the value of β could not be adjusted independently for the two lasers, we had to choose the value of f_m to realize a symmetric envelope spectral profile of the two OFC's. We confirmed experimentally that the value of f_m for the symmetric OFC envelope spectrum varied 0.84 MHz per 1 nm change of the laser wavelength. Tuning between the FSR of the FP cavity and f_m was done by adjusting the EO crystal temperature. Experimental results show that the FP resonant frequency shifts one FSR if the crystal temperature changes by 0.8 °C.

The heterodyne phase-locked loop technique was used to link the two OFC's. The heterodyne signal between the OFC's was detected by a commercial Si-avalanche photodiode (APD) and was amplified using a 20-dB RF amplifier. The amplified signal was phase compared with the reference signal from a stable RF local oscillator using a double balance mixer (DBM). This provides an error signal. After passing through a first-order active loop filter, the signal was separated into two channels and was feedback to laser 2 via a PZT driver for the slow component of the control signal and the injection current for the fast component of the control signal. Fig. 2 shows the heterodyne signals between OFC's under phase locking at 2.6-THz difference-frequency observed with an RF spectrum analyzer. It was observed at around 16 MHz with 4-MHz span and 3-kHz resolution bandwidth. The SNR of the heterodyne signal is higher than 40 dB. Substituting the experimental values of the parameters ($k = 418$, $\eta_{\mathrm{FP}} = 0.15$, $\eta_{\mathrm{PD}} = 0.7$, $\beta = 0.36$, Pi $= 5$ mW, $B = 100$ kHz) into (1), the calculated SNR_k is 58 dB. This value agrees with the measured value, because the shot-noise limited detection was not realized in this experiment due to the low total power of the OFC and large excess noise of the APD. Frequency difference as large as 3.5 THz was already measured with the SNR of large than 32 dB. From the heterodyne signal, we estimate that the phase error noise was about 0.08 rad^2 and the loop bandwidth was about 1 MHz. Although the cycle slip is induced in this lock loop, the frequency of this cycle slip is negligibly small. The loop bandwidth was limited by the delay time effect of the high-order sideband from the carrier. For the FP cavity length of 22 mm, the 418'th sideband delays

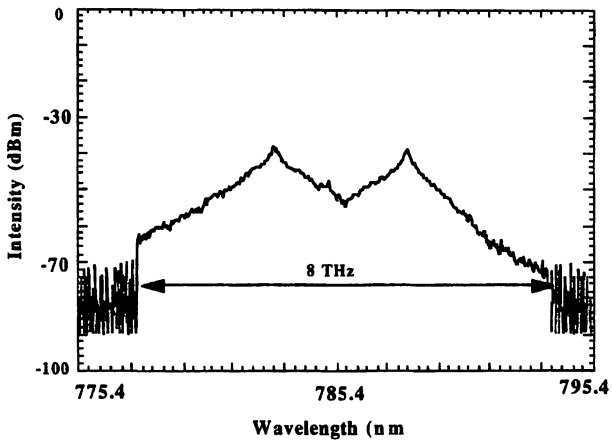

Fig. 3. Envelopes of the two OFC spectra under phase-locked condition measured by an optical spectrum analyzer with 0.1-nm resolution and 20-nm span.

about 0.2 μs from carrier. We observed that the loop bandwidth was decreased by increasing the difference frequency between the two lasers. At 0.5-THz difference frequency the locking bandwidth could be set, with loop stability, as high as 2.2 MHz. One of the problems in this phase locking is the large phase fluctuation of the higher order sideband of the OFC's due to the microwave noise. Although the kth sideband noise magnitude is k times large than the microwave noise, we can expect lower magnitude using a high stability microwave oscillator. The FP length fluctuation due to the temperature instability also contributes to increasing the phase noise, however it can be reduced by controlling of the FP resonant frequency.

A portion of the output of OFC generator was monitored by an optical spectrum analyzer. Fig. 3 shows the observed envelope of two OFC's under phase-locked condition. The wavelengths corresponding to the carrier frequency ν_1 and ν_2, measured by an optical wavemeter, were 0.7828 μm and 0.7881 μm, respectively. From these values the frequency difference $\nu_1 - \nu_2$ was estimated as 2.62 THz. This figure clearly shows that the total span covered by the two linked OFC's is about 8 THz, reaching to the material dispersion limit of the EO crystal.

In order to expand the frequency-difference, it can be advantageous to use a digital phase comparator because of its higher sensitivity and the absence of cycle slips [10]. Using the digital phase comparator, phase can be locked even if the SNR is as low as 20 dB. Since Fig. 3 shows that the slope of the SNR is -9.6 dB/THz, it is possible to expand the frequency difference under phase locking up to 4.5 THz. The SNR was also limited by the dispersion of the EO crystal. However, by substituting the experiment values to (1) it was confirmed that the dispersion material did not give any contribution. Thus 20 dB of SNR can be obtained at a frequency difference as wide as 6 THz. It means that phase locking can be realized at 6-THz frequency difference by using two separate OFC generators and a digital phase comparator. Another way to increase the SNR is to use the cavity-coupled OFC generator [6] because it can increase the efficiency of the OFC generation to about 25% so that the S/N will be increased by $\sim$40 dB.

In addition, an OFC link also can be used to compress an optical pulse if we employ homodyne phase locking because the optical spectra are broadened with the equal frequency separation between the adjacent sidebands. However if two pulses of the OFC are generated by a separate OFCG, the time delay must be added to syncronize the phase between two pulses.

In summary, we realized an OFC chain by injecting two lasers into one OFC generator and phase locking. Heterodyne phase locking was done even though the frequency difference between the two lasers was as large as 2.6 THz. The total span of the two linked OFC's of about 8 THz was achieved.

REFERENCES

[1] K. Nakagawa, M. Kourogi, and M. Ohtsu, "Proposal of a frequency-synthesis chain between the microwave and optical frequencies of the Ca intercombination line at 657 nm using diode lasers," *Appl. Phys. B*, pp. 425–430, 1993.

[2] R. Wynands, T. Mukai, and T. W. Hansch, "Coherent bisection of optical frequency intervals as large as 530 THz," *Opt. Lett.*, vol. 17, pp. 1749–1751, 1992.

[3] N. C. Wong, "Optical frequency division using an optical parametric oscillator," *Opt. Lett.*, vol. 15, pp. 1129–1131, 1990.

[4] F. Schmidt-Kaler, D. Leibfried, S. Seel, C. Zimmermann, W. K"onig, M. Weitz, and T. W. Hansch, "High-resolotion spectroscocy of the 1S-2S transition of atomic hydrogen and deiterium," *Phy. Rev. A*, vol. 51, no. 4, pp. 2789–2800, 1995.

[5] M. Kourogi, K. Nakagawa, and M. Ohtsu, "Wide-span optical frequency comb generator for accurate optical frequency difference meassurement," *IEEE. J. Quantum Electron.*, vol. 29, pp. 2693–2701, Oct. 1993.

[6] M. Kourogi, T. Enami, and M. Ohtsu, "A coupled-cavity monolithic optical frequency comb generator," *IEEE Photon. Technol. Lett.*, vol. 8, pp. 1698–1700, Dec. 1996.

[7] M. Kourogi, B. Widiyatmoko, T. Takeuchi, and M. Ohtsu, "Limit of optical-frequency comb generation due to material dispertion," *IEEE. J. Quantum Electron.*, vol. 31, pp. 2120–2126, Dec. 1995.

[8] K. Imai, M. Kourogi, and M.Ohtsu, "30-THz span optical frequency comb generation by self-phase modulation in optical fiber," *IEEE J. Quantum Electron.*, vol. 34, pp. 54–60, Jan. 1998.

[9] M. Kourogi, B. Widiyatmoko, and M. Ohtsu, "3.17 THz frequency-difference measurenent between laser using two optical frequency combs," *IEEE Photon. Technol. Lett.*, vol. 8, pp. 560–562, Apr. 1996.

[10] M. Prevedelli, T. Freegarde, and T. W. Hansch, "Phase locking of grating-tuned diode lasers," *Appl. Phys. B*, vol. 60, pp. 241–248, 1995.

Second-harmonic generation of an optical frequency comb at 1.55 μm with periodically poled lithium niobate

B. Widiyatmoko* and K. Imai

Interdisciplinary Graduate School of Science and Engineering, Tokyo Institute of Technology, 4259 Nagatsuta, Midori-ku, Yokohama 226, Japan

M. Kourogi and M. Ohtsu

Interdisciplinary Graduate School of Science and Engineering, Tokyo Institute of Technology, 4259 Nagatsuta, Midori-ku, Yokohama 226, Japan, and Kanagawa Academy of Science and Technology, KSP East Building, Room 408, 3-2-1 Sakado, Takatsu-ku, Kawasaki 213, Japan

Received October 1, 1998

To expand the span of the optical frequency comb (OFC), we generated the second harmonics of an OFC at 1.55 μm, using a multiperiod periodically poled lithium niobate (PPLN) crystal. A coupled-cavity OFC generator with an average output power of 0.2 mW was amplified and expanded with a fiber amplifier and a dispersion-flattened fiber. The fundamental OFC average power and span were 100 mW and 45 THz, respectively. The second-harmonic comb's span was 3.2 THz; however, we tuned the center frequency over 30 THz by changing the poling period. We also demonstrated that the second-harmonic comb can be used for frequency-difference measurement. © 1999 Optical Society of America

OCIS codes: 120.3930, 300.6210, 190.0190, 230.4320, 190.2620, 160.3370.

Recently laser frequency-difference measurement has become important for applications in optical communication and high-resolution spectroscopy.[1] For these purposes, optical frequency-difference measurement systems made with an optical frequency comb (OFC) generator have been proposed.[2-4] The measurable frequency difference, however, is limited by the span of the OFC. The limit of OFC generation that is due to material dispersion was experimentally studied.[5] Recently we succeeded in expanding the span of an OFC in excess of the dispersion limit to 30 THz, using self-phase modulation in a dispersion-flattened optical fiber.[6] For this expanded OFC a 12-THz frequency-difference measurement was reported.[7] However, this method was applied only near 1.55 μm because a low-dispersion optical fiber was needed. To expand the OFC span to the order of petahertz we propose adding a method of nonlinear optical frequency conversion such as second-harmonic generation (SHG), sum-frequency generation, and difference-frequency generation of the OFC, producing two OFC's by using only one OFC generator.

In this Letter we report SHG pumped by an OFC fundamental. The large optical nonlinearity of periodically poled lithium niobate[8] (PPLN) and the high peak power of an amplified OFC were exploited. The OFC generated by a Fabry–Perot electro-optic modulator followed by amplification and self-phase modulation has a wide frequency span, a short pulse duration, and high peak power.[9] These are properties that are well matched to this nonlinear frequency-conversion application. The total frequency span of the fundamental comb was 45 THz. Individual second-harmonic comb spans were 3.2 THz, and we tuned center frequencies over 30 THz by changing the poling period. In SHG of the OFC, the sum frequencies of comb elements are generated, and the frequency spacing of the harmonic comb is equal to the frequency spacing of the fundamental comb. Within the limits of phase matching, or equivalently of group-velocity walk-off, the same frequency component of harmonic generation and sum-frequency generation will have the same phase and add constructively.

Figure 1 shows the experimental setup. We used an extended-cavity laser diode (LD1) at 1.54-μm wavelength and 4-mW power as a light source. The coupled-cavity optical frequency comb generator (C-C-OFCG) used here has the same configuration and control system as one previously reported.[6] The output of the coupled-cavity OFC generator had a 10-THz span and 0.2 mW of average power. This OFC was amplified to 100 mW average power by an erbium-doped fiber amplifier (FA). After amplification we expanded the OFC span by using a dispersion-flattened fiber (DFF). The output of

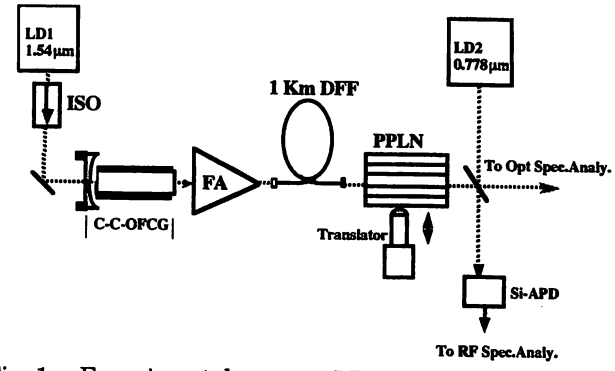

Fig. 1. Experimental setup: LD1, LD2, extended-cavity laser diodes; ISO, isolator; Si-APD, Si avalanche photodiode; other abbreviations defined in text.

0146-9592/99/050315-03$15.00/0

the expanded OFC was incident upon a 19-mm-long PPLN crystal. A 60-mm focal-length achromatic lens focused the output of the DFF beam onto the PPLN crystal to a spot size of ~80 μm. The PPLN crystal contained 10 0.5-mm-wide, 19-mm-long regions of fixed domain inversion period, each spaced 0.1 mm from the next. The poling periods varied from 18.6 to 20.4 μm in 0.2-μm increments along the y direction of the z-cut $LiNbO_3$ crystal. These periods coincide with second-harmonic phase matching from 1.52 to 1.62 μm. By translating the crystal along the y axis, perpendicular to the beam propagation direction, we tuned phase matching through nonoverlapping, adjacent frequency spans. The PPLN crystal was installed in a temperature-controlled oven to permit temperature tuning of the phase match. Portions of the fundamental OFC and the second-harmonic OFC (SH OFC) were monitored with an optical spectrum analyzer.

Figure 2 illustrates the SH OFC spectra at various poling periods obtained by translation of the crystal along the y axis. The inset at the left shows the fundamental OFC spectrum after the DF. The fundamental OFC span was expanded to ~45 THz. Phase matching was possible only over a 15-THz region of the fundamental comb with the available PPLN periods. Even though the individual span of the second-harmonic combs was only 3.2 THz (inset at the right), we could tune these SHG combs over a 30-THz range by changing the grating period. This span is four times that of the span of OFC that was generated by use of the same electro-optic modulator as a fundamental OFC at 0.78-μm wavelength.[5] The center frequency of the comb could be tuned over a 90-THz range, or twice the fundamental comb span, with a greater range of PPLN grating periods. However, the phase of SHG combs will change slightly when the crystal is tuned because of the difference in refractive index. Therefore the crystal must be fixed when we use the SHG combs for frequency-difference measurement.

The inset at the right in Fig. 2 shows one SHG comb that was generated with a 19.2-μm poling period. The narrow span is caused by the effect of the group-velocity mismatch of the pulse propagation in the long crystal. Because the length of the PPLN crystal, l = 19 mm, was much greater than the group-velocity walk-off length, L_{wf}, which is defined as the distance at which the second-harmonic pulse becomes delayed with respect to the transform-limited fundamental pulse by its initial pulse length τ_0, $L_{wf} = \Delta\tau_p/\delta v$, where $\Delta\tau_p$ and δv are the pulse width and the group-velocity mismatch, respectively. The pulse width $\Delta\tau_p$ at the FWHM intensity of the OFC is given by $\Delta\tau_p = 1/2f_m\beta F$, where β is the modulation index, f_m is the modulation frequency, and F is the finesse. From the measured values of β, f_m, and F we estimated that the pulse width was ~250 fs. However, because of the dispersion of the electro-optic crystal effect we measured the pulse to be ~1 ps. In this SH OFC at 1.548 μm, δv = 0.30 ps/mm, so L_{wf} is 3 mm. One can expand this individual span by shortening the crystal below the walk-off length. The individual span of 5 THz was achieved from the PPLN length of 10 mm. In this case, the SH OFC power will be decreased, but we can increase the fundamental power by using a high-power fiber amplifier. The individual span can also be increased by use of a Fourier synthetic quasi-phase-matching grating.[10]

To generate all SH OFC's together we can use a fanout-type PPLN[11] combined with a grating and a cylindrical lens. In this method the fundamental OFC is spectrally separated by a grating and then collimated and focused by a cylindrical lens. From Fig. 2 we observe that the SHG power at the OFC combs' peak spectrum is ~ −38 dBm at 0.1 nm, or 50-GHz resolution bandwidth. So it is clear that the power of one sideband in the central SH OFC was a few nanowatts. This value is sufficient for frequency-difference measurement. To confirm this SH OFC we measured the difference frequency between 0.778 and 1.544 μm. The fundamental laser (1.5436 μm) was stabilized to the $p(16)$ acetylene (C_2H_2) molecular spectral line. From this laser we generated an OFC and a SHG OFC. A second laser, laser 2, was tuned to 0.77822 μm near a Rb two-photon transition frequency. The frequency of laser 2 was 3 THz away from the frequency of the SHG of laser 1. We chose the poling period and the temperature such that the SH OFC was close to laser 2. This period and temperature were 19.6 μm and 95 °C, respectively. SH OFC and laser 2 were focused onto a 1-GHz Si avalanche photodiode, and the beat signal was amplified with a low-noise 30-dB rf amplifier. Figure 3 shows the beat signal observed with a rf spectrum analyzer whose

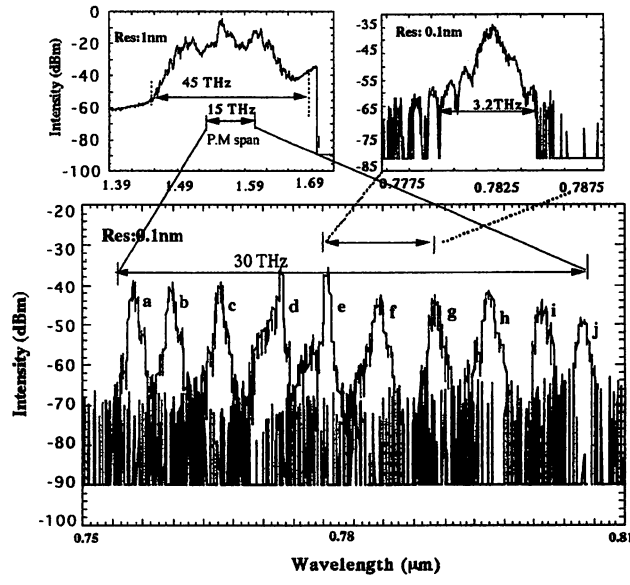

Fig. 2. Spectral envelope of the SHG combs at various poled periods and temperatures observed with an optical spectrum analyzer at 0.1 resolution bandwidth. The curves are SHG combs generated from PPLN with poling periods and temperatures of a, 18.6 μm (T = 65° C); b, 18.8 μm (T = 50° C); c, 19 μm (T = 80° C); d, 19.2 μm (T = 62° C); e, 19.4 μm (T = 60° C); f, 19.6 μm (T = 75° C); g, 19.8 μm (T = 65° C); h, 20 μm (T = 65° C); i, 20.2 μm (T = 72° C); j, 20.4 μm (T = 90° C). Insets, fundamental comb spectrum observed with 1 nm-resolution (right) and the SH OFC generated by a 19.4-μm poled period (left). P. M., phase-matching bandwidth.

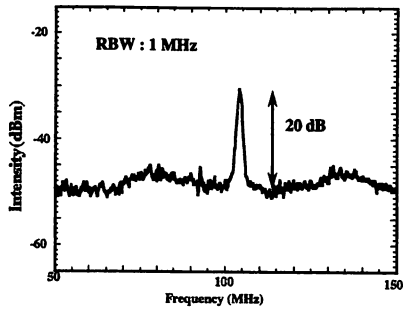

Fig. 3. Spectrum of the beat note between a laser at 0.7782-μm wavelength and a SH OFC sideband generated from 1.5443 μm. RBW, resolution bandwidth.

span and resolution were 100 and 1 MHz, respectively. The signal-to-noise ratio was ~18 dB. The noise in Fig. 3 was dominated by the excess photocurrent noise owing to the Si avalanche photodiode that was set at a current gain of 5 and by the rf amplifier noise. The signal-to-noise ratio is low because the nearest center of the SH OFC was separated by 1.2 THz from laser 2, whereas the maximum span of this SH OFC was only 3.2 THz. We estimate that the signal-to-noise ratio will increase to ~40 dB when the center of the SH OFC coincides with laser 2. We can vary the crystal temperature to attain this condition. We measured that the center of the SH-OFC spectrum can be shifted ~6 GHz/°C. The signal-to-noise ratio can be improved by use of more closely spaced PPLN periods, so the individual combs are overlapping. In principle, from this OFC it is possible to measure the difference frequency between two lasers separated by as much as 90 THz near 0.78 μm of wavelength by employing two crystals with different phase matching.

In summary, we have proposed a method to expand the span of an OFC by adding nonlinear optical frequency conversion to the OFC. We demonstrated the SHG of an OFC for which the center frequency can be tuned over a 30-THz range. By beat signal measurement, we also confirmed that this SHG comb can be used for frequency-difference measurement.

We gratefully thank A. Onae of the National Research Laboratory of Metrology, Tsukuba, Japan, and K. Nakagawa of The University of Electro-Communication, Tokyo, for help and advice in preparing the stabilized laser.

*Permanent address, Research and Development Center for Applied Physics, Indonesia Institute of Sciences, Komplek PUSPIPTEK, Serpong, Tangerang 15314, Indonesia; e-mail, bambang@ae.titech.ac.jp.

References

1. F. Schimidt-Kaler, D. Leibfried, S. Seel, C. Zimmermann, W. König, M. Weitz, and T. W. Hänsch, Phys. Rev. A **51,** 2789 (1995).
2. M. Kourogi, K. Nakagawa, and M. Ohtsu, IEEE J. Quantum Electron. **29,** 2693 (1993).
3. M. Kourogi, T. Enami, and M. Ohtsu, IEEE Photon. Technol. Lett. **6,** 214 (1994).
4. L. R. Brothers, D. Lee, and N. C. Wong, Opt. Lett. **19,** 245 (1994).
5. M. Kourogi, B. Widiyatmoko, T. Takeuchi, and M. Ohtsu, IEEE J. Quantum Electron. **31,** 2120 (1995).
6. K. Imai, M. Kourogi, and M. Ohtsu, IEEE J. Quantum Electron. **34,** 54 (1998).
7. K. Imai, M. Kourogi, B. Widiyatmoko, and M. Ohtsu, in *Conference on Lasers and Electro-Optics (CLEO)*, Vol. 6 of 1998 OSA Technical Digest Series (Optical Society of America, Washington, D.C., 1998), paper CThY4.
8. M. M. Fejer, G. A. Magel, D. H. Jundt, and R. L. Byer, IEEE J. Quantum Electron. **28,** 2631 (1992).
9. G. M. Macfarlane, A. S. Bell, E. Rais, and A. I. Fegurson, Opt. Lett. **21,** 534 (1996).
10. G. Imeshev, A. Galvanauskas, D. Harter, M. A. Arbore, M. Proctor, and M. M. Fejer, Opt. Lett. **23,** 864 (1998).
11. P. E. Powers, T. J. Kulp, and S. E. Bisson, Opt. Lett. **23,** 159 (1998).

Accuracy of optical frequency comb generation in optical fiber

K. Imai

Interdisciplinary Graduate School of Science and Engineering, Tokyo Institute of Technology, 4259 Nagatsuta, Midori-ku, Yokohama 226-8502 Japan

Y. Zhao

Department of Electrical Engineering, University of Sydney, Sydney NSW 2006, Australia

M. Kourogi

Interdisciplinary Graduate School of Science and Engineering, Tokyo Institute of Technology, 4259 Nagatsuta, Midori-ku, Yokohama 226-8502 Japan, and Kanagawa Academy of Science and Technology, Takatsu-ku, Kawasaki, Kanagawa 213 Japan

B. Widiyatmoko

Interdisciplinary Graduate School of Science and Engineering, Tokyo Institute of Technology, 4259 Nagatsuta, Midori-ku, Yokohama 226-8502 Japan

M. Ohtsu

Interdisciplinary Graduate School of Science and Engineering, Tokyo Institute of Technology, 4259 Nagatsuta, Midori-ku, Yokohama 226-8502 Japan, and Kanagawa Academy of Science and Technology, Takatsu-ku, Kawasaki, Kanagawa 213 Japan

Received October 14, 1998

We evaluated the accuracy of an optical frequency comb in optical fibers by measuring the frequency shift after a sideband from an electro-optic modulator had passed through the fiber. We found that a frequency drift of a few hertz was due largely to a variation in the ambient temperature that corresponded to an increase in the square root of the Allan variance to 0.66 Hz. © 1999 Optical Society of America

OCIS codes: 120.3930, 120.5050, 060.4370, 230.4110.

An optical frequency comb (OFC) generated from an efficient electro-optic (EO) modulator was successfully applied for accurate measurement of large optical frequency intervals,[1] optical frequency synthesizers, and optical short-pulse synthesizers.[2] We examined the measurement accuracy by comparing this device with others used for optical difference frequency measurement, such as optical parametric oscillators[3] and optical frequency internal dividers.[4] It was shown[4] that the accuracy of the two approaches agreed within the experimental limit of 6.8×10^{-15}.[4]

Recently, we applied self-phase modulation (SPM) in optical fibers to the output of a conventional electro-optic OFC generator (OFCG).[5] An OFC span of 50 THz was obtained by SPM in the fiber by use of the high-intensity pulse train from a conventional OFCG.[6] This is a fivefold increase in frequency span from that of a conventional OFCG at a wavelength of ~1.55 μm. The sidebands created by SPM were those that are characteristic of a narrow linewidth.[6]

The frequency fluctuations of an OFC that were generated by SPM in an optical fiber has not been observed previously to our knowledge. Long-term stability of the sidebands is essential to optical frequency measurements for which an OFC is used. The acoustic noise[7] and the temperature and intensity dependence of the refractive index[8] of the optical fiber may induce output frequency fluctuation in the SPM process. In practice, a long length of optical fiber is used to enhance the SPM effect. A temperature change of 1 °C/h may result in a 2-Hz shift at 1.55-μm carrier frequency. In this Letter we report, for the first time to our knowledge, the experimental results of frequency variation measurements of SPM-induced sidebands in optical fibers. Because the accuracy of a conventional OFC is known we compare the frequency of a SPM sideband with that of a conventional OFC.

The experimental setup is shown in Fig. 1. Single-frequency laser diode LD1 at 1.54 μm was used for the input of a conventional OFCG. The output power of 4 mW was amplified to ~30 mW in an erbium-doped optical fiber amplifier (EDFA) in front of a coupled-cavity OFCG (C-C-OFCG).[9] The C-C-OFCG consists of three mirrors. One Fabry–Perot (FP) cavity, which consists of a front and a central mirror, acts as an optical bandpass filter to prevent the modulation sidebands from reflecting into the input direction. The main FP cavity in which an EO phase modulator (EOM) is placed is a FP EO modulator. The modulation frequency was adjusted to 6.06 GHz (= 2× the free spectral range) so the sidebands would resonate in the main FP cavity. The modulation index was 0.6–0.75 rad, and the finesse of the FP cavity was ~600. The OFC was generated with a span of ~7–8 THz. After the OFC passed through the EDFA, the OFC span was increased to more than 30 THz by SPM in a dispersion-flattened optical fiber (DFF).[10] An average power of ~100 mW from the EDFA was obtained. The inset of Fig. 1 is

0146-9592/99/040214-03$15.00/0

a schematic that compares spectra during various processes. We mixed a common reference laser, LD2, with a sideband in the OFC directly after the OFCG and produced a beat signal at frequency f. A second beat signal, at $f + df$, was produced when LD2 was mixed with the same sideband after the EDFA and the DFF, where df is the frequency drift that is due to the change in environmental conditions in the SPM process. Another signal, at 57 MHz from a rf synthesizer, was used to mix the two beat signals. A bandpass filter for the 57-MHz signal, with a bandwidth of 3 MHz, was used to filter out any nonuseful frequencies. df, together with the 57-MHz modulation signal, is shown on a frequency counter.

To investigate the effect of spectral broadening, we also measured the frequency difference without the OFC generator as a reference. Without the OFC generator the frequency of LD2 was close to that of LD1. The average power propagating in the fiber was low enough to suppress SPM. Figure 2 shows the frequency difference between two beat signals generated before and after the sideband passed through the EDFA and the DFF. The gate time of the frequency measurement was 10 s. For simplicity we show 400 experimental points from a total of 3000 measurements. Figure 2 shows the difference between the offset frequency and the rf synthesizer frequency. It can be seen that the frequency fluctuation is periodic and has an amplitude of ~2 Hz. The period of 700 s was due to the room-temperature variation caused by an air conditioner. This temperature variation caused an average frequency fluctuation of ~0.24 Hz during 4000 s. We confirmed the temperature dependence of the frequency by turning off the air conditioner. In the uncontrolled condition the period was longer than 5000 s.

Figure 3 shows the measured frequency difference between the sideband that is 1.7 THz off the carrier frequency of LD1 from the EO modulator and the same sideband when it passed through the optical fiber and the amplifier. We chose the sideband such that we obtained a sufficiently high signal-to-noise ratio from the conventional OFCG. The measurement was carried out 100 times with a gate time of 10 s. Only 84 experimental points are included in the figure, except for incorrect counting at beginning and end of the measurement. The two beat signals had a signal-to-noise ratio of more than 40 dB at 1-MHz bandwidth. The signal-to-noise ratio of the i.f. signal from the second double-balanced mixer was decreased to 30 dB but was still sufficient to permit the frequency counter to work correctly. Because the intensities of SPM sidebands are sensitive to the output power of a conventional OFCG, the output power fluctuation caused incorrect counting. We had to suppress the output power fluctuation of the C-C-OFCG to less than approximately 5% of the average. Because environmental conditions outside the laboratory were different, a periodic change was not observed. Because the measurement time was not long enough, the measured frequency shift of the SPM sideband from the EOM sideband was 1.2 Hz on average. It was difficult for the C-C-OFCG to suppress the intensity fluctuation for more than 1000 s. The stability of the intensity depended not only on the bandwidth of the cavity length control but also on the stability of the carrier laser.

Figure 4 shows the square root of the Allan variance of the measured frequencies. The open circles show the frequency difference between the two carrier frequencies. The filled circles show the sidebands before and after the EDFA and the DFF. Because the experimental setup is similar to that of a delayed self-heterodyne method, the fluctuations of the carrier frequencies of the lasers are measured in addition to the thermal or acoustic fluctuation of the sideband. The measured Allan variance depends on the linewidth of the lasers and the time delay that is due to the optical fiber. The solid curve is the result of a theoretical calculation that we derived from the following equation by assuming a typical frequency fluctuation of laser diodes:

$$\sigma_y^2(\tau) = 2\int_0^\infty S_y(f)\,|1 - \exp(j2\pi f\tau_d)|^2\,\frac{\sin^4(\pi f\tau)}{(\pi f\tau)^2}\,df, \tag{1}$$

where S_y and τ_d are the one-sided power spectral density of the frequency fluctuation of lasers and the delay time that is due to a 1-km optical fiber, respectively. We assumed typical FM noise from an

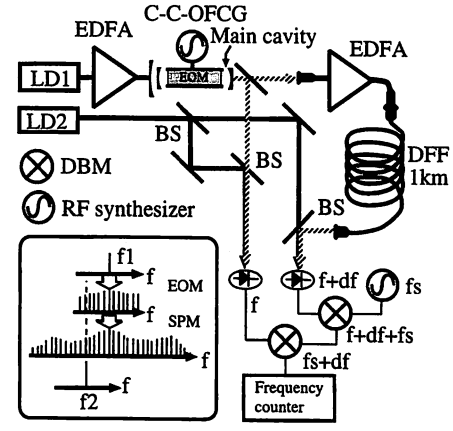

Fig. 1. Experimental setup for comparison of two combs generated by electro-optic modulation and self-phase modulation. LD1, LD2, extended-cavity laser diodes; BS's, beam splitters; DBM, double-balanced mixer; EOM, EO modulator; other abbreviations are defined in text. Inset, schematic explanation of the frequency comparison.

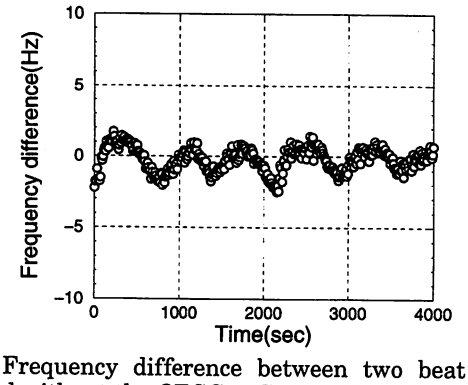

Fig. 2. Frequency difference between two beat signals measured without the OFCG. Gate time, 10 s.

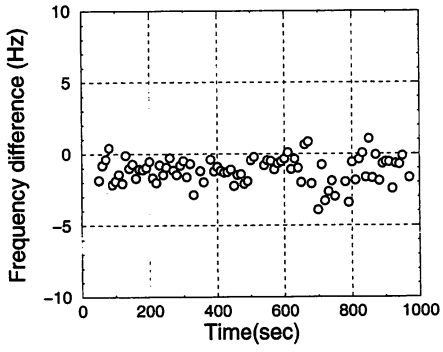

Fig. 3. Measured frequency difference between the EO modulation sideband and the SPM sideband. Gate time, 10 s.

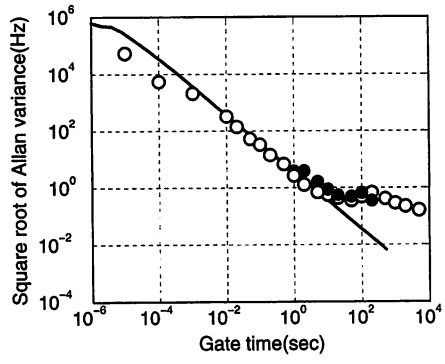

Fig. 4. Square root of the Allan variance of the frequency difference without (open circles) and with (filled circles) OFC generators. Solid curve, result of theoretical calculation derived by assumption of a typical frequency fluctuation in the laser diode.

extended-cavity semiconductor laser diode, which consists of $1/f$ noise up to 100 kHz and white frequency noise. We determined the white frequency noise from the linewidths of the lasers by assuming that both laser linewidths were 50 kHz. The delay time was 5 μs for a 1-km optical fiber. The theoretical result can be approximated as $5\tau^{-1}$ for gate times τ longer than 10^{-4} s. The result measured without the OFCG was in good agreement with the theoretical result at $10^{-2} \leq \tau \leq 5$ s. Because of this delay, phase variations that were due to the acoustic noise could not be observed. Although the Allan variances for the sideband were larger than that of the carrier for $\tau < 10$ s, the slope was same as for the theoretical result. The effect of the temperature variation was observed near $\tau = 100$–200 s. The Allan variance was increased to 0.66 Hz for the sideband at $\tau = 100$ s and to 0.67 Hz for the carrier at $\tau = 200$ s. These gate times correspond to approximately the half-period of the variation of the measured frequencies. The measured Allan variances show that the main frequency fluctuation of the SPM sidebands originated from temperature drift even though the spectral broadening owing to SPM was efficient. Therefore the phase shift owing to the power drift in SPM was negligible.

Although the measured frequency shift suggests that the sideband frequencies drifted following the SPM process in optical fibers, the accuracy of the sideband separation remained high. The shifts experienced by the sidebands and the carrier frequencies were different, but the effect on measurement of the difference frequency was manageable. For example, if the carrier frequency shift is 2 Hz, the normalized accuracy in the difference-frequency measurement can be maintained at $\sim 1 \times 10^{-14}$. Slow variations are controlled by temperature near the long fiber. For the fast variations, all the sideband fluctuations can be suppressed by an external phase canceler such as an acousto-optic modulator.[7]

In summary, we measured the frequency of the optical sideband generated by self-phase modulation. Frequency fluctuation and drift for both the carrier frequency and the sidebands at 1.7 THz off the carrier were experimentally determined. The square root of the Allan variance was increased to 0.66 Hz at a gate time of 100 s. We found that frequency fluctuation was caused mainly by variations in ambient temperature, which could be managed by use of a temperature controller and an external phase controller.

K. Imai's e-mail address is imai@ae.titech.ac.jp.

References

1. M. Kourogi, K. Nakagawa, and M. Ohtsu, IEEE J. Quantum Electron. **29,** 2693 (1993).
2. D.-S. Kim, M. Arisawa, A. Morimoto, and T. Kobayashi, IEEE J. Sel. Topics Quantum Electron. **2,** 493 (1996).
3. S. Slyusarev, T. Ikegami, S. Ohshima, and E. Sakuma, Opt. Commun. **135,** 223 (1997).
4. T. Udem, M. Kourogi, J. Reichert, and T. W. Hänsch, Opt. Lett. **23,** 1387 (1998).
5. K. Imai, M. Kourogi, and M. Ohtsu, IEEE J. Quantum Electron. **34,** 54 (1998).
6. K. Imai, M. Kourogi, B. Widiyatmoko, and M. Ohtsu, in *Conference on Lasers and Electro-Optics (CLEO'98),* Vol. 6 of 1998 OSA Technical Digest Series (Optical Society of America, Washington, D.C., 1998), paper CThY4, pp. 472–473.
7. L.-S. Ma, P. Jungner, J. Ye, and J. L. Hall, Opt. Lett. **19,** 1777 (1994).
8. T. Yoshino, K. Kurosawa, K. Itoh, and T. Ose, IEEE J. Quantum Electron. **18,** 1624 (1982).
9. M. Kourogi, T. Enami, and M. Ohtsu, IEEE Photon. Technol. Lett. **8,** 1698 (1996).
10. Y. Kubo, H. Kanamori, H. Yokota, and S. Tanaka, in *European Conference on Optical Communication (ECOC '90)* (Eindhoven U. of Technology, Eindhoven, The Netherlands, 1990), pp. 505–508.

OPTICAL REVIEW Vol. 5, No. 5 (1998) 267-270

Continuous Wavelength Sweep of External Cavity 630 nm Laser Diode without Antireflection Coating on Output Facet

Takuya NAYUKI,[1] Takashi FUJII,[1,*] Koshichi NEMOTO,[1] Mikio KOZUMA,[2] Motonobu KOUROGI[2] and Motoichi OHTSU[2]

[1]*Electrical Physics Department, Komae Research Laboratory, Central Research Institute of Electric Power Industry, 11-1, Iwado Kita 2-chome, Komae, Tokyo, 201-8511 Japan*

[2]*Interdisciplinary Graduate School of Science and Engineering, Tokyo Institute of Technology, 4259, Nagatsuta, Midori-ku, Yokohama, Kanagawa, 226-8502 Japan*

(Received June 5, 1998; Accepted July 3, 1998)

We developed a simple method of continuous wavelength sweep using a commercial laser diode (LD) without antireflection (AR) coating. A 630 nm AlGaInP LD was installed in a Littrow-type external cavity. In this cavity, the LD has the same effect as an etalon, and its free spectral range can be controlled easily by the LD drive current. By scanning the grating angle of the external cavity and LD drive current simultaneously, we obtained single-mode oscillation and continuous wavelength sweep of over 22 GHz without mode hopping. This technique is simple and inexpensive because it does not need AR coating on its output facet, and does not use a servo system which requires apparatuses such as a lock-in amplifier and local oscillator.

Key words: laser diode, external cavity, wavelength tuning, short wavelength, antireflection coating

1. Introduction

For spectroscopic applications of a laser diode (LD), the laser frequency must be tuned precisely to various atomic absorption spectra. Distributed feedback (DFB) and distributed Bragg reflector (DBR) lasers can oscillate in a single mode and tune their frequency continuously, however, LDs with short wavelengths of about 600 nm have conventional Fabry-Perot structures. Therefore, in this case, an external cavity is necessary to obtain a narrow spectrum and single-mode oscillation, and the LD output facet is usually antireflection (AR) coated for wide-range continuous wavelength tuning.[1,2] The application of an AR coating to the output facet of a LD, however, requires special equipment and the process sometimes causes breakdown of the LD. Moreover, wavelength selection elements, such as an etalon, are necessary for single-mode oscillation when the Littrow-type external cavity[3-6] is applied to the AR-coated LD because the resolution of a diffraction grating is not high enough to reduce the spectral bandwidth. It was recently reported that the laser frequency of a commercial 670 nm LD without AR coating was tuned continuously over a range of 18 GHz by incorporating a grating feedback external cavity.[7] The etalon which is usually required in single-mode oscillation can be removed because the laser cavity of the LD without AR coating is short enough to act as an etalon, and its free spectral range (FSR) can be controlled easily by the drive current. However, in this LD frequency control method, the diode drive current was controlled along with the external-cavity length with electrical negative feedback. This required additional apparatuses of a lock-in amplifier and a local oscillator.

In this paper, we report a simpler method which does not involve electrical negative feedback control, but only simultaneous scanning of the diode drive current and the diffraction grating angle of the external cavity at an appropriate rate. We used this technique to develop a continuous wavelength-tunable 630 nm AlGaInP LD, which has the shortest wavelength among all commercial LDs, and analyzed its wavelength tuning characteristics using a simple model.

2. Littrow-Type External Cavity LD and Experimental Setup

Index-guided AlGaInP LD (SDL-7501-G1), the output facet of which was not AR coated, was installed in the Littrow-type external cavity LD.[8] The lasing wavelength λ_0 of this LD was 628 nm without an external cavity at a room temperature of 25°C. Figure 1 shows the arrangement of the external cavity with respect to the LD. The output beam from the LD was collimated by a lens and irradiated onto a grating mounted on an aluminium block. The zero-order diffracted beam from the grating was used as the output beam, and the first-order diffracted beam was returned to the LD output facet using a long-focal-length lens. The grating was rotated around point C which is a vertex of the rectangle OACB in this figure. OA is the optical axis of the LD output beam, and AB is the line extrapolated from the surface of the diffraction grating. The rotation of the grating was electrically controlled by a piezoelectric transducer (PZT). The operating temperature of the LD was kept at 25°C using a platinum-resistance thermometer and a thermo-electric cooler. Figure 2 shows a block diagram of the experiment for wavelength control. For continuous wavelength tuning of the LD, the grating angle and the LD drive current were controlled using a personal computer. The output signals from the computer were converted into analog values by a D/A converter, and fed to the PZT driver and the LD driver. The lasing spectrum and the wavelength tuning characteristics of the Littrow-type external cavity LD were measured by a

*E-mail: fujii@criepi.denken.or.jp

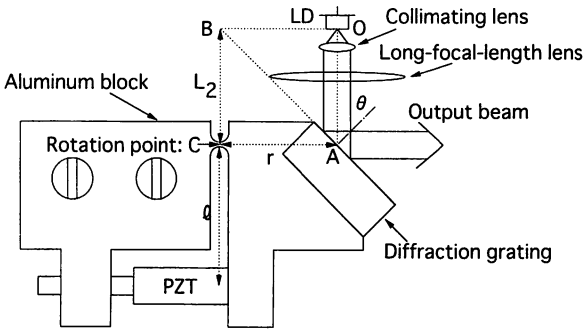

Fig. 1. Configuration of Littrow-type external cavity LD.

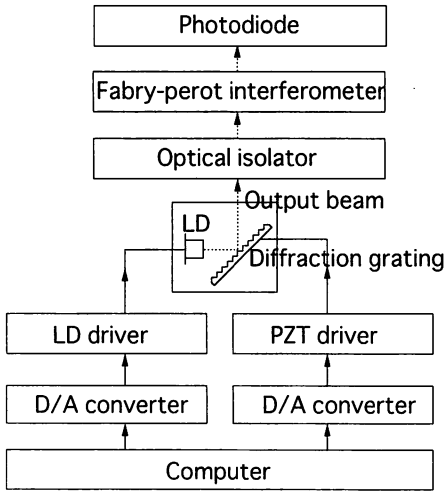

Fig. 2. Block diagram of the experiment for wavelength control of Littrow-type external cavity LD.

Fabry-Perot interferometer (FPI). An optical isolator was placed between the Littrow-type external cavity LD and the FPI to prevent a retroreflected beam from the FPI.

3. Theory of Continuous Wavelength Tuning Using Two-Resonator Model

For single-mode oscillation and continuous wavelength sweeping, the following three spectra must be tuned synchronously:

(a) Spectrum of the first diffracted beam from the grating
(b) Longitudinal-mode spectrum of the external cavity
(c) Longitudinal-mode spectrum of the LD

Resolution of the diffraction $\Delta\nu$ is determined from the effective irradiated region and the number of grooves per unit length of the diffraction grating. In our experiment, since the groove number is 1800/mm, $\Delta\nu$ is estimated to 26 GHz. The longitudinal mode interval, which is determined from the FSR of the external cavity between the diffraction grating and the LD output facet, is about 6 GHz. Generally, in the case of a commercial LD, the width of the gain curve is about 20 nm, and the interval between the longitudinal modes is about 100 GHz. Spectra (a) and (b) are also considered in the case of a Littrow-type external cavity LD with AR coating on its output facet, and (c) is added when using the LD without AR coating. The operating temperature and drive current of the LD can be used as parameters to control the longitudinal mode spectrum of the LD. However, in the case of fast frequency control, it is adequate to keep the operating temperature constant and to vary the drive current, considering the response time of each parameter. The spectrum of the first-diffracted beam from the grating depends on the angle of the grating, while the longitudinal-mode spectrum of the external cavity depends on the external cavity length. In the Littrow-type grating configuration, by determining the rotation axis of the grating, the spectrum of the first-diffracted beam from the grating and the longitudinal mode spectrum of the external cavity can be scanned at the same speed.[9,10] Therefore, spectra (a), (b) and (c) can be scanned at the same speed by controlling the LD drive current and the grating angle of the external cavity simultaneously.

We consider the method of controlling the LD drive current and the grating angle of the external cavity for continuous wavelength sweeping. In this case, we can consider two independent cavities. One is a short cavity A, which is defined by the two facets of the LD and has an optical length of L_1; this cavity has the same function as an etalon. The other is a long cavity B, which is defined by the output facet of the LD and the grating and has an optical length of L_2. In order to shift the laser wavelength by $\Delta\lambda$ without mode hopping, L_1 and L_2 must be controlled so that the number of longitudinal modes, N_1 and N_2 of cavity-A and cavity-B, respectively, are not changed. The relation between the laser wavelength λ and the optical cavity lengths is as follows:

$$L_1=N_1\lambda/2,\ L_2=N_2\lambda/2\,. \tag{1}$$

Therefore, when the laser wavelength is changed by $\Delta\lambda$, changes of L_1 and L_2 are shown using

$$\Delta L_1=N_1\Delta\lambda/2,\ \Delta L_2=N_2\Delta\lambda/2\,. \tag{2}$$

By eliminating N_1 and N_2 from Eqs. (1) and (2), we obtain

$$\Delta L_2=\Delta L_1\times L_2/L_1\,. \tag{3}$$

In order to sweep the laser wavelength without mode hopping, L_1 and L_2 must be changed while satisfying Eq. (3). ΔL_2 can also be expressed using $\Delta\theta$ by

$$\Delta L_2=r\Delta\theta \tag{4}$$

where r is the distance between the irradiated spot of LD beam on the grating and rotation axis of the grating, and $\Delta\theta$ is the change of θ which is the angle of incident of LD output beam with respect to the grating. In the Littrow configuration, to return the first-diffracted beam to the LD output facet, the following equation must be satisfied:

$$2d\sin\theta=\lambda\,, \tag{5}$$

where d is the groove interval of the grating. From Eqs. (1), (2) and (5), the condition that the first-diffracted beam from the grating always returns to the LD output facet when the grating angle is changed is given by

$$\Delta L_2 = N_2 d\cos\theta\Delta\theta = 2L_2 d\cos\theta\Delta\theta/\lambda = L_2\Delta\theta/\tan\theta . \quad (6)$$

From Eqs. (4) and (6), the geometrical relation of θ, L_2 and r is given by

$$\tan\theta = L_2/r . \quad (7)$$

In our experiment, L_2=26 mm and r=38 mm.

Next, we calculate an optimum sweeping ratio of the LD driving current ΔI_{LD} versus the grating angle variation. The relation between $\Delta\lambda$ and ΔI_{LD} is given by

$$\Delta\lambda = \beta\Delta I_{LD} , \quad (8)$$

where β is the proportional constant which determines the wavelength change relative to the drive current of the LD. Substitution of Eqs. (1), (2), (4) and (8) into Eq. (3) yields

$$\Delta I_{LD} = (\lambda r)/(\beta L_2)\Delta\theta . \quad (9)$$

By eliminating L_2 from Eqs. (7) and (9), we obtain

$$\Delta I_{LD} = \lambda/(\beta\tan\theta)\Delta\theta . \quad (10)$$

Equation (10) must be satisfied to control the wavelength without mode hopping. In our experiment, the values of λ, θ, and β are 628 nm, 34 deg. and 5×10^{-3} nm/mA,* respectively. Substitution of these values into Eq. (10) yields

$$\Delta I_{LD}[\mathrm{mA}] = 1.8\times10^5\Delta\theta[\mathrm{rad}] . \quad (11)$$

From the geometrical configuration shown in Fig. 1, $\Delta\theta$ can be expressed by $-\delta\Delta V_{PZT}/l$ where δ is the change of the PZT length versus applied voltage, ΔV_{PZT} is the variation of the voltage applied to the PZT and l is the length between the PZT and the rotation point C of the grating. Therefore, the continuous wavelength sweeping condition is:

$$\Delta I_{LD}[\mathrm{mA}] = -\lambda/(\beta\tan\theta)\delta\Delta V_{PZT}/l[\mathrm{V}] . \quad (12)$$

In using the LD, the output facet of which is not AR coated with a Littrow-type external cavity, we can sweep the laser wavelength continuously by scanning the LD drive current and the grating angle of the external cavity simultaneously, using the proportions shown in Eq. (12). In this experiment, since the values of δ and l were 0.15 μm/V and 32 mm, respectively, the proportional ratio of the LD drive current to the PZT applied voltage for continuous wavelength sweeping was -0.84 mA/V.

4. Experimental Results

Figure 3 shows the lasing spectra of the Littrow-type external cavity LD. The spectra was measured by scanning the cavity length of the FPI, the FSR and finesse of which are 2 GHz and 300, respectively. The single-mode oscillation and spectrum narrowing of the LD was obtained by constructing the external cavity. The linewidth was estimated to less than 30 MHz from the FSR of the FPI. This value was the limit of measurement determined by the finesse of the FPI and the accuracy of the optical alignment in measurement.

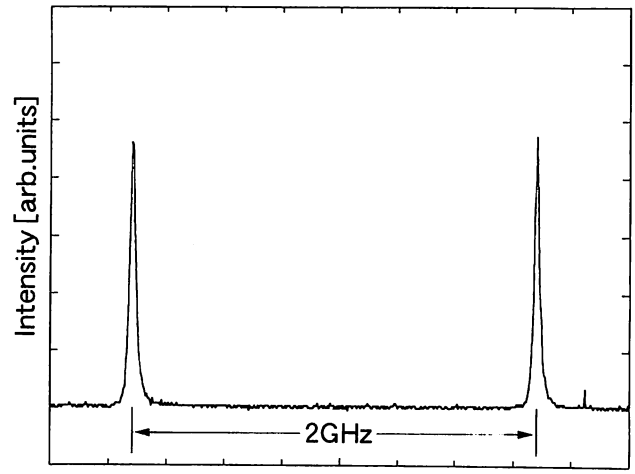

Fig. 3. Lasing spectrum of Littrow-type external cavity LD measured by scanning FPI.

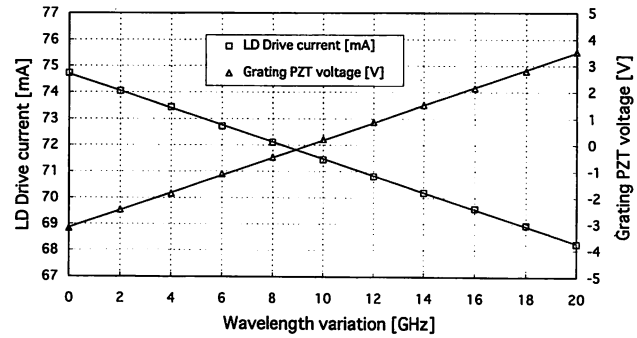

Fig. 4. Variation of LD drive current and voltage applied to PZT used to control the diffraction grating angle for continuous wavelength sweeping.

We carried out a continuous wavelength sweep without mode hopping of the Littrow-type external cavity LD by changing the grating angle and the LD drive current simultaneously using a personal computer. The continuous wavelength sweep range was measured by monitoring the transmitted laser power through the FPI of which cavity length was fixed. We examined several LD current control ratios to the PZT applied voltage. The largest continuous wavelength sweep range was obtained when the PZT applied voltage was changed over a range of 7.76 V linearly with time, and the LD drive current was likewise decreased from 75.4 mA to 67.9 mA. The optimum proportional ratio was -0.97 mA/V in the experiment, while the expected optimum ratio by calculation was -0.84 mA/V. Therefore, Eq. (12) gives us a good approximation of the optimum sweeping ratio. The uncertainty of β value and nonlinearity of the PZT characteristics are considered to be causes of the difference between experimental and calculated results. With this optimum sweeping ratio, we observed eleven transmission peaks of the FPI with intervals of 2 GHz during one control cycle of the grating angle and the LD drive current; from this

*Value quoted in supplier's catalog.

result, the range of continuous wavelength sweep is estimated to be more than 20 GHz. Figure 4 shows the voltage applied to the PZT and the LD drive current when the wavelength was varied continuously by over 20 GHz. We also measured the continuous wavelength sweep of this device using a wavemeter, and obtained a sweep of 22 GHz, which is from 477.200 THz to 477.222 THz. The result obtained using the FPI is therefore reasonable. The continuous wavelength sweeping range was limited in this experiment by the performance of the LD and the PZT drivers.

5. Conclusions

In conclusion, we developed a Littrow-type external cavity LD using a commercial 630 nm LD, the output facet of which was not AR coated. The LD acts as an etalon because the cavity length of the LD is much shorter than that of the external cavity. We demonstrated single-mode oscillation and the LD continuous wavelength sweep of over 22 GHz without mode hopping by scanning the grating angle of the external cavity and the LD drive current linearly and simultaneously. This experimental result agrees with that calculated using the simple model which consists of an etalon and an external cavity. The Littrow-type external cavity LD developed in this study has the following advantages. First, it does not require AR coating on its output facet. Secondly, wavelength selection devices, such as an etalon, are not required. Thirdly, the system is simple and inexpensive because it does not use a servo system which requires expensive apparatuses such as a lock-in amplifier and a local oscillator.

Acknowledgments

The authors thank Dr. S. Sasaki, Dr. S. Yokoyama and Dr. Y. Nakano of CRIEPI for their useful advice.

References

1) M.G. Boshier, D. Berkeland, E.A. Hinds and V. Sandoghdar: Opt. Commun. 85 (1991) 355.
2) H. Asakura, K. Hagiwara, M. Iida and K. Eda: Appl. Opt. 32 (1993) 2031
3) T.W. Hansch: Appl. Opt. 11 (1972) 895.
4) S. Filimonov and J. Borysow: Appl. Opt. 34 (1995) 438.
5) P. Zorabedian: J. Lightwave Technol. 10 (1992) 330.
6) P. Zorabedian: IEEE J. Quantum Electron. 30 (1994) 1542.
7) S.N. Atutov, E. Mariotti, M. Meucci, P. Bicchi, C. Marinelli and L. Moi: Opt. Commun. 107 (1994) 83.
8) T. Fujii, T. Nayuki, K. Nemoto, M. Kozuma, M. Kourogi and M. Ohtsu: Jpn. J. Appl. Phys. 35 (1996) 6090.
9) F. Favre, D. Le. Guen, J.C. Simon and B. Landousies: Electron. Lett. 22 (1986) 795.
10) M. de Labachelerie, C. Latrasse, P. Kemssu and P. Cerez: J. Phys. III Fr. 2 (1992) 1557.